Title
Bending, Buckling, Tumbling, Trapping: Viscous Dynamics of Elastic Filaments

Author
Manikantan, Harishankar

Publication Date
2015

UNIVERSITY OF CALIFORNIA, SAN DIEGO

Bending, Buckling, Tumbling, Trapping: Viscous Dynamics of Elastic Filaments

A dissertation submitted in partial satisfaction of the
requirements for the degree
Doctor of Philosophy

in

Engineering Sciences (Applied Mechanics)

by

Harishankar Manikantan

Committee in charge:

Professor David Saintillan, Chair
Professor Bo Li
Professor Stefan G. Llewellyn Smith
Professor Alison L. Marsden
Professor William R. Young

2015

The dissertation of Harishankar Manikantan is approved, and it is acceptable in quality and form for publication on microfilm or electronically:

Chair

University of California, San Diego

2015

EPIGRAPH

… I have sought knowledge. I have wished to understand the hearts of men. I have wished to know why the stars shine. And I have tried to apprehend the Pythagorean power by which number holds sway above the flux.

A little of this, but not much, I have achieved.

— The Autobiography of Bertrand Russell

TABLE OF CONTENTS

LIST OF FIGURES

ACKNOWLEDGEMENTS

In a PhD that has taken me geographically (and perhaps metaphorically) to the brutal winters of the Midwest and the sunny shores of California, I have amassed a long list of people who deserve more gratitude than a passing mention on these pages. But I shall try to do some justice to recognize their parts, small or big, in what has been an incredibly enriching journey.

I begin by sincerely thanking David Saintillan for teaching me not just the skills, but also the art of scientific exploration. His encouragement, combined with his generosity with time and resources has enabled me to explore so many avenues of academic curiosity – all of which have gone a long way into shaping this work, and through it, my own outlook towards teaching and research. I am indebted to David for his mentorship, and for being an ideal to strive towards.

I also express my gratitude to the Theoretical and Applied Mechanics program at the University of Illinois at Urbana-Champaign, and the wonderful instructors there who first exposed me to the beauty of mathematics and fluid dynamics in my many foundational graduate classes. Particular mention is due to Sascha Hilgenfeldt who, apart from being a great teacher, has been a motivating and supportive figure in my academic growth. And I thank the faculty and administration here at UC San Diego for fostering me, and for making me one of their own. Specifically, I wish to thank Stefan Llewellyn Smith, Bill Young, Alison Marsden and Bo Li for their time, comments and encouraging words en route to completing this dissertation.

I thank Saverio Spagnolie for sharing with me his initial ideas on sedimentation, and along with them his contagious enthusiasm for similar problems. I have learnt and benefited a lot through the course of a very fruitful collaboration with Saverio and his student Lei Li. I also thank Anke Lindner, Olivia du Roure, and Nawal Quennouz at ESPCI ParisTech, Vasily Kantsler and Raymond Goldstein at Cambridge, Michael Shelley at the Courant Institute, and Randy Ewoldt at UIUC for enlightening discussions on various aspects of this work.

I am grateful to the members of the Saintillan group for the countless discussions, laughs, and lunches we have shared. When I started off, Jae Sung Park was as resourceful in teaching me the intricacies of graduate student life as he was in opening my eyes to the delights of Korean BBQ. Work wouldn't be half the fun if I did not share my office for five years with Debasish Das, whose dedication to the boundary integral method is matched only by his wry sense of humor. Barath Ezhilan, Ku Da, Adrien Lefauve, Roberto Alonso, Maxime 'Minime' Bollard, and Maxime 'Max' Theillard have all helped me learn and develop into what I am today – academically and personally. Thank you guys!

I also wish to recognize the tremendous impact of a dedicated high school physics teacher on my academic life. Malarvizhi Madam, through four years of fantastic instruction and mentoring, sparked in me this interest in the physical and mathematical sciences which has lead me here.

Outside of work, I will cherish the friendships that have played influential roles in these past years. I thank my buddies from Surathkal for believing in me, for patiently being in touch even when I missed the many long-overdue calls from across the planet, and for their constant support. Bhargav Rallabandi, especially, has been my go-to person for about a decade now for discussions ranging from gastronomy to astronomy and everything in between. I won't name every one of them, but I am truly grateful to a whole lot of folks in Champaign-Urbana, my housemates at Pacific Beach, the UCSD racquetball group, and the lunch bunch in La Jolla, for throwing craziness of different degrees at me, and through that, making me feel at home at each of these places.

I thank my parents for their selfless love and for always doing what was best for me. They have believed in and supported me through every one of my adventures – foolish or brave, obvious or obscure – and for that I am eternally grateful. I sincerely hope I have made them proud.

And finally, I am thankful beyond words to Bindu for being the most insistent supporter of my possibly unpragmatic career choice, and for not giving up when I moved to San Diego. In an otherwise hazy world, she continues to provide clarity and comfort.

Financial support for this work came from the National Science Foundation through Grants No. CBET-1150590 and No. CBET-1532652, the University of Illinois Research Board, an FMC Educational Fund Fellowship, and numerous teaching appointments at the University of Illinois at Urbana-Champaign.

This dissertation borrows in large parts, as listed below, from published or prepared manuscripts.

- A part of Chapter 2 is based on the Master's thesis by Harishankar Manikantan, submitted in May 2012 at the University of Illinois at Urbana-Champaign [1].
- Chapter 2 also contains material that has appeared in *Physical Review E* (2015), authored by Harishankar Manikantan and David Saintillan [2].
- Chapter 3 is based largely on material that has appeared in *Physics of Fluids* (2013), authored by Harishankar Manikantan and David Saintillan [3].
- Chapter 4 is based largely on material that has appeared in *Journal of Fluid Mechanics* (2013), authored by Lei Li, Harishankar Manikantan, David Saintillan, and Saverio E. Spagnolie [4].
- Chapter 5 is based largely on material that has appeared in *Journal of Fluid Mechanics* (2014), authored by Harishankar Manikantan, Lei Li, Saverio E. Spagnolie, and David Saintillan [5].
- The material in Chapter 6 is being considered for publication in *Physics of Fluids* (2015), authored by Harishankar Manikantan and David Saintillan.

VITA

2010	B. Tech. in Mechanical Engineering, National Institute of Technology, Surathkal (India)
2010 - 2013	Graduate Research and Teaching Assistant, University of Illinois at Urbana-Champaign
2012	M. S. in Theoretical and Applied Mechanics, University of Illinois at Urbana-Champaign
2014 - 2015	Graduate Research Assistant, University of California, San Diego
2015	Ph. D. in Engineering Sciences (Applied Mechanics), University of California, San Diego

ABSTRACT OF THE DISSERTATION

Bending, Buckling, Tumbling, Trapping: Viscous Dynamics of Elastic Filaments

by

Harishankar Manikantan
Doctor of Philosophy in Engineering Sciences (Applied Mechanics)

University of California San Diego, 2015

Professor David Saintillan, Chair

Elastic filaments subjected to hydrodynamic forcing are a common class of fluid-structure interaction problems. In biology, they are crucial to cytoskeletal motions of the cell, the locomotion of micro-organisms, and mucal transport. In engineering, they are often the source of non-Newtonian rheological properties and a variety of complex fluid behavior such as hydrodynamic instabilities and chaotic mixing. At the heart of many of these dynamics is the competition between an elastic backbone and viscous forces acting to deform it, tangled with the anisotropic shape of such filaments as well as slowly decaying hydrodynamic interactions in a Stokesian fluid. In this work, we use slender-body theory for low-Reynolds-number hydrodynamics to address theoretically and computationally a few such problems of physical and biological significance. We first describe the tumbling of polymers in shear flow and the suppression of thermal fluctuations in extensional flow. A theory for the stretch-coil transition of semiflexible polymers is also developed. We then turn to the transport properties of semiflexible filaments in a flow setup that mimics some of the dynamics of biological polymers in motility assays. Thermal fluctuations frequently trap polymers within vortical cells, and are shown to lead to subdiffusive transport at long times. The mechanism behind this anomalous feature and the subtle role of flexibility is emphasized. Then we focus on the sedimentation of flexible filaments. In the weakly flexible regime, a multiple-scale asymptotic expansion is used to obtain expressions for filament shapes and peculiar trajectories. In the highly flexible regime, we show that a filament sedimenting along its long axis is susceptible to a buckling instability. Our predictions are corroborated by detailed numerical simulations. Finally, we look at suspensions of sedimenting elastic fibers, emphasizing the role of filament shape, flexibility, and long-ranged hydrodynamic interactions. We develop a mean-field theory for such a suspension, and its stability to perturbations of fiber concentration is analytically explored. Detailed numerical simulations are also performed to verify these predictions and elucidate the microstructural mechanisms tied to the growth or suppression of this instability.

Chapter 1

Introduction

Nature abounds with ingenious examples of rendering dynamical capabilities at the cellular level. These abilities require structural or functional elements with properties that enable them to perform, in a very efficient fashion, the basic tasks of locomotion, reproduction and growth. The deformation and transport of elastic filaments in viscous fluids play central roles in many of them. In cellular biology, stiff biopolymers confer to cells their mechanical properties [6] and are essential for functions as diverse as cell division, differentiation and morphogenesis [7, 8], cell motility [9, 10], reproduction [11, 12], mucus transport [13], wound healing [14], and hearing [15], among others. These are biological polymers that are highly inextensible and with a rigidity that energetically suppresses bending [16]. Actin filaments comprise the cytoskeleton of most eukaryotic cells. With their resistance to tensile and compressive forces at the subcellular scale, they play highly versatile roles in motility, cellular shape changes and mechanical support. Microtubules (rope-like polymers of tubulin proteins) are stiffer and play critical roles in maintaining cell structure, intracellular transport and cell reproduction. Flagella are tail-like protrusions from a cell body that lash back and forth like a whip, and are responsible for locomotion of many micro-organisms and cells like spermatozoa. Cilia are similar slender protuberances that play roles in mobility and sensing. And of course, one of the most critical and well known macromolecules in all known life forms is Deoxyribonucleic acid (DNA). These single or double stranded polymers of simple units called nucleotides are contained in the nucleus or the cytoplasm, and carry genetic instructions that are passed on across generations of cells. DNA has, over the years, gained the attention of scientists outside of biology too - its applications in forensics, bioinformatics, nanotechnology and anthropology are widespread. The dynamics of DNA in a fluid have been studied in detail [17, 18], and both experiments and numerical simulations have established that the dynamics of such chains are governed by the competition of entropic forces that favor coiled configurations versus viscous flow forces that can cause unraveling and stretching [17, 19–21]. This competition is at the origin of the viscoelastic properties of DNA solutions [17, 22], which can lead to hydrodynamic instabilities [23, 24] and spatiotemporally chaotic flows [25].

The case of shorter and stiffer filaments with longer persistence lengths such as actin and microtubules, however, has received much less attention. For such filaments, the dynamics result mainly from the interplay between internal elastic forces that resist bending and ensure inextensibility, and external viscous forces that can cause deformations and hence non-trivial transport properties. When such filaments are placed in a fluid flow or external field, the competition of external forces, viscous stresses, and internal elastic forces can result in complex deformations and dynamics, which in turn can have a significant impact on the macroscopic transport properties of large-scale suspensions. There have been many studies, both experimental and theoretical, of the dynamics of such filaments in various types of microscale flows, including simple shear flow [26–31], extensional flows [2, 32, 33], pressure-driven channel flows [34], vortex arrays [3, 35, 36], and other more complex microfluidic flows [37, 38]. Others have considered the case of a filament subject to either external or internal forces, such as forcing of various types at the filament ends [39, 40], internal actuation [41–43], two-body interactions [44], and self-attraction as a result of capillary interactions [45], to name a few.

Dynamics of flexible fibers in a viscous fluid are also key to understanding many interesting problems in engineering involving a wide range of polymers including xantham gum, carbon nanotubes, and certain elastomers. The non-Newtonian bulk behavior of suspensions can, in many cases, be attributed to the fibers that make up their microstructure [27, 28]. Flexible filaments immersed in viscous fluids are also relevant in understanding the rich and interesting field of soft materials. Synthetic polymers are often encountered in technological applications, specifically in chemical engineering and materials sciences. With recent advances in nanofabrication techniques and experimental capabilities using microfluidic devices [32, 46–48], there has been a renewed interest in the dynamics of macromolecules. For instance, an elastic filament under compression along its backbone can, much like a macroscopic beam, undergo a buckling instability if compressive stresses overcome the elastic restoring force that resists bending. Such buckling events were first noted by Becker and Shelley [27] in simulations of non-Brownian flexible fibers in simple shear flow at high enough strain rate, and the storage and subsequent release of elastic energy during this process has been shown to lead to first normal stress differences [27, 28] as are indeed known to arise in many polymer solutions [22]. Such non-Newtonian rheological properties [49], which can lead to a variety of complex flow behaviors including hydrodynamic instabilities [23, 50] and chaotic mixing [25, 51].

The goal of this work is to explore some problems of biological and physical significance involving elastic filaments immersed in a viscous fluid. In particular, a key objective is to highlight the mechanisms underlying these dynamics, which as we shall discover are the common threads connecting these vastly different problems. We seek to model these polymers in an efficient and robust manner that captures both detailed internal dynamics and long-ranged hydrodynamic interactions. Our theoretical arguments will be aided with numerical simulations, and therefore computational economy is also a key factor. One common feature of the examples listed above is the large aspect ratio of length to characteristic thickness, ranging from order ten to many thousands in some biological settings. This fact has been historically exploited in many ways to develop models describing such polymers. One such model is the *bead-spring model* [52, 53]. Here, a polymer is modeled as a sequence of beads, each offering hydrodynamic resistance to flow of the surrounding medium and connected to each other with springs that provide for elastic and deformational properties of the chain as a whole. This model is appropriate for very long chains, and detailed internal dynamics are not captured. A related class is the *bead-rod model* [54, 55] that uses rigid links with bending moments to connect beads. This latter model is prevalent in the study of short semiflexible biological polymers. However, hydrodynamic interactions are not naturally included in bead-rod models, in which drag only occurs at the beads, and the drag anisotropy of slender polymer segments is not captured by these models, with a few exceptions [55].

A very different approach is based on *slender-body theory* [56–58] for hydrodynamics, which exploits the aforementioned large aspect ratio of the fibers. This model does capture drag anisotropy due to the slenderness, and can be easily extended to include hydrodynamic interactions within and between filaments. This model, along with Euler-Bernoulli elasticity, has been used recently [28, 30, 35] to model non-Brownian flexible filaments in flow. Versions of this model have been used to study the forced dynamics of stiff polymers [40, 59]. The primary appeal of using this model lies in the reduction of a filament-fluid interaction problem to a relatively simple equation describing the filament centerline, along with constraints imposed by the physics of the problem under consideration. Numerical methods based on this approximation have been designed [28] that reduce computational cost as compared to grid based methods that may be required if the problem was not simplified to a set of coupled equations describing the filament centerline. Understanding slender-body theory for creeping flow warrants a brief visit to the world of the extremely small, extremely slow, or extremely gooey: that of *microhydrodynamics*.

1.1 The world of the vanishing Reynolds number

The dynamics of a particle suspended in a fluid, which is the subject of this work in its essence, are governed by Newton's laws of motion. These laws, when written down for material particles inside a volume of the fluid, result in the famous Navier-Stokes equations. However, at scales relevant to the examples we shall restrict ourselves to here, both particle and fluid inertia are negligible compared to the effects of viscous forces. The traditional way of thinking about this is in terms of a vanishing Reynolds number:

$$Re = \frac{\rho U a}{\mu} \to 0. \tag{1.1}$$

Here, U and a are characteristic values of velocity and length of the immersed particle. A quick calculation using the length scales associated with biopolymers (1 to 100 μm), the properties of water (density of 1 kg/m^3 and viscosity of about 10^{-3} Pa $\cdot$ s at room temperature) and motion of such particles in the range of a few body lengths per second tells us that the Reynolds number ranges from 10^{-6} to 10^{-4}. Another example, again drawn from biology, is blood flow through a capillary. Blood cells have a typical size range of 5 to 50 μm and flow at speeds in the range of 0.1 to 10 mm/s in a fluid medium that has approximately the same density and viscosity of water. The corresponding Reynolds number here is the the range of 10^{-4} to 0.1, again substantiating the use of the so called Stokes equations which govern this realm of microhydrodynamics [60].

The low-Reynolds-number regime encompasses a wide variety of physical phenomena, and an equally broad spectrum of mathematical and computational tools has been developed over the years to probe different aspects of biologically and industrially relevant fluid dynamics problems. Models that shed light on suspension microstructure [61], the motility of single [10] and multiple [62] microorganisms, the complicated deformations of blood cells [63], and the bulk rheology of suspensions [64] have resulted from studies in this field, and these illustrate the richness and variety of applications of microhydrodynamics. We shall focus in this section on certain fundamental aspects of the Stokes equations.

1.1.1 Stokes equations

As mentioned above, assuming zero Reynolds number reduces the Navier-Stokes equations to the Stokes equations:

$$-\boldsymbol{\nabla} p + \mu \nabla^2 \boldsymbol{u} = \boldsymbol{0}, \quad \boldsymbol{\nabla} \cdot \boldsymbol{u} = 0, \tag{1.2}$$

which are, respectively, simply mathematical statements of conservation of momentum and mass in the fluid. Here, $p(\boldsymbol{x})$ is the pressure field, μ the fluid viscosity, and $\boldsymbol{u}(\boldsymbol{x})$ the velocity field. These equations, we may observe, are steady[†] and linear. The former means that unsteadiness can result only from a time-dependent force (which would enter the right-hand side of the momentum equation) or unsteady boundary conditions. The latter observation, that of linearity, holds the key to a plethora of solution techniques, and is a powerful tool in the arsenal of mathematical methods used to tackle Equations (1.2).

[†] The implicit assumption is that the unsteady term in the Navier-Stokes equations is as insignificant as the non-linear convective term, sometimes justified as the Stokes number limiting to zero. See Guazzelli and Morris [65].

A few more properties of the Stokes equations deserve a quick mention here. Although not directly obvious, the Stokes equations are reversible – meaning a reversal in the direction of forcing (by, say, the arm of a micro-swimmer) completely reverses the direction of the velocity field. This, along with the instantaneity of the equations, has a direct physical consequence that has famously come to be known as Purcell's theorem [66]: a simple two-armed swimmer cannot produce net thrust in Stokes flow. This is at the center of microorganism motility, and the methods that nature has used to circumvent this have been of interest to biologists, physicists, and, in recent times, to engineers designing micro-robots as well. Finally, the solution to the Stokes equations is unique.

When a particle is immersed in a fluid, the net force and torque acting on the body should equal the hydrodynamic force and torque on it (by Newton's third law, again ignoring inertia). The hydrodynamic force and torque are simply surface integrals of the stress $\boldsymbol{\sigma}$ exerted by the fluid on the particle, where the stress tensor corresponding to viscous incompressible flow is $\boldsymbol{\sigma}(\boldsymbol{x}) = -p\boldsymbol{I} + \mu[\boldsymbol{\nabla}\boldsymbol{u}(\boldsymbol{x}) + \boldsymbol{\nabla}\boldsymbol{u}(\boldsymbol{x})^T]$. The solution to the full problem then requires solving the Stokes equations in conjunction with the force (and torque) balance on the particle. Such solution techniques stem from a crucial integral identity which we now describe.

1.1.2 Fundamental solutions and integral representations

One approach to solving the Stokes equations is by deriving their fundamental solution or Green's function. This is the solution corresponding to a point force $\boldsymbol{F}\delta(\boldsymbol{x} - \boldsymbol{x}_0)$ on the right hand side of the momentum equation. This solution can be formally derived using Fourier transforms [60], with the solution to the velocity field (commonly called the *Stokeslet*) being $\boldsymbol{u}(\boldsymbol{x}) = \boldsymbol{G}(\boldsymbol{x}, \boldsymbol{x}_0) \cdot \boldsymbol{F}$ where $\boldsymbol{G}$ is the *Oseen tensor*:

$$\boldsymbol{G}(\boldsymbol{r}) = \frac{1}{8\pi\mu}\left(\frac{\boldsymbol{I}}{r} + \frac{\boldsymbol{r}\boldsymbol{r}}{r^3}\right). \tag{1.3}$$

Here, $\boldsymbol{I}$ is the identity tensor, $\boldsymbol{r} = \boldsymbol{x} - \boldsymbol{x}_0$ is the separation vector, $r = |\boldsymbol{r}|$ its magnitude, and $\boldsymbol{r}\boldsymbol{r}$ is a dyadic product. The corresponding pressure field is $p(\boldsymbol{x}) = \boldsymbol{\Pi}(\boldsymbol{x}, \boldsymbol{x}_0) \cdot \boldsymbol{F}$, where

$$\boldsymbol{\Pi}(\boldsymbol{r}) = \frac{1}{4\pi}\frac{\boldsymbol{r}}{r^3}. \tag{1.4}$$

Higher order singularities may be constructed by differentiating Equation (1.3), and the solution to a more general problem can be expressed (thanks to linearity) as a sum of appropriately chosen fundamental solutions that satisfies the boundary conditions.

However, when a particle is immersed in the fluid, the solution requires information from the surface of the particle where the fluid-structure interaction takes place. Imposing the no-slip condition on its surface ∂S and the requirement that the velocity far away equal a background velocity $\boldsymbol{u}^\infty(\boldsymbol{x})$ which is also a solution to the Stokes equations gives

$$\boldsymbol{u} = \boldsymbol{u}_{\partial S} \quad \text{on} \quad \partial S, \quad \boldsymbol{u} \to \boldsymbol{u}^\infty \quad \text{for} \quad ||\boldsymbol{x}|| \to \infty. \tag{1.5}$$

Further, let $\boldsymbol{n}$ denote the inward normal on the surface ∂S. Then, a generalized version of the Lorentz reciprocal theorem [60, 67] lets us write down an integral relation between the velocity at a point $\boldsymbol{x}$ in the fluid and convolution integrals over the surface of the particle:

$$u_i(\boldsymbol{x}) = u_i^\infty(\boldsymbol{x}) - \int_{\partial S} G_{ij}(\boldsymbol{x} - \boldsymbol{x}_0) f_j(\boldsymbol{x}_0)\, \mathrm{d}S - \int_{\partial S} J_{ijk}(\boldsymbol{x} - \boldsymbol{x}_0) u_j(\boldsymbol{x}_0) n_k(\boldsymbol{x}_0)\, \mathrm{d}S, \tag{1.6}$$

where we have resorted to Einstein summation notation for clarity. Here, $\boldsymbol{f} = \boldsymbol{\sigma} \cdot \boldsymbol{n}$ is the traction evaluated at the surface, $\boldsymbol{G}$ is the Oseen tensor again, and $\boldsymbol{J}$ is the associated stress tensor (such that $\boldsymbol{\sigma} = \boldsymbol{J} \cdot \boldsymbol{F}$ for a point force). In index notation,

$$G_{ij}(\boldsymbol{x}) = \frac{1}{8\pi\mu}\left(\frac{\delta_{ij}}{r} + \frac{x_i x_j}{r^3}\right), \tag{1.7}$$

$$J_{ijk}(\boldsymbol{x}) = -\Pi_k \delta_{ij} + \mu(G_{ik,j} + G_{jk,i}) = -\frac{3}{4\pi}\frac{x_i x_j x_k}{r^5}. \tag{1.8}$$

This integral relation is the cornerstone of the family of computational techniques called the boundary integral method, which is particularly efficient as it reduces a three-dimensional problem to a two-dimensional manifold. The entire velocity field can be determined if one knows the velocity $\boldsymbol{u}(\boldsymbol{x}_0)$ and the traction field $\boldsymbol{f}(\boldsymbol{x}_0)$ on the surface ∂S. As mentioned earlier, this traction is directly related to the total hydrodynamic force $\boldsymbol{F}^h$ and torque $\boldsymbol{T}^h$:

$$\boldsymbol{F}^h = -\boldsymbol{F}^e = \int_{\partial S} \boldsymbol{f}(\boldsymbol{x}_0)\, \mathrm{d}S, \quad \boldsymbol{T}^h = -\boldsymbol{T}^e = \int_{\partial S} \boldsymbol{x}_0 \times \boldsymbol{f}(\boldsymbol{x}_0)\, \mathrm{d}S, \tag{1.9}$$

where $\boldsymbol{F}^e$ and $\boldsymbol{T}^e$ are net external force and torque on the particle. With this, the system is closed, and the fluid-structure interaction problem can in principle be solved.

The boundary integral relation from Equation (1.6) requires knowledge of the traction field on the entire surface of the particle immersed in the fluid. This problem can be simplified further when one is interested in flow fields far from particles via the so multipole expansion. The basic idea of this line of analysis is that the kernel of the integral can be expanded in a Taylor series, resulting in a sum of sequential products of derivatives of the Stokeslet and moments of the force distribution on the surface (see Kim and Karrila [60], for example, for mathematical details). To a good approximation, the first few terms (the force, torque and 'stresslet') can approximate the flow field to good accuracy far away from the particle. We shall not delve into the details of the multipole expansion, but will return to this idea of a truncated expansion of force moments in Chapter 6.

For now, we focus the power of the boundary integral equation on cases where the geometry of the immersed particle is especially conducive to further simplifications. This is the case of elongated bodies that approximate polymers. In this case, the force distribution on the surface may be suitably replaced by an effective force distribution along the centerline of the body. This leads to a theory that forms the crux of all analysis in this work: the slender-body theory.

1.1.3 Slender-body theory

The notion behind the development of slender-body theory for hydrodynamics is that the disturbance felt due to the presence of a body whose length is much larger than its characteristic thickness is the same as that due to a line distribution of Stokeslets. This formulation exploits the strong shape anisotropy of the elongated filament. The idea of capitalizing on the slenderness of a body in viscous flow has been around since Cox [68, 69] and was developed in great detail by Batchelor [56], Keller and Rubinow [58], and Johnson [57]. Simply put, the flow very close to the body is similar to that near a cylinder with the no-slip condition imposed (the 'inner flow') which is then asymptotically matched to the flow far away as felt due to the line distribution (the 'outer flow'). That way, the force distribution on the surface of the body in Equation (1.6) is replaced by a suitable force distribution along the centerline of the filament.

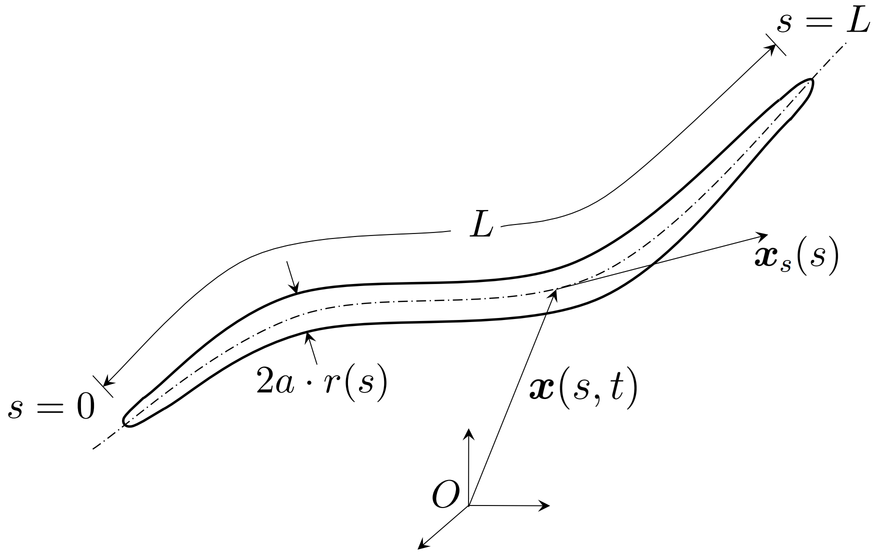

Figure 1.1: The geometry of the slender body.

We consider a filament of length L parametrized by arclength $s \in [0, L]$ with $\boldsymbol{x}(s,t) = (x(s,t), y(s,t), z(s,t))$ representing the filament centerline (Figure 1.1) placed in a fluid of viscosity μ and an imposed velocity field $\boldsymbol{u}_0(\boldsymbol{x}(s,t),t)$. It is important to note that s is a material parameter, and is thus independent of time. The filament is assumed to be radially symmetric at every point with a thickness given by $a \cdot r(s)$, where a is a characteristic radius and $r(s)$ is dimensionless. A non-local slender-body approximation [28, 57, 70] for the velocity of the centerline is then given by

$$8\pi\mu \left(\frac{\partial \boldsymbol{x}(s,t)}{\partial t} - \boldsymbol{u}_0(\boldsymbol{x}(s,t),t) \right) = -\boldsymbol{\Lambda}[\boldsymbol{f}] - \boldsymbol{K}[\boldsymbol{f}], \tag{1.10}$$

where $\boldsymbol{f}$ is the force per unit length acting on the filament and μ is the fluid viscosity. This expression is accurate to $O(\epsilon^2 \ln(\epsilon))$ for the velocity $\partial \boldsymbol{x}/\partial t$, where $\epsilon = a/L \ll 1$ is the body aspect ratio. Here, $\boldsymbol{\Lambda}[\boldsymbol{f}](s)$ is the local operator given by

$$\boldsymbol{\Lambda}[\boldsymbol{f}](s) = [(c(s)+1)\boldsymbol{I} + (c(s)-3)\boldsymbol{x}_s(s)\boldsymbol{x}_s(s)] \cdot \boldsymbol{f}(s), \tag{1.11}$$

where $c(s) = \ln(4s(1-s)/\epsilon^2 r(s)^2)$ and $\boldsymbol{x}_s(s)\boldsymbol{x}_s(s)$ is a dyadic product. We shall use subscripts to succinctly represent differentiation, and $\boldsymbol{x}_s$ is the unit tangent vector along the filament backbone. The integral operator $\boldsymbol{K}[\boldsymbol{f}](s)$ is given by

$$\boldsymbol{K}[\boldsymbol{f}](s) = \int_0^L \left(\frac{\boldsymbol{I} + \hat{\boldsymbol{r}}(s,s')\hat{\boldsymbol{r}}(s,s')}{|\boldsymbol{r}(s,s')|} \cdot \boldsymbol{f}(s') - \frac{\boldsymbol{I} + \boldsymbol{x}_s(s)\boldsymbol{x}_s(s)}{|s-s'|} \cdot \boldsymbol{f}(s) \right) \mathrm{d}s', \tag{1.12}$$

where $\boldsymbol{r}(s,s') = \boldsymbol{x}(s) - \boldsymbol{x}(s')$, and $\hat{\boldsymbol{r}} = \boldsymbol{r}/|\boldsymbol{r}|$. The particular choice of the filament shape $r(s)$ affects Equation (1.10) through the coefficient $c(s)$, which for a spheroidal profile of $r(s) = 2\sqrt{s(1-s)}$ reduces to $c(s) = c = \ln(1/\epsilon^2)$, a constant. For most of this dissertation, we shall resort to this spheroidal geometry and use $\lambda_1 = c + 1$ and $\lambda_2 = c - 3$ as constants in the local operator in Equation (1.11). The only exception will be in Chapter 4 where the effects of the choice of a non-spheroidal shape will be elucidated.

Clearly, the operators $\boldsymbol{\Lambda}$ and $\boldsymbol{K}$ depend on the shape of the filament at any given time. The local operator $\boldsymbol{\Lambda}$ accounts for drag anisotropy due to the slenderness of the filament. The leading order effect of this operator has the form $(\boldsymbol{I} + \boldsymbol{x}_s\boldsymbol{x}_s)$, and inverting this gives the 'resistance' tensor $(\boldsymbol{I} - \frac{1}{2}\boldsymbol{x}_s\boldsymbol{x}_s)$. This suggests that for a rigid needle (with $\boldsymbol{x}_s$ constant), the drag on the body for translations perpendicular to the long axis is twice as that for translations parallel to the axis – a well-known hydrodynamic result [60] which we will call upon soon in Section 1.2.1. The integral operator captures the disturbance field induced by forces acting at one point of the filament on every other point. Hence, this term will be called the non-local or intra-chain interactions operator from here on.

The fluid velocity $\boldsymbol{u}(\boldsymbol{x})$ at any point $\boldsymbol{x}$ outside the filament is approximated by

$$8\pi\mu\,(\boldsymbol{u}(\boldsymbol{x}) - \boldsymbol{u}_0(\boldsymbol{x})) = -\int_0^L \left(\frac{\boldsymbol{I} + \hat{\boldsymbol{r}}(s')\hat{\boldsymbol{r}}(s')}{|\boldsymbol{r}(s')|} + \frac{\epsilon^2}{2}\frac{\boldsymbol{I} - 3\hat{\boldsymbol{r}}(s')\hat{\boldsymbol{r}}(s')}{|\boldsymbol{r}(s')|^3} \right) \boldsymbol{\cdot} \boldsymbol{f}(s')\,\mathrm{d}s', \quad (1.13)$$

where now $\boldsymbol{r}(s') = \boldsymbol{x} - \boldsymbol{x}(s')$. Note that Equation (1.13) follows directly form Equation (1.3), with the additional second term representing a doublet.

To study the dynamics of several filaments in, say, a suspension of fibers, one can simply add up the contribution to the total velocity field from each individual filament. This works due to the superposition principle for linear Stokes flow. In particular, the centerline equation becomes

$$8\pi\mu \left(\frac{\partial \boldsymbol{x}_\beta(s,t)}{\partial t} - \boldsymbol{u}_0(\boldsymbol{x}_\beta(s,t),t) \right) = -\boldsymbol{\Lambda}_\beta[\boldsymbol{f}_\beta](s) - \boldsymbol{K}_\beta[\boldsymbol{f}_\beta](s) - \sum_{\alpha=1,\alpha\neq\beta}^{N} \boldsymbol{\Upsilon}_\alpha(\boldsymbol{x}_\beta(s)), \quad (1.14)$$

where the summation is over $1 \leq \alpha \leq N$ filaments, with the contribution of the filament β omitted, as it is accounted by the other terms as in Equation (1.10). Here

$\boldsymbol{\Upsilon}_{\alpha}$ denote the terms on the right hand side of Equation (1.13) evaluated to obtain the disturbance velocity due to filament α on the centerline of filament β.

1.2 A few preliminaries

1.2.1 Sedimentation

The sedimentation of multiple particles in a viscous fluid at low Reynolds number is marked by long-range hydrodynamic interactions resulting in strong velocity fluctuations. This slowly decaying nature of multi-body interactions readily complicates even the seemingly simple case of a random dilute dispersion of sedimenting spheres [71]. The disturbance velocity at a distance r induced by a sphere decays as $1/r$ (cf. Equation (1.3)), and a naive pairwise summation of the contributions of all spheres promptly leads to a divergent value of the settling velocity. This issue was first addressed by Batchelor [64] who noted that, in a finite-sized container, the presence of a bottom wall in fact results in a vertical backflow that cancels the diverging part of the settling velocity; this can alternatively be interpreted as the effect of a modified pressure field, whose gradient balances the weight of the suspension. While this observation resolved the problem with the mean settling speed, the variance of the particle velocities was later shown, in what has become known as the Caflisch-Luke paradox [71–73], to increase unboundedly with system size, notwithstanding Batchelor's renormalization. Such a divergence is not supported by experimental observations [74–76], and various mechanisms have been suggested over the years to resolve this oddity, each with experiments and numerical simulations to support and challenge the notion. These mechanisms have included the hydrodynamic screening of long-range interactions as a result of local microstructural changes [77] or by vertical no-slip walls [78], homogenization of the suspension due to recirculating currents induced by horizontal boundaries [79, 80], and the damping of fluctuations by vertical density gradients [81, 82].

As the first step, consider a single spherical particle of radius a sedimenting due to its own weight F_g in a fluid of viscosity μ. If the acceleration due to gravity is g, the gravitational force including buoyancy (or, in general, an external body force) acting on it is

$$F_g = \left(\frac{4}{3}\pi a^3\right) \mathit{\Delta}\rho\, g, \tag{1.15}$$

where $\mathit{\Delta}\rho$ is the relative density of the sphere with respect to the surrounding fluid. As discussed in Section 1.1, this is balanced (in the absence of inertia) exactly by the net hydrodynamic force acting in the opposite direction. In this simplified case, this is the viscous drag, which is given by Stokes law as

$$F_d = 6\pi\mu a U, \tag{1.16}$$

where U is the steady state sedimentation velocity of the sphere. Equating the two gives us a relation for velocity:

$$U = \frac{2a^2}{9\mu}\mathit{\Delta}\rho\, g. \tag{1.17}$$

Now, for the sake of illustration, we take the smallest step in describing hydrodynamic interactions among multiple sedimenting spheres: that of an infinite fluid with two spheres. The distance between the two will be assumed to be large relative to their radii. Then, the leading order disturbance velocity field induced by one sphere at $\boldsymbol{x}_0$ on the other at $\boldsymbol{x}$ can be determined directly using the Stokeslet: $\boldsymbol{u}(\boldsymbol{x}) = \boldsymbol{G}(\boldsymbol{x} - \boldsymbol{x}_0) \cdot \boldsymbol{F}_g$. The particular form of the Stokeslet then results in a disturbance field that is twice as strong at a point along the direction of the external force as it is in a direction perpendicular to it but at the same distance from the force. In other words, the net sedimentation velocity of a pair of spheres (notice the symmetry: both spheres would settle at the same speed) separated by a distance r but along a vertical line ($U_{||}$) and a horizontal line ($U_{\perp}$), with gravity being along the vertical, are given by

$$U_{||} = \frac{2a^2}{9\mu}\mathit{\Delta}\rho\, g\left(1 + \frac{3a}{2r}\right), \quad U_{\perp} = \frac{2a^2}{9\mu}\mathit{\Delta}\rho\, g\left(1 + \frac{3a}{4r}\right). \tag{1.18}$$

The anisotropy in the disturbance velocity field is obvious, and the implications of this feature will be the basis for arguments in Chapter 4.

Suspension microstructure becomes all the more important in the case of anisotropic particles. Consider for the moment a collection of rigid spheroids with a defined geometry, with the configuration of each particle now specified by its position and orientation. While the contribution of particle geometry to hydrodynamic interactions is not obvious *a priori*, we can readily see that such a dispersion is fundamentally different from one containing only spherical particles in that spheroids can orient in flow. This orientation, in turn, decides the direction of sedimentation, which no longer has to be vertically downward even in the case of a single particle in a quiescent fluid. This simple consequence of viscous drag anisotropy has been well studied and knowledge of the hydrodynamic mobilities along and perpendicular to the particle major axis lets one evaluate its settling velocity. Specifically, for a rigid spheroid whose major axis is parallel to the unit orientation vector $\boldsymbol{p}$ $(= \boldsymbol{x}_s$, but constant throughout its length), the local leading order relation between net force $\boldsymbol{F}_g$ and velocity $\boldsymbol{U}$ $(= \boldsymbol{x}_t$, a constant again) can be determined by integrating Equation (1.10) along its length, and one has

$$\begin{aligned}\boldsymbol{U} = \frac{\ln(1/\epsilon^2)}{8\pi\mu}(\boldsymbol{I} + \boldsymbol{pp}) \cdot \boldsymbol{F}_g &= \frac{\ln(1/\epsilon^2)}{8\pi\mu}[(\boldsymbol{I} - \boldsymbol{pp}) + 2\boldsymbol{pp}] \cdot \boldsymbol{F}_g \\ &= [\mu_\perp(\boldsymbol{I} - \boldsymbol{pp}) + \mu_{||}\boldsymbol{pp}] \cdot \boldsymbol{F}_g. \end{aligned} \tag{1.19}$$

The mobility tensor is clearly anisotropic, with mobilities $\mu_{||}$ and $\mu_\perp$ in directions along and perpendicular to the force (gravity in this case). These mobility coefficients are closely tied to the geometry of the rod with $\mu_{||} \approx 2\mu_\perp$ for the leading order in $\ln(1/\epsilon)$ considered here. But the main takeaway is that a shape anisotropy leads to a direction of settling that is no longer along that of the force. This is further complicated if the particle is composed of several rigid rods that are joined at the ends and constrained to move together but with different orientations, which is a very simple model for a polymer. Several non-trivial dynamics and effects can be explained following such a line of thought, and we shall return to this in Chapter 4, as well as to the combined effect of shape anisotropy and hydrodynamic interactions discussed above in Chapter 5, where large scale concentration instabilities are known to result.

1.2.2 Elastohydrodynamics

The very title of this dissertation reveals the coupling between overdamped viscous hydrodynamics and elasticity theory. We saw that the slender-body equation (1.10) connects the velocity at each point on the fiber to the force distribution along its centerline. If the fiber is elastic, this force distribution has to follow the laws of elasticity, and this coupling will be introduced in this section.

One convenient way to describe elasticity theory is using the calculus of variations. For this, we seek an expression for the elastic energy of a bent filament. Bending a fiber is energetically expensive, and therefore the energy $\mathcal{E}$ has to be a function of the curvature $\boldsymbol{x}_{ss}$ of the fiber. Also, bending energy must not depend on the sign of the curvature, and hence the leading order dependence can only be quadratic. So we write the energy as

$$\mathcal{E} = \frac{\kappa}{2} \int_0^L \boldsymbol{x}_{ss}^2 \, \mathrm{d}s. \tag{1.20}$$

Here, κ is the bending modulus, a property of the material and geometry of the filament, which can be alternatively expressed as the product of the Young's modulus (E) of the filament material and its area moment of inertia across a section ($\kappa = \pi E a^4/4$: recall that a is the characteristic radius of a section of the filament). The functional derivative of this energy then provides a first approximation for the restorative elastic force per unit length on the filament backbone. A direct path to the elastic force is through the Euler-Lagrange equation for $\mathcal{E}$:

$$\frac{\partial \mathcal{E}}{\partial \boldsymbol{x}} - \frac{\partial}{\partial s}\left(\frac{\partial \mathcal{E}}{\partial \boldsymbol{x}_s}\right) + \frac{\partial^2}{\partial s^2}\left(\frac{\partial \mathcal{E}}{\partial \boldsymbol{x}_{ss}}\right) = \boldsymbol{f}_e, \tag{1.21}$$

which yields the elastic force per unit length $\boldsymbol{f}_e = \kappa \boldsymbol{x}_{ssss}$. A theme that we shall return to several times in this work is buckling, and filaments buckle when a compressional force exceeds a critical threshold set by its balance with $\boldsymbol{f}_e$. Energetic descriptions such as the one above have been successfully used to describe, for example, buckling of microtubules by gliding kinesin motor molecules [83] or by vesicles using micropipet aspiration [84], as well as the morphoelastic buckling of plant tendrils or bacterial filaments [85].

A useful starting point for connecting this elastic restoring force to the fluid problem are the illustrative examples provided by Wiggins *et al.* [59]. Much like the classic first and second Stokes problems of a plate abruptly moved or oscillated in a viscous fluid, Wiggins *et al.* [59] propose elastohydrodynamic problems of an ealstic filament anchored to a wall that is moved or oscillated in a viscous fluid. Analogous to the Stokes problems where the Navier-Stokes equations reduce to a simple diffusion equation, the elastohydrodynamic problems are governed by a 'hyperdiffusion' problem. Considering just the transverse motion $y(x)$ of a filament and a linear mobility relation to the force, this relation is simply a balance between viscous and elastic forces:

$$\frac{1}{\mu_\perp} y_t = \kappa y_{xxxx}, \tag{1.22}$$

where $\mu_\perp$ is the transverse mobility that we first encountered in Section 1.2.1. Solving this problem with appropriate boundary conditions and comparing with actin and microtubule experiments, Wiggins *et al.* [59] demonstrate the power of such a model in describing the elastohydrodynamics of biopolymers.

We follow in the same spirit with more involved and appropriate models for both the fluid and elastic problem. For the fluid problem, we use the full slender-body theory described in Section 1.1.3. For the latter, we use Euler-Bernoulli elasticity by starting with a modified elastic energy functional:

$$\mathcal{E} = \frac{1}{2} \int_0^L \left[\kappa \boldsymbol{x}_{ss}^2 + T(s)(\boldsymbol{x}_s \cdot \boldsymbol{x}_s - 1) \right] \mathrm{d}s - \int_0^L \boldsymbol{f}(s) \cdot \boldsymbol{x}(s)\ \mathrm{d}s. \tag{1.23}$$

Here, the first term represents the same bending contribution as before and $T(s,t)$ is a Lagrangian multiplier that acts to keep the the filament locally inextensible ($\boldsymbol{x}_s \cdot \boldsymbol{x}_s = 1$) at all times. Mathematically, $T(s)$ is an energetic penalty paid to extend (or contract) the filament beyond its base length. Physically, it corresponds to a line tension along the filament centerline that acts to keep it at a constant length. The second integral is introduced here to complete the energetic relation of the filament, with $\boldsymbol{f}(s)$ being the fluid force per unit length on the filament. Modulations in extension and twist relax much faster than those in bending (by a factor of $1/\epsilon^2$, see Powers [86]) and so we shall restrict ourselves to the dynamics of inextensible filaments with no twist.

Minimizing this energy via the Euler-Lagrange equation then gives us

$$\boldsymbol{f}(s) = -(T(s)\boldsymbol{x}_s)_s + \kappa \boldsymbol{x}_{ssss}. \tag{1.24}$$

This enters Equation (1.10) as the force distribution acting on the fiber. To close the problem, appropriate boundary condition of force- and torque-free ends may be imposed if the filament is freely suspended. In the case of sedimenting filaments that we shall encounter in Chapter 4, the boundary conditions are not as obvious, but they emerge as solvability conditions by systematically taking the functional derivative of the elastic energy.

1.2.3 Brownian motion

At length scales characteristic of the kind of problems we address, a particle immersed in a fluid becomes susceptible to thermal fluctuations of individual molecules of the fluid. The constant bombardment by Brownian molecules on the polymer can distort it if the elastic backbone is sufficiently compliant, or move the particle leading to a random walk. In long floppy chains such as DNA molecules, such thermal fluctuations and the thermodynamic desire to maximize configurational entropy is the basis for the 'spring' force that resists straightening the polymer. However, in the case of stiffer polymers like actin and microtubules, this is not quite the case: bending costs energy too and an intricate balance between entropy, elasticity and viscous drag, if present, needs to be struck.

Tracking each fluid particle through Newton's laws of motion is a significantly expensive affair, and forms the basis for molecular dynamics simulations. Furthermore, the continuum hypothesis that permits using the Stokes equations requires individual fluid molecules to be sufficiently smaller than the immersed particle. So we seek a link between the random jiggling of countless tiny fluid particles that we would like to treat as a continuum and the relatively 'large' immersed body on which a net Brownian force results due to these fluctuations. This issue of scale separation is addressed by a famous result from statistical thermodynamics: the fluctuation-dissipation theorem. It broadly states that this random fluctuating force acting on an immersed particle as a results of Brownian kicks is equal to the dissipative frictional force that one must do work against to move it at all.

An illustrious embodiment of this idea is the connection between the diffusion $\boldsymbol{D}$ of the immersed particle (due to the random walk as a result of thermal fluctuations) and its mobility $\boldsymbol{M}$, called the Einstein-Smoluchowski relation:

$$\boldsymbol{D} = k_B T \boldsymbol{M}, \tag{1.25}$$

where k_B is Boltzmann's constant and T is the temperature. The product of the two represents the unit of thermal energy. A particularly relevant form is the diffusion of a sphere due to Brownian motion in a fluid. Borrowing the 'mobility' (which is, thanks to linearity, simply the velocity divided by the force that caused it to move) from Equation (1.16), the diffusivity of a sphere in viscous flow is then

$$\boldsymbol{D} = \frac{k_B T}{6\pi\mu a}\boldsymbol{I}. \tag{1.26}$$

The diffusion is isotropic, and this relation is commonly referred to as the Stokes-Einstein-Sutherland relation. Similar results can be drawn for rotational diffusion and, more generally, for diffusion tensors of anisotropic shapes (using $\boldsymbol{M} = [\mu_\perp(\boldsymbol{I} - \boldsymbol{pp}) + \mu_{||}\boldsymbol{pp}]$ from Equation (1.19) for a rod, for instance). We shall see more of this when we derive conservation laws for probability fluxes in the coming chapters, where diffusion enters the governing equation.

As mentioned previously, Brownian fluctuations can alter the configuration of the filament if it is sufficiently compliant. Having briefly reviewed elasticity and Brownian motion, we are now in a position to ask a central question: exactly how flexible is 'semiflexible'? We have so far been rather informal about the definition of semiflexibility, and shall now see precisely what the term means.

For this, we first introduce the concept of the persistence length, ℓ_p. This can be thought of as a length scale at which thermal fluctuations and elastic forces in the filament strike a balance. More rigorously, ℓ_p is the characteristic length associated with the exponential decay of tangent vector autocorrelation [16, 87]. In other words, tangent vectors lose memory of the direction of each other over this length:

$$\langle \boldsymbol{x}_s(s) \cdot \boldsymbol{x}_s(s') \rangle = \exp\left[\frac{-|s-s'|}{\ell_p}\right], \tag{1.27}$$

where the angle brackets denote a statistical average. A more useful relation, directly associated with the idea of a balance between elasticity and thermal fluctuations, is [29, 88]

$$\ell_p = \frac{\kappa}{k_B T}. \tag{1.28}$$

If the tangential correlations decay rapidly, as in the case of DNA and many synthetic polymers, the persistence length is very small. Such flexible or floppy polymers, for which $\ell_p \ll L$, energetically favor coiled states. On the other end of the spectrum are extremely rigid (with respect to Brownian fluctuations) fibers with

$\ell_p \gg L$ which almost do not yield to shape fluctuations due to Brownian forces. The semiflexible regime is in between where ℓ_p and L are of comparable magnitudes. As examples, in the classic experiments of Gittes *et al.* [16], microtubules were found to have a rigidity of $\kappa \sim 10^{-23}\,\mathrm{Nm}^2$ corresponding to a persistence length of $\ell_p \sim 5\,\mathrm{mm}$, whereas the corresponding values for actin were $\kappa \sim 10^{-26}\,\mathrm{Nm}^2$ and $\ell_p \sim 18\,\mu\mathrm{m}$. Both these biopolymers occur naturally with lengths of the order of $L \sim 10\,\mu\mathrm{m}$.

When Brownian fluctuations become relevant, an additional term is required in Equation (1.24) to model thermal fluctuations in the solvent. This additional term is a stochastic force distribution $\boldsymbol{f}^{\mathrm{Br}}$ that must satisfy the fluctuation-dissipation theorem. $\boldsymbol{f}^{\mathrm{Br}}$ can be shown to satisfy:

$$\langle \boldsymbol{f}^{\mathrm{Br}}(s,t) \rangle = \mathbf{0}, \tag{1.29a}$$

$$\langle \boldsymbol{f}^{\mathrm{Br}}(s,t)\boldsymbol{f}^{\mathrm{Br}}(s',t') \rangle = 2k_B T \boldsymbol{M}^{-1}\delta(t-t')\delta(s-s'), \tag{1.29b}$$

where $\langle \cdot \rangle$ represents an ensemble average, and δ is the Dirac delta function. Equations (1.29a)–(b) are essentially a mathematical restatement of the equivalence between the random fluctuations felt by a particle and the dissipative frictional drag (which is the inverse of the mobility $\boldsymbol{M}$) it experiences. A Brownian force that satisfies these statistics gets added to Equation (1.24) and this captures the effect of stochastic thermal fluctuations. A computational analogue of Equations (1.29a)–(b) might not seem very straightforward, but we shall see how this can be treated in Section 2.3.

1.3 Overview of current work

This work attempts to shed light on some dynamics resulting from the balance of some or all of viscous, elastic, Brownian, and gravitational forces on the configurations, transport and bulk behavior of flexible elastic filaments. We have seen in the preceding sections the basics of each of these forces and how they act on slender elongated bodies. Their complex interplay and the resulting non-trivial dynamics in problems of physical and biological significance will be the focus of this work.

Chapter 2 starts by describing a single filament model and the associated computational algorithm to solve it, based on the slender-body theory described in Section 1.1.3. This model is then applied to study the dynamics of semiflexible polymers in simple flows, particularly those that are prevalent in microfluidics. Some of these phenomena have been previously studied theoretically and/or experimentally, and this serves to validate our methods. Numerical simulations and associated theoretical arguments describe the tumbling of polymers in shear flow and the stretching or buckling of filaments in extensional flow. This will also be the first encounter with the competition of line tension and elastic rigidity, which is a common theme across many problems discussed in this dissertation. Chapter 2 ends with the development, for the first time, of a theory for the so called 'stretch-coil transition' of semiflexible polymers in extensional flows.

In Chapter 3, the transport of semiflexible polymers across a lattice of counter-rotating vortices is explored in detail. We will see how such a flow mimics bio-assays with actin filaments, and our simulations reveal a subdiffusive transport of polymers. A trapping mechanism which leads to a 'stick-slip'-like process that results in this anomalous transport is discussed, and the subtle role of flexibility in migration or entrapment of polymers in a non-uniform flow is illustrated.

Having looked at free filaments thus far, we move on to fibers under a constant external force in Chapter 4, where we talk about sedimentation. Sedimentation of flexible particles is relatively unexplored, and a wide range of non-trivial dynamics are discussed in this chapter. In terms of an elasto-gravitation number, two vastly separate regimes are focused on. The first, that of *weakly* flexible fibers, is shown to be amenable to a multiple-scale asymptotic analysis, which results in expressions for the bent shape, the rate of reorientation, and the peculiar trajectory of a sedimenting fiber. The second, that of *highly* flexible fibers, is where a buckling instability exists that shares mechanistic features with buckling as seen in Chapter 2. In this regime, a linear stability analysis gives the growth rates and wave speeds of perturbations. Theoretical predictions from both regimes are corroborated with detailed numerical simulations.

We use the main result from the theory on weakly flexible fibers and head into the world of long-ranged hydrodynamic interactions at the level of a suspension in Chapter 5. Even in suspensions of rigid rods, drag anisotropy and hydrodynamic interactions have been found to cause large-scale concentration instabilities. We develop a mean-field description of weakly flexible fibers, and using a stability analysis, illustrate the effects of flexibility on the instability. Fiber flexibility is shown to affect suspension stability in two distinct and competing ways: the anisotropy of the base state of orientations renders the suspension more unstable to perturbations, while individual particle reorientation acts to stabilize the suspension. In the presence of thermal noise, the dominant effect is shown to depend critically upon the relative scales of flexible fiber self-rotation compared to rotational Brownian motion.

Chapter 6 describes accurate and efficient large-scale particle simulations that serve to verify our mean-field model from Chapter 5 on the one hand, and explore some avenues that were not so amenable to theoretical analysis on the other. The mechanism for the competing effects of fiber flexibility is illustrated using velocity and orientation statistics from our simulations, and the suspension-level behavior is tied to microstructural dynamics. These simulations are also used to predict stability of initially well-stirred suspensions which might serve for comparison with future experiments.

Concluding remarks and directions for future work are given in Chapter 7.

Chapter 2

Dynamics of elastic filaments in simple flows

2.1 Introduction

The nonlinear dynamics of elastic filaments driven by hydrodynamic forces have received significant attention in recent times, sparked mainly by advances in experiments ranging from microscopic [31, 32, 34] to macroscopic [36] lengthscales, as well as by the development of efficient low-dimensional models to describe them quantitatively [28, 35, 86, 89]. Of particular interest are semiflexible filaments, which are between the extremes of entropy-dominated floppy polymers and rigid rods in terms of elastic stiffness. Pertinent to the contents of this chapter is that these particles allow for a competition between bending forces and flow-induced internal stresses in the presence of thermal fluctuations.

Understanding the configurational transitions of semiflexible filaments is key to deciphering a plethora of dynamics ranging from tumbling [31, 34] to buckling [32, 33] to helical coiling [89], which in turn could result in atypical transport [3, 90, 91] or non-Newtonian behavior [28, 92]. Beside offering rich mechanical properties that enable such dynamics, semiflexible biopolymers are of paramount importance to living cells: eukaryotic cells are structurally supported by a cytoskeletal system comprised of filamentous actin. Configurational transitions in such systems have been suggested to lie at the core of biological pattern formation via self-organizational phenomena such as cytoplasmic streaming [93].

As described in Chapter 1, the presence of the filament or fiber is exhibited only by the disturbance velocity of the line distribution of Stokeslets. In other words, the filament is assumed to have zero thickness. Hence, the equation of motion of the centerline of the filament as given by the slender-body theory in Section 1.1.3 is assumed to represent the dynamics of the entire filament. This approximation is valid in the high-aspect-ratio limit which applies in the case of the biopolymers that we consider, with the characteristic thickness being a few orders of magnitude less that the characteristic length. Furthermore, unless expressly stated, we shall assume the the material of the fiber is homogeneous with uniform bending rigidity throughout.

In this chapter, we consider a single filament far away from other filaments or walls and placed in simple linear flows. This can be thought to represent physically the setting in a microchannel experiment (a single DNA separation device, for instance) with the channel width being significantly larger than the filament size. This free-draining approximation allows us the use of slender-body theory as described in Section 1.1.3 without significant modifications. Specifically, after describing the model and computational methods, we shall apply it to study the dynamics of free filaments placed in simple shear and extensional flows. Introducing the effect of confinement in this model is a topic of future interest, and a brief perspective will be provided in Chapter 7. For now, we neglect wall interactions so as not to resort to modified Green's functions of the Stokes equations [55, 94] or using auxiliary solutions to correct for the presence of boundaries [95].

2.2 Single filament model

We begin by rewriting the centerline equation from Equation (1.10) that accounts for the motion of a filament of position $\boldsymbol{x}(s,t)$ in a fluid with imposed velocity $\boldsymbol{u}_0(\boldsymbol{x}(s,t),t)$ as:

$$8\pi\mu\left(\boldsymbol{x}_t(s,t)-\boldsymbol{u}_0(\boldsymbol{x}(s,t),t)\right)=-\boldsymbol{\Lambda}[\boldsymbol{f}(s)]-\boldsymbol{K}[\boldsymbol{f}(s)]. \tag{2.1}$$

Here, $\boldsymbol{f}(s)$ is the force per unit length exerted by the fluid on the filament body, which we know from the discussion in Sections 1.2.2 and 1.2.3 to be

$$\boldsymbol{f}(s) = -(T(s)\boldsymbol{x}_s)_s + \kappa \boldsymbol{x}_{ssss} + \boldsymbol{f}^{\mathrm{Br}}(s). \tag{2.2}$$

Here, $T(s)$ is the non-uniform line tension, κ the (homogeneous) bending rigidity of the filament, and $\boldsymbol{f}^{\mathrm{Br}}(s)$ is the stochastic Brownian force acting on the filament as described by the fluctuation-dissipation theorem. We neglect twist and stretch elasticity (the latter consistent with the inextensibility condition described below) whose effects are known to relax significantly faster than those of bending [86, 96]. Also, we do not explicitly add any forces to maintain physical uniqueness of different filament point locations – excluded volume is assumed.

Regarding boundary conditions, the filament ends are 'free', i.e., there are no forces or moments acting at the ends of the filament. This is true for an untethered filament suspended freely in a fluid [28, 29, 59]. This gives

$$\boldsymbol{x}_{ss}|_{s=0,L} = \boldsymbol{x}_{sss}|_{s=0,L} = \mathbf{0}, \quad T|_{s=0,L} = 0. \tag{2.3}$$

2.2.1 Non-dimensionalization

In the problems that we consider in this chapter, the imposed flow is assumed to be of a constant flow strength $\dot{\gamma}$. We scale time by the relaxation time of the elastic backbone, $8\pi\mu L^4/\kappa$, while lengths are made dimensionless using the contour length L and forces with κ/L^2. Notice that the operators $\boldsymbol{\Lambda}$ and $\boldsymbol{K}$ are already dimensionless.

For Brownian forces, following Munk *et al.* [29], we use a different scaling:

$$\boldsymbol{f}^{\mathrm{Br}} = \left[\sqrt{\frac{L}{\ell_p}}\frac{\kappa}{L^2}\right]\boldsymbol{\xi}, \tag{2.4}$$

where $\boldsymbol{\xi}$ is the dimensionless Brownian force, and the ratio $\sqrt{L/\ell_p}$ is introduced so that the dimensionless noise has the second moment, following our discussion in Section 1.2.3, of the form

$$\langle \boldsymbol{\xi}(s,t)\boldsymbol{\xi}(s',t')\rangle = 2\boldsymbol{M}^{-1}\delta(t-t')\delta(s-s'). \tag{2.5}$$

Here, $\boldsymbol{M}$ is the effective mobility tensor corresponding to the problem. Note that we have made use of Equation (1.28) to arrive at the above form. This, in addition to the condition of zero mean ($\langle \boldsymbol{\xi}(s,t)\rangle = 0$), defines the Brownian force.

The dimensionless centerline equation thus becomes

$$\boldsymbol{x}_t(s,t) = \bar{\mu}\boldsymbol{u}_0(\boldsymbol{x}(s,t),t) - \boldsymbol{\Lambda}[\boldsymbol{f}](s) - \boldsymbol{K}[\boldsymbol{f}](s), \tag{2.6}$$

with the corresponding force being

$$\boldsymbol{f}(s) = -(T(s)\boldsymbol{x}_s)_s + \boldsymbol{x}_{ssss} + \sqrt{\frac{L}{\ell_p}}\boldsymbol{\xi}(s), \tag{2.7}$$

where all variables are now dimensionless. The parameter $\bar{\mu}$ is a ratio of the characteristic fluid drag to the filament elastic force (or alternatively, the ratio of the elastic timescale to that of the imposed flow):

$$\bar{\mu} = \frac{8\pi\mu\dot{\gamma}L^2}{\kappa/L^2}. \tag{2.8}$$

This ratio, sometimes called an effective viscosity [28, 35], along with the ratio L/ℓ_p, controls the relative importance of viscous, elastic and Brownian forces in this formulation. The only other parameter now is ϵ which appears in the mobility operator $\boldsymbol{\Lambda}$ (through the constants λ_1 and λ_2) and this is taken to be a constant for our purposes.

2.2.2 The tension equation

We recollect from our discussion in Section 1.2.2 that the line tension in Equation (2.2) acts in a way so as to keep the filament inextensible. This tension is configuration-dependent and has to be evaluated at every instant based on the shape and viscous forces at that instant. What this means is that we need to construct, in addition to Equation (2.6), a coupled equation that will evaluate the tension. This tension can be then fed into the force distribution to evaluate the position of the filament centerline.

For this, we consider the condition of inextensibility $\boldsymbol{x}_s \cdot \boldsymbol{x}_s = 1$ where $\boldsymbol{x}_s$ is the unit tangent vector at s. We can write:

$$\frac{\partial}{\partial t}(\boldsymbol{x}_s \cdot \boldsymbol{x}_s) = 0 \quad \Rightarrow \quad \boldsymbol{x}_s \cdot \boldsymbol{x}_{ts} = 0, \tag{2.9}$$

where we have used the fact that s is a material parameter to interchange the s and t derivatives. This condition can be combined with Equation (2.6) to get

$$\boldsymbol{x}_s \cdot \frac{\partial}{\partial s}\left(\bar{\mu}\boldsymbol{u}_0(\boldsymbol{x}(s,t),t) - \boldsymbol{\Lambda}[\boldsymbol{f}](s) - \boldsymbol{K}[\boldsymbol{f}](s)\right) = 0. \tag{2.10}$$

Further simplification requires a ladder of differential identities, derived from the filament inextensibility condition:

$$\boldsymbol{x}_s \cdot \boldsymbol{x}_s = 1, \tag{2.11a}$$

$$\boldsymbol{x}_s \cdot \boldsymbol{x}_{ss} = 0, \tag{2.11b}$$

$$\boldsymbol{x}_s \cdot \boldsymbol{x}_{sss} = -\boldsymbol{x}_{ss} \cdot \boldsymbol{x}_{ss}, \tag{2.11c}$$

$$\boldsymbol{x}_s \cdot \boldsymbol{x}_{ssss} = -3\boldsymbol{x}_{ss} \cdot \boldsymbol{x}_{sss}, \tag{2.11d}$$

$$\boldsymbol{x}_s \cdot \boldsymbol{x}_{sssss} = -3\boldsymbol{x}_{sss} \cdot \boldsymbol{x}_{sss} - 4\boldsymbol{x}_{ss} \cdot \boldsymbol{x}_{ssss}. \tag{2.11e}$$

The resulting form of the dimensionless line tension equation reads

$$\begin{aligned} -2(c-1)T_{ss} + (c+1)(\boldsymbol{x}_{ss} \cdot \boldsymbol{x}_{ss})T - \boldsymbol{x}_s \cdot \frac{\partial}{\partial s}\boldsymbol{K}[(T(s)\boldsymbol{x}_s)_s] \\ = \bar{\mu}\boldsymbol{x}_s \cdot \frac{\partial \boldsymbol{u}_0}{\partial s} + (7c-5)(\boldsymbol{x}_{ss} \cdot \boldsymbol{x}_{ssss}) + 6(c-1)(\boldsymbol{x}_{sss} \cdot \boldsymbol{x}_{sss}) \\ -2(c-1)\sqrt{\frac{L}{\ell_p}}(\boldsymbol{\xi}_s \cdot \boldsymbol{x}_s) - (c-3)\sqrt{\frac{L}{\ell_p}}(\boldsymbol{\xi} \cdot \boldsymbol{x}_{ss}) \\ -\boldsymbol{x}_s \cdot \frac{\partial}{\partial s}\boldsymbol{K}[\boldsymbol{x}_{ssss}] - \sqrt{\frac{L}{\ell_p}}\boldsymbol{x}_s \cdot \frac{\partial}{\partial s}\boldsymbol{K}[\boldsymbol{\xi}]. \end{aligned} \tag{2.12}$$

This is a second-order inhomogeneous integro-differential equation in $T(s)$, and can be solved if the position and Brownian forces are known. The tension acts as a Lagrangian multiplier, constraining the motion of the filament so as to ensure inextensibility. In practice however, numerical errors will be introduced into our computations from the finite difference approximations that will be made to the derivatives, and additional correction might be required to ensure this constraint. This is accounted [28] by replacing the inextensibility condition in Equation (2.9) by

$$\frac{1}{2}\frac{\partial}{\partial t}(\boldsymbol{x}_s \cdot \boldsymbol{x}_s) = \boldsymbol{x}_s \cdot \boldsymbol{x}_{ts} = \zeta(1 - \boldsymbol{x}_s \cdot \boldsymbol{x}_s). \tag{2.13}$$

Clearly, this is equivalent to the original condition when $\boldsymbol{x}_s \cdot \boldsymbol{x}_s = 1$ and acts to counter the error if there is one. The penalization parameter ζ is chosen based on the computational parameters. This modified constraint only changes the tension equation (2.12) with an additional $-\zeta(1 - \boldsymbol{x}_s \cdot \boldsymbol{x}_s)$ term on the right-hand side.

2.3 Computational methods

In this section, we discuss the numerical methods applied to the single filament model described in the preceding sections. We also describe in detail how the stochastic terms are computed and conditioned for numerical stability.

2.3.1 Semi-implicit time marching

The spatial derivatives in Equations (2.6) and (2.12) are discretized using second-order divided differences, and time marching is performed using a second-order time-stepping scheme. The fourth derivatives of $\boldsymbol{x}$ with respect to arclength in Equation (2.6) will yield a strict fourth-order stability limit on the time-step size. The obvious way to get past this constraint is to use an implicit scheme. Instead of making the entire equation implicit, thus increasing computing cost, we use a semi-implicit scheme [28] wherein all occurrences of $\boldsymbol{x}_{ssss}$ are treated implicitly. Specifically, we separate the terms in Equation (2.6) as

$$\frac{\partial \boldsymbol{x}}{\partial t} = \boldsymbol{M}(\boldsymbol{x}, \boldsymbol{x}_{ssss}) + \boldsymbol{N}(\boldsymbol{x}). \tag{2.14}$$

Here, the terms in $\boldsymbol{M}$ are to be treated implicitly, whereas $\boldsymbol{N}$ is completely explicit.

Time-marching is second order accurate using a backward differentiation formula. The stiffest terms are treated implicitly while the remaining terms are extrapolated to the current time [28]. For timestep Δt and subscripts denoting the time at which the term is being evaluated, we have

$$\frac{1}{2\Delta t}(3\boldsymbol{x}^{n+1} - 4\boldsymbol{x}^{n} + \boldsymbol{x}^{n-1}) = \boldsymbol{M}(2\boldsymbol{x}^{n} - \boldsymbol{x}^{n-1}, \boldsymbol{x}^{n+1}_{ssss}) + 2\boldsymbol{N}(\boldsymbol{x}^{n}) - \boldsymbol{N}(\boldsymbol{x}^{n-1}). \tag{2.15}$$

To illustrate this, applying the above scheme to the centerline equation in (2.6) requires us to first separate the terms that will be treated implicitly and explicitly:

$$\begin{aligned} \frac{\partial \boldsymbol{x}}{\partial t} + \boldsymbol{\Lambda}\left[\boldsymbol{x}_{ssss}\right] + \boldsymbol{K}\left[\boldsymbol{x}_{ssss}\right] &= \boldsymbol{N}(\boldsymbol{x}) \\ &= \bar{\mu}\boldsymbol{u}_0 - \boldsymbol{\Lambda}\left[(-T\boldsymbol{x}_s)_s + \sqrt{\frac{L}{\ell_p}}\boldsymbol{\xi}\right] - \boldsymbol{K}\left[(-T\boldsymbol{x}_s)_s + \sqrt{\frac{L}{\ell_p}}\boldsymbol{\xi}\right]. \end{aligned} \tag{2.16}$$

Here, the mobility operators $\boldsymbol{\Lambda}$ and $\boldsymbol{K}$ acting on the fourth derivative (moved to the left-hand side) are evaluated implicitly and the terms grouped into the right-hand side are treated explicitly. For the sake of illustration, we shall consider the case when the non-local term is not evaluated (a frequent approximation that we shall use in many examples in this dissertation). In this case, at time n, following Equation (2.15) and using the definition of $\boldsymbol{\Lambda}$, the time-stepping scheme reads

$$\begin{aligned}&\frac{1}{2\Delta t}(3\boldsymbol{x}^{n+1} - 4\boldsymbol{x}^{n} + \boldsymbol{x}^{n-1}) + (c+1)\boldsymbol{x}_{ssss}^{n+1}\\ +&(c-3)\left[(2\boldsymbol{x}_s^n - \boldsymbol{x}_s^{n-1})\cdot\boldsymbol{x}_{ssss}^{n+1}\right](2\boldsymbol{x}_s^n - \boldsymbol{x}_s^{n-1}) = 2\boldsymbol{N}(\boldsymbol{x}^n) - \boldsymbol{N}(\boldsymbol{x}^{n-1}).\end{aligned} \tag{2.17}$$

The only difference is the very first time time step, where we do not have a previous time level available, and there we use a simple forward Euler step. This form is particularly convenient as the discrete version is a banded matrix of the form $-(1+c)\boldsymbol{D}^4+(3-c)(2\boldsymbol{x}_s^n-\boldsymbol{x}_s^{n-1})(2\boldsymbol{x}_s^n-\boldsymbol{x}_s^{n-1})$, where $\boldsymbol{D}^4$ is a fourth-derivative finite difference stencil tensor, which can be solved efficiently using specialized inversion routines. For the corresponding local tension equation (same as Equation (2.12) without the $\boldsymbol{K}$ operator), the numerical analog is a tridiagonal matrix system which is inverted at every time step.

In cases where shall indeed include the effect of intra-chain interactions, a regularized version of the non-local operator from Equation (1.12) is used:

$$\boldsymbol{K}_\delta[\boldsymbol{f}](s) = \int_0^1 \left(\frac{\boldsymbol{I} + \hat{\boldsymbol{r}}(s,s')\hat{\boldsymbol{r}}(s,s')}{\sqrt{|\boldsymbol{r}(s,s')|^2+\delta^2}} \cdot \boldsymbol{f}(s') - \frac{\boldsymbol{I} + \hat{\boldsymbol{s}}(s)\hat{\boldsymbol{s}}(s)}{\sqrt{|s-s'|^2+\delta^2}} \cdot \boldsymbol{f}(s) \right) \mathrm{d}s'. \tag{2.18}$$

A constant regularization parameter is chosen, $\delta = 2\epsilon$, which introduces an error of $O(\epsilon^2 \log(\epsilon))$ in the interior of the filament and $O(\epsilon)$ near its ends. This could be further improved by using a non-uniform regularization parameter $\delta(s)$ as in the work of Tornberg and Shelley [28].

As to spatial discretization, we consider N equally spaced points on the filament with spacing h such that $h = \Delta s = 1/(N-1)$. Hence, the discrete points become $s_j = jh$ where $j = 0, 1, .., N$. All spatial derivative are approximated by second-order divided differences, so the approximation is valid to an $O(h^2)$ error. Standard centered stencils are used wherever applicable, except at the boundaries where skewed operators are applied. The boundary conditions of force- and moment-free ends from Equation (2.3) enter the system through finite difference stencils applied at or near the endpoints.

2.3.2 Evaluating Brownian terms

Recollect from Section 1.2.3 that the Brownian forces are specified only by their mean and second moment – properties that make them satisfy the fluctuation-dissipation theorem. Numerically, this force distribution $\boldsymbol{\xi}$ is approximated as:

$$\boldsymbol{\xi}(s,t) = \sqrt{\frac{2}{\Delta s \Delta t}}\,\boldsymbol{B}\cdot\boldsymbol{w}, \tag{2.19}$$

where $\boldsymbol{w}$ is a random vector from a Gaussian distribution of zero mean and unit variance. Δs is the spatial grid spacing, Δt is the time step, and $\boldsymbol{B}$ is the tensor square root of the resistance tensor $[\boldsymbol{\Lambda} + \boldsymbol{K}]^{-1}$. This approximation can be seen to satisfy Equation (2.5) directly.

The random vector $\boldsymbol{w}$ is generated from a uniform distribution at each evaluation. Calculating the square root of the inverse of the mobility tensor can be costly, especially since the tensor depends on the current position and this is updated at every time-step. This is especially costly when the non-local operator is involved as the interactions result in a dense matrix. However, for the local problem, the form of $\boldsymbol{B} \approx \sqrt{\boldsymbol{\Lambda}^{-1}}$ can be analytically determined using the following manipulation: we represent the mobility operator $\boldsymbol{\Lambda}$ in the form $(c+1)(\boldsymbol{I} - \alpha \boldsymbol{x}_s\boldsymbol{x}_s)$, where $\alpha = (3-c)/(c+1)$. Then assuming $\boldsymbol{\Lambda}^{-1}$ to be of the form $(\boldsymbol{I} + \beta \boldsymbol{x}_s\boldsymbol{x}_s)/(c+1)$, one can write:

$$\boldsymbol{\Lambda}\boldsymbol{\Lambda}^{-1} = (\boldsymbol{I} - \alpha \boldsymbol{x}_s\boldsymbol{x}_s)(\boldsymbol{I} + \beta \boldsymbol{x}_s\boldsymbol{x}_s) = \boldsymbol{I}. \tag{2.20}$$

This allows us to solve for β and we get $\beta = \alpha/(1-\alpha) = -(c-3)/2(c-1)$ which then yields the form of $\boldsymbol{\Lambda}^{-1}$:

$$\boldsymbol{\Lambda}^{-1} = \frac{1}{c+1}\left[\boldsymbol{I} - \left(\frac{c-3}{2(c-1)}\right)\boldsymbol{x}_s\boldsymbol{x}_s\right]. \tag{2.21}$$

Finding the tensor square root of $\boldsymbol{\Lambda}^{-1}$ is now a similar exercise: we assume that $\sqrt{\boldsymbol{\Lambda}^{-1}}$ is of the form $(\boldsymbol{I} + \gamma \boldsymbol{x}_s\boldsymbol{x}_s)/\sqrt{(c+1)}$ and then

$$(\boldsymbol{I} + \gamma \boldsymbol{x}_s\boldsymbol{x}_s)(\boldsymbol{I} + \gamma \boldsymbol{x}_s\boldsymbol{x}_s) = \boldsymbol{I} + \beta \boldsymbol{x}_s\boldsymbol{x}_s.$$

One can solve for $\gamma = -1 \pm \sqrt{1+\beta} = -1 \pm \sqrt{(c+1)/2(c-1)}$ where either of the roots may be used. This then gives the form of the inverse of the square root of the mobility tensor

$$\boldsymbol{B} = \sqrt{\boldsymbol{\Lambda}^{-1}} = \sqrt{1/(c+1)}\left[\boldsymbol{I} + \left(-1 \pm \sqrt{(c+1)/2(c-1)}\right)\boldsymbol{x}_s\boldsymbol{x}_s\right], \tag{2.22}$$

which goes into Equation (2.19). Of course, this method is possible only due to the form of $\boldsymbol{\Lambda}$; if hydrodynamic interactions were to be included, the mobility operator would include the integral in Equation (1.12) and a full square root algorithm or asymptotics must be applied (see Chapter 6.

There are two important points to notice here. The first is that the tension equation (2.12) contains spatial derivatives of the Brownian force $\boldsymbol{\xi}(s)$. Brownian forces at adjacent grid points are uncorrelated and using Equation (2.19) directly in Equation (2.12) can lead to numerical instabilities resulting from the very large terms obtained by directly differentiating $\boldsymbol{\xi}(s)$. Noting that high wavenumber force fluctuations do not result in high wavenumber shape fluctuation owing to the strongly smoothing nature of the fourth derivative in Equation (2.6), one strategy to solve this problem consists of applying a 'low-pass-filter' to the stochastic force distribution. This is achieved by taking a Fourier transform of $\boldsymbol{\xi}(s)$. The largest few wavenumbers (representing the sharpest gradients) are removed and the distribution is transformed back. The magnitude of $\boldsymbol{\xi}(s)$ is then rescaled to conserve the total energy by matching the variance to that of Equation (2.5). It is important here not to remove so many wavenumbers that one loses the dynamics due to thermal fluctuations; we have filtered out not more than the top 40% of wavenumbers and this is seen not to affect the equilibrium properties (see below).

The other caveat is that the Brownian force in Equation (2.19) is proportional to the square root of the timestep. This means that during integration, the effective order of the time marching scheme is reduced from second to first order. This has been noted previously [52] and will result in a stricter time constraint to ensure stability and accuracy. The way to get past this would be to implement specialized stochastic integration algorithms [97–99], like a mid-point scheme, tailored to increase the order of accuracy. This gain in order of accuracy is at the price of more evaluations at every time-step. Implementing a more accurate, while at the same time economical scheme, is a challenging open problem.

2.4 Equilibrium properties

Before we proceed to examine the dynamics of Brownian polymers in external flows, we take a quick look at polymers in the absence of flow, which will also serve as a check for the numerical methods defined in Section 2.3. One straightforward way to validate the Brownian dynamics algorithm is to compare its results against predictions from statistical mechanics. The end-to-end distance and the radius of gyration are two obvious candidates for this comparison, both having direct physical significance in characterizing the dimensions of a microchannel or a pore that the polymer can pass through. The end-to-end distance is the magnitude of the vector connecting the two ends, while the radius of gyration is the root-mean-square distance of the parts of the polymer from its center of mass. Their mean-square values take the forms, respectively,

$$\langle R^2 \rangle = \frac{1}{L^2} \int_0^L \int_0^L \langle \boldsymbol{x}_s(s_1) \cdot \boldsymbol{x}_s(s_2) \rangle \mathrm{d}s_1 \mathrm{d}s_2, \tag{2.23}$$

$$\langle S^2 \rangle = \frac{1}{L^2} \int_0^L \int_0^L \langle (\boldsymbol{x}(s_1) - \boldsymbol{x}^0) \cdot (\boldsymbol{x}(s_2) - \boldsymbol{x}^0) \rangle \mathrm{d}s_1 \mathrm{d}s_2. \tag{2.24}$$

Here, $\boldsymbol{x}^0$ is the center of mass of the polymer. These can be simplified [87] using the definition of the persistence length from Equation (1.27) to expressions in terms of ℓ_p and obtain, for instance, equilibrium distributions of these lengthscales.Wilhelm and Frey [100] derived a probability distribution function for semiflexible filaments in Brownian solvents, and they observed a characteristic shift of the peak towards $R \sim L$ as the filament got stiffer, a result consistent with our intuitions as $\ell_p \gg L$, and one that has been experimentally verified [101]. As an example, the probability distribution as obtained from our simulations are shown in Figure 2.1, and this shift in peak is clearly seen.

Validation with equilibrium values of polymers such as end-to-end distance and radius of gyration does not tell us much about the performance of the model *before* it reaches equilibrium. There is a characteristic time scale (usually referred to as the longest relaxation time of the single filament) at which these equilibrium values are realized. To account for the transient dynamics before this relaxation is achieved, we need a property that is time-dependent and preferably one that shows a clear transition to equilibrium. For this, we use the mean-square displacement (MSD)

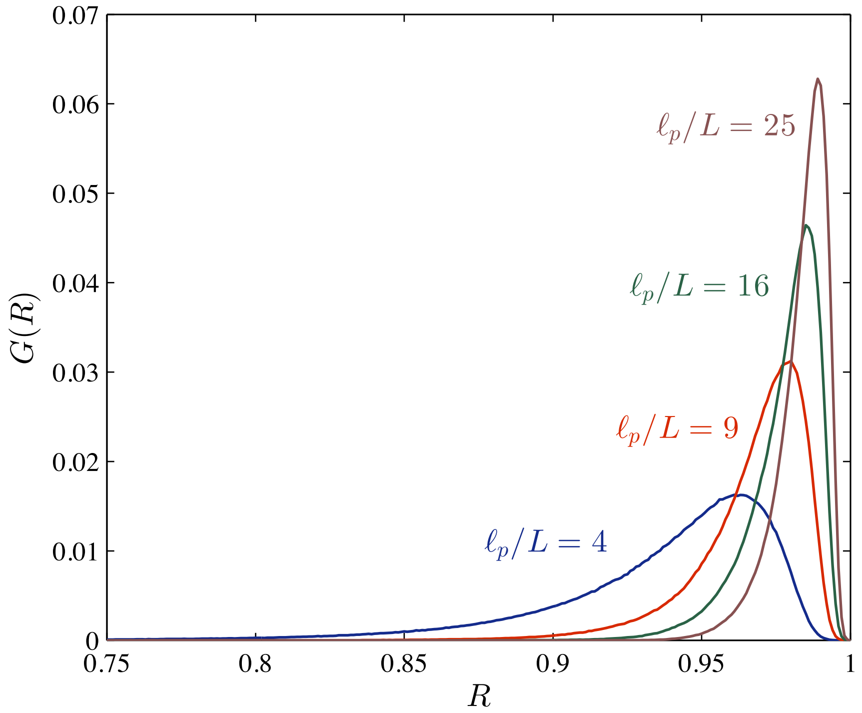

Figure 2.1: Probability distribution function $G(R)$ of the end-to-end distance from simulations.

of the end-to-end distance. The MSD is defined as [29]

$$\varDelta_R(t) = \left\langle (R(t) - R(0))^2 \right\rangle . \tag{2.25}$$

The MSD of polymers with free boundary conditions has been previously studied analytically [88] and verified experimentally [101]. It is known to grow subdiffusively like $t^{3/4}$, and for long times to approach an equilibrium value of

$$\varDelta_R(t \gtrsim \tau) = \frac{2}{45}\left(\frac{L}{\ell_p}\right)^2 , \tag{2.26}$$

where τ is the longest relaxation time of the polymer. This is also the timescale at which both the end-to-end distance and the radius of gyration saturate to their equilibrium values. Results from our simulations reproduce this behavior closely. The subdiffusive growth as $t^{3/4}$ is clearly seen, until it reaches the correct equilibrium asymptote. It must also be noted that the characteristic relaxation time is very close to that reported in the experiments of Le Goff *et al.* [101]. The ensemble averages from 50 runs for each value of flexibility ($\ell_p/L = 4, 9, 16$ and 25) are shown in Figure 2.2.

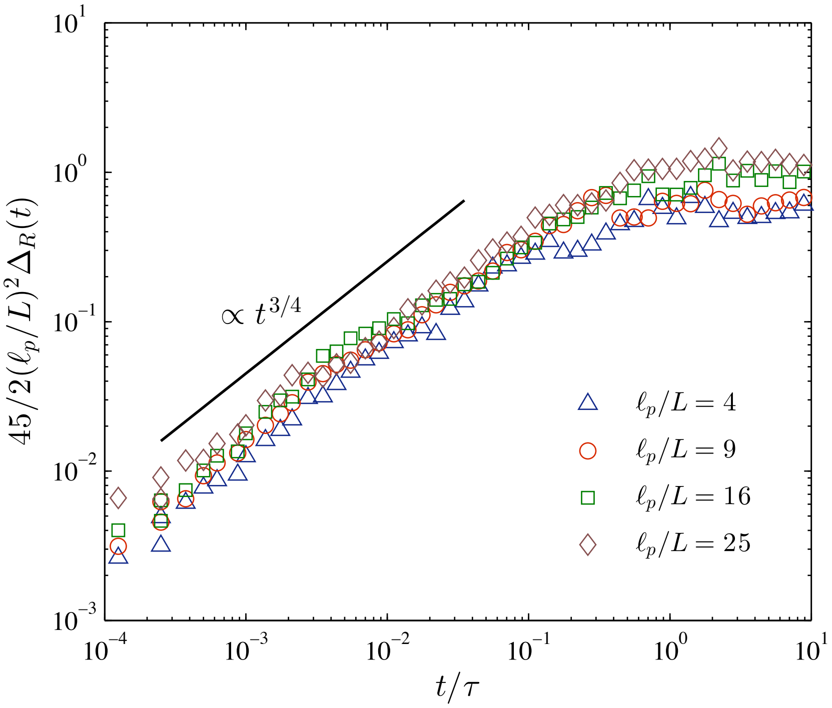

Figure 2.2: Mean-square displacement of the end-to-end distance.

It is interesting to note here that for very short times, $t/\tau < 10^{-3}$, both experiments [101] and theory [29] report a downturn in the slope to approximately $t^{7/8}$. Our numerical results seem to indicate a downturn too, that qualitatively agrees with previous findings.

2.5 Shear flow

We now move on to the first application of our slender-body model – that of deciphering the dynamics of polymers in an imposed flow. We focus particularly on the kind of flows seen commonly in micro-channel devices used to trap, separate and manipulate single macromolecules. Such applications arise in single polymer studies, genetic engineering and related experiments that use hydrodynamic ‘trap’ devices [47, 48]. We begin by applying the slender-body model to free filaments in simple shear flow. Analytical results can be obtained for simplified cases (if one neglects Brownian forces), and numerical solutions enable us to explore more complicated cases. We then move on to studying the suppression of fluctuations and buckling

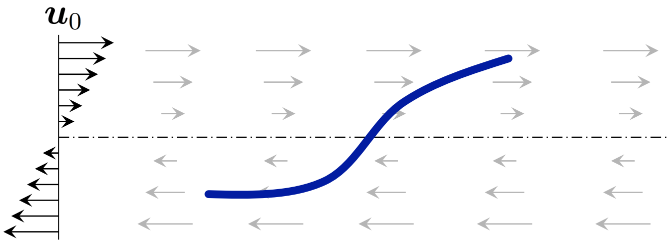

Figure 2.3: A flexible filament in planar shear flow.

instability that are displayed in the neighbourhood of hyperbolic stagnation points.

In this section, we are concerned with the dynamics of a filament placed in a laminar shear flow as depicted in Figure 2.3. In terms of the position vector $\boldsymbol{x} = (x, y, z)$ of the filament, the velocity felt by the body is of the form $\boldsymbol{u}_0 = (\dot{\gamma} y, 0, 0)$. Before we go on to the general case of a filament in shear with Brownian forces, it is helpful to look at the dynamics in the absence of thermal fluctuations.

2.5.1 The non-Brownian case

The model we derived in Section 2.2 accounts for hydrodynamic as well as Brownian forces. If, for the sake of illustration, one neglects Brownian fluctuations as well as non-local interactions, we get the following set of equations governing the centerline and the tension:

$$\bar{\mu}\boldsymbol{x}_t(s,t) = \bar{\mu}\boldsymbol{u}_0(\boldsymbol{x}(s,t),t) - \left[(c+1)\boldsymbol{I} + (c-3)\boldsymbol{x}_s\boldsymbol{x}_s\right]\cdot\left[-(T(s)\boldsymbol{x}_s)_s + \boldsymbol{x}_{ssss}\right], \quad (2.27a)$$

$$\begin{aligned} -2(c-1)T_{ss}(s) + (c+1)(\boldsymbol{x}_{ss}\cdot\boldsymbol{x}_{ss})T(s) = \bar{\mu}\boldsymbol{x}_s\cdot\frac{\partial \boldsymbol{u}_0}{\partial s} &+ (7c-5)(\boldsymbol{x}_{ss}\cdot\boldsymbol{x}_{ssss}) \\ &+6(c-1)(\boldsymbol{x}_{sss}\cdot\boldsymbol{x}_{sss}). \end{aligned} \quad (2.27b)$$

Note that in this case, the only timescale is the one associated with the shear rate, i.e. $\dot{\gamma}^{-1}$, and the centerline equations get modified to accommodate this change of non-dimensionalization [28]. All other characteristic scales remain the same as before, and $\bar{\mu} = 8\pi\mu\dot{\gamma}L^4/\kappa$ is the ratio between viscous and elastic forces as we have defined before.

If the line tension induced in the filament backbone overcomes its flexural rigidity, it can become unstable to buckling. We shall see examples of buckling due to simple shear in the following pages. However, to start with, a particularly simple

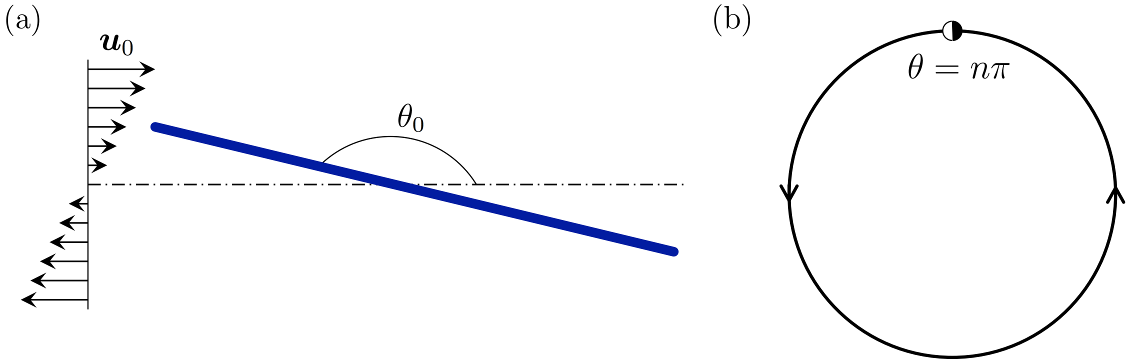

Figure 2.4: A straight filament in planar shear flow and its dynamical analogue of a flow on the circle. (a) The filament makes at initial angle θ_0 alone the mid-plane of a simple shear flow $\boldsymbol{u}_0$. (b) Flow on the circle with semi-stable fixed points at $\theta = n\pi$.

case is that of a rigid rod. Such a rod would simply rotate about its center (which we assume is in the central plane where the velocity is zero, as in Figure 2.4(a)). It turns out that the Equations (2.27) can be solved analytically under these assumptions and this can give us some insight into the dynamics of such rotational motion.

To obtain the analytical solution, we consider a perfectly straight filament with position vector $\boldsymbol{x} = (x, y, z)$ in the dimensionless planar shear flow $\boldsymbol{u}_0 = (y, 0, 0)$, with the rod at an instantaneous angle $\theta(t)$ with the x-axis. This gives the local tangent $\boldsymbol{x}_s = (\cos\theta, \sin\theta, 0)$ which is constant throughout its length. Higher arclength derivatives are zero, and Equations (2.27a)-(b) then have the exact solution:

$$\boldsymbol{x}(s,t) = \left(\frac{1}{2} - s\right)\hat{\boldsymbol{e}}_\theta, \qquad T = \frac{\bar{\mu}\sin 2\theta}{8(c-1)} s(1-s), \tag{2.28}$$

where $s \in [0,1]$ is the arclength and $\hat{\boldsymbol{e}}_\theta = (\cos\theta, \sin\theta, 0)$. θ then solves the non-linear ordinary differential equation

$$\frac{\partial \theta}{\partial t} = -\sin^2\theta. \tag{2.29}$$

Assuming an initial angle of $\theta(t=0) = \theta_0$, we then have the exact solution

$$\theta(t) = \cot^{-1}(t + \cot\theta_0). \tag{2.30}$$

This solution can be shown [28] to be identical up to $O(\epsilon^2)$ to the Jeffery orbit solution [102] for a long slender ellipsoid in a shear flow, consistent with our choice of a spheroidal filament shape (cf. Section 1.1.3).

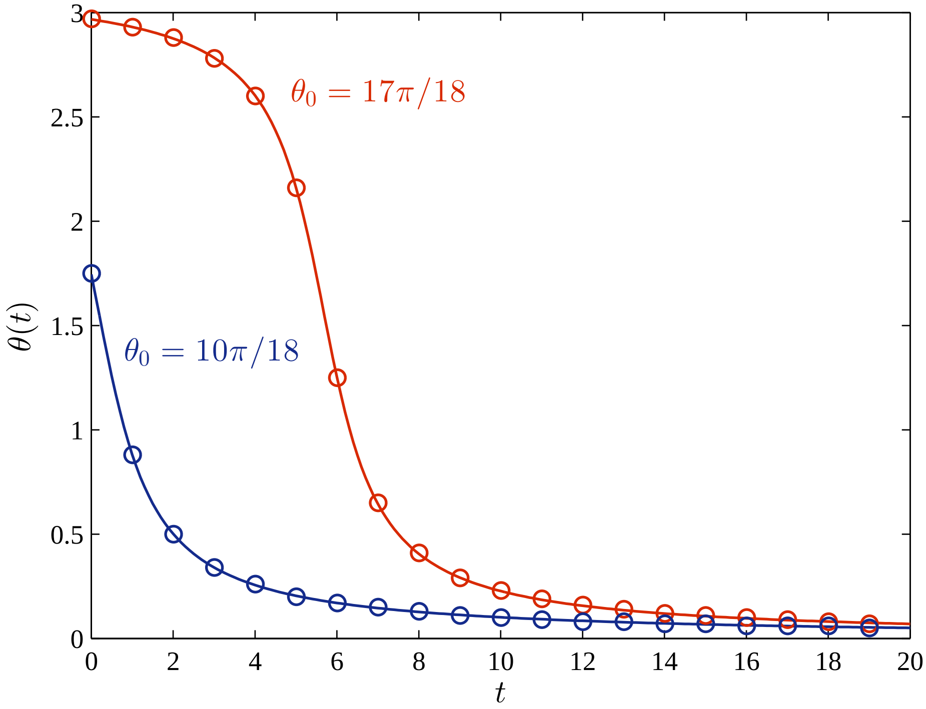

Figure 2.5: Evolution of the angle $\theta(t)$ of a straight filament with respect to the x-axis in a planar shear flow. The symbols are from simulations corresponding to initial orientations $\theta_0 = 17\pi/18$ and $\theta_0 = 10\pi/18$, and the lines follow Equation (2.30).

We can see from the solution in Equation (2.30) that the filament merely rotates about its center to align with the shear plane. Figure 2.5 shows $\theta(t)$ in the case of a filament starting at two different initial orientations, $\theta_0 = 17\pi/18$ and $\theta_0 = 10\pi/18$. It is vital to note that the filament is assumed to have zero thickness the way the slender-body theory is formulated, and once aligned with the plane of zero shear, it stays aligned until externally perturbed. This is not the case for particles of finite width which will continue to rotate in Jeffery orbits [102]. The rotation is initially slow due to the low shear rate at small distances from the x-axis, and as θ approaches $\pi/2$, the rotational speed is maximum. It slows down again as the shear rate lessens and then aligns with the flow very slowly. In fact, Tornberg and Shelley [28] note that for $\epsilon = 0.01$ (the value we use in our simulations), the filament takes only about 4% of the time period to cover 90% of the orbit, and most of the time is spent aligning with the x-axis. It can also be seen by dimensionalizing Equation

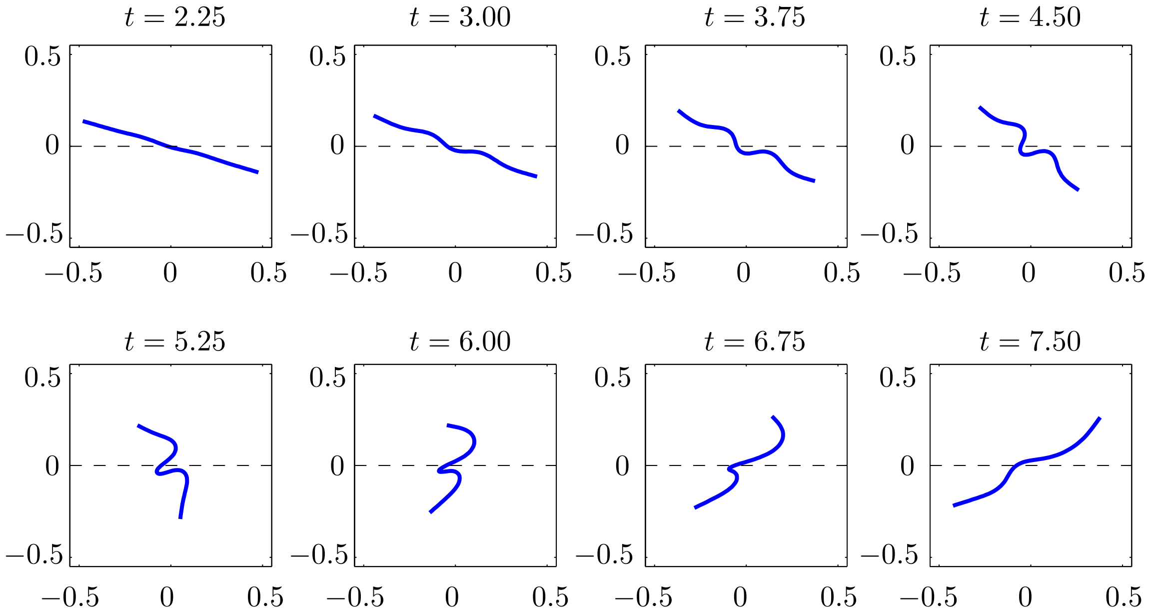

Figure 2.6: Buckling of a flexible filament for $\bar{\mu} = 4 \times 10^5$.

(2.30) that the orbit is faster for a higher shear rate, which one would expect by intuition.

Another point of view of looking at Equation (2.30) is to think of it as a flow on the circle [103]. As shown in Figure 2.4(b), the system has fixed points at $\theta = n\pi$, all of which are semi-stable. These equilibria can be attained approaching only from one direction, and once there a filament will stay in equilibrium until externally perturbed. If perturbed, the filament is either pushed back to equilibrium or it takes a full turn to the next fixed point, based on the direction of perturbation. Such an approach is particularly insightful when we include Brownian fluctuations, and we shall return to it soon.

When the filament is flexible (note that 'flexible' in this context refers to flexibility with respect to viscous forces), the equations are not so amenable to analytical treatment and we solve them numerically. The feature most predominant in flexible fibers is the buckling instability, caused by the non-uniform tension developed in the filament due to hydrodynamic forces. A perfectly straight fiber remains straight for the entire orbit, but the tiniest of perturbations (which is externally imposed in our simulations) leads to interesting buckling patterns. These dynamics and their impact

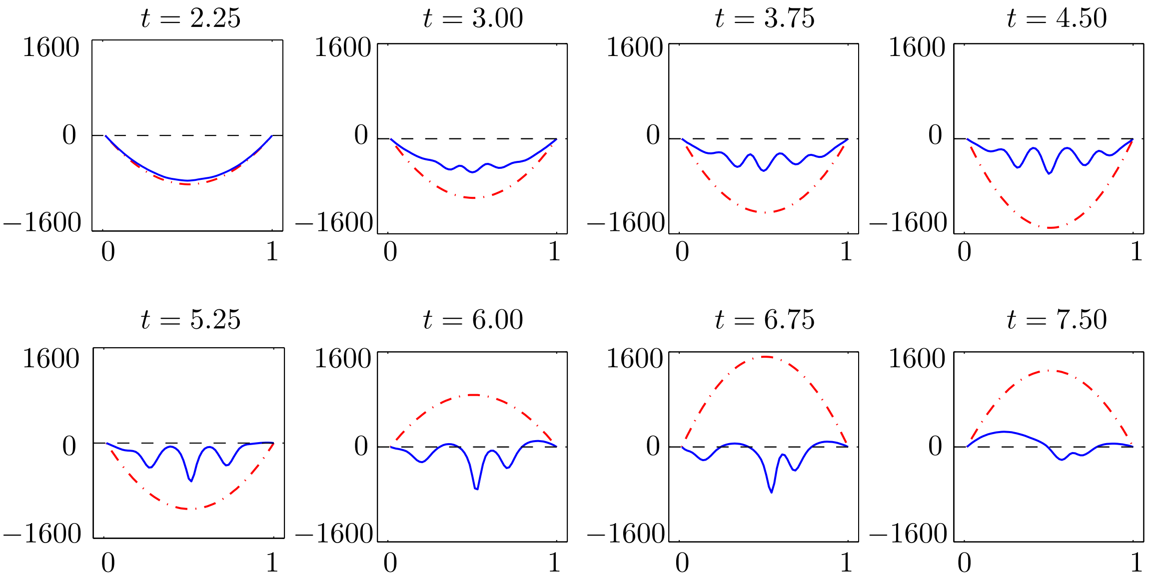

Figure 2.7: Tension induced in the filament as a result of buckling at $\bar{\mu} = 4 \times 10^5$ shown as a function of arclength s. The corresponding values for a rigid rod are shown in dashed red lines.

on suspension rheology have been recently studied by Tornberg and Shelley [28]. As a test of our numerical algorithm, and for illustration, Figure 2.6 shows pronounced buckling for a filament placed initially at $\theta_0 = 17\pi/18$ and tracked through an entire rotation $\bar{\mu} = 4 \times 10^5$. These results are in good agreement with those presented in Tornberg and Shelley [28].

As was mentioned earlier, this buckling is a result of the non-uniform tension induced in the filament due to the hydrodynamic forces that cause shape fluctuations. In the case of rigid rods, the tension is known to have a parabolic profile which we derived in Equation (2.28). This tension is negative in the second and fourth quadrants, to resist compression; beyond that, in the first and third quadrants, the tension becomes positive, actively resisting elongation as the flow tends to straighten the filament. But, when the filament buckles, tension starts out negative and takes on more complicated patterns (Figure 2.7) to enforce inextensibility through the complex shapes taken by the filament.

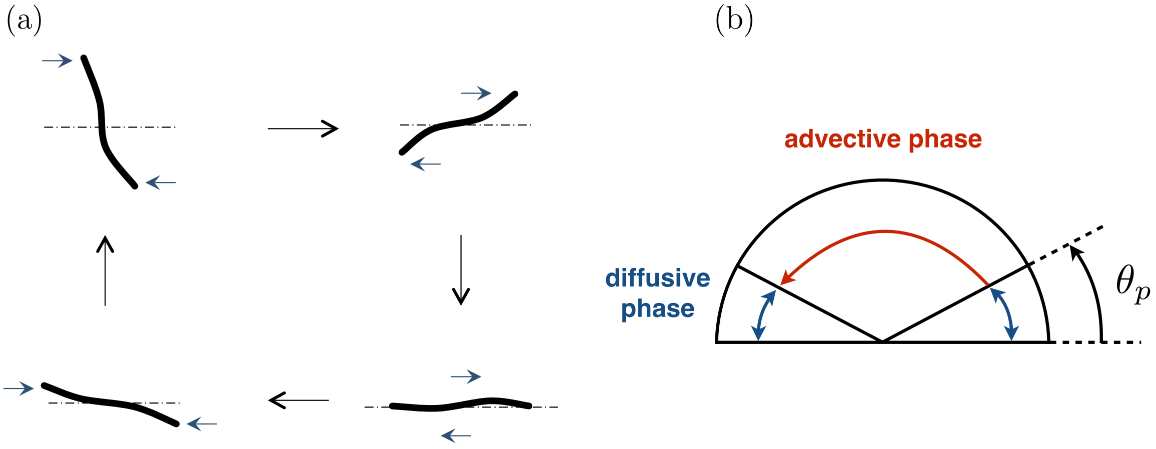

Figure 2.8: The tumbling cycle of a polymer in shear flow. (a) Descriptive cycle of one tumble of a filament. (b) Diffusive and advective phases of a tumbling event.

2.5.2 Tumbling in shear flow

A good place to start the discussion on the effect of Brownian motion on filaments in shear flows is to go back to Figure 2.4. As mentioned earlier, a non-Brownian filament aligns itself with the shear plane and stays aligned. There are no perturbations that can cause it to move out of plane once $\theta = n\pi$. Now if we consider Brownian forces acting along the filament, there is a possibility that the filament (or a part of it) may be pushed out of the stable axis once it aligns with the flow. One can visualize the effect, and intuitively predict that if the fluctuation causes the filament to rotate counter-clockwise (with reference to Figure 2.4), the shear tends to push it back to a position where the forces might be balanced. If, however, the fluctuation is such that the filament rotates clockwise, it now faces the shearing action of the background flow that drives it away from the shear plane and the filament takes a tumble. Figure 2.8(a) shows this possible tumbling mechanism. The Brownian kicks happen in a phase that is diffusion-dominant ($\theta < \theta_p$ in Figure 2.8(b)) and outside this range, the shear flow simply rotates the fiber in an advection-dominated ($\theta > \theta_p$) phase.

Following the analysis of non-Brownian rods, we attempt to understand the dynamics by considering a simpler case, that of perfectly straight filaments. It can be shown [29, 104] that the equation governing θ in this case, similar to Equation (2.29)

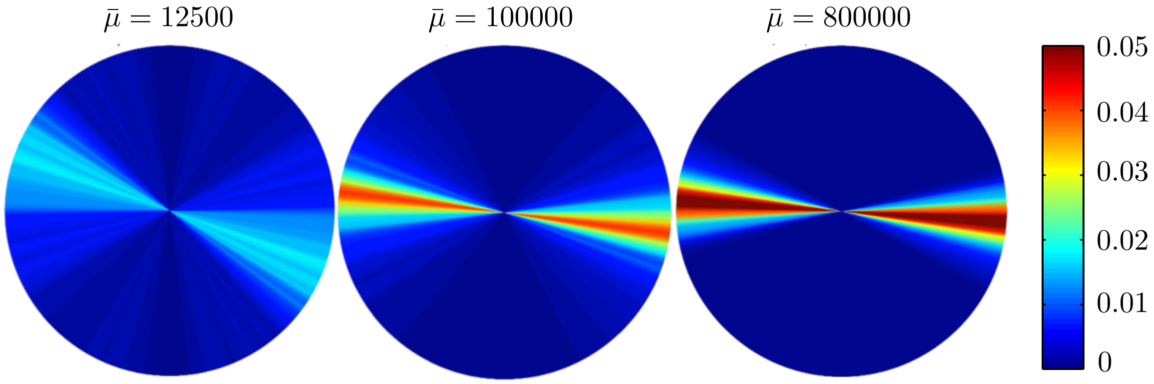

Figure 2.9: Polar probability density of the mean orientation of the polymer from simulations at three different flow strengths. The shear flow is from right to left in the upper half and vice versa.

for non-Brownian rods, is (in dimensional form)

$$\theta_t = -\dot{\gamma} \sin^2 \theta + \xi(t), \tag{2.31}$$

where ξ is a stochastic term that is related to the rotational diffusivity of a rod, d_r [29], with $\langle \xi(t) \rangle = 0, \langle \xi(t)\xi(t') \rangle = 4 d_r \delta(t - t')$. An alternative way to interpret this term is as a control parameter in a saddle node bifurcation at $\xi = 0$ [103]. The unstable branch in this bifurcation physically corresponds to the Brownian forces driving the filament out of the horizontal axis, where shear effects kick in and a new rotation cycle begins.

Our full simulations with flexible polymers also show this typical tumbling behavior. Fibers are seen to maintain a more or less stretched state, especially for large strain rates. In order to quantify a mean orientation of a flexible polymer, we introduce the gyration tensor [105]:

$$\boldsymbol{S} = \frac{1}{L^2} \int_0^L \int_0^{s_1} (\boldsymbol{x}(s_1) - \boldsymbol{x}(s_2))(\boldsymbol{x}(s_1) - \boldsymbol{x}(s_2)) \, \mathrm{d}s_2 \, \mathrm{d}s_1. \tag{2.32}$$

Then, we define the eigenvector corresponding to the largest eigenvalue of $\boldsymbol{S}$, evaluated at each time step, as the mean orientation of the filament. Statistics of the orientation collected this way is shown in Figure 2.9, which clearly illustrates the advective and diffusive regimes separated at an angle θ_p, which in turn depends on the rate of strain (in the form of $\bar{\mu}$ here). We also see that polymers spend shorter durations in the advective phase as $\bar{\mu}$ increases (consistent with faster flow), leading

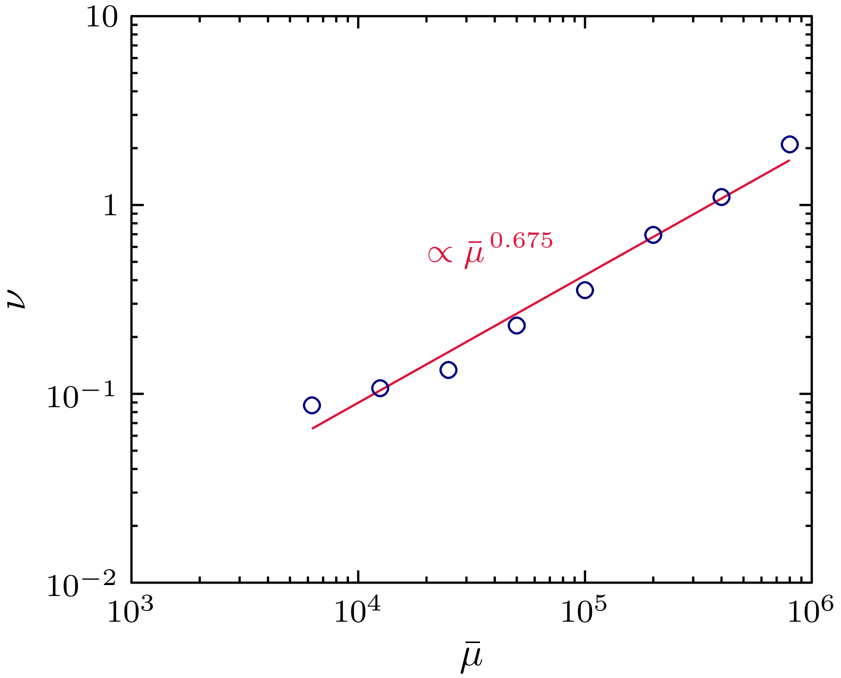

Figure 2.10: Scaling of tumbling frequency ν with dimensionless flow strength $\bar{\mu}$ for a filament with $\ell_p/L = 4$.

to a build up of probability in the range $\theta < \theta_p$ in the second and fourth quadrants where advection and diffusion balance out. The shear flow is from right to left in the upper half in these simulations.

This tumbling phenomenon has long been observed in single DNA experiments using fluorescence microscopy [105, 106]. However, DNA is a floppy polymer with negligible bending resistance. Recently, careful shear flow experiments [31] on actin filaments (which are semiflexible) revealed the same phenomenon. Harasim *et al.* [31] recorded a quasi-periodic tumbling, whose characteristic frequency can be estimated as follows.

The peak probability in Figure 2.9 can be determined by solving a Fokker-Planck equation corresponding to the Langevin equation (2.31) for $\theta(t)$. Physically, this corresponds to the balance of shear-driven advection and thermal diffusion in the stationary probability flux, which is seen to be [31, 107] at $\theta = \theta_p \sim (d_r/\dot{\gamma})^{1/3}$. Knowing this, the time spent in the advective phase can be estimated by solving the non-Brownian part of Equation (2.31): $\theta_t \approx -\dot{\gamma}\sin^2\theta$ between θ_p and $\pi - \theta_p$:

$$t_{\mathrm{adv}} = \int_{\theta_p}^{\pi-\theta_p} \frac{\mathrm{d}\theta}{\dot{\gamma}\sin^2\theta} = \frac{2}{\dot{\gamma}\tan\theta_p} \sim d_r^{-1/3}\dot{\gamma}^{-2/3}. \tag{2.33}$$

The time spent in the diffusive phase can be estimated similarly by considering just the Brownian part of Equation (2.31): $\theta_t \approx \xi(t)$. This is a random walk in orientation and the timescale associated with it can be estimated directly from the explored range and rotational diffusivity as

$$t_{\mathrm{diff}} \sim \frac{\theta_p^2}{d_r} \sim d_r^{-1/3}\dot{\gamma}^{-2/3}. \tag{2.34}$$

The characteristic timescale of the tumbling events, then, is the sum of the two which yeilds the tumbling frequency:

$$\nu = \frac{1}{t_{\mathrm{adv}} + t_{\mathrm{diff}}} \sim \dot{\gamma}^{2/3}. \tag{2.35}$$

Figure 2.10 shows the tumbling frequency extracted from our simulations against the strain rate ($\bar{\mu}$ in dimensionless terms). Recall that the phenomenon is quasiperiodic – the frequency spectrum corresponding to the orientation data reveals a spectrum and not a single peak. The frequency we identify in Figure 2.10 corresponds to the maximum of this spectrum, and the scaling is seen to match very well will the predicted value of the 2/3rd power law.

2.6 Extensional flow

We now focus on a family of flows commonly observed in microfluidic devices, particularly in four-roll mills and hydrodynamic trap devices. These flow fields are hyperbolic and a filament placed at the stagnation point displays interesting non-linear behavior. Tension induced in the filament can suppress fluctuations when aligned with the extensional axis, or can cause a buckling instability analogous to Euler buckling of beams [108] when aligned with the axis of compression. Recently, there have been attempts to study this ‘stretch-coil’ transition in macroscopic flows by electrodynamic forcing [36]. Young and Shelley [35] used slender-body theory to describe the dynamics in the case of non-Brownian elastic filaments, extending the theory to predict transport of fibers in cellular flows like in the experiments of Wandersman *et al.* [36]. At the microscopic scale, this phenomenon can be particularly useful in designing devices meant to separate and trap single particle for long timescales as in the microfluidic device developed by Tanyeri *et al.* [47, 48]. A notable attempt at investigating this effect with the inclusion of thermal fluctuations is a recent work by Kantsler and Goldstein [32] where a variational method is used to justify experimentally observed trends.

Free polymers in Brownian solvents have been well studied [16, 88], but the effect of non-uniform tension has only begun to receive attention. Here, we consider the two aforementioned phenomena this non-uniform tension can induce: suppression of thermal fluctuations in extension and the buckling instability in compression.

2.6.1 Suppression of thermal fluctuations by stretching

Consider a filament placed in an extensional flow $\boldsymbol{u}_0 = (u, v, w) = (\dot{\gamma}x, -\dot{\gamma}y, 0)$. This would correspond to a controlled microfluidic device [32, 47] that, by carefully controlled pressures at the entrances and exits, traps the filament at the center. Figure 2.11 (a) illustrates this set-up.

For our purposes here, we consider a filament nearly aligned with the extensional axis (the horizontal axis in Figure 2.11 (b)) such that its mean orientation is near zero. For simplicity of analysis, we also assume a two-dimensional system with small-amplitude fluctuations from a mean position represented by $h(x)$ (Figure 2.11 (b)). Filament rotations away from the axis are assumed small [32] which allows us to approximate the mean position to be along the axis, and the end-to-end distance R of the filament is approximately the same as its contour length L. Then, the energy of the filament (assumed to be placed with its center at the origin) follows a Monge representation:

$$\mathcal{E} = \frac{1}{2}\int_{-L/2}^{L/2} \left[\kappa h_{xx}^2 + T(x)h_x^2\right] \mathrm{d}x. \tag{2.36}$$

The tension $T(s)$ can be approximated if we assume a 2-D background flow $\boldsymbol{u}_0 = (x, -y)$ (made dimensionless by standard scales that we have been using). Note that thermal fluctuations will be introduced in Equation (2.36) as an external forcing and so we consider the governing equation for the non-Brownian rod as in Equation

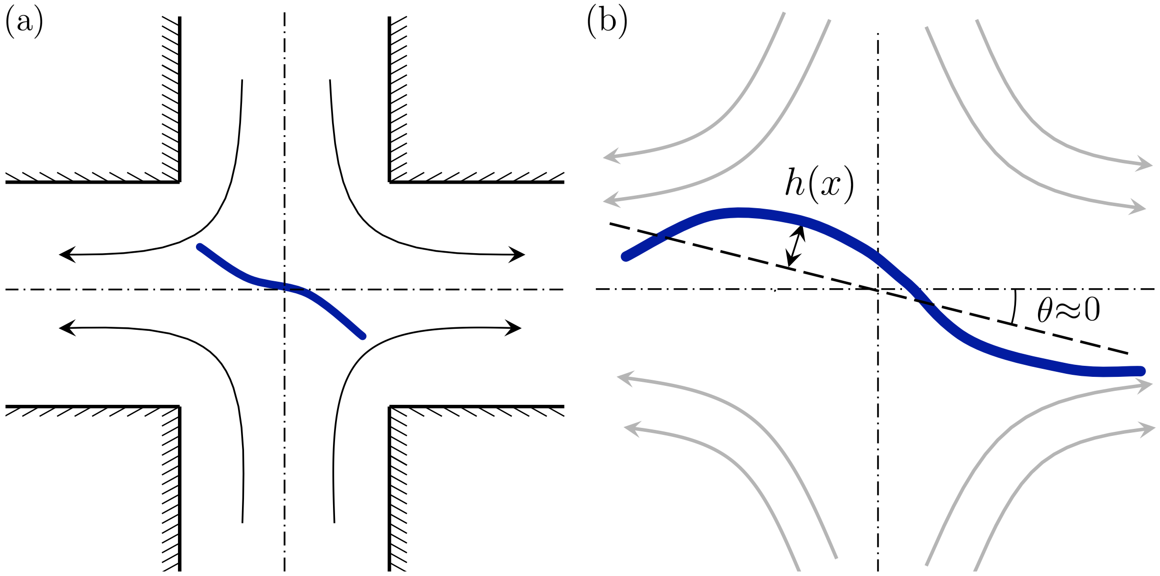

Figure 2.11: Illustration of a polymer placed in extensional flow. (a) Polymer placed at the hyperbolic stagnation point of a cross-flow device. (b) Polymer geometry as used in the analysis of suppression of fluctuations in extensional flow, showing the variable h and the mean orientation θ.

(2.27a). For a straight filament, noting that $\boldsymbol{x}_{ss} = 0$ and that $\boldsymbol{x}_t = 0$ if placed perfectly symmetrically, the steady centerline equation reduces to

$$\bar{\mu}\boldsymbol{u}_0 = [(c+1)\mathbf{I} + (c-3)\boldsymbol{x}_s\boldsymbol{x}_s] \cdot (-T_s\boldsymbol{x}_s) = -2(c-1)T_s\boldsymbol{x}_s. \tag{2.37}$$

The filament is assumed to lie along the x-axis between $x = -L/2$ and $L/2$. In dimensionless terms, this corresponds to a position vector $\boldsymbol{x} = (-1/2 + s, 0)$, unit tangent vector $\boldsymbol{x}_s = (1, 0)$ and a corresponding background velocity $\boldsymbol{u}_0 = (-1/2+s, 0)$ for $s \in [0, 1]$. Using this in Equation (2.37) along with the boundary conditions for tension, $T(s = 0) = T(s = 1) = 0$, the tension can be found to be

$$T(s) = \frac{\bar{\mu}}{4(c-1)} s(1-s). \tag{2.38}$$

In dimensional terms, Equation (2.38) gives the familiar form of the non-uniform tension in an almost straight thread aligned with the extensional axis [32, 56]:

$$T(x) = \frac{2\pi\mu\dot{\gamma}}{\ln(1/\epsilon^2 e)} \left[\frac{L^2}{4} - x^2\right], \tag{2.39}$$

where we have used $\bar{\mu} = 8\pi\mu\dot{\gamma}L^4/\kappa$ and $c = \ln(1/\epsilon^2)$.

Using this expression for tension in Equation (2.36) and the Euler-Lagrange equation, we can derive a set of eigenfunctions $W^{(n)}(x)$ and corresponding eigenvalues λ_n (see Appendix A for derivation and details) that satisfy the boundary conditions $W^{(n)}_{xx}(x=\pm L/2) = W^{(n)}_{xxx}(x=\pm L/2) = 0$, which represent force-free and moment-free ends. These eigenfunctions (shown here under the convenient rescaling $\xi = \pi x/L$ and $\mathit{\Lambda}_n = \lambda_n L^4/\pi^4\kappa$) are governed by

$$W^{(n)}_{\xi\xi\xi\xi} - \tilde{\Sigma}\left[\left(\frac{\pi^2}{4} - \xi^2\right) W^{(n)}_{\xi}\right]_{\xi} = \mathit{\Lambda}_n W^{(n)}. \tag{2.40}$$

Here, $\tilde{\Sigma} = \bar{\mu}/4\pi^4 \ln(1/\epsilon^2 e)$ is a dimensionless group that is a ratio of tensile force to elastic force, which we use to compare directly with the experiments of Kantsler and Goldstein [32], defined as

$$\tilde{\Sigma} = \frac{2\mu\dot{\gamma}L^4}{\pi^3\kappa\ln(1/\epsilon^2 e)}. \tag{2.41}$$

Now, projecting the amplitude of fluctuations onto the basis $\{W^{(n)}(x)\}$ so that $h(x) = \sum_n a_n W^{(n)}(x)$, it can be shown using integration of parts and the boundary conditions described above (see Appendix A) that the energy decomposes exactly into contributions from each mode independently: $\mathcal{E} = L/2 \sum_n \lambda_n a_n^2$. The principle of equipartition then allows us to derive the variance of the amplitudes a_n to be

$$\langle a_m a_n \rangle = \frac{\delta_{mn} L^3}{\pi^4 \ell_p \mathit{\Lambda}_n}. \tag{2.42}$$

Then, if the mean amplitude is assumed to be $\langle a_n \rangle = 0$, the mean filament fluctuation amplitude is $\bar{h} = 0$, which tells us that the local variance $V(x) = \left\langle [h(x) - \bar{h}]^2 \right\rangle$ is

$$V(x;\tilde{\Sigma}) = \frac{L^3}{\ell_p \pi^4} \sum_{n=1}^{\infty} \frac{W^{(n)}(x;\tilde{\Sigma})^2}{\mathit{\Lambda}_n(\tilde{\Sigma})}. \tag{2.43}$$

For the case of $\tilde{\Sigma} = 0$, Equation (2.40) is a one-dimensional biharmonic equation that can be solved analytically (see Appendix A), and $\mathit{\Lambda}_n$ grows like $(n+1/2)^4$. For $\tilde{\Sigma} \neq 0$, a numerical solution is straightforward and Figure 2.12 shows $V(x,\tilde{\Sigma})$ from Equation (2.43) evaluated to the first 1000 terms for four different values of $\tilde{\Sigma}$; the suppression of amplitude fluctuations with increasing strain rate is evident.

Following Kantsler and Goldstein [32], we note that the eigenfunctions for $\tilde{\Sigma} \neq 0$ are strikingly similar to those for $\tilde{\Sigma} = 0$ (see Appendix A) with the peaks flattened

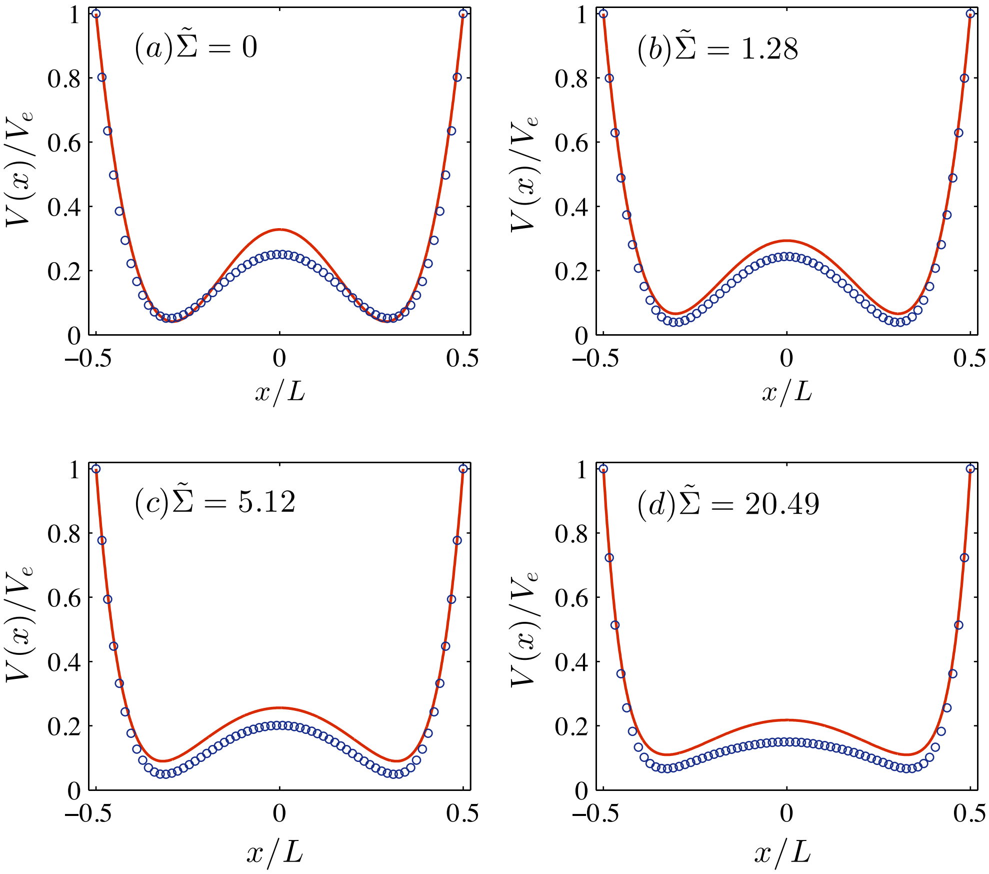

Figure 2.12: Local variance of shape fluctuations, $V(x)$, for four different flow rates. The symbols are from numerical simulations and corresponding theoretical predictions following Equation (2.43) are shown in solid lines. The normalization factor V_e is the variance of filament-end fluctuations: $V_e = [V(-L/2) + V(L/2)]/2$.

out, mirroring the suppression of amplitude fluctuations by the extensional flow. Furthermore, the form of $V(x, \tilde{\Sigma})$ in Equation (2.43) is such that the first few terms dominate, a fact reflected in the 'W' shape corresponding to the fundamental mode in Figure 2.12. Simulations show that the variance closely follows the predicted pattern with fluctuations being suppressed as $\tilde{\Sigma}$ increases. The slight mismatch between the predictions and our numerical results may be attributed to the fact that while the theory is entirely two-dimensional, the simulations allow for motion in all three dimensions. In other words, energy from fluctuations can be dissipated in the third dimension and this is not captured by the expansion in Equation (2.43).

A clearer picture of the suppression of amplitude fluctuations is the magnitude

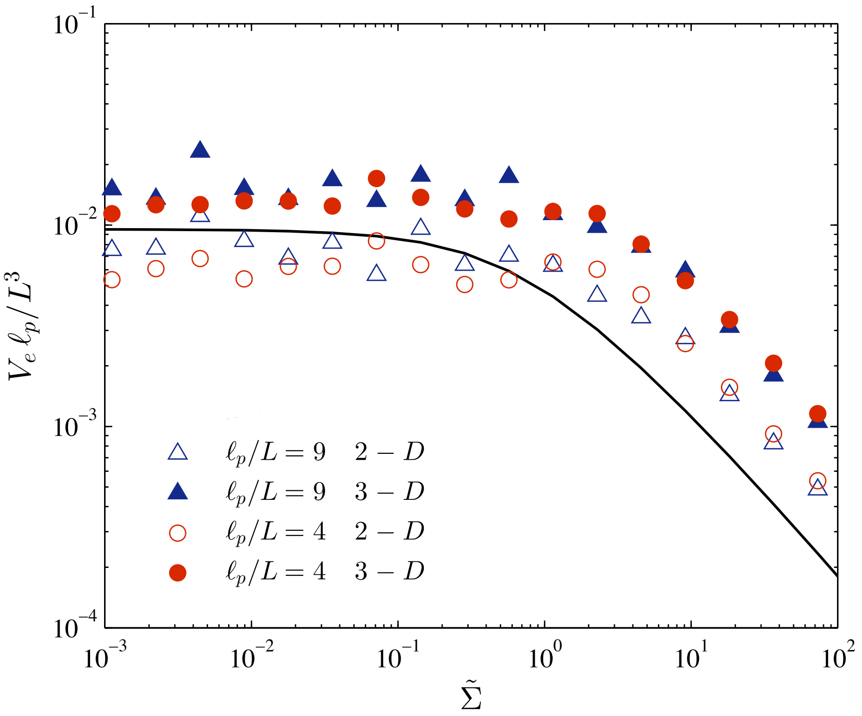

Figure 2.13: Variance of filament-end fluctuations, V_e, as a function of strain rate showing the systematic suppression of fluctuations. Three-dimensional amplitude fluctuations and the corresponding two-dimensional values for the projection on the x-y plane, as obtained from simulations, are shown with symbols. The corresponding theoretical prediction is the solid line.

of variance of the filament-end fluctuations, $V_e = [V(-L/2)+V(L/2)]/2$. Figure 2.13 shows that for small $\tilde{\Sigma}$, this value is almost the same as that for $\tilde{\Sigma} = 0$. However, for $\tilde{\Sigma} > 1$ the variance is heavily suppressed. The factor ℓ_p/L^3 in Figure 2.13 follows from Equation (2.43) and scales out the dependence on flexibility. Suppression of the fluctuations directly indicates that the mean angle of the filament with respect to the x-axis is also suppressed for $\tilde{\Sigma} \gtrsim 1$, a useful result that validates our assumption in developing the equation for tension in the filament as in Equation (2.39).

2.6.2 The buckling transition of a semiflexible filament

Much like an elastic beam simply loaded at its ends, an elastic filament placed in a viscous fluid can undergo a buckling transition if the hydrodynamic force acting on it overcomes its elastic restoring force. This may be driven by internal forces generated in response to an imposed flow [3, 28, 32, 33, 35, 89], or by an external force [4, 45]. Motivated by the recent experiments of Kantsler and Goldstein [32] and by the rising ubiquity of microfluidic trap devices [48, 109] that employ such flows, we focus here on the former scenario – specifically, the buckling transition of a semiflexible filament placed at the stagnation point in a linear hyperbolic flow. Adapting our approach to simple shear is straightforward. Inextensibility of such filaments is ensured by an internal tensile force that acts to resist length changes. It is the competition of this line tension with bending forces that results in non-trivial shape instabilities, and the effect of thermal fluctuations on such instabilities is the subject of this section.

Euler buckling, where an elastic beam is loaded constantly at its ends, is well understood, and recent efforts [110, 111] have shown that the effect of stochastic forces is to smoothen the otherwise sharp transition from a straightened to a buckled configuration. Although we expect a rounded transition in the case of filaments placed in a viscous fluid as well, extending these theories to the fluid-structure interaction problem is not straightforward, primarily due to the *non-uniform* tensile force that drives the buckling instability. In the non-Brownian limit, Young and Shelley [35] were the first to quantify a dynamic instability leading to the so-called *stretch-coil* transition when the driving flow strength exceeds a critical value. Following this, Kantsler and Goldstein [32] comprehensively observed this transition in single actin filaments using microfluidics, and showed that while fluctuations smooth the bifurcation, it is broadly consistent with the athermal linear predictions. More recently, Deng *et al.* [112] approached the same problem numerically and reported such a smoothed transition. While their simulations captured the interactions of thermal fluctuations and nonlinear filament dynamics, an analytical description of the smoothed transition is still lacking. The exact nature of this stochastic bifurcation has yet to receive a quantitative treatment, and here we present the first mathematical description of the stretch-coil transition in the presence of thermal fluctuations.

We again resort to a local version of the slender-body theory following Equation (2.6) with the only modification that the arclength parameter is now in the range $s \in [-L/2, L/2]$, which is convenient to work with in extensional flows. Recall that the force distribution $\boldsymbol{f}(s,t)$ on the filament is $\boldsymbol{f} = -(T\boldsymbol{x}_s)_s + \boldsymbol{x}_{ssss} + \boldsymbol{f}^{\mathrm{Br}}$, where the Brownian contribution follows from the fluctuation-dissipation theorem

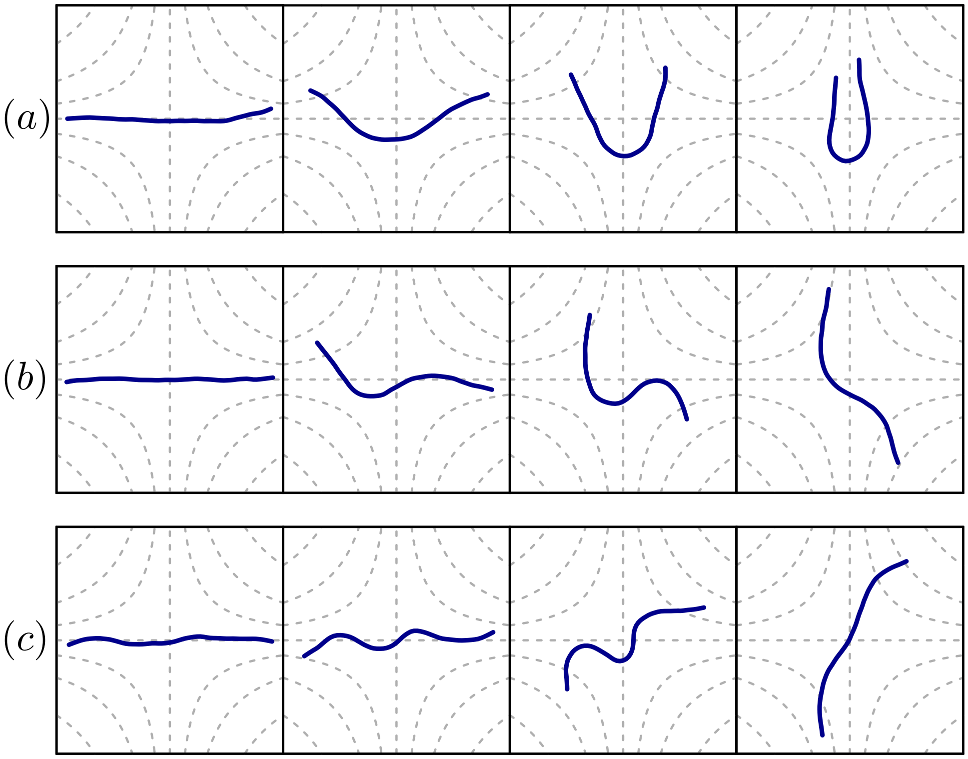

Figure 2.14: Snapshots from three separate numerical simulations showing typical filament shapes as a result of the buckling instability. Higher modes are observed as we increase the flow strength from (a) $\bar{\mu} = 16000$ to (b) $\bar{\mu} = 32000$ to (c) $\bar{\mu} = 64000$. Streamlines of the hyperbolic flow are shown in dotted lines, and the flow is compressional along the horizontal and extensional along the vertical. The persistence length in each case is $\ell_p = 10\,L$.

and, under the current non-dimensionalization, is such that $\langle \boldsymbol{f}^{\mathrm{Br}}(s,t)\rangle = \boldsymbol{0}$ and $\langle \boldsymbol{f}^{\mathrm{Br}}(s,t)\boldsymbol{f}^{\mathrm{Br}}(s',t')\rangle = 2(L/\ell_p)\boldsymbol{\Lambda}^{-1}\delta(t-t')\delta(s-s')$.

Simplifying the slender-body equation and using $\boldsymbol{x}_s \cdot \boldsymbol{x}_s = 1$ (following inextensibility) and hence $\boldsymbol{x}_s \cdot \boldsymbol{x}_{ss} = 0$, one finds

$$\begin{aligned}\boldsymbol{x}_t = \bar{\mu}\boldsymbol{u}_0 + \lambda_1 T\boldsymbol{x}_{ss} + (\lambda_1+\lambda_2)T_s\boldsymbol{x}_s - \lambda_1\boldsymbol{x}_{ssss}\\ - \lambda_2(\boldsymbol{x}_s\cdot\boldsymbol{x}_{ssss})\boldsymbol{x}_s + (\lambda_1\boldsymbol{I} + \lambda_2\boldsymbol{x}_s\boldsymbol{x}_s)\cdot\boldsymbol{f}^{\mathrm{Br}}.\end{aligned} \tag{2.44}$$

The simulations shown here follow the computational methods described in Section 2.3, with an aspect ratio $\epsilon = 0.01$ and free-end boundary conditions: $\boldsymbol{x}_{ss}|_{s=\pm1/2} = \boldsymbol{x}_{sss}|_{s=\pm1/2} = \boldsymbol{0}$ and $T|_{s=\pm1/2} = 0$.

Figure 2.14 shows snapshots from our simulations, and they resemble the shapes seen in the experiments of Kantsler and Goldstein [32] at corresponding flow

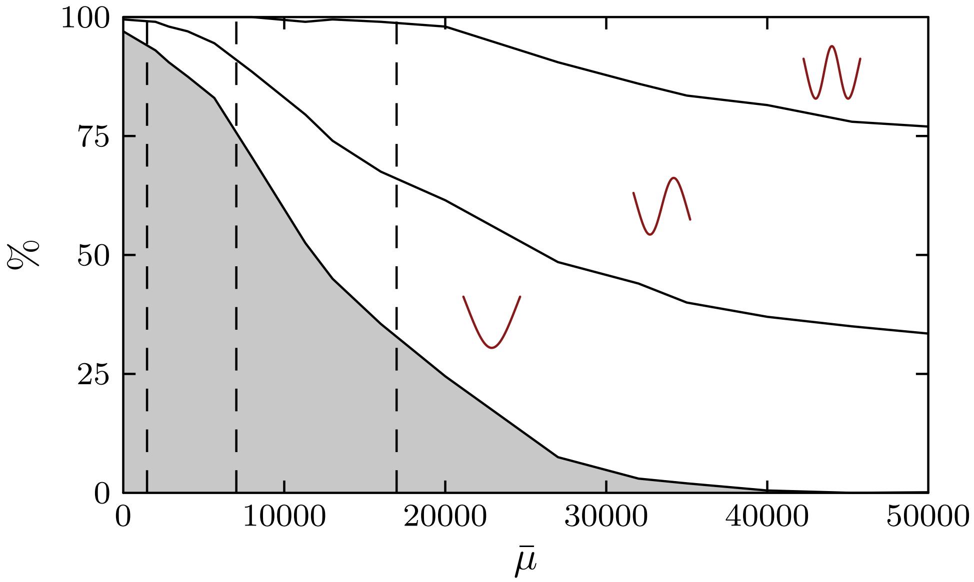

Figure 2.15: Percentage of excited modes across a range of flow strengths. The vertical dashed lines denote the deterministic thresholds for the first three modes (shapes shown), and the shaded area represents the percentage of cases where no buckling was recorded. All simulations are for $\ell_p/L = 10$. Each vertical section is a distribution across 200 simulations.

strengths ($\tilde{\Sigma}$ in their notation being equal to $\bar{\mu}/4\lambda_1\pi^4$). When placed along the compressional axis of a sufficiently strong flow, the filament experiences a *negative* tension along its backbone whose balance with viscous, elastic, and thermal forces dictates the observed shapes. As it buckles, it also reorients and eventually aligns with the extensional axis where the now *positive* tension acts to stretch it. Solving for the non-Brownian and linearized dynamics of an initially straight filament in such a flow, Young and Shelley [35] deduced that an instability first occurs at $\bar{\mu}_{\text{cr}} \approx 1478$, and that higher modes are destabilized at subsequent thresholds. Experiments as well as our simulations show qualitatively similar modes as the deterministic predictions, albeit with shape fluctuations owing to Brownian kicks. A key difference is that thermal fluctuations excite multiple modes regardless of flow strength by equipartition of energy [32], thus affecting the distribution of modes seen in the event of buckling. To quantify this, we identify the predominant mode whose amplitude grows beyond a noise floor of $0.05\,L$ in 200 different simulations each for various flow strengths. The distribution of excited modes is shown vs. $\bar{\mu}$ in Figure 2.15, and the trends in dominant shapes, although strongly rounded by fluctuations, are consistent with the deterministic predictions. This is reminiscent of the stochastic Euler buckling problem [110, 111], where thermal fluctuations have been shown to round the transition near the deterministic critical force. This motivates the following analysis where we quantify the transition near the first deterministic threshold, or critical flow strength associated with the first buckling mode.

To analyze this transition, we first adopt a Monge representation and write $\boldsymbol{x}(s,t) = (s,h)$ where $h(s,t)$ is the deflection away from the axis of compression in the hyperbolic flow $\boldsymbol{u}_0 = (-x, y) = (-s, h)$. Further, we assume that the parabolic form of tension corresponding to a straightened filament placed at the origin holds even when it is deformed – an assumption that is justified for small deflections away from the axis as arise near the onset of buckling. This tension profile can be determined by manipulating Equation (2.44) and takes the form $T(s) = \bar{\mu}(s^2 - 1/4)/2(\lambda_1 + \lambda_2)$. Also, since the variable h measures vertical deflections away from the $y = 0$ axis, we consider only thermal fluctuations in this direction. Then, the scalar equation for h reads:

$$\begin{aligned} \frac{\partial h}{\partial t} = \bar{\mu} &\left[h + \frac{1}{2} \frac{\lambda_1}{\lambda_1 + \lambda_2} \left(s^2 - \frac{1}{4} \right) h_{ss} + s h_s \right] \\ &- \lambda_1 h_{ssss} - \lambda_2 h_s^2 h_{ssss} + \sqrt{2\lambda_1 \frac{L}{\ell_p}}\, \xi(s,t), \end{aligned} \tag{2.45}$$

where $\xi(s,t)$ is a white noise with zero mean and correlation $\langle \xi(s,t)\xi(s',t') \rangle = \delta(s - s')\delta(t - t')$.

Ignoring the non-linear and stochastic terms above and assuming a form $h(s,t) = \phi(s)e^{\varsigma t}$ leads directly to the linear stability results of Young and Shelley [35]. Defining the terms within the square brackets in Equation (2.45) as $\mathcal{L}[h]$, marginal linear stability ($\mathrm{Re}[\varsigma] = 0$) in the non-Brownian case corresponds to the eigenvalue problem

$$\bar{\mu}_{\mathrm{cr}}^{(n)} \mathcal{L}[\phi^{(n)}(s)] = \lambda_1 \phi_{ssss}^{(n)}(s), \tag{2.46}$$

where $\phi^{(n)}$ is the n-th buckling mode that is destabilized at a critical flow strength $\bar{\mu}_{\mathrm{cr}}^{(n)}$. Since our interest is in the effect of fluctuations near the first buckling transition, we use $n = 1$ from here on and avoid the superscripts. Also, we introduce a parameter m which is the distance from the deterministic threshold: $\bar{\mu} = \bar{\mu}_{\mathrm{cr}} + m$. In order to reduce to a form amenable to treatment as a stochastic supercritical bifurcation [113], we introduce the ansatz $h(s,t) = a(t)\phi(s)$ near $\bar{\mu}_{\mathrm{cr}}$. Using Equation (2.46), the governing equation becomes:

$$\phi \frac{da}{dt} = \frac{m\lambda_1}{\bar{\mu}_{\mathrm{cr}}} a\phi_{ssss} - \lambda_2 a^3 \phi_s^2 \phi_{ssss} + \sqrt{2\lambda_1 \frac{L}{\ell_p}}\, \xi. \tag{2.47}$$

Recall that ϕ and its derivatives solve the eigenvalue problem (2.46), which admits orthogonal eigenfunctions. Projecting Equation (2.47) on the first eigenfunction ϕ then yields a Langevin equation governing the time dynamics of the amplitude $a(t)$:

$$\frac{da}{dt} = m\gamma a - 2\omega a^3 + \sqrt{\sigma}\zeta(t). \tag{2.48}$$

This is, in fact, a time-dependent stochastic Ginzburg-Landau model for the amplitude of the first buckled mode. Here, $\gamma = \lambda_1 A_1/\bar{\mu}_{\mathrm{cr}}$, $\omega = \lambda_2 A_2/2$, and $\sigma = 2\lambda_1 L/\ell_p$ are all positive parameters. A_1 and A_2 are constants that depend on the shape of the eigenfunctions, given respectively by $\int_{-1/2}^{1/2} \phi\phi_{ssss}\,\mathrm{d}s$ and $\int_{-1/2}^{1/2} \phi\phi_s^2\phi_{ssss}\,\mathrm{d}s$. $\zeta(t) = \int_{-1/2}^{1/2} \xi(s,t)\phi(s)\,\mathrm{d}s$ is a normal variate with zero mean and correlation $\langle \zeta(t)\zeta(t')\rangle = \delta(t-t')$.

Equation (2.48) has as its deterministic ($\sigma = 0$) and linear ($\omega = 0$) limit the solution $a(t) \sim \exp[m\gamma t]$, which, consistent with the predictions of the linear stability analysis, decays when $m < 0$ ($\bar{\mu} < \bar{\mu}_{\mathrm{cr}}$) and grows otherwise. Analyzing the deterministic yet non-linear problem ($\sigma = 0 \neq \omega$) reveals a supercritical pitchfork bifurcation at $m = 0$ with $a = \sqrt{\gamma m/2\omega}$ when $m > 0$. The stochastic bifurcation will be shown to limit to this form correctly as $\sigma \to 0$.

We now look to quantify the thermal rounding of this bifurcation for finite ℓ_p ($\sigma \neq 0$). We first obtain the Fokker-Planck equation corresponding to Equation (2.48), which provides a deterministic equation for the probability density $\psi(a,t)$ of the amplitude a:

$$\frac{\partial \psi}{\partial t} = -\frac{\partial}{\partial a}\left[(m\gamma a - 2\omega a^3)\psi\right] + \frac{\sigma}{2}\frac{\partial^2 \psi}{\partial a^2}. \tag{2.49}$$

A steady solution for the stationary probability density $\psi_S = \psi(t \to \infty)$ can be obtained as

$$\psi_S(a; m, \gamma, \omega, \sigma) = \frac{1}{N} \exp\left[\frac{1}{\sigma}(m\gamma a^2 - \omega a^4)\right], \tag{2.50}$$

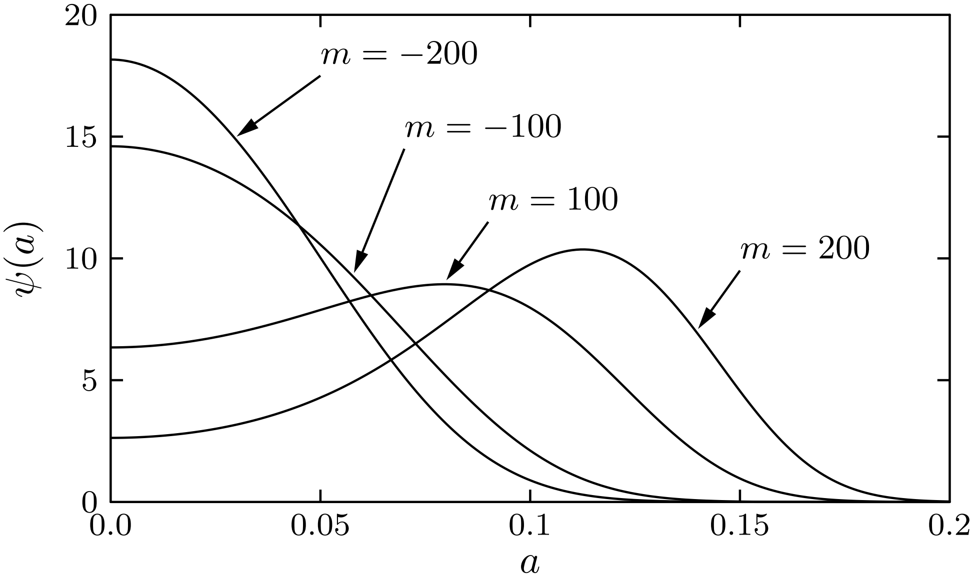

Figure 2.16: Probability density of the amplitude a of the first buckled mode corresponding to $\sigma = 2.04$ ($\ell_p/L = 10$). The deterministic buckling threshold is $m = 0$, and the distribution consistently shift towards higher amplitudes as m increases, following Equation (2.50).

where $N(m, \gamma, \omega, \sigma)$ is a normalization constant such that $\int_0^\infty \psi_S \; \mathrm{d}a = 1$. The effect of the sign of m is obvious in Equation (2.50), shown also in Figure 2.16: $\psi_S(a; m \leq 0)$ always peaks at $a = 0$, whereas a positive value of m shifts the peak to a finite positive value of a. The non-linearity is critical as well, as $\omega = 0$ is a Gaussian that always peaks at $a = 0$.

We can now solve for the expected value $\langle a \rangle = \int_0^\infty a\psi_S \; \mathrm{d}a$ of the amplitude, which reads:

$$\langle a \rangle = \frac{1}{\mathcal{G}} \sqrt{\frac{2\sigma}{\gamma |m| \pi}} \; \exp\left[\frac{\gamma^2 m^2}{8\omega\sigma}\right] \left[1 + \mathrm{erf}\left(\frac{\gamma m}{2\sqrt{\omega\sigma}}\right)\right], \tag{2.51}$$

where

$$\mathcal{G} = \begin{cases} \dfrac{\sqrt{2}}{\pi} \, K_{1/4}\left[\dfrac{\gamma^2 m^2}{8\omega\sigma}\right] & : m < 0, \\ I_{-1/4}\left[\dfrac{\gamma^2 m^2}{8\omega\sigma}\right] + I_{1/4}\left[\dfrac{\gamma^2 m^2}{8\omega\sigma}\right] & : m \geq 0, \end{cases} \tag{2.52}$$

and $I_\nu(x)$ and $K_\nu(x)$ are, respectively, the modified Bessel functions of the first and second kind.

Figure 2.17 shows the predicted amplitude as the flow strength is varied across

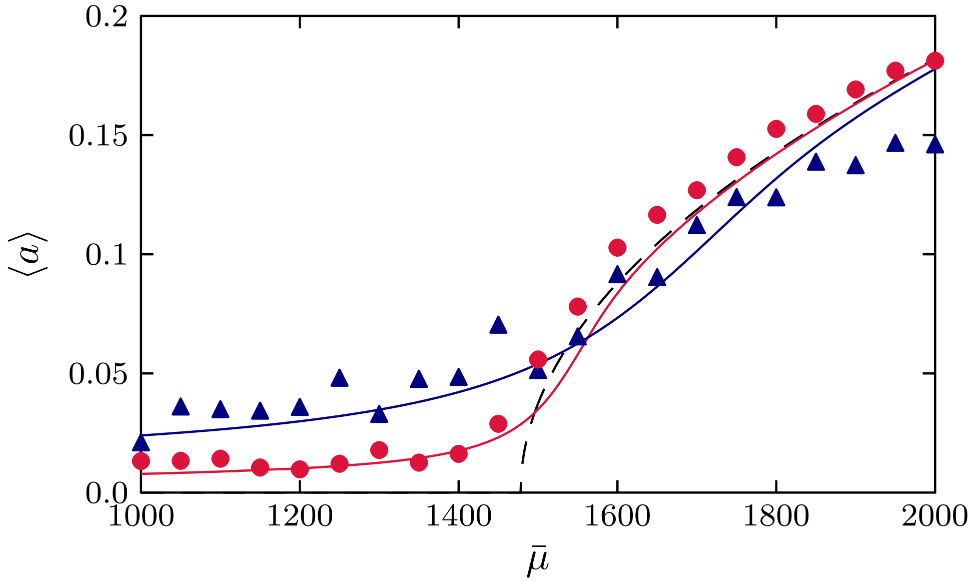

Figure 2.17: Expected value of the amplitude of the first buckled mode as a function of flow strength. The dashed line is the deterministic pitchfork bifurcation; the solid lines (red for $\ell_p/L = 100$ and blue for $\ell_p/L = 10$) follow Equation (2.51) and depart from the sharp transition for increasingly noisy systems. The symbols (red circles for $\ell_p/L = 100$ and blue triangles for $\ell_p/L = 10$) are extracted from simulations without any fitting parameters.

the deterministic threshold. Akin to constantly loaded fibers, the effect of thermal fluctuations is to round the sharp transition. Non-trivial modes are excited at arbitrary flow strengths as a consequence of equipartition of energy, and this manifests as a finite amplitude of the first buckled mode well below $\bar{\mu}_{\mathrm{cr}}$. Evaluating the limit of Equation (2.51) as $m \to 0$ indicates that the corresponding expected value is indeed non-zero and varies as $\sigma^{1/4} \sim \ell_p^{-1/4}$, i.e., the amplitude at the deterministic threshold is larger for more flexible filaments. Beyond $\bar{\mu}_{\mathrm{cr}}$, $\langle a \rangle$ crosses over and approaches the deterministic pitchfork bifurcation value of $\sqrt{\gamma m / 2\omega}$. This approach is slower as ℓ_p decreases, suggesting a larger mean projected length in the buckled state. Recall from Equation (2.48) that the finite buckled amplitude in the deterministic case is set by the component of the elastic force along the local tangent vector. The effect of thermal fluctuations beyond the transition is to reduce this amplitude, which can be viewed as an effectively stiffer spring against hydrodynamic compression. This coupling between elasticity and Brownian motion is crucial – an increase in temperature hardens the filament and acts to straighten it out, which is contrary to floppy polymers that are driven solely by configurational entropy and shrink in response to increasing temperature. This again is reminiscent of constantly loaded beams under the influence of thermal fluctuations, where an apparent stretching has been reported past the critical force [110].

In order to test this prediction, we compare it against full numerical simulations of Equation (2.44) (cf. Section 2.3). We place a filament in a hyperbolic flow which is dynamically adjusted to remain compressional along the direction of the end-to-end vector. This eliminates filament reorientation and provides long-time statistics, which are necessary for comparison with the stationary probability distribution derived above. After an initial transience, a stochastically steady state is reached. This is ensemble-averaged and compared to $\phi(s)$ to obtain a numerical prediction for the expected value of a. Higher modes may be excited by thermal fluctuations, and we eliminate these in our averages. The result is shown in Figure 2.17 for two different values of ℓ_p and matches excellently with our predictions without any fitting parameters. The simulations also display the smoothed trend in the transition, as well as the apparent pre-buckling softening and post-buckling hardening due to the particular nature of the stochastic bifurcation.

2.7 Conclusion

In this chapter, we developed a model for single free-flowing semiflexible polymers in an external flow and applied it study their dynamics in simple flows. We particularly focused on flows that are commonly seen in microfluidic devices.

We started with the simple case of a non-Brownian straight rod for which an analytical solution is straightforward: the filament tends to align itself with the shearing axis which we saw is a stable fixed point (Section 2.5.1). In the numerical simulations of fibers, it is seen that the trajectory is identical to the analytical case when the filament is rigid. Furthermore, flexible fibers show interesting buckling phenomena which are ascribed to the non-uniform tension that is generated in the filament. Even in this case, however, the filament approaches the stable solution by aligning with the axis.

When Brownian motion is introduced, the dynamics are different. It was shown that the Brownian term introduces a bifurcation leading to a stable and unstable branch, with the unstable branch corresponding to a scenario where the shear flow can now drive the filament over an entire half period to align with the axis. This led us to studying polymer tumbling (Section 2.5.2) in shear flows, where the tumbling frequency we obtained was found to be consistent with previous experimental findings.

Section 2.6 introduced the applications and recent literature on the dynamics of semiflexible filaments near hyperbolic stagnation points. Using a variational method and assuming small-amplitude fluctuations away from the axis, we were able to derive the eigenfunctions for the shape of a filament when placed along the extensional axis (Section 2.6.1 and Appendix A). The variance of fluctuations away from the axis is predicted to be suppressed as the rate of strain increases, and our simulations reproduced this well. This is attributed to the tensile force generated in the filament that tries to extend it, thereby flattening out the fluctuations.

In the case when the filament is along with the compressional manifold (Section 2.6.2) the tension is negative, causing the filament to be pulled inward along its length. We develop, for the first time, an analytical expression that quantifies this stretch-coil transition as a stochastic supercritical bifurcation, with the resulting expression specifying the exact nature of the finite-temperature rounding of the transition. While this analysis solves a vital facet of fluid-filament interaction problems at the microscale, it also provides a powerful tool for experimentalists to extract mechanical properties of single macromolecules by fitting shape deformations around critical points. The theory presented here, while elaborated for extensional flows, is also sufficiently general to be extended to other flows commonly encountered in microfluidics. For instance, predicting the transition to the first deformed mode in simple shear, often called 'hairpins' [31, 92], is straightforward once the appropriate form of the tension is known [27]. Generalization of the analysis to include multiple modes is an open problem that warrants attention, as is the coupled description of deformation and rotation after buckling.

A part of Chapter 2 is based on the Master's thesis by Harishankar Manikantan, submitted in May 2012 at the University of Illinois at Urbana-Champaign [1]. Chapter 2 also contains material that has appeared in *Physical Review E* (2015), authored by Harishankar Manikantan and David Saintillan [2].

Chapter 3

Subdiffusive transport of semiflexible filaments in cellular flows

3.1 Introduction

We ended Chapter 2 with a filament placed in a hyperbolic stagnation point, aligned with the axis of compression of the flow, and being subjected to a compressive tensile force. Using linearized Euler-Bernoulli elasticity and slender-body theory [56] for Stokes flow, Young and Shelley [35] showed that this situation is amenable to a linear stability analysis and found that beyond a critical strain rate a non-Brownian elastic filament undergoes a compressive buckling instability analogous to Euler buckling in beams, which we called the *stretch-coil transition* [35]. As the strain rate (and hence the tension in the filament) increases, higher mode shapes can become unstable and corresponding thresholds for each successive filament shape have been calculated [35]. This buckling instability appears to be a generic feature of strain-dominated flows when the polymer is aligned along a direction of compression, and the case of an elastic filament tethered normal to a rigid wall at the stagnation point of a compressive extensional flow was also recently discussed by Guglielmini *et al.* [33].

The results of the stability analysis of Young and Shelley [35], though strictly valid in the absence of thermal fluctuations, were also recently tested experimentally by Kantsler and Goldstein [32] using actin filaments trapped at the stagnation point of a microfluidic cross-slot device, where buckling was indeed observed. A succession of mode shapes was also reported with increasing strain rate. The instability, however, no longer occurred at a critical flow strength but was seen to gradually transition from the straight (though susceptible to thermal fluctuations) state to the buckled state in the vicinity of the theoretical athermal threshold. To quantify the extent of buckling, Kantsler and Goldstein tracked the mean end-to-end distance as a function of the imposed strain rate. As opposed to the sharp cusp expected at the instability threshold in the non-Brownian limit, they found that thermal fluctuations strongly round the transition, as is already known to be the case for classic Euler buckling [110]. The theory developed in Section 2.6.2 corroborated this, revealing a smoothed transition in the way of a stochastic supercritical bifurcation.

Such buckling events can be significant driving factors behind transport properties of elastic filaments. One example of this effect comes from actin motility assays [90, 91, 114], in which actin filaments are transported over a two-dimensional carpet of wall-tethered myosin molecular motors. These assays are typically characterized by motility defects, in which a polymer gets pinned at its leading tip, causing it to buckle in plane and curl up towards the tip [90, 91]. The pinned tip eventually breaks free, allowing the filament to continue to move in a different direction. In cases of high myosin density, the result of these dynamics is a meandering motion with every instance of buckling randomly changing the direction the polymer is headed. The prevalence of polymer buckling in complex flows of elastic filaments has also been reported in other biophysical systems, such as two-dimensional suspensions of microtubule bundles and kinesin clusters [115], where stretching of the bundles as a result of the relative sliding of individual microtubules under the action of the kinesin motors can cause them to deform and buckle.

A simple illustration of the relation between buckling and spatial transport was also provided by Young and Shelley [35], who proposed that a periodic lattice of steady counter-rotating Taylor-Green vortices in a viscous incompressible fluid can capture some of the dynamics observed in actin motility assays. The vortices create hyperbolic junctions connected by straight streamlines, defining ‘cells’ that enclose an entire family of closed curved streamlines as illustrated in Figure 3.1. An initially straight

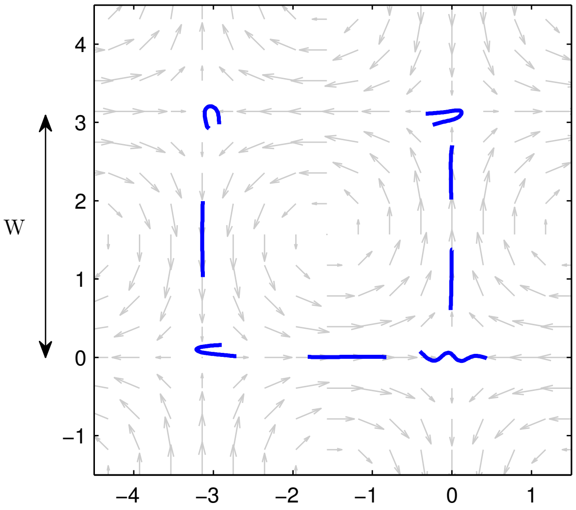

Figure 3.1: Snapshots from a simulation showing the buckling instability at the stagnation points at cell corners for $\bar{\mu} = 80000$, $\ell_p/L = 1000$, and $w = 1$.

filament placed along one of the edges is transported along the straight streamline until it approaches a stagnation point. There, the flow is locally an extensional flow, and the linear stability analysis of Young and Shelley [35] predicts a buckling event if the local strain rate is sufficiently high. The 'stretched' filament is expected to slow down and buckle or 'coil' (analogous to pinning and curling in actin motility assays), and to subsequently relax to a stretched configuration in an arbitrarily chosen perpendicular direction. Using non-Brownian simulations, Young and Shelley [35] indeed showed that an elastic filament in such a flow moves across the lattice like a random walker executing arbitrary $\pi/2$ turns at each hyperbolic junction. On long time scales, such a random walk was found to be diffusive in the absence of thermal fluctuations, at least over a certain range of flow strengths. Recent experiments by Wandersman *et al.* [36] and by Quennouz [116] using macroscopic elastic fibers in an electrodynamically generated cellular flow verified predictions from the simulations of Young and Shelley [35], and clearly showed the relevance of the stretch-coil transition on the dynamics. By tuning the flow strength and mechanical properties of the fibers, they [36, 116] measured the onset and probability of buckling in terms of an elastoviscous number S_p and observed good agreement with the predictions of the stability analysis [35] within experimental limitations. They confirmed that flexibility facilitates transport between and across cells as a result of buckling, and observed random trajectories akin to those obtained by Young and Shelley [35], albeit on shorter scales owing to the limited size of the flow device used in the experiments.

A central question that has yet to be addressed and that is directly relevant to the transport of biological polymers such as actin is the effect of thermal fluctuations on the dynamics, and this chapter represents the first comprehensive attempt at addressing this issue. Using numerical simulations based on a slender-body model with a stochastic Brownian force distribution obeying the fluctuation-dissipation theorem, we systematically analyze the effect of Brownian fluctuations (measured by the persistence length of the polymer) on the dynamics of isolated chains in a periodic Taylor-Green vortex flow. Our main finding is that in the limit of infinite dilution, fluctuations have a tendency to cause more frequent trapping of the filaments inside cells, thereby hindering their ability to diffuse in the plane of the flow; in fact, we even observe a transition to subdiffusive transport as the persistence length is decreased. The main findings are discussed in Section 3.2, where we analyze the effect of fluctuations on transport properties, velocity distributions, and mass distributions of the filaments, and also compare our results to the case of rigid Brownian fibers.

We consider the transport of a flexible Brownian filament in a prescribed flow field consisting of a two-dimensional periodic array of counter-rotating Taylor-Green vortices:

$$\boldsymbol{u}_0(\boldsymbol{x}) = (\sin(x/w)\cos(y/w), -\cos(x/w)\sin(y/w), 0), \tag{3.1}$$

where x and y are made dimensionless with L as usual, and $w = W/\pi L$ is the dimensionless cell size (see Figure 3.1). Note that this imposed flow field is two-dimensional, while we will be allowing for three-dimensional motion of the polymer arising solely from thermal fluctuations, unlike in the previous simulations of Young and Shelley [35] and the experiments of Wandersman *et al.* [36], where the filaments where confined on a two-dimensional interface.

As was described earlier, a polymer in the vicinity of one of the stagnation points in such a flow experiences a locally hyperbolic extensional flow. Within this approximation, the linear stability results for the buckling instability should hold, for which, in the language of this work, the first (and from here on, the 'critical') threshold [35] is $\bar{\mu}_{\rm cr} \approx 1478$. It can be shown that increasingly higher buckling modes become unstable above subsequent thresholds ($\bar{\mu}_{\rm cr} \approx 7000, 17000, ...$). Furthermore,

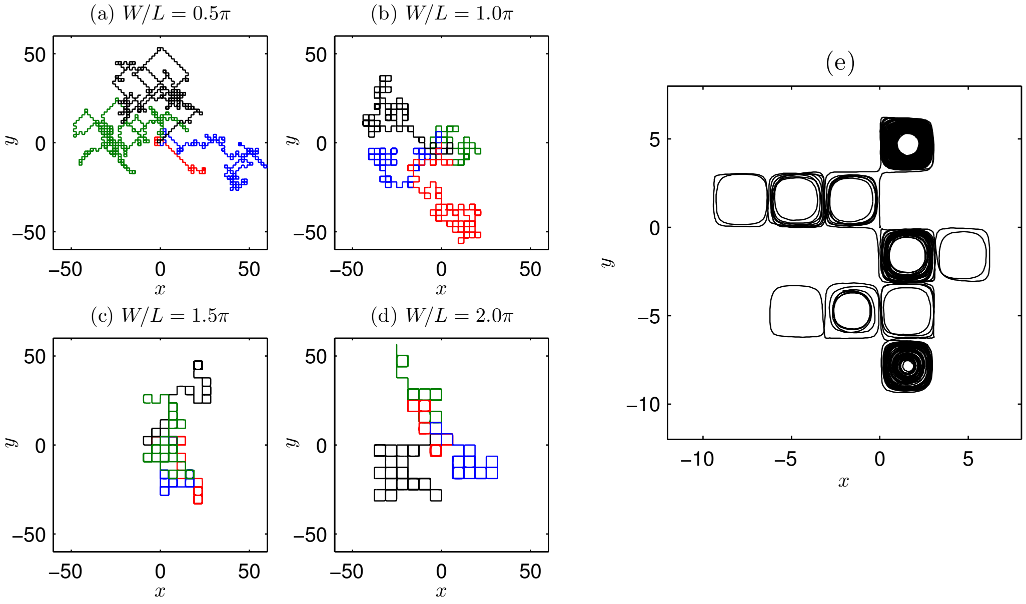

Figure 3.2: Effect of cell size and filament stiffness on its trajectories. Center-of-mass trajectories of polymers: (a)-(d) correspond to four different cell sizes W at the same $\bar{\mu} = 20000$ and $\ell_p/L = 1000$, each showing four different trajectories; (e) shows the case of a single polymer with $W = \pi L$ and $\bar{\mu} = 20000$, but $\ell_p/L = 10$.

as was seen in the experiments of Kantsler and Goldstein [32] and in our discussion in Section 2.6.2, these thresholds remain broadly consistent even in the presence of thermal fluctuations.

3.2 Results and discussion

3.2.1 Polymer transport: diffusion vs. subdiffusion

In the following, we focus entirely on flow strengths that exceed the critical threshold ($\bar{\mu} > \bar{\mu}_{\text{cr}}$). The objective is to systematically describe the change in transport properties of a polymer in a cellular flow due to thermal fluctuations, in a regime where buckling events at the hyperbolic points of the vortex array lead to 'Brownian-like' transport across the lattice [35].

The center-of-mass trajectories of a few representative cases are illustrated in Figure 3.2. The key observation is that while a larger reduced persistence length allows polymers to migrate farther away from their initial position (the origin, in the case of the examples in Figure 3.2), those with smaller reduced persistence lengths exhibit much slower transport from their initial position. Figure 3.2(e) for the low value of $\ell_p/L = 10$ shows a characteristic trap-and-go motion wherein a polymer appears to be trapped in a cell for significantly longer time periods before escaping to another neighboring cell. This is qualitatively different from previous observations in non-Brownian experiments [36] and simulations, [35] which are comparable to the case of $\ell_p/L = 1000$. In this context, Young and Shelley [35] calculated a 'transport region' enveloping the unit cell boundary that recorded a trapping probability of less than 50%. Their observation was that for a range of values of $\bar{\mu}$, filaments placed in this region would migrate across the lattice like a random walker and undergo a diffusive motion in space at long times as a result. Our simulations for $\ell_p/L = 1000$ show a similar behavior [Figure 3.2(a)–(d)], with relatively rare trapping occasions. This suggests that transport in this regime is akin to the non-Brownian case, with thermal fluctuations only changing the outcome from transport to trapping in very few cases. The dynamics are qualitatively different when $\ell_p/L = 10$, where we find that such a transport region cannot be defined. The effect of thermal fluctuations is very strong in this case, and as seen in Figure 3.2(e) polymers often become trapped and migrate deep into a cell, only to jump out and transition to a neighboring cell at a later time and further proceed in this trap-and-release fashion. It should be noted here that for all our simulations, the polymer is released at the cell boundaries: we expect the probability of such trapping events to be significantly higher if the filament were released near the center of a cell.

It is interesting to compare the dynamics seen in Figure 3.2 to that of a particle moving randomly across a periodic lattice with specified distributions of length and frequency of jumps. [117, 118] Jumps of unit cell length at a fixed rate give rise to the traditional random walk, one that approaches the behavior predicted by a diffusion equation. If the jumps follow a heavy-tailed length distribution but still occur at a fixed rate, then they lead to so-called Lévy flights characterized by superdiffusion. The complementary case is that of 'fractal time' [117], which applies particularly to the behavior seen in Figure 3.2(e), where a walker always moves a unit cell length but waits disparate amounts of times between jumps. For such random walks, the mean-square displacement is slower than that of a diffusive process, and numerical

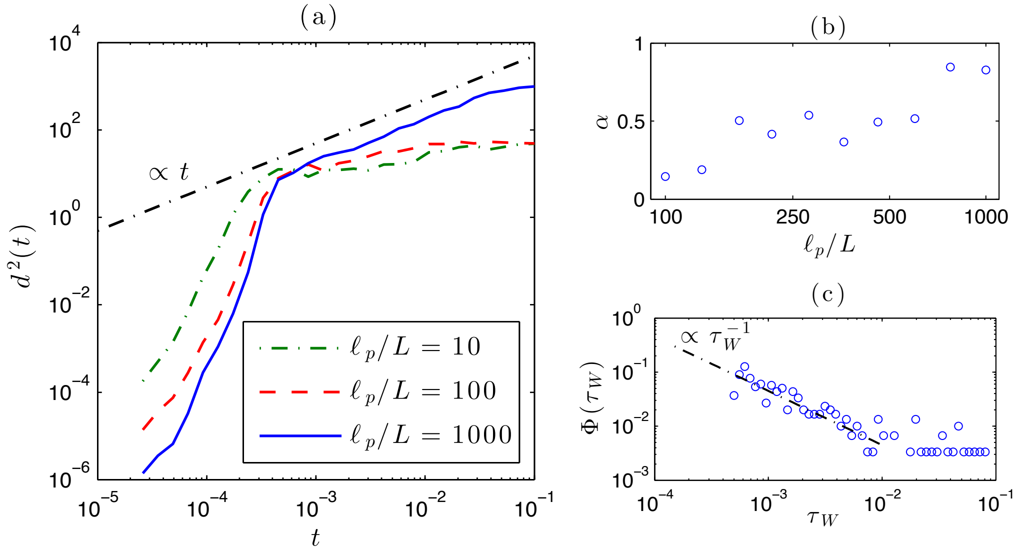

Figure 3.3: Subdiffusive transport and the corresponding waiting time distribution. (a) Mean-square displacement $d^2(t)$ of the filament center-of-mass as a function of time at $\bar{\mu} = 20000$ for three values of ℓ_p/L, where the long-time behavior follows an approximate power law $d^2(t) \propto t^{\alpha}$. (b) Dependence of the exponent α on the reduced persistence length ℓ_p/L. (c) Distribution of waiting times, defined as periods of time spent by a filament inside a given cell, in simulations with $\bar{\mu} = 20000$ and $\ell_p/L = 10$.

studies [118] have reported that such waiting times lead to subdiffusion.

The diffusivity of polymers across the cellular lattice in the current problem can be characterized by the mean-square displacement of the center of mass $\boldsymbol{x}_0(t)$ of a chain from its initial position: $d^2(t) = \langle |\boldsymbol{x}_0(t) - \boldsymbol{x}_0(0)|^2 \rangle$ (Figure 3.3). Recall that we only consider isolated polymers, corresponding to the limit of an infinitely dilute suspension where the effects of the disturbance velocity due to other chains on the transport properties are negligible. These results are ensemble averages of 50 simulations for each value of ℓ_p/L shown, and were all obtained for $\bar{\mu} = 20000$. The initial condition is the same, but thermal fluctuations soon change the long-time dynamics in each simulation. For $\ell_p/L = 1000$, we observe a roughly linear increase in the mean-square displacement with time, consistent with the case of non-Brownian filaments [35]. The initial climb in the beginning corresponds to the motion of the polymer moving along a cell boundary until it encounters the first stagnation point. For subsequent smaller values of $\ell_p/L = 100$ and 10, the initial climb is larger because the polymer no longer moves along the cell edges but rather is pushed further in towards the center of the cell by thermal fluctuations, thereby increasing the average distance traversed before it encounters the first stagnation point. Beyond this initial climb, however, the growth of the mean-square displacement exhibits a clear subdiffusive behavior of the form $d^2(t) \propto t^\alpha$ with $\alpha < 1$. Within the timespan of the simulations, we observe that the slope of $d^2(t)$ in a log-log plot in fact reduces to almost zero in these cases. The filament tends to become trapped in almost every cell it comes by, and the occasional jump from cell to cell is seen in the very small positive slope in Figure 3.3(a). In many cases, the filament even remained trapped in a given cell until the simulation had to be stopped. The precise dependence of the exponent α on the persistence length is shown in Figure 3.3(b), where it is seen to transition from nearly zero for low values of ℓ_p/L to approximately 1 for high persistence lengths.

This transition from diffusive to subdiffusive transport with decreasing ℓ_p/L can be further characterized by considering the waiting-time distribution of the polymer in a cell, shown for $\ell_p/L = 10$ in Figure 3.3(c). The waiting time τ_W is defined as the time a polymer spends within a given cell (quantified by its center-of-mass position). While moving along the boundary between cells, the center-of-mass often abruptly jumps back and forth between them. We discard these small values of τ_W by introducing a cut-off on the recorded waiting times: only those values of τ_W that are above the average time it takes a polymer to go on an entire loop around a cell are considered. Also, we discard cases when the polymer gets trapped at the center of the cell and stays there for the entire span of the simulation. This distribution for the smaller values of the reduced persistence length displays approximately a power-law behavior that goes as $\Phi(\tau_W) \propto \tau_W^{-1}$. Such distributions of waiting times that follow a non-integrable form of $\Phi(\tau_W) \propto \tau_W^{-(1+\alpha)}$ with $\alpha < 1$ have been predicted theoretically [119] and reported in various physical systems [120, 121] to result in subdiffusion with a mean-square displacement growing as t^α. According to this prediction, the exponent α is expected to be nearly zero in the case of $\ell_p/L = 10$, which is indeed very close to what is observed for the slope of $d^2(t)$ in Figure 3.3(a). This qualitative change in the waiting-time distribution clearly confirms that polymer trapping is indeed enhanced by thermal fluctuations.

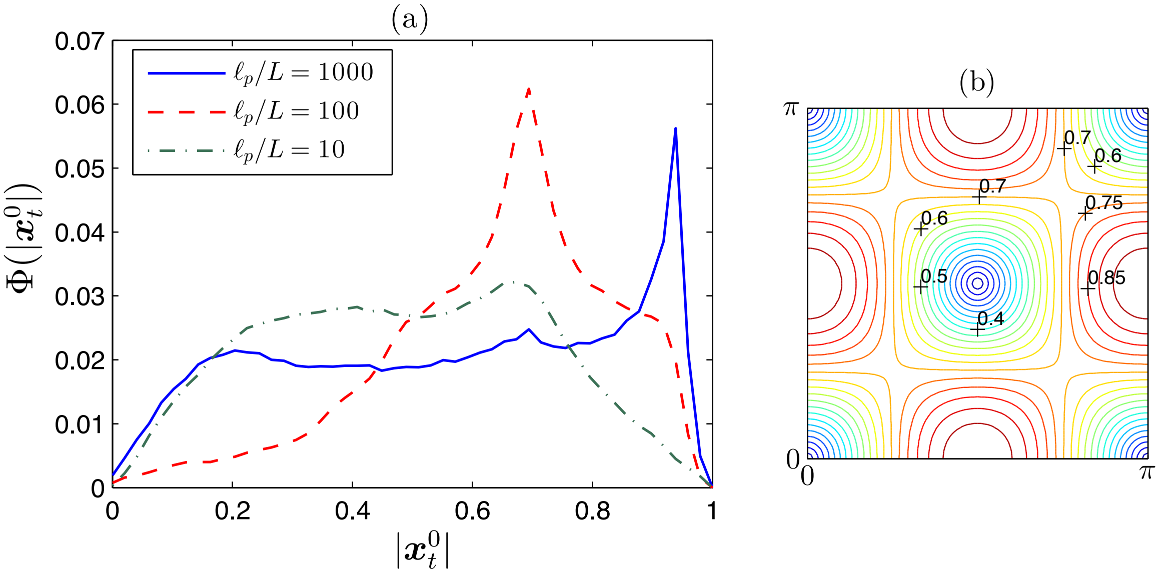

Figure 3.4: Velocity distribution of polymers within a cell. (a) Frequency distribution of the magnitude of the center-of-mass velocity $|\boldsymbol{x}_t^0|$ for various values of ℓ_p/L at $\bar{\mu} = 20000$. (b) Contours of the fluid velocity magnitude inside a given cell, indicating that the value of $|\boldsymbol{x}_t^0| = 0.7$ corresponds approximately to the largest ring of uniform velocity within the cell.

3.2.2 Velocity distributions

In the actin motility experiments of Bourdieu *et al.* [90, 91], the frequency distribution of the velocity of the polymer was found to be bimodal at select temperatures. This bimodality was attributed to the 'slip-stick' nature of polymer transport, in which periods of regular motion at a roughly constant velocity alternate with states when the polymer becomes pinned and the velocity is almost zero. In the present model, similar dynamics are expected in the case of $\ell_p/L = 1000$, when Brownian motion plays a negligible role in disturbing this cycle of motion-and-stagnation. This is indeed the case, as seen in Figure 3.4(a) where we show the normalized frequency distribution of the center-of-mass velocity magnitude $|\boldsymbol{x}_t^0|$, which agrees qualitatively with the experiments [91] and quantitatively with non-Brownian simulations [35]. One noticeable difference is the presence of a minor peak near 0.7, which represents the rare occasions when the polymer does get trapped in a cell. The value of $|\boldsymbol{x}_t^0| = 0.7$ for the velocity in the trapped state is not very obvious, but one can see that it approximately corresponds to the largest ring of uniform velocity within a particular

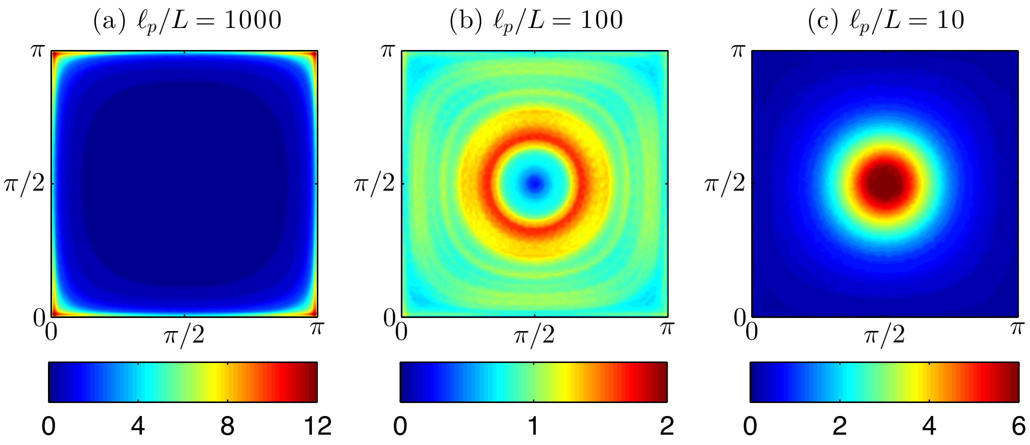

Figure 3.5: Probability distributions of mass of the polymer in a unit cell at $\bar{\mu} = 20000$ for different values of ℓ_p/L. Probabilities are normalized to be unity for a uniform distribution.

cell [Figure 3.4(b)].

Thermal fluctuations change this picture drastically, as seen for lower values of the reduced persistence length. For $\ell_p/L = 100$, our simulations show a sharp velocity selection near 0.7. This corresponds to a predominance of trajectories in which the polymer becomes trapped in a ring near the part of the cell where the external flow is of this magnitude, and will be further elucidated in the mass distribution results in Sec. 3.2.3. For $\ell_p/L = 10$, this peak persists but the distribution is more spread-out towards lower velocities, i.e., the polymer now preferentially becomes trapped in positions ranging all the way from the center of the cell to the ring of maximum uniform velocity.

3.2.3 Mass distribution of polymers

The preferred position of polymers inside the unit cell can be analyzed by considering the probability distributions of the mass of the entire polymer (which is assumed to be homogeneous along its backbone). Figure 3.5 shows such distributions averaged over at least 50 simulations for three values of ℓ_p/L at $\bar{\mu} = 20000$. The plots are averaged across all cells that a polymer happens to be in, and are normalized to be unity for a uniform distribution.

The distribution for $\ell_p/L = 1000$ is unsurprising, as we recollect that this case is almost identical to the non-Brownian simulations [35] and the polymer is found to spend almost all of its time along the cell boundaries. Here again, the probability peaks near the corners, which reflects the slowing-down of the chain and time spent during buckling events around stagnation points (see Figure 3.1). The floppier case of $\ell_p/L = 100$ looks qualitatively different and shows a characteristic ring of probability at a distance from the cell boundary. Here, we recall from the velocity distributions (Section 3.2.2) that the preferred center-of-mass velocity of a trapped polymer in this case is about 0.7. The ring that the center of mass must be on for this to happen is to the immediate outside of the concentration peak seen in Figure 3.5(b). This shift inward is due to the cases when the polymer is aligned radially, thereby increasing the probability of finding a part of the chain in a circle of smaller radius. It is quite remarkable, however, that the polymer very rarely goes deeper into the cell beyond this ring, as shown by the low probability near the center. The floppiest case of $\ell_p/L = 10$ is qualitatively different from both previous cases. Here, the polymer selects velocities that place it closer to the center (Section 3.2.2) and the mass distribution indeed peaks there. Polymer centers-of-mass still move in rings around the center of the cell, but the effect of radial alignment causes the peak to be at the center of the cell in this case. It should be noted when considering the distributions of Figure 3.5 that they represent averages over a finite period of time and that their shape might change slightly if the simulations were run longer; also, they were obtained for polymers released along one of the cell edges and would likely show a stronger probability near the cell center for filaments released at arbitrary locations.

3.2.4 Cellular transport of rigid rods

We have thus far demonstrated that flexibility affects transport properties in two distinct ways: on the one hand, it allows the filaments to buckle at the hyperbolic points, which facilitates their transport across the lattice; on the other hand, it can also increase the importance of thermal fluctuations (by decreasing the persistence length), which has the opposite effect of driving polymers towards cell centers where they can become trapped. To further elucidate the effect of polymer flexibility in this transport process, we also approach the complementary problem of rigid Brownian rods from a continuum perspective. We do so by solving a conservation equation for the probability distribution function $\Psi(\boldsymbol{x}_0, \boldsymbol{p}, t)$ of a single rod in a cellular flow, where the configuration of the rod is now described by its center-of-mass position $\boldsymbol{x}_0$ and a unit orientation vector $\boldsymbol{p}$ ($= \boldsymbol{x}_s$ which is constant for the entire length of a rigid rod). Neglecting hydrodynamic interactions and limiting ourselves to two spatial dimensions (so that the rod orientation in the plane of the flow can be described by a single angle θ), we write down a Fokker-Planck equation [122] for the configuration of a particle as:

$$\frac{\partial \Psi}{\partial t} + \boldsymbol{\nabla}_x \cdot (\dot{\boldsymbol{x}}_0 \Psi) + \frac{\partial (\dot{\theta} \Psi)}{\partial \theta} - \boldsymbol{\nabla}_x \cdot (\boldsymbol{D} \cdot \boldsymbol{\nabla}_x \Psi) - d_r \frac{\partial^2 \Psi}{\partial \theta^2} = 0, \tag{3.2}$$

where $\boldsymbol{D}$ and d_r denote the translational and rotational diffusivities, respectively, and dots are meant to represent time derivatives. This conservation equation merely balances the time rate of change of the probability distribution Ψ with advection due to the effect of the external flow, and diffusion due to thermal fluctuations.

For a slender Brownian rodlike particle of length L and characteristic cross-sectional radius a, the rotational diffusivity [122] is $d_r = 3k_B T \ln(1/\epsilon)/\pi\mu L^3$, where we use the same definition of the aspect ratio $\epsilon = a/L$ as in Section 1.1.3. The translational diffusivity tensor $\boldsymbol{D}$ is a sum of the contributions from the direction along the orientation of the rod, and that perpendicular to it. Given the translational diffusion coefficients [122] $D_{\parallel} = k_B T \ln(1/\epsilon)/2\pi\mu L$ and $D_{\perp} = k_B T \ln(1/\epsilon)/4\pi\mu L$ for motions in directions parallel and perpendicular to the rod axis, respectively, we express the diffusivity tensor as $\boldsymbol{D} = D_{\parallel}\boldsymbol{pp} + D_{\perp}(\boldsymbol{I} - \boldsymbol{pp})$, which simplifies to

$$\boldsymbol{D} = \frac{k_B T \ln(1/\epsilon)}{4\pi\mu L}(\boldsymbol{I} + \boldsymbol{pp}). \tag{3.3}$$

Noting that this tensor only depends on the orientation of the rod and not on its position, and by virtue of its symmetry, we may write: $\boldsymbol{\nabla}_x \cdot (\boldsymbol{D} \cdot \boldsymbol{\nabla}_x \Psi) = \boldsymbol{D} : \boldsymbol{\nabla}_x \boldsymbol{\nabla}_x \Psi$.

The Fokker-Planck equation (3.2) requires knowledge of the translational and rotational fluxes, and these are evaluated based on slender-body theory in Appendix

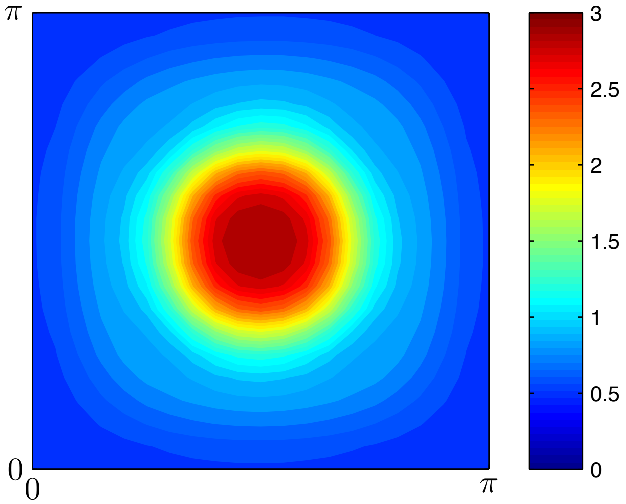

Figure 3.6: Steady-state solution of the Fokker-Planck equation at $Pe = 10000$ for rigid rods of aspect ratio $\epsilon = 0.01$.

B. The final form of the conservation equation is then

$$\begin{aligned}\frac{\partial \Psi}{\partial t} + Pe \Bigg[\boldsymbol{\nabla}_x \cdot \left\{ \Psi \int_{-1/2}^{1/2} \boldsymbol{u}(\boldsymbol{x} + s\boldsymbol{p})\,\mathrm{d}s \right\} \\ + \frac{\partial}{\partial \theta} \left\{ 12\Psi \hat{\boldsymbol{e}}_\theta \cdot (\boldsymbol{I} - \boldsymbol{pp}) \cdot \int_{-1/2}^{1/2} s\boldsymbol{u}(\boldsymbol{x} + s\boldsymbol{p})\,\mathrm{d}s \right\} \Bigg] \\ + \ln \epsilon^2 \left[\boldsymbol{\nabla}_x^2 \Psi + \boldsymbol{pp} : \boldsymbol{\nabla}_x \boldsymbol{\nabla}_x \Psi + 12 \frac{\partial^2 \Psi}{\partial \theta^2} \right] = 0,\end{aligned} \tag{3.4}$$

where we have introduced a Péclet number capturing the relative importance of advection by the flow to thermal diffusion:

$$Pe = \frac{8\pi\mu\dot{\gamma}L^3}{k_B T} = \bar{\mu}\frac{\ell_p}{L}. \tag{3.5}$$

We note that this Péclet number also formally corresponds to the product of the dimensionless viscosity $\bar{\mu}$ and reduced persistence length ℓ_p/L, though neither quantity is defined on its own in the case of a rigid rod ($\bar{\mu} \to 0$ and $\ell_p/L \to \infty$).

To determine the steady probability distribution function $\Psi(\boldsymbol{x}_0, \boldsymbol{p})$, we integrate the conservation equation (3.4) by time-marching using an Adams-Bashforth scheme until it converges to a steady state. The imposed velocity $\boldsymbol{u}$ is of the same form as in Equation (3.1), the aspect ratio is again set to $\epsilon = 0.01$, and the problem is solved on a four-cell unit ($W = \pi L$ here) of $\{x, y\} \in [-\pi, \pi]^2$ with periodic boundary conditions.

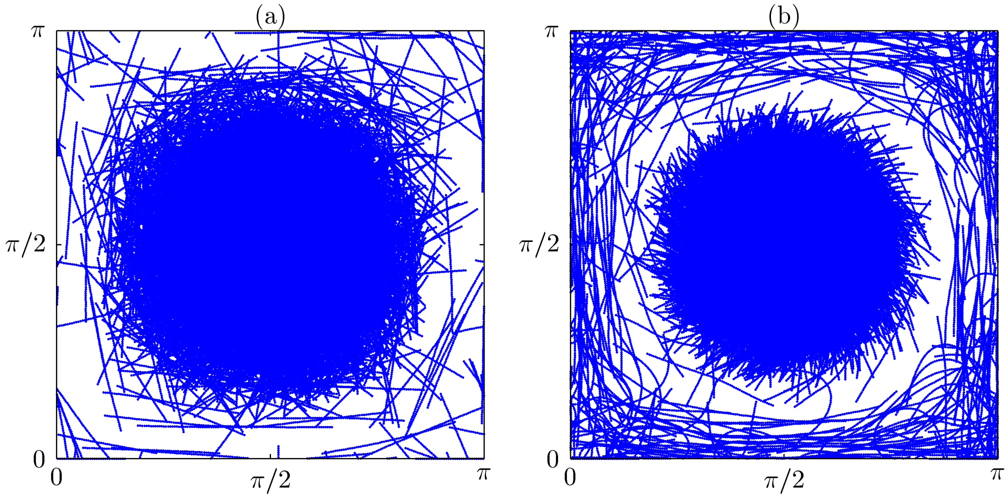

Figure 3.7: Characteristic distributions of filament configurations in a unit cell. (a) $\bar{\mu} = 1000$ and $\ell_p/L = 1000$, and (b) $\bar{\mu} = 10000$ and $\ell_p/L = 100$.

From the discussion of the buckling instability, we expect that polymers with rigid backbones (alternately interpreted as $\bar{\mu} < \bar{\mu}_{\text{cr}}$) should not migrate past the cell they are initially placed in, a prediction indeed borne out by the experiments of Wandersman *et al.* [36] The numerical solution to the Fokker-Planck equation (3.4) corroborates this observation, as is seen in the steady probability contours of Figure 3.6: for all values of Pe we considered, the probability peaks at the center of the cell at steady state, with negligible presence near the cell boundaries. Unsurprisingly, this migration is found to become stronger with increasing Péclet number.

This case of rigid rods, characterized by a systematic drift towards and trapping near the center of the cells as seen in Figure 3.6, can be contrasted to the case of elastic filaments to highlight the importance of filament flexibility in this transport process. Indeed, recalling that the Péclet number as defined here can be formally written as a product of the effective viscosity with the dimensionless persistence length, we compare distributions of filament configurations in two distinct simulations of semi-flexible polymers at a same value of Pe but with different appropriately chosen values of $\bar{\mu}$ and ℓ_p/L (i.e., with different values of the bending resistance). We first set these parameters to $\bar{\mu} = 1000$ and $\ell_p/L = 1000$ (corresponding to $Pe = 10^6$) and show a superposition of representative filament configurations in Figure 3.7(a). At this value of $\bar{\mu}$, the flow is not strong enough to induce buckling, and we observe that the filament, which is hardly deformed by the flow, spends most of its time near the center of the cell, which follows from the prediction of the rigid rod theory in Figure 3.6. However, the distribution of filament configurations looks qualitatively different in Figure 3.7(b), where we choose parameter values of $\bar{\mu} = 10000$ and $\ell_p/L = 100$ (the product of which is the same as in the previous case) that do allow buckling. Here, the dynamics are found to differ from the predictions of the rigid rod theory, and a significant probability of finding the filament near the cell boundaries is clearly seen. As expected, we observe larger filament deformations, and fully buckled configurations are also seen near the corners of the cell. This increased probability of presence near the cell boundaries leads to more probable jumps across cells, which in turn results in more efficient transport across the cellular lattice as discussed previously.

3.3 Conclusion

We have used numerical simulations based on a slender-body model to study the dynamics and transport properties of semiflexible polymers in a periodic two-dimensional cellular flow in the presence of thermal fluctuations. This work extends previous theoretical [35] and experimental [36, 116] studies that considered macroscopic non-Brownian filaments, and may also provide insight into some of the dynamics previously reported in actin motility assays. [90, 91] As in the non-Brownian case, the strong compressive flows that occur near the hyperbolic stagnation points at the cell junctions can cause buckling of the filaments, which facilitates their transport between cells, resulting in an effective two-dimensional random walk. However, we find that thermal fluctuations, quantified by the inverse of the dimensionless persistence length, tend to cause the filaments to drift towards and become trapped inside vortical cells for long periods of time. These frequent trapping events significantly hinder the spatial transport of the polymers, which shifts from diffusive to subdiffusive as fluctuations become significant, and this change in behavior is also evinced by the velocity and mass distributions of the chains. By comparing our simulation results to a simple theory for rigid Brownian rods, we also highlighted the subtle effect of flexibility on the transport properties. On the one hand, some level of flexibility is critical for effective transport across cells as it enables buckling; on the other hand, very floppy filaments with short persistence lengths are strongly affected by thermal fluctuations, which cause their frequent trapping and hinder their transport across the lattice.

The model flow field considered in this chapter (periodic lattice of steady Taylor-Green vortices), through its simplicity, allowed us to arrive at a simple qualitative description of the dynamics in terms of transport and buckling along strain-dominated directions vs. drifting and trapping inside vortical regions. It remains to be seen how this description would carry over to more complex flows, and in particular to unsteady chaotic flows with a spectrum of length scales such as a turbulent flow. While we expect the basic features of the dynamics observed here to also arise in that case, the net effect of flexibility and of thermal fluctuations on macroscopic rheological and transport properties [123, 124] in complex flow fields remains difficult to anticipate.

Chapter 3 is based largely on material that has appeared in *Physics of Fluids* (2013), authored by Harishankar Manikantan and David Saintillan [3].

Chapter 4

The sedimentation of flexible filaments

4.1 Introduction

Though seemingly simple, the sedimentation of elastic filaments in a constant and uniform gravitational field has received limited attention and has yet to be fully analyzed, even in the case of isolated filaments. The sedimentation of rigid fibers has been the subject of many studies and is well understood. At zero Reynolds number, as we saw in Section 1.2.1, a rigid fiber with unit director $\boldsymbol{p}$ sedimenting under gravity in an unbounded fluid will maintain its orientation and travel at a constant velocity $\boldsymbol{U} = [\mu_\perp(\boldsymbol{I} - \boldsymbol{pp}) + \mu_\parallel \boldsymbol{pp}] \cdot \boldsymbol{F}_G$, where $\boldsymbol{F}_G$ is the net gravitational force on the particle. The mobility coefficients $\mu_\perp$ and $\mu_\parallel$ depend on the exact shape of the particle ($\mu_\parallel \approx 2\mu_\perp$ for a slender body) [67]. Because of its drag anisotropy, the particle does not generally translate in the direction of gravity, but rather at a fixed angle θ that depends on its orientation ($\theta = 0$ when the fiber is either parallel or perpendicular to gravity). As first predicted by Koch and Shaqfeh [125], this very simple picture is seriously complicated when multiple rigid fibers are allowed to interact hydrodynamically. In that case, long-range interactions drive a concentration instability as a result of the coupling between the orientation of the particles, which determines their settling direction, and the disturbance flows they drive in the fluid, which reorient them. This instability is indeed observed in both experiments [126] and simulations [127, 128] and takes the form of dense dynamic particle clusters which settle at significantly higher speeds than isolated particles. Even two sedimenting particles can undergo complex periodic sedimentation dynamics [129].

Any small amount of flexibility is expected to change the dynamics described above qualitatively, even for an isolated filament. If the filament is allowed to bend as it sediments, this loss of symmetry will result in a coupling between its translational and rotational motions, leading to reorientation of the filament with respect to the direction of gravity. Because the orientation of the filament directly determines the direction of its velocity, we can also expect a non-trivial translational motion in both vertical and horizontal directions. The effect of fiber asymmetry on the dynamics was demonstrated experimentally by Tozzi *et al.* [130] using rigid curved fibers, where particle rotations and unsteady trajectories were reported. Complex spatial dynamics of curved fibers have also been observed in other situations such as in simple shear flow [131]. The situation is yet more complex in the presence of flexibility, as the filament shape and grand mobility matrix evolve dynamically in time. Using a model based on the slender-body theory of Cox [68], Xu and Nadim [132] argued that this coupling should cause a weakly flexible filament to reorient in a direction perpendicular to gravity regardless of its initial configuration and to assume a steady U-shape that depends on the relative magnitude of gravitational and elastic forces. These predictions were confirmed by Cosentino Lagomarsino *et al.* [133] and Schlagberger and Netz [134] using numerical simulations based on a discrete model of a filament as a string of rigidly connected beads with bending moments. However, a complete theoretical description of the shape evolution and reorientation dynamics and their influence on spatial trajectories has yet to be realized.

The case of a floppy filament with weak bending resistance is even more challenging, as large deformations may occur. For reasons that will be made clear in Section 4.4, a filament oriented parallel to gravity is subject to a compressive tension profile which, in some cases, may overcome bending resistance and lead to a buckling instability, much like that for a macroscopic Euler beam [135]. Buckling of elastic filaments in viscous fluid flows has already been reported in a number of situations, and we have already seen this in the case of free filaments in Section 2.6.2. Becker and Shelley [27] simulated the dynamics of isolated elastic filaments in simple shear flow and showed that buckling occurs when the filaments are aligned with the axis of compression of the flow, resulting in normal stress differences; these dynamics were also shown to persist at finite concentration [28]. A theoretical analysis of this buckling was later provided by Young and Shelley [35] in a simpler setting, namely at the hyperbolic stagnation point of a two-dimensional linear extensional flow when the filament is initially aligned with the axis of compression. They demonstrated that above a critical flow strength compressive viscous forces indeed induce buckling, and showed that a series of unstable modes characterized by increasingly higher wavenumbers can become excited as the strain rate is increased. Instability was also observed in more complex flows such as vortex arrays in both simulations [3, 35] and experiments [36], where it was shown to have a strong impact on the spatial transport of the filaments (cf. Chapter 3). As we discuss in Section 4.4, a similar buckling instability is also predicted under sedimentation for nearly vertical floppy filaments, though more complex asymmetric mode shapes are expected as the base tension profile can be shown to be compressive only over the leading half of the filament.

This chapter is organized as follows. In Section 4.2 we describe the energetics of a single flexible filament under the influence of gravity and derive the equations for the filament position and tension. The dynamics of the filament are characterized by a dimensionless quantity which we term the elasto-gravitation number. Filaments of both non-uniform and uniform cross-sectional thickness are considered. In Section 4.3 we study weakly flexible filaments, where the elasto-gravitation number is large, and show that the introduction of filament compliance can alter dramatically the long-time sedimentation orientation and velocity. Equilibrium shapes are derived, and the assumption of timescale separation allows for predictions of slowly varying filament shapes and rotation rates. The buckling instability of a sedimenting filament is studied in Section 4.4, where a linear stability analysis is used to predict the most unstable waveforms, growth rates, and wave speeds; the results are shown to compare favorably with numerical simulations.

4.2 Mathematical formulation

To model the dynamics of a slender elastic filament in a viscous fluid, we first describe the energetics of the system from which a local force balance may be derived. We then proceed to discuss the model for the fluid-body interactions: we solve the Stokes equations of viscous flow using the slender-body theory of Johnson [57].

4.2.1 Energy functional and local force balance

Consider a filament of length L with a centerline described by $\boldsymbol{x}(s,t)$, where s is the arc length and t is time. The filament is assumed to be radially symmetric at each cross-section with a thickness given by $a \cdot r(s)$ (with $r(s)$ dimensionless). The following functional describes the energetics of the system,

$$\begin{aligned}\mathcal{E} =& \frac{1}{2}\int_0^L B(s)|\boldsymbol{x}_{ss}|^2\,\mathrm{d}s + \frac{1}{2}\int_0^L T(s)(|\boldsymbol{x}_s|^2 - 1)\,\mathrm{d}s \\ & - \int_0^L \boldsymbol{f}(s)\cdot\boldsymbol{x}(s)\,\mathrm{d}s - \int_0^L \boldsymbol{F}_g(s)\cdot\boldsymbol{x}(s)\,\mathrm{d}s,\end{aligned} \tag{4.1}$$

where index s denotes differentiation with respect to arc length. The first term corresponds to a Hookean bending energy, proportional to the curvature of the filament: $B(s) = EI(s)$ is the bending stiffness, with E the elastic modulus and $I(s) = \pi a^4 r(s)^4/4$ the area moment of inertia. (We shall use the notation $B(s)$ in this chapter instead of κ used in the rest of the dissertation to stress that the former is, in general, a function of s whereas the latter is always assumed a constant.) The second term imposes filament inextensibility, with the tension $T(s)$ acting as a Lagrange multiplier. The third term is due to the fluid force per unit length $\boldsymbol{f}(s)$ acting on the body at station s. Finally, the last term is a gravitational potential energy, where $\boldsymbol{F}_g(s) = -\pi a^2 r(s)^2 \mathit{\Delta}\rho\, g\, \hat{\boldsymbol{y}}$. Here $\mathit{\Delta}\rho$ is the density difference between the filament and the fluid, and $g > 0$ is the gravitational acceleration.

By the principle of virtual work, the pointwise force on the filament is found by taking a variational derivative of the energy (4.1). Perturbing $\boldsymbol{x}$ by $\varepsilon\boldsymbol{h}(s)$ and taking $\varepsilon \to 0$, we find

$$\begin{aligned}\frac{\delta \mathcal{E}}{\delta \boldsymbol{x}} &= \int_0^L B(s)\boldsymbol{x}_{ss} \cdot \boldsymbol{h}_{ss} \,\mathrm{d}s + \int_0^L T(s)\boldsymbol{x}_s \cdot \boldsymbol{h}_s \,\mathrm{d}s - \int_0^L (\boldsymbol{f}(s) + \boldsymbol{F}_g(s)) \cdot \boldsymbol{h} \,\mathrm{d}s \\ &= \int_0^L \Big[-(T(s)\boldsymbol{x}_s)_s + (B(s)\boldsymbol{x}_{ss})_{ss} - \boldsymbol{f}(s) - \boldsymbol{F}_g(s) \Big] \cdot \boldsymbol{h} \,\mathrm{d}s \\ &\quad + \Big[B(s)\boldsymbol{x}_{ss} \cdot \boldsymbol{h}_s + (T(s)\boldsymbol{x}_s - (B(s)\boldsymbol{x}_{ss})_s) \cdot \boldsymbol{h} \Big]_0^L .\end{aligned} \tag{4.2}$$

Setting the above to zero for all perturbations $\boldsymbol{h}(s)$, we see that the fluid force acting on the filament is given by

$$\boldsymbol{f}(s) = -\boldsymbol{F}_g(s) - (T(s)\boldsymbol{x}_s)_s + (B(s)\boldsymbol{x}_{ss})_{ss}, \tag{4.3}$$

and we also observe the boundary conditions for solvability,

$$(B\boldsymbol{x}_{ss})(0) = 0, \quad (B\boldsymbol{x}_{ss})(L) = 0, \tag{4.4}$$

$$(T\boldsymbol{x}_s)(0) = (B\boldsymbol{x}_{ss})_s(0), \quad (T\boldsymbol{x}_s)(L) = (B\boldsymbol{x}_{ss})_s(L). \tag{4.5}$$

As expected, the integrated fluid force along the filament is equivalent to the net gravitational force,

$$\int_0^L \boldsymbol{f} \,\mathrm{d}s = \int_0^L \Big[-\boldsymbol{F}_g(s) - (T(s)\boldsymbol{x}_s)_s + (B\boldsymbol{x}_{ss})_{ss} \Big] \,\mathrm{d}s = -\int_0^L \boldsymbol{F}_g(s) \,\mathrm{d}s = -\boldsymbol{F}_G. \tag{4.6}$$

Scaling lengths with L and forces with the total gravitational force, $F_G = |\boldsymbol{F}_G|$, the dimensionless fluid force per unit length on the filament is given by

$$\bar{\boldsymbol{f}}(\bar{s}) = -\bar{\boldsymbol{F}}_g(\bar{s}) - (\bar{T}(\bar{s})\bar{\boldsymbol{x}}_{\bar{s}})_{\bar{s}} + \beta(\bar{B}(\bar{s})\bar{\boldsymbol{x}}_{\bar{s}\bar{s}})_{\bar{s}\bar{s}}, \tag{4.7}$$

where $\boldsymbol{x} = L\bar{\boldsymbol{x}}$, $s = L\bar{s}$, $T = F_G\bar{T}$, $B = (\pi/4)Ea^4\bar{B}$, and $\bar{\boldsymbol{F}}_g(\bar{s})$ integrates to $-\hat{\boldsymbol{y}}$. Here we have introduced an elasto-gravitation number, $\beta = \pi E a^4/(4F_G L^2)$, which compares the elastic forces acting on the filament to the gravitational force. With all variables now understood to be dimensionless, we drop the bars in Equation (4.7) for the duration of this chapter.

4.2.2 Fluid-body interaction and filament dynamics

As a filament settles in a fluid, the elasto-gravitation forces acting along the body are coupled to the body's orientation and shape dynamics. When the Reynolds number is small ($Re = \rho UL/\mu \ll 1$, with U a characteristic speed and μ the fluid viscosity), the fluid flow is well-described by the Stokes equations and we shall resort to the the slender-body theory we introduced in Section 1.1.3. Scaling upon a sedimentation timescale $8\pi\mu L^2 F_G$, the dimensionless velocity of a point s along the body centerline is approximated as

$$\boldsymbol{x}_t = -\boldsymbol{\Lambda}[\boldsymbol{f}](s) - \boldsymbol{K}[\boldsymbol{f}](s), \tag{4.8}$$

where $\boldsymbol{f}$ is the scaled fluid force acting on the body given by Equation (4.7). Using the local inextensibility condition $\boldsymbol{x}_s \cdot \boldsymbol{x}_s = 1$, the position equation can then be manipulated to give an equation for the tension [28],

$$\begin{aligned} &-2(c-1)T_{ss} + (c+1)|\boldsymbol{x}_{ss}|^2 T - 2c_s T_s - \boldsymbol{x}_s \cdot \partial_s \boldsymbol{K}[(T\boldsymbol{x}_s)_s] \\ &\quad = (7c-5)\beta B(s)\boldsymbol{x}_{ss} \cdot \boldsymbol{x}_{ssss} + 6(c-1)\beta B(s)|\boldsymbol{x}_{sss}|^2 + 6\beta c_s B(s)\boldsymbol{x}_{ss} \cdot \boldsymbol{x}_{sss} \\ &\qquad + \beta(4c_s B_s + (5c-3)B_{ss})|\boldsymbol{x}_{ss}|^2 + 4(4c-3)\beta B_s \boldsymbol{x}_{ss} \cdot \boldsymbol{x}_{sss} - \beta \boldsymbol{x}_s \cdot \partial_s \boldsymbol{K}[(B\boldsymbol{x}_{ss})_{ss}] \\ &\qquad + (c-3)\boldsymbol{x}_{ss} \cdot \boldsymbol{F}_g + 2(c-1)\boldsymbol{x}_s \cdot \partial_s \boldsymbol{F}_g + 2c_s \boldsymbol{x}_s \cdot \boldsymbol{F}_g + \boldsymbol{x}_s \cdot \partial_s \boldsymbol{K}[\boldsymbol{F}_g(s)]. \end{aligned} \tag{4.9}$$

If the filament is cylindrical with constant cross-section ($r(s) = 1$), then $\boldsymbol{F}_g(s) = -\hat{\boldsymbol{y}}$ and $B(s) = B$ are constants, while $c(s) = \ln(4s(1-s)/\epsilon^2)$ varies, though the slender-body theory loses accuracy at the endpoints in this case [57]. Instead, if the filament thickness is described by the spheroidal profile $r(s) = 2\sqrt{s(1-s)}$, we have $c(s) = c = \ln(1/\epsilon^2)$, a constant. For such a filament shape, assuming uniform material distribution, the gravitational force is spatially varying, $\boldsymbol{F}_g(s) = -6s(1-s)\hat{\boldsymbol{y}}$, as is the bending stiffness, $B(s) = r(s)^4 = 16s^2(1-s)^2$. In this case the boundary condition (4.4) disappears. This limiting case is singular and is associated with an elastic boundary layer at the endpoints. Throughout this chapter, we shall alternatingly discuss theoretical results for both geometries, and compare the case of a spheroidal profile with corresponding numerical simulations.

Finally, for convenience, we define here two integral operators that will appear in the asymptotic evaluation of the non-local integral operator (Equation (1.12)),

$$S[g](s) = \int_0^1 \frac{g(s') - g(s)}{|s'-s|}\, \mathrm{d}s', \qquad P[g](s) = \int_0^1 \frac{\Delta g(s,s') - g_s(s')}{|s'-s|}\, \mathrm{d}s', \tag{4.10}$$

where

$$\varDelta g(s,s') = \frac{g(s)-g(s')}{s-s'}. \tag{4.11}$$

The governing equations are solved numerically using a variation of the method suggested by Tornberg and Shelley [28] as elaborated in Section 2.3. We have chosen $c(s) = c$ a constant and $\boldsymbol{F}_g(s) = -6s(1-s)\hat{\boldsymbol{y}}$ as previously described, but we have assumed $B(s) = 1$, an approximation that we justify later. Boundary conditions from Equations (4.4) and (4.5) are translated onto the discrete points via one-sided finite differences. For all the results presented in this chapter, we use $N = 256$ and $\zeta = 400$. This value of N is chosen to ensure the minimum radius of curvature remains at least an order of magnitude larger than the grid spacing $\varDelta s = 1/(N-1)$ without having to use adaptive refinement, even in the case of severely buckled shapes in Section 4.4. The penalization parameter in Equation (2.13) is decided by numerical stability (quantified in terms of contour length error), and the value chosen here is such that numerical errors in the filament length do not exceed 0.1% in the weakly flexible case in Section 4.3, and remain under 4% in the most buckled case described in Section 4.4. The dimensionless time step is $\varDelta t = 10^{-5}$, except for the linear stability results of Section 4.4 where it is further reduced to 10^{-6}. The filament aspect ratio ϵ is fixed at 0.01 throughout.

4.3 Weakly flexible filaments

It is a well known result that straight, rigid rods sediment in an infinite viscous fluid without any body reorientation [60]. Curved filaments, however, have been shown to rotate during sedimentation until an equilibrium orientation is achieved [130]. The introduction of filament flexibility, then, can result in filament shape changes but can also lead to complex body reorientation. To investigate the first effects of elasticity, we focus on the dynamics of a weakly flexible filament, where the elasto-gravitation number β is assumed to be large.

There are two different effects that can lead to shape changes of a weakly flexible sedimenting filament. As we will show, the leading-order effect is due to non-uniformity of the filament thickness along its length. Consider a filament of non-

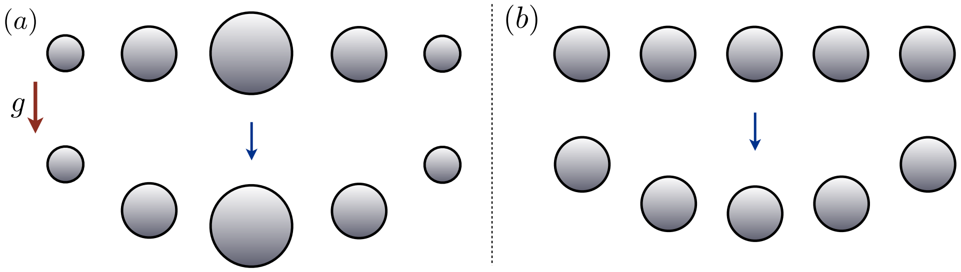

Figure 4.1: Illustration of the source of bending in model "filaments." (*a*) The leading-order effect: larger bodies sediment faster than smaller bodies in a viscous fluid, and filaments of non-uniform thickness will bend as a consequence. (*b*) The secondary effect: the central bodies in a line of identical sedimenting spheres experience a stronger disturbance fluid flow, and will sediment faster than those near the ends.

uniform thickness sedimenting in the direction of its minor axis, and for the sake of intuition consider as a simple model the distribution of sedimenting spheres of varying radii shown in Figure 4.1(*a*). In a highly viscous fluid, a sphere of radius a settles with speed $U = 2a^2 g\, \Delta\rho / 9\mu$ (cf. Section 1.2.1). The spheres near the center of the row will sediment faster than those near the ends, resulting in bending of the assemblage as depicted. A filament of uniform thickness is also expected to bend but as a consequence of a secondary effect, namely by non-local hydrodynamic interactions. Modeling such a filament as a row of *identical* spheres, as illustrated in Figure 4.1(*b*), note that the disturbance flow experienced by the central spheres, due to the motion of the other spheres, will increase the sedimentation speed of the former. Bending from non-local hydrodynamics will be shown to be a higher-order effect. In this section we will study the behavior of spheroidal filaments, where $r(s) = 2\sqrt{s(1-s)}$, while similar calculations for the case $r(s) = 1$ are included in Appendix C.

Returning to the full model described in Section 4.2, the complex interactions between shape changes and body reorientation can be seen in the numerical results of Figure 4.2. In Figure 4.2(*a*), an initially straight filament is released at the origin in a nearly vertical orientation and is allowed to deform and sediment freely under gravity. The initial angle between the tangent at the particle center and gravity is $\theta_0 = \pi/64$, and we choose what we will find to be a relatively large value of $\beta = 0.02$. As a result

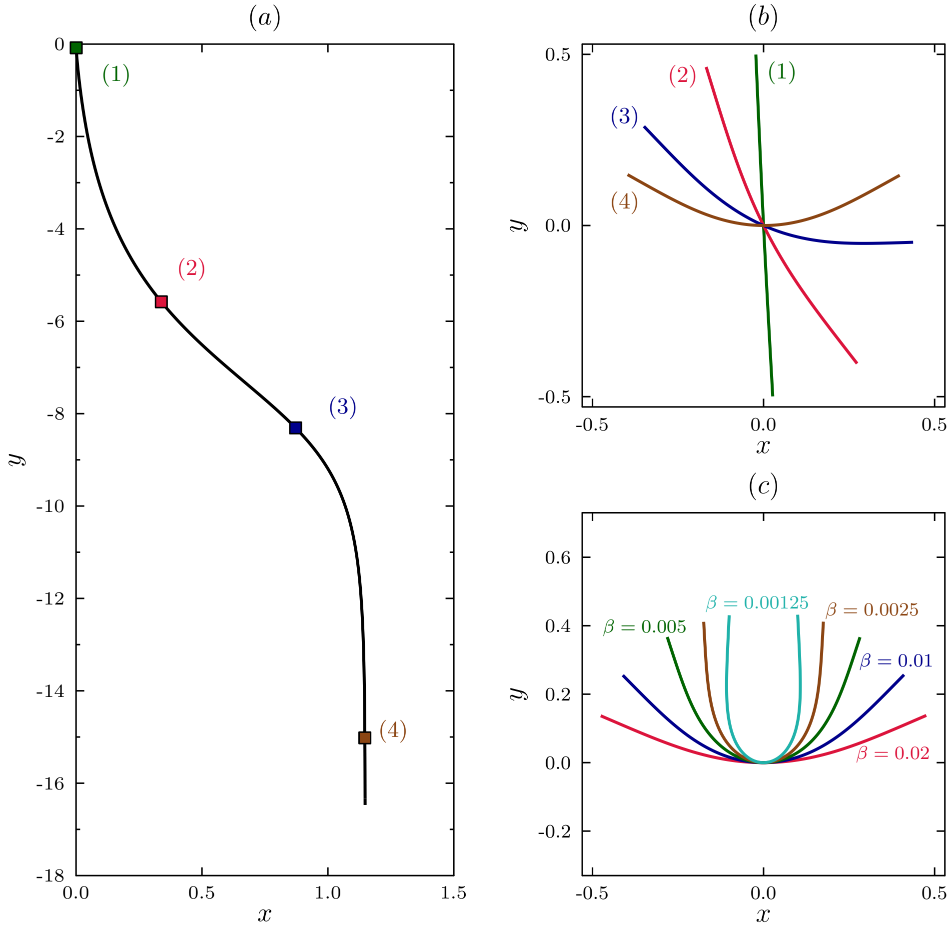

Figure 4.2: The trajectory and shape of a sedimenting flexible filament obtained from numerical simulations with $r(s) = 2\sqrt{s(1-s)}$ and $B(s) = 1$. (a) Trajectory of a filament with initial orientation angle $\theta_0 = \pi/64$, with "large" elasto-gravitation number $\beta = 0.02$, from numerical simulations. (b) Shape of the filament as it sediments in a frame moving with its midpoint, also showing the reorientation process. Snapshots correspond to indicated points on the trajectory in (a). (c) Steady-state shapes for β in the range $0.00125 - 0.02$. The deflections are shown in a frame moving with the filament midpoint.

of its flexibility, weak deformations arise which cause the slow reorientation of the filament to a direction perpendicular to gravity, as shown in Figure 4.2(b). As the filament rotates away from its initial orientation, its settling motion incurs a lateral drift, which is strongest when the mean orientation forms an angle of approximately $\pi/4$ with the direction of gravity. As the filament eventually aligns horizontally, the

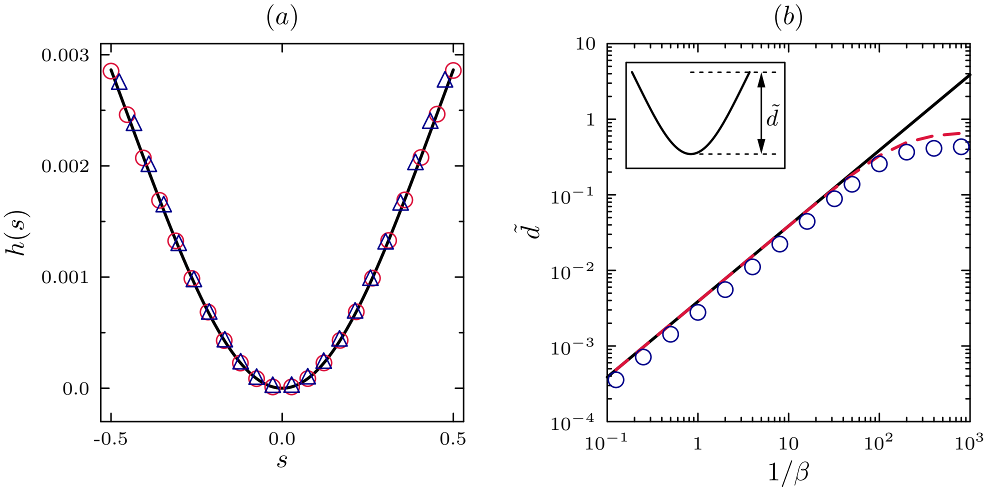

Figure 4.3: Terminal shape and maximum deflection along with corresponding theoretical predictions. (a) The final sedimenting shape, normalized by β, corresponding to $\beta = 8\,(○)$ and $\beta = 0.02\,(△)$ from simulations, along with the prediction from Equation (4.37) (solid line) showing the validity of the theory down to relatively small values of β. Here, $h(s)$ is the scaled deflection perpendicular to the straightened state at parametric position s. (b) Maximum deflection of the filament shape $\tilde{d} = \max[\hat{\boldsymbol{n}} \cdot \boldsymbol{d}(s)]$ as a function of $1/\beta$. Also shown by the solid line is the theoretical prediction following Equation (4.37). The dashed line shows a correction to the theoretical prediction in which the filament shape was rescaled to preserve length.

drift slows and the trajectory asymptotes to a vertical line.

We observe in the weakly flexible regime that the only stable filament orientation is when the tangent at the center is perpendicular to the direction of gravity. In this configuration, the filament assumes a symmetric, nearly parabolic shape as shown in Figure 4.2(b). The steady ‘terminal’ shapes of more flexible filaments are plotted in Figure 4.2(c) for a decreasing sequence of values of the elasto-gravitation number, where more flexible filaments are seen to adopt horseshoe shapes. Furthermore, these steady shapes obtained in simulations in the limit of weak flexibility are found to collapse onto a single self-similar curve $h(s)$, as shown in Figure 4.3(a) upon normalization by β (as will be shown theoretically in the following section). The final extent of bending can be characterized by the maximum deflection $\tilde{d}$ of the filament, which is shown in Figure 4.3(b) against $1/\beta$, exhibiting linear growth in the weakly flexible regime that extends as far down as $\beta \approx 0.02$. For elasto-gravitation numbers $\beta \lesssim 0.01$, the curve plateaus with the appearance of the horseshoe shape towards the maximum possible symmetric deflection value of one half. The weakly flexible regime may therefore be defined by "large" values of the elasto-gravitation number, $\beta \gtrsim 0.01$.

4.3.1 A separation of timescales

We now set out to describe the filament shapes and dynamics analytically in the weakly flexible regime. The position of the filament centerline at time t can be written without loss of generality as

$$\boldsymbol{x}(s,t) = \boldsymbol{r}(t) + (s - 1/2)\hat{\boldsymbol{t}}(\theta(t)) + \boldsymbol{d}(s,t), \tag{4.12}$$

where $\boldsymbol{r}(t) = \boldsymbol{x}(1/2,t)$ is the position of the filament center, $\hat{\boldsymbol{t}} = \boldsymbol{x}_s(1/2,t)$ is the unit tangent vector there, and $\boldsymbol{d}(s,t)$ is the time-dependent deviation of the filament from its straightened state (with $\boldsymbol{d}(1/2,t) = 0$). The filament is illustrated in Figure 4.4. The natural coordinate system that rotates in time with the body is then described by

$$\hat{\boldsymbol{t}}(\theta) = -\cos\theta\,\hat{\boldsymbol{y}} + \sin\theta\,\hat{\boldsymbol{x}}, \tag{4.13}$$

$$\hat{\boldsymbol{n}}(\theta) = \sin\theta\,\hat{\boldsymbol{y}} + \cos\theta\,\hat{\boldsymbol{x}}, \tag{4.14}$$

where $\theta = \theta(t)$ measures the angle between $-\hat{\boldsymbol{y}}$ and the unit tangent vector $\hat{\boldsymbol{t}}$, and $\hat{\boldsymbol{n}}$ is the vector normal to the filament at its midpoint. The translational velocity of the midpoint is written as $\boldsymbol{r}'(t) = \boldsymbol{U}(t) = U(t)\hat{\boldsymbol{t}} + V(t)\hat{\boldsymbol{n}}$.

As we have observed in the numerical simulations of Figure 4.2, when the elasto-gravitation number is large, the filament rotates in a time much longer than is required for the body to traverse many body lengths. Meanwhile, the filament is relatively stiff, so for a given orientation angle the body rapidly reaches its equilibrium shape. These observations suggest that there is a separation of timescales that will aid in the analysis of the system; the filament shape can be determined separately from the body rotation rate, and the rotation rate can be determined given a fixed body shape.

More specifically, there are three distinct timescales of note in the simulations. For large values of the elasto-gravitation number, $\beta \gg 1$, the first is a very short

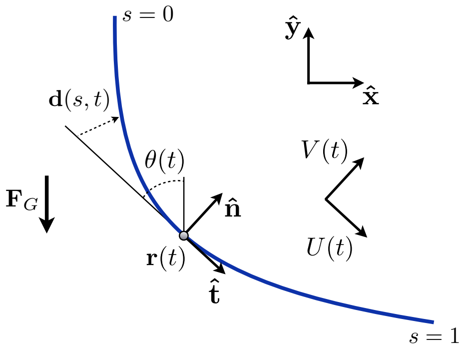

Figure 4.4: Illustration of the filament centerline. The unit tangent and unit normal vectors at the single point $\boldsymbol{r}(t) = \boldsymbol{x}(s = 1/2, t)$ are given by $\hat{\boldsymbol{t}}$ and $\hat{\boldsymbol{n}}$, respectively. $\theta(t)$ measures the angle between $\hat{\boldsymbol{t}}$ and the direction of gravity, $-\hat{\boldsymbol{y}}$.

elastic relaxation timescale of $O(\beta^{-1})$. The second is the timescale of $O(1)$ on which the body sediments a distance comparable with its length. The third is a very long timescale of $O(\beta)$ on which the body may reorient on account of its nontrivial shape. Our aim is to study the shape changes of the filament on the latter two timescales, during which the body translates and rotates through the fluid. Defining the scaled time $\tau = \beta^{-1}t$, we analyze the system by the method of multiple scales wherein variables are assumed to have a separate explicit dependence upon both t and τ (see Bender and Orszag [136]). A uniform solution to Equations (4.8) and (4.9) is then sought by assuming regular expansions of the tension and filament shape in powers of the small number β^{-1} of the form

$$T(s,t,\tau;\beta) = T^{(0)}(s,t,\tau) + \beta^{-1}T^{(1)}(s,t,\tau) + O\left(\beta^{-2}\right). \tag{4.15}$$

Upon inspection of equation (4.7), we observe that the sedimentation and elastic effects are balanced when $\beta(B(s)\boldsymbol{d}_{ss})_{ss} = O(\boldsymbol{F}_g)$, and we have that $O(|\boldsymbol{F}_g|) = O(1)$. Therefore when these effects are balanced the deflection of the filament is such that $\boldsymbol{d} = O(\beta^{-1})$. A general expression for $\boldsymbol{d}$ is then given by

$$\boldsymbol{d}(s,t,\tau;\beta) = \beta^{-1}u(s,t,\tau)\hat{\boldsymbol{n}}(\theta) + \beta^{-2}u_1(s,t,\tau)\hat{\boldsymbol{n}}(\theta) + \beta^{-2}v_1(s,t,\tau)\hat{\boldsymbol{t}}(\theta) + O\left(\beta^{-3}\right), \tag{4.16}$$

with the functions u, u_1, and v_1 to be determined. Note that $\boldsymbol{x}_s = \hat{\boldsymbol{t}} + \boldsymbol{d}_s$, and filament inextensibility ($\boldsymbol{x}_s \cdot \boldsymbol{x}_s = 1$) requires that the only filament deflections at first order in

β^{-1} are normal to $\hat{\boldsymbol{t}}$. The definition of $\boldsymbol{d}$ implies $\boldsymbol{d}_s(1/2, t, \tau; \beta) = 0$. The translational velocity and orientation angle are similarly expressed,

$$U(t, \tau; \beta) = U^{(0)}(t, \tau) + \beta^{-1} U^{(1)}(t, \tau) + O\left(\beta^{-2}\right), \tag{4.17}$$

$$V(t, \tau; \beta) = V^{(0)}(t, \tau) + \beta^{-1} V^{(1)}(t, \tau) + O\left(\beta^{-2}\right), \tag{4.18}$$

$$\theta(t, \tau; \beta) = \theta^{(0)}(t, \tau) + \beta^{-1} \theta^{(1)}(t, \tau) + O\left(\beta^{-2}\right). \tag{4.19}$$

Inserting the expressions above into Equation (4.8), and dotting separately with either $\hat{\boldsymbol{t}}(\theta)$ and $\hat{\boldsymbol{n}}(\theta)$, we find the leading-order relations,

$$U^{(0)} = 2(c-1)\left[T_s^{(0)} - F_g \cos\theta^{(0)}\right] + 2S\left[T_s^{(0)} - F_g \cos\theta^{(0)}\right], \tag{4.20}$$

$$V^{(0)} + (s - 1/2)\theta_t^{(0)} = -(c+1)\left[(Bu_{ss})_{ss} - F_g \sin\theta^{(0)}\right] - S\left[(Bu_{ss})_{ss} - F_g \sin\theta^{(0)}\right], \tag{4.21}$$

where $S[\cdot]$ is the non-local hydrodynamic contribution for a straight filament defined in Equation (4.10). Recall that $B = B(s)$, $F_g = F_g(s)$, and $c = \ln(1/\epsilon^2)$. Following Götz [70], if we denote by $\mathcal{L}_n(s)$ the n^{th} shifted Legendre polynomial (defined on $s \in [0, 1]$), we have $S[\mathcal{L}_n(s)] = \lambda_n \mathcal{L}_n(s)$, with $\lambda_n = -2\sum_{i=1}^{n}(1/i)$. Hence, the equations above are made tractable by expressing variables in the Legendre polynomial basis. Using the orthogonality of the Legendre polynomials, we recover the leading-order sedimentation velocity,

$$\boldsymbol{U}^{(0)} = 2(c-1)\cos\theta^{(0)}\, \hat{\boldsymbol{t}}(\theta^{(0)}) - (c+1)\sin\theta^{(0)}\, \hat{\boldsymbol{n}}(\theta^{(0)}), \tag{4.22}$$

and in addition we find

$$T_s^{(0)} - F_g \cos\theta^{(0)} = \cos\theta^{(0)}, \tag{4.23}$$

$$(Bu_{ss})_{ss} - (F_g + 1)\sin\theta^{(0)} = \frac{s - 1/2}{1 - c}\theta_t^{(0)}. \tag{4.24}$$

The case of uniform filament thickness, with $F_g(s) = -1$, is considered in Appendix C. The leading-order effect illustrated in Figure 4.1 is studied now by inserting $F_g(s) = -6s(1-s)$, which results in the leading-order tension,

$$T^{(0)} = s(1-2s)(1-s)\cos\theta^{(0)}. \tag{4.25}$$

Meanwhile, multiplying Equation (4.24) by $(s-1/2)$ and integrating, we find $\theta_t^{(0)} = 0$. The filament therefore does not rotate on the timescale t, but may still rotate on the longer timescale, $\theta^{(0)}(t,\tau) = \theta^{(0)}(\tau)$. The leading-order deflection of the filament from its straightened state can now be determined by integrating Equation (4.24) (inserting $\theta_t^{(0)} = 0$ and $F_g = -6s(1-s)$) and imposing the boundary conditions in Equation (4.4), giving

$$u(s,\tau) = h(s)\sin\theta^{(0)}(\tau), \tag{4.26}$$

with

$$B(s)h_{ss} = \frac{1}{2}s^2(1-s)^2, \tag{4.27}$$

$$h(1/2) = h_s(1/2) = 0. \tag{4.28}$$

If the filament is composed of a uniform material, a corresponding bending stiffness $B(s) = r(s)^4 = 16s^2(1-s)^2$ then results in the filament deflection profile

$$h(s) = \frac{1}{64}\left(s - \frac{1}{2}\right)^2. \tag{4.29}$$

Surprisingly, the shape of the filament is symmetric about its midpoint at leading order for any orientation, and the scaling of the deflection with the orientation angle is given simply by $\sin\theta^{(0)}(\tau)$. In order to determine the orientation angle $\theta^{(0)}(\tau)$, we must look to higher order. At $O(\beta^{-1})$, Equation (4.8) yields the expression

$$\begin{aligned} V^{(1)} + (s-1/2)\left(\theta_\tau^{(0)} + \theta_t^{(1)}\right) &= (c+1)\left[(T^{(0)}u_s)_s - (Bu_{1,ss})_{ss} + \theta^{(1)}\cos\theta^{(0)}F_g\right] \\ &\quad + (c-3)u_s\cos\theta^{(0)} + S\left[(T^{(0)}u_s)_s - (Bu_{1,ss})_{ss} + \theta^{(1)}\cos\theta^{(0)}F_g\right] \\ &\quad + \cos\theta^{(0)}S[u_s] + \cos\theta^{(0)}P[u], \end{aligned} \tag{4.30}$$

where the integral operator $P[\cdot]$ is defined in Equation (4.10). Multiplying Equation (4.30) by $(s-1/2)$ and integrating, we have

$$\theta_\tau^{(0)} + \theta_t^{(1)} = \frac{A}{2}\sin(2\theta^{(0)}), \tag{4.31}$$

$$A = 12((c-1)I_1 + (c-5)I_2 + I_3), \tag{4.32}$$

where

$$I_1 = \int_0^1 (1 - 6s + 6s^2) h(s) \,\mathrm{d}s, \tag{4.33}$$

$$I_2 = \int_0^1 (s - 1/2) h_s(s) \,\mathrm{d}s, \tag{4.34}$$

$$I_3 = \int_0^1 (s - 1/2) P[h](s) \,\mathrm{d}s. \tag{4.35}$$

The secular behavior in the expansion is removed by taking $\theta^{(1)} = \theta^{(1)}(\tau)$, and we are left with an equation for the dynamics of $\theta^{(0)}$,

$$\theta^{(0)}_\tau = \frac{A}{2} \sin(2\theta^{(0)}). \tag{4.36}$$

Inserting the expression for $h(s)$ obtained in Equation (4.29), we have $I_1 = 1/1920$ and $I_2 = I_3 = 1/384$, so that $A = 3(c - 7/2)/80 = 3(\ln(1/\epsilon^2) - 7/2)/80$. The constant A is positive (and the result is physical) in the slender-body regime, or specifically when: $\epsilon < \exp(-7/4) \approx 0.17$. We therefore have that the orientation angle $\theta = 0$ is unstable, and that $\theta = \pm\pi/2$ are stable. From Equation (4.36) we see that the filament will reorient on a timescale $O(\beta/c)$ until its central tangent vector is perpendicular to gravity. This matches our prediction of reorientation on a timescale of $O(\beta)$, but includes a coefficient that depends on the filament aspect ratio.

In the calculation above, if we were to take the bending stiffness to be constant along the centerline ($B(s) = 1$), we instead find

$$h(s) = \frac{1}{64}\left[\left(s - \frac{1}{2}\right)^2 - \frac{4}{3}\left(s - \frac{1}{2}\right)^4 + \frac{16}{15}\left(s - \frac{1}{2}\right)^6\right], \tag{4.37}$$

which matches Equation (4.29) in the interior of the filament, but predictably leads to a slightly smaller filament deflection from the horizontal plane. The corresponding orientation dynamics are still given by Equation (4.36), but now we have $I_1 = 1/2520$, $I_2 = 1/560$, and $I_3 = 101/50400$, so that $A = 11(c - 369/110)/420$. We still find $A > 0$ in a similar range of body aspect ratios, $\epsilon \lesssim 0.19$. This calculation is not to be confused with that for a filament of uniform thickness, as described in Appendix C. However, the similarity between Equation (4.29) and Equation (4.37) suggests that computing with the assumption $B(s) = 1$ even for a spheroidal body, which avoids the computational issues related to an elastic boundary layer, is reasonable. We therefore choose $B(s) = 1$ for our computations for the remainder of the chapter (and in the previous section).

The body shapes predicted by Equation (4.37) are shown in Figure 4.3(a) as a solid line, from which we see excellent agreement with the results of the numerical simulations (shown as symbols) all the way down to $\beta \approx 0.02$. The maximum deflection of the filament shape is shown in Figure 4.3(b), with the results from the full simulations shown as circles and from the prediction as a solid line, which provides a quantitative measure of the accuracy and breakdown of the simple theory. At the order of our consideration the filament is not inextensible, and as a consequence we observe a systematic overestimation of the numerical results. A simple improvement of the prediction is obtained by rescaling the shape to unit length, as shown by a dashed line in Figure 4.3(b).

For $\beta \lesssim 0.01$, the shapes are no longer self-similar and depart significantly from the expression in Equation (4.37). Viscous stresses associated with the gravitational forcing are now strong enough to overwhelm the elastic stiffness, and a horseshoe-like shape emerges as seen from numerical simulations in Figure 4.2(c). The two ends of the filament approach one another for smaller β, and for $\beta \lesssim 0.001$ the filament can overlap itself unless steric effects are taken into account.

4.3.2 Filament trajectories and particle clouds

We have shown that appreciable changes in the filament shape and orientation are found on the scale over which the filament sediments many body lengths through the fluid. Writing the dynamics from Equation (4.36) in terms of the single time t, the filament rotation rate at leading order is given by

$$\theta_t = \frac{A}{2\beta}\sin(2\theta), \tag{4.38}$$

with $A = 3(c - 7/2)/80$ for $B(s) = 16s^2(1-s)^2$. Integrating Equation (4.38) and setting $\theta(0) = \theta_0$, we find

$$\tan(\theta(t)) = \tan(\theta_0)\exp(At/\beta). \tag{4.39}$$

The filament velocities in the horizontal and vertical directions were previously approximated to $O(1/\beta)$; inserting Equation (4.38) into Equation (4.22), and writing

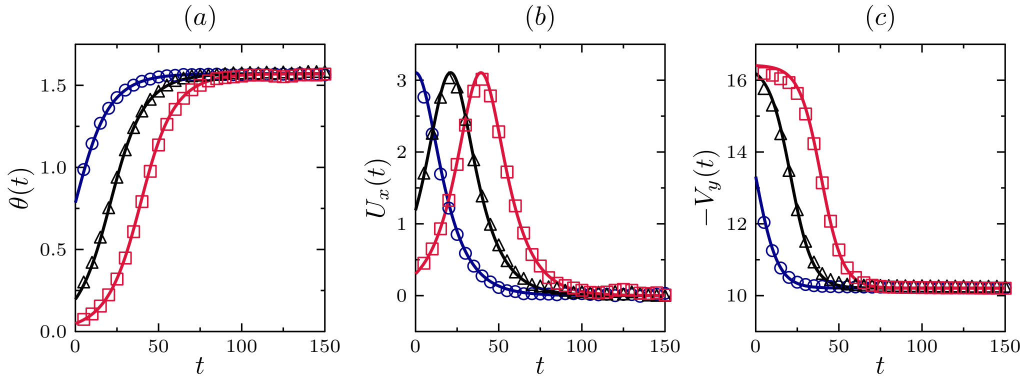

Figure 4.5: Filament orientation and velocity at $\beta = 2$. The initial orientations are $\pi/4$ (○), $\pi/16$ (△) and $\pi/64$ (□). The symbols are from numerical simulations, and solid lines are theoretical predictions for: (*a*) filament orientation $\theta(t)$, (*b*) horizontal filament velocity $U_x(t)$, and (*c*) downward filament velocity $-V_y(t)$.

$\boldsymbol{U}(t) = U_x\hat{\boldsymbol{x}} + V_y\hat{\boldsymbol{y}}$, we find:

$$U_x(t) = \frac{(c-3)\tan(\theta_0)\exp(At/\beta)}{1+\tan^2(\theta_0)\exp(2At/\beta)}, \tag{4.40}$$

$$V_y(t) = -(c+1) - (c-3)\left(\frac{1}{1+\tan^2(\theta_0)\exp(2At/\beta)}\right). \tag{4.41}$$

Integrating the velocities above leads to an approximation of the filament trajectory accurate to $O(1)$. Assuming that the filament is initially centered at the origin, the material point $s = 1/2$ follows the path $(X(t), Y(t))$, where

$$\tan\left(\frac{A}{\beta(c-3)}X(t) + \theta_0\right) = \tan(\theta_0)\exp(At/\beta), \tag{4.42}$$

$$Y(t) = -(c+1)t - \frac{\beta(c-3)}{2A}\ln\left(\frac{(1+\tan^2(\theta_0))\exp(2At/\beta)}{1+\tan^2(\theta_0)\exp(2At/\beta)}\right). \tag{4.43}$$

The full trajectory is described implicitly by the equation

$$\begin{aligned}\tan^\alpha(\theta_0)\sin(\theta_0)\exp\left(-\frac{A}{\beta(c-3)}Y(t)\right) &= \\ \tan^\alpha\left(\frac{A}{\beta(c-3)}X(t)+\theta_0\right)&\sin\left(\frac{A}{\beta(c-3)}X(t)+\theta_0\right),\end{aligned} \tag{4.44}$$

where $\alpha = (c+1)/(c-3) > 1$. In contrast to the constant horizontal velocity of a straight sedimenting rod, the filament drifts horizontally a finite distance (assuming $0 < \theta_0 \leq \pi/2$),

$$X(\infty) = \int_0^\infty U_x(t)\,\mathrm{d}t = \frac{\beta(c-3)}{A}\left(\frac{\pi}{2} - \theta_0\right), \tag{4.45}$$

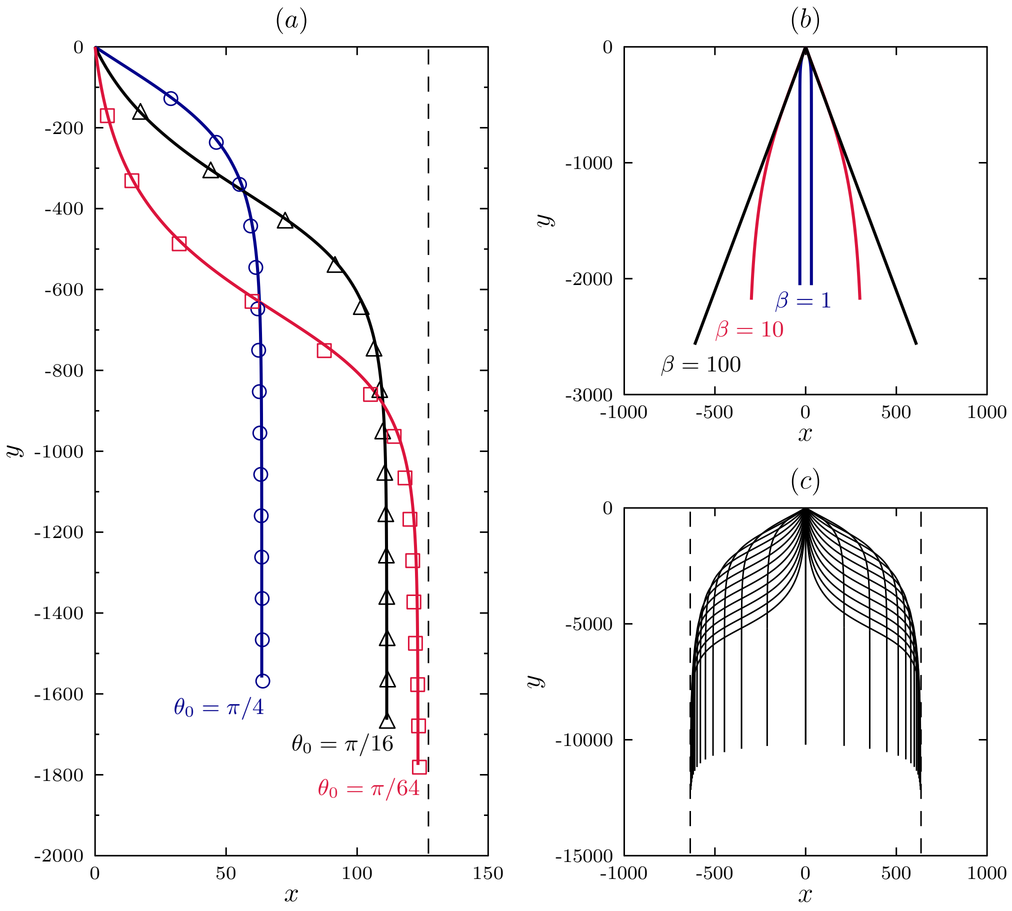

Figure 4.6: Analytical predictions and results from simulations showing the trajectories and cloud spreading of sedimenting flexible filaments. (a) Results from simulations (symbols) and from analytical predictions (solid lines) showing the trajectory of sedimentation of the midpoint of a filament for $\beta = 2$ released with three different initial orientations. The dashed line represents the maximum width of spreading as predicted by Equation (4.45). (b) Predicted trajectories for different values of β when the filament is released at an angle of $\pm\pi/4$. (c) A visualization of the predicted spreading of sedimenting flexible filaments. Here, $\beta = 10$ and the initial angle of release varies in the range $[-\pi/2, \pi/2]$. Also shown is the maximum extent of cloud spreading.

and $X(\infty) = 0$ for $\theta_0 = 0$. The horizontal drift is monotonic in the initial orientation angle on this domain. The maximum drift is given for $\theta_0 \to 0^+$, where $X(\infty) \to \pi\beta(c-3)/2A$. The drift is also monotonic in the elasto-gravitation number in this regime, with larger distances traversed by stiffer filaments, and $X(\infty) \to \infty$ for rigid fibers, $\beta \to \infty$.

The horizontal and vertical velocities and the filament rotation rate following Equations (4.39), (4.40) and (4.41), respectively, are shown in Figure 4.5 for $\beta = 2$ and three different initial orientations. Also shown are numerical results for these parameters that show excellent agreement with the predictions. One can clearly see from the figures that the filament initially drifts increasingly faster in a direction perpendicular to gravity, attaining a maximum horizontal velocity at approximately $\theta = \pi/4$. $U_x(t)$ then decreases to zero, which corresponds to the trajectory in Figure 4.2(a) tending asymptotically to a vertical line. The vertical velocity at this point settles to a constant value of $V_y(t \to \infty) = -(c+1)$, which gives $V_y \approx -10.21$ using $\epsilon = 0.01$ as in the simulations. This value corresponds to the minimum speed of sedimentation in the entire process, corresponding to the drag being maximized in this regime for bodies sedimenting perpendicular to the long filament axis.

The monotonic increase of the span of spreading $X(\infty)$ with both the initial orientation and the elasto-gravitation number suggests interesting trajectories for filaments in this regime. Figure 4.6 shows the trajectories associated with these dynamics. Numerical results for three different initial orientations, all for $\beta = 2$, are shown in Figure 4.6(a) to match excellently with the predicted trajectories. Note again that the maximum width of spreading is attained for $\theta_0 = 0^{\pm}$, and the vertical asymptote of the trajectory approaches this value for small initial orientations. The qualitative difference between weakly flexible filaments and rigid rods is illustrated in Figure 4.6(b). With increasing values of the elasto-gravitation number, the trajectories of filaments placed at the same initial orientation ($\theta_0 = \pm\pi/4$ in this case) approach the $\beta \to \infty$ limit of rigid rods, which sediment without rotating and at an angle that depends only on their initial orientation.

Finally, in Figure 4.6(c), we show how in this regime the lateral spreading of filament trajectories is confined to a cloud whose width is dictated by the elasto-gravitation number. The different trajectories correspond to different initial orientations with initially horizontal filaments sedimenting vertically downwards, and the widest spreading attained, as mentioned above, for $\theta_0 = 0^{\pm}$. Neglecting hydrodynamic interactions between bodies, consider the release of many filaments at the origin, with

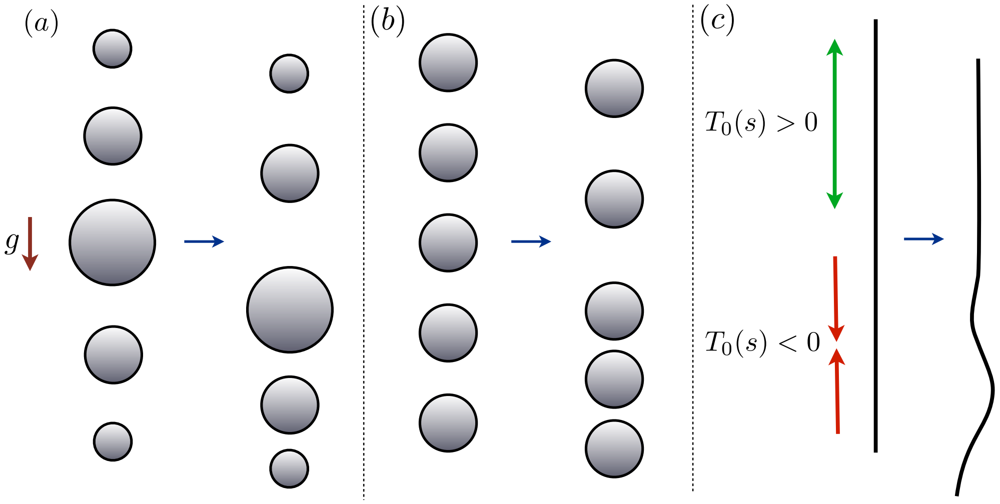

Figure 4.7: Illustration of the source of tension and buckling in model "filaments," as in Figure 4.1. (a) The leading-order effect: larger bodies sediment faster than smaller bodies in a viscous fluid. (b) The secondary effect: the central bodies in a line of identical sedimenting spheres experience a stronger disturbance fluid flow, and will sediment faster than those near the ends. (c) The effects in (a) or (b), along with inextensibility, can lead to buckling of a sedimenting filament.

a probability density function of their orientations given by $\rho(\theta_0)$ on $\theta_0 \in [0, \pi/2]$. Once the bodies have settled into their vertical trajectories, the radial distances from the origin (in the plane perpendicular to gravity) are distributed as $\rho(\theta_0)X(\infty)$. Assuming uniformly distributed filaments, $\rho(\theta_0) = \sin(\theta_0)$, then the radial distribution of the filament cloud as seen in Figure 4.6 is given by $[\beta(c-3)/A]\left(\frac{\pi}{2} - \theta_0\right)\sin(\theta_0)$. Integrating, the mean filament drift is given by $(\pi-2)\beta(c-3)/(2A)$, and the variance by $(\pi-3)\beta^2(c-3)^2/A^2$.

4.4 Buckling of flexible filaments

Our attention now turns to the opposite extreme, the case of extremely flexible filaments for which the elasto-gravitation number is small, $\beta \lll 1$. Of particular interest in this case is the possibility of a dramatic buckling event, which may be exhibited by an elastic body when compressive forces overcome its structural rigidity. Potential sources of a buckling instability in the context of sedimentation are illustrated in Figure 4.7, and are identical to the sources of bending shown in Fig-

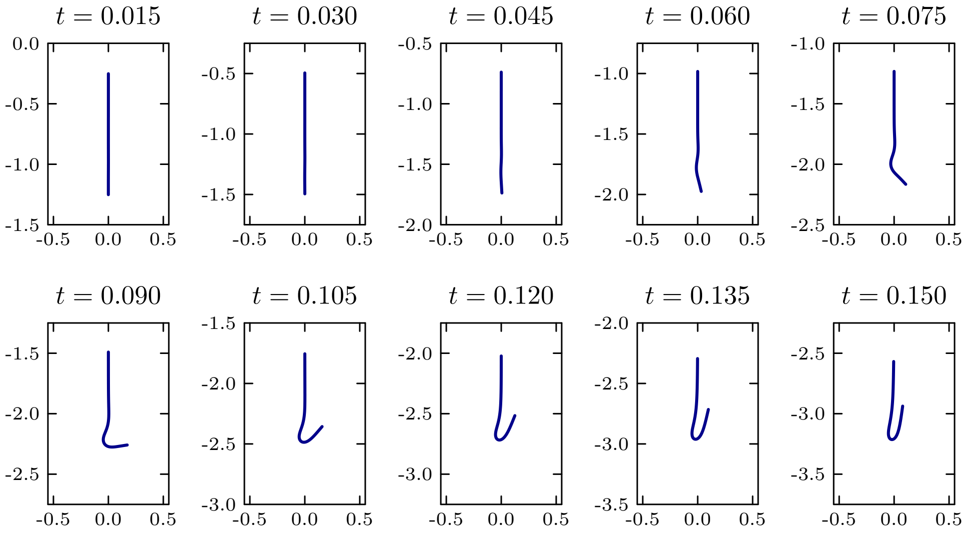

Figure 4.8: Moderate buckling is observed in simulations for $\beta = 10^{-4}$ and $B(s) = 1$. The filament is initially placed with its trailing end at the origin.

ure 4.1. With spheres sedimenting according to their sizes, the array of spheres in Figure 4.7(a) will separate in the top half of the train, and collapse in the bottom half (in the direction of gravity). If the spheres are constrained so that their relative positions are fixed, there will be a positive tension in the top half of the train, and a negative (compressive) tension in the bottom half. This compression can cause a sufficiently flexible filament to buckle, as we show below. It is similarly argued that this source of instability will vanish if the filament density increases monotonically in the direction of gravity.

If the filament is of uniform thickness, the secondary effect from non-local hydrodynamic interactions can also lead to buckling. As illustrated in Figure 4.7(b), the spheres nearer to the center of the train sediment faster than those at the leading and trailing ends. This effect can also lead to buckling of a sufficiently flexible filament. Once again, the leading-order effect is now considered by studying a spheroidal filament shape, and comments on the case $r(s) = 1$ are included in Appendix C.

Choosing the spheroidal filament profile $r(s) = 2\sqrt{s(1-s)}$, so that $c(s) = \ln(1/\epsilon^2)$, and setting $B(s) = 1$ as before, considerable buckling is observed in the full simulations for sufficiently small values of the elasto-gravitation number. Figures 4.8 and 4.9 show time sequences of filaments buckling with $\beta = 10^{-4}$ and $\beta = 6.25 \times 10^{-5}$,

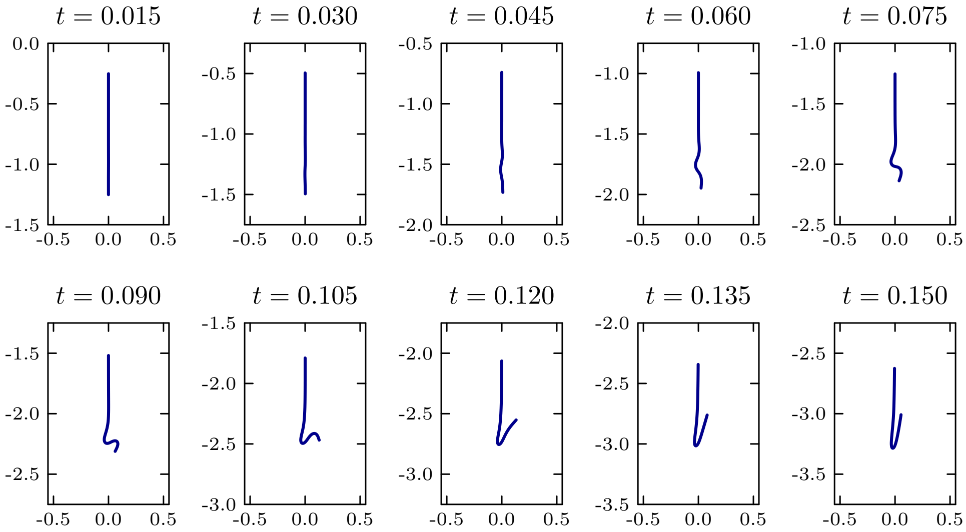

Figure 4.9: Substantial buckling is observed in simulations for $\beta = 6.25 \times 10^{-5}$ and $B(s) = 1$. The filament is initially placed with its trailing end at the origin.

respectively. In both cases, an initial transverse perturbation of $10^{-4}\cos(4\pi s)$ is imposed along the entire filament length and is found to amplify and lead to the observed dynamics. Two points are to be noted here, both of which we analyze in further detail in the following sections. First, it can be seen that the buckling instability only occurs in the leading half of the filament, whereas perturbations are observed to decay in the trailing half. This is consistent with the aforementioned argument that the negative (compressive) tension in the leading half drives this instability. Second, perturbations are found to propagate upward in the form of traveling waves in the body frame, eventually dying out once they reach the trailing half. Beyond the times shown in the figures, the filament undergoes substantial bending where the curvature becomes so large that the linearized Euler-Bernoulli formulation used in our model may no longer accurately describe the filament elastodynamics. Additionally, excluded volume effects are expected to come into play as the filament nears itself in the later stages of buckling, though we do not account for direct steric interactions in our simulations.

4.4.1 Linear stability analysis and buckling criterion

For sufficiently small values of the elasto-gravitation number, there is no timescale separation between elastic relaxation and sedimentation. We recall the fluid force per unit length,

$$\boldsymbol{f}(s) = -(T(s)\boldsymbol{x}_s)_s + \beta(B(s)\boldsymbol{x}_{ss})_{ss} - \boldsymbol{F}_g(s). \tag{4.46}$$

As in the simulations just described, we choose the filament profile $r(s) = 2\sqrt{s(1-s)}$ and the distributed gravitational forcing $\boldsymbol{F}_g(s) = F_g(s)\hat{\boldsymbol{y}} = -6s(1-s)\hat{\boldsymbol{y}}$. Once again we will consider the corresponding bending stiffness profile, $B(s) = r(s)^4$, but we also study the case $B(s) = 1$ for the sake of comparison with the computations.

Consider a straightened filament sedimenting along the $-\hat{\boldsymbol{y}}$ direction, whose centerline position is expressed as $\boldsymbol{x}(s,t) = -(s - 1/2 + Ut)\hat{\boldsymbol{y}}$, with U the constant sedimentation speed. Then Equation (4.8), along with the boundary conditions (4.5), may be written as

$$U = 2(c-1)(T_s - F_g) + 2S[T_s - F_g], \tag{4.47}$$

$$T(0) = T(1) = 0, \tag{4.48}$$

where $S[\cdot]$ is the integral operator defined in Equation (4.10) which is diagonalized under the Legendre polynomial basis as discussed in Section 4.3.1. Therefore, upon multiplication of Equation (4.47) by Legendre polynomials and integrating on $s \in [0,1]$ we see that $T_s(s) - F_g(s) = 1$, and that the sedimentation speed is given by $U = 2(c-1)$. In addition, noting Equation (4.48), we find that the tension along the filament is given by

$$T(s) = T_0(s) = s(1-s)(1-2s). \tag{4.49}$$

We will refer to the straightened filament conformation with sedimentation speed $U = 2(c-1)$ and tension $T_0(s)$ as the base state for the analysis to come. Importantly, due to the spatial variation in the gravitational potential, we observe that the tension in the base state is positive for $s \in (0, 1/2)$, but negative for $s \in (1/2, 1)$. Hence, while the trailing half of the filament experiences a tension, the leading half of the filament (in the direction of sedimentation) experiences a compression. Buckling, therefore, is to be expected in a certain range of β, but in a non-uniform fashion along the filament backbone (see Figures 4.8 and 4.9).

Dynamics of filament perturbations

We now perform a classical linear stability analysis on the filament by perturbing the filament position in a plane perpendicular to gravity. Assume that the filament position is given by

$$\boldsymbol{x}(s,t) = -(s - 1/2 + Ut)\hat{\boldsymbol{y}} + \varepsilon u(s,t)\hat{\boldsymbol{x}} + O(\varepsilon^2), \tag{4.50}$$

with $\varepsilon \ll 1$. By a symmetry argument (taking $\varepsilon \to -\varepsilon$), it is apparent that there can be no variation in the vertical component of the filament velocity (either in the sedimentation speed or varying spatially along the filament), so the speed U in Equation (4.50) is that from the leading-order calculation, $U = 2(c-1)$. Performing a regular expansion of the tension about the base state for small ε, we also write

$$T(s) = T_0(s) + \varepsilon T_1(s) + O(\varepsilon^2), \tag{4.51}$$

where $T_1(0) = T_1(1) = 0$. Note that ε at the outset has no relationship to the body aspect ratio ϵ. Inserting these expansions into the $\hat{\boldsymbol{y}}$ component of the position Equation (4.8), we have

$$0 = 2(c-1)T_1'(s) + 2S[T_1](s), \tag{4.52}$$

from which we see that the tension does not vary at first order in ε: $T_1(s) = 0$. However, upon inspection of the $\hat{\boldsymbol{x}}$ component of the filament position equation, we find an equation for the dynamics of the perturbation,

$$\begin{aligned} u_t = {} & (c+1)[(T_0 u_s)_s - \beta(B(s)u_{ss})_{ss}] + (c-3)u_s \\ & + S\left[(T_0 u_s)_s - \beta(B(s)u_{ss})_{ss} + u_s\right] + P[u], \end{aligned} \tag{4.53}$$

with $P[\cdot]$ defined in Equation (4.10).

The analysis of Equation (4.53) is no longer as simple as an expansion in the Legendre polynomial basis. Instead, we proceed to consider the action of the integral operators on Fourier perturbations of a given high wavenumber k. Specifically, for $k \gg 1$, and for points s sufficiently well removed from the filament endpoints, we have

$$S[\mathrm{e}^{\mathrm{i}ks}] \approx -\ln\left(\mathrm{e}^{2\gamma}k^2 s(1-s)\right)\mathrm{e}^{\mathrm{i}ks}, \tag{4.54}$$

$$P[\mathrm{e}^{\mathrm{i}ks}] \approx 2\mathrm{i}k\mathrm{e}^{\mathrm{i}ks}, \tag{4.55}$$

as shown in Appendix D, where γ is Euler's constant. Hence, for filament perturbations of high wavenumber, the eigenfunctions of $S[\cdot]$ and $P[\cdot]$ are approximately the Fourier basis functions $\mathrm{e}^{\mathrm{i}ks}$. Accordingly, for $k \gg 1$, we may replace $P[u]$ in Equation (4.53) by $2u_s$.

As a first approximation justified in Appendix D, we analyze the dynamics of the perturbation in the two halves $s \in (0, 1/2)$ (where $T_0(s) > 0$) and $s \in (1/2, 1)$ (where $T_0(s) < 0$) as separate and decoupled. We begin by considering the trailing half of the filament, $s \in (0, 1/2)$. While it would be more exhaustive to consider a continuously varying basis for the perturbations, much will be learned by the simpler confinement to a countable Fourier basis. The Fourier transform and inverse transform pair on this interval are given by

$$u(s,t) = \sum_{k=-\infty}^{\infty} \hat{u}_k(t)\mathrm{e}^{4\pi\mathrm{i}ks}, \qquad \hat{u}_k(t) = 2\int_0^{1/2} u(s,t)\mathrm{e}^{-4\pi\mathrm{i}ks}\,\mathrm{d}s. \tag{4.56}$$

We also express $(T_0u_s)_s$ and $(Bu_{ss})_{ss}$ in the Fourier basis,

$$(T_0u_s)_s = \sum_{k=-\infty}^{\infty} a_k\mathrm{e}^{4\pi\mathrm{i}ks}, \qquad (B(s)u_{ss})_{ss} = \sum_{k=-\infty}^{\infty} b_k\mathrm{e}^{4\pi\mathrm{i}ks}. \tag{4.57}$$

Using the base-state tension Equation (4.49), we find

$$a_k = -(\pi k)^2\hat{u}_k + \sum_{m\neq k} \frac{3km(-\mathrm{i} + (m-k)\pi)}{\pi(m-k)^3}\hat{u}_m. \tag{4.58}$$

Also, with $B(s) = 1$ we find

$$b_k = (4\pi k)^4\hat{u}_k, \tag{4.59}$$

or with $B(s) = r(s)^4 = 16s^2(1-s)^2$ we find

$$b_k = 8\left(\frac{1}{15}(4\pi k)^4 - 2\pi\mathrm{i}k\right)\hat{u}_k - \sum_{m\neq k} C(k,m)\hat{u}_m, \tag{4.60}$$

where

$$\begin{aligned} C(k,m) = 128\Bigg[&m^4\left(\frac{3 + 3\mathrm{i}(m-k)\pi + \mathrm{i}(m-k)^3\pi^3}{(m-k)^4}\right) \\ &-3m^2(m+k)\frac{1 + \mathrm{i}(m-k)\pi}{(m-k)^3}\Bigg]. \end{aligned} \tag{4.61}$$

Inserting these expressions into Equation (4.53) returns an equation for the perturbation dynamics in Fourier space,

$$\hat{u}_k'(t) = (c+1)(a_k - \beta b_k) + (c-1)4\pi \mathrm{i} k \hat{u}_k - 2\ln(2\pi k \mathrm{e}^{-(1-\gamma)})(a_k - \beta b_k + 4\pi \mathrm{i} k \hat{u}_k). \tag{4.62}$$

The spatially varying tension and bending stiffness lead to the transmission of energy from each wavelength of u to nearby wavelengths through the coefficients a_k and b_k. However, consider the case that the filament is seeded with a perturbation with a single wavenumber k. For short times, during which the coupling between the Fourier modes can be neglected, we have

$$\hat{u}_k(t) \approx \hat{u}_k(0)\mathrm{e}^{\sigma(k)t}. \tag{4.63}$$

Inserting this ansatz into Equation (4.62) and neglecting coupling terms, we find the growth rate if $B(s) = 1$,

$$\begin{aligned} \sigma(k) &= \left(c - \ln(4(\pi k)^2 \mathrm{e}^{2\gamma-3})\right)\left(-\pi^2 k^2 - \beta(4\pi k)^4\right) + 4\pi \mathrm{i} k (c - \ln(4\pi^2 k^2 \mathrm{e}^{2\gamma-1})) \\ &\approx -\ln\left(\frac{1}{\epsilon^2 k^2}\right)\left(\pi^2 k^2 + \beta(4\pi k)^4 - 4\pi \mathrm{i} k\right), \end{aligned} \tag{4.64}$$

or if $B(s) = 16s^2(1-s)^2$,

$$\begin{aligned} \sigma(k) &= \left(c - \ln(4\pi^2 k^2 \mathrm{e}^{2\gamma-3})\right)\left(-\pi^2 k^2 - \frac{8(4\pi k)^4}{15}\beta + 16\pi \mathrm{i} k \beta\right) \\ &\quad + 4\pi \mathrm{i} k \left(c - \ln\left(4\pi^2 k^2 \mathrm{e}^{2\gamma-1}\right)\right) \\ &\approx -\ln\left(\frac{1}{\epsilon^2 k^2}\right)\left(\pi^2 k^2 + \frac{8}{15}\beta(4\pi k)^4 - 4\pi \mathrm{i} k(1+4\beta)\right), \end{aligned} \tag{4.65}$$

where we have inserted $c = \ln(1/\epsilon^2)$ with ϵ the filament aspect ratio. The growth rate $\sigma(k)$ exhibits rapid damping due to bending rigidity ($\propto -k^4$) as well as damping due to filament tension ($\propto -k^2$). The perturbation is thus expected to return rapidly to its straightened state. The dispersion relation also shows that the perturbation travels as a wave along the filament in the direction opposite gravity with approximate speed $\ln(1/\epsilon^2 k^2)$. The approximation clearly breaks down if the filament aspect ratio is on the order of the perturbation wavelength, $\epsilon k = 1$, so we assume $\epsilon k \ll 1$.

Meanwhile, in the leading half of the filament, $s \in (1/2, 1)$, there is a slight but critical adjustment to the approximations above, as a consequence of the negative

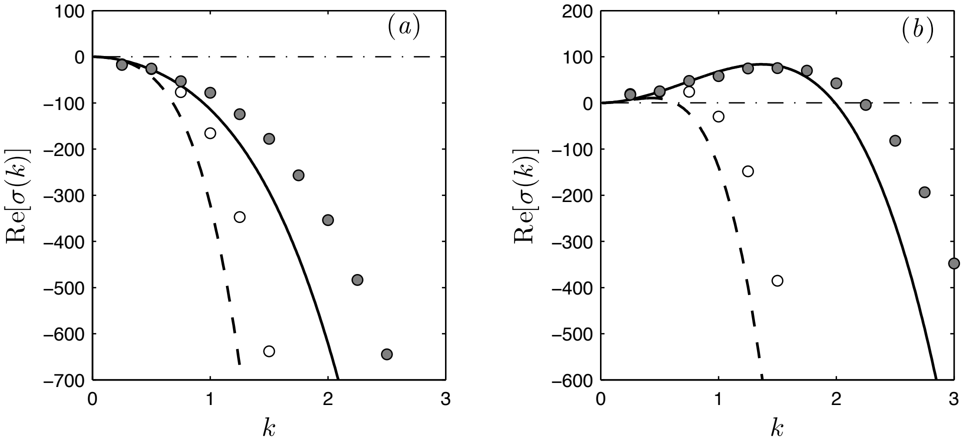

Figure 4.10: Real part of the growth rate $\sigma(k)$, for two different values of β in the (a) trailing and (b) leading halves of the filament. The lines are theoretical predictions and symbols follow from simulations. The solid lines and filled circles correspond to $\beta = 10^{-4}$ while the dashed line and open symbols correspond to $\beta = 10^{-3}$.

tension there. By a similar calculation, we find the short-time growth rates for $B(s) = 1$,

$$\sigma(k) \approx \ln\left(\frac{1}{\epsilon^2 k^2}\right)\left(\pi^2 k^2 - \beta(4\pi k)^4 + 4\pi \mathrm{i} k\right), \tag{4.66}$$

and separately for $B(s) = 16s^2(1-s)^2$,

$$\sigma(k) \approx \ln\left(\frac{1}{\epsilon^2 k^2}\right)\left(\pi^2 k^2 - \frac{8}{15}\beta(4\pi k)^4 + 4\pi \mathrm{i} k(1-4\beta)\right). \tag{4.67}$$

In the leading half, we observe a competition between the effect of tension, which acts to amplify the perturbation exponentially fast, and the effect of bending rigidity, which acts to dampen the system. In the case $B(s) = 16s^2(1-s)^2$, the filament is predicted to buckle for wavenumbers smaller than a critical value, $k^* = \sqrt{15}/(16\pi\sqrt{8\beta})$, and the most unstable wavenumber (corresponding to the largest positive growth rate) is given by $k_m = \sqrt{15/\beta}/(64\pi)$. While arbitrarily small wavenumbers can be supported by a free filament, the critical value of β for which at least one wavelength of buckling can be observed ($k^* = 1/2$) is $\beta^* = 15/(8(8\pi)^2) \approx 0.0030$ in this case. Once again, the growing perturbation travels as a wave in the body frame in the direction opposite gravity, as observed in the numerical simulations of figures 4.8 and 4.9.

To compare the analytical predictions with the full numerical results quantitatively, we perform simulations in which an initially straight and vertically aligned filament is weakly perturbed at a given wavenumber k across its entire length at $t = 0$: $u(s, 0) = 10^{-4}\cos(4\pi ks)$, and we set $B(s) = 1$. The effective growth rates of such perturbations in the linear regime are extracted numerically and are compared to the predictions of the linear analysis in figure 4.10 for two different values of β. In agreement with the theoretical predictions, the trailing half of the filament is always found to be stable to single wavenumber perturbations, while the leading half is unstable over a finite range of wavenumbers where the competition between compressive tension and elasticity is favorable for buckling to occur. The numerical results and theoretical growth rates follow similar trends, though damping is always found to be smaller in the simulations. This systematic shift, which becomes more apparent for larger values of k, may be due to the coupling between the two halves, the coupling between modes, and the filament boundary conditions, which have all been neglected for this first approximation. In particular, to achieve the above estimation the assumption was made that the region of interest is well-separated from the filament endpoints, whereas the instability observed in the simulations is dominant near the leading tip of the filament. Perturbations in the trailing half do indeed decay as predicted, in the form of upward traveling waves.

As discussed earlier and illustrated in Figure 4.7(b), the tension in the leading half of a filament with uniform thickness is also negative in the straightened (base) state, but due instead to non-local hydrodynamic interactions. An approximation of the tension accurate to $O((\ln 1/\epsilon)^{-2})$ for this case is derived in Appendix C.

4.4.2 Linear eigenmodes of the local theory

The growth rate derived above was based on the short-time behavior of a Fourier perturbation of wavenumber k, where we neglected the couplings between wavenumbers and assumed that the stability of the leading and trailing halves of the filament could be analyzed independently. Fourier modes, however, are not exact eigenfunctions of the linearized Equation (4.53), in particular near the filament endpoints, which may explain the quantitative discrepancies we observed between the theoretical and numerical growth rates in Figure 4.10. A different approach which is semi-analytical consists in solving for the exact eigenfunctions of the problem that

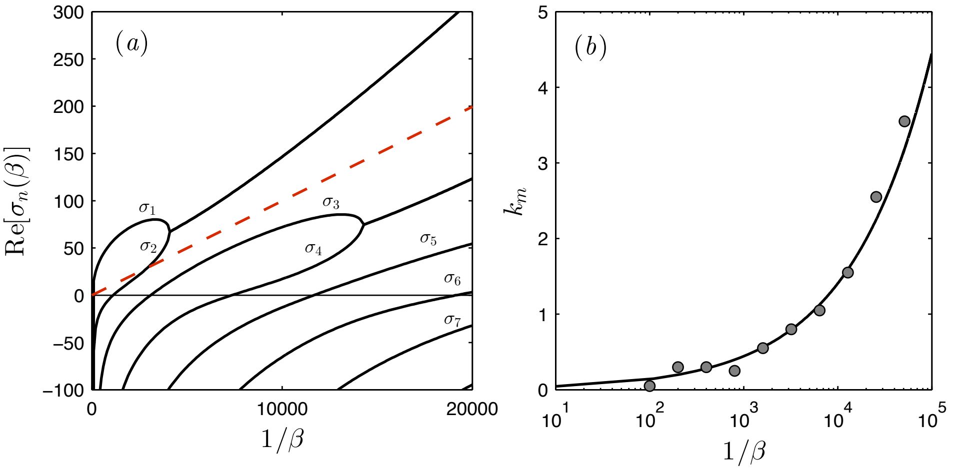

Figure 4.11: Growth rates and wavenumber content from the local theory. (*a*) Real parts of the largest few eigenvalues σ_n as a function of $1/\beta$. Also shown with a dashed line is the maximum growth rate as predicted by the local dispersion relation of Equation (4.66). (*b*) The wavenumber corresponding to the largest discrete Fourier component of the most unstable eigenfunction (circles) compared against the wavenumber with the largest growth rate in the local dispersion relation (solid line).

are valid along the entire length of the filament, as was previously done by Young and Shelley [35] and Guglielmini *et al.* [33] for the buckling of elastic fibers in extensional flows near hyperbolic stagnation points.

We determine numerically the linear eigenmodes of the problem in the case where the non-local contribution is neglected. Keeping only the local contribution in Equation (4.53) and setting $B(s) = 1$ for simplicity, the linearized equation for the amplitude of the shape fluctuations becomes

$$u_t(s,t) = (c+1)[(T_0 u_s)_s - \beta u_{ssss}] + (c-3)u_s, \tag{4.68}$$

with $T_0(s)$ the base-state tension from Equation (4.49). In the linear regime, we seek exponentially growing solutions of the form $u(s,t) = \varphi_n(s)\mathrm{e}^{\sigma_n t}$, where the eigenfunctions $\varphi_n(s)$ satisfy

$$\sigma_n\varphi_n = 2[c-1-3(c+1)s(1-s)](\varphi_n)_s + (c+1)[s(1-s)(1-2s)(\varphi_n)_{ss} - \beta(\varphi_n)_{ssss}]. \tag{4.69}$$

Given that $B(s) = 1$ and that the tension profile vanishes at the ends in the linear regime, the boundary conditions (4.4)–(4.5) simply become

$$\varphi_n''(0) = \varphi_n''(1) = \varphi_n'''(0) = \varphi_n'''(1) = 0. \tag{4.70}$$

Equation (4.69) is an eigenvalue problem for the mode shapes $\varphi_n(s)$, with corresponding eigenvalues σ_n, whose real parts define the growth rates. We solve the equation numerically using a second-order accurate finite-difference discretization, which yields a countable set of eigenfunctions and eigenvalues. The eigenvalues are ordered by decreasing values of the growth rate, $\mathrm{Re}(\sigma_1) \geq \mathrm{Re}(\sigma_2) \geq \ldots$ The largest growth rates, which correspond to the most unstable modes, are plotted as functions of $1/\beta$ in Figure 4.11(a), where we observe that an increasing number of modes become unstable with increasing filament flexibility (decreasing β). Nevertheless, we find that the first mode with eigenvalue σ_1 always remains the most unstable (though it merges with the second mode when $\beta \lesssim 2.5 \times 10^{-4}$ as we discuss below), and the maximum growth rate is found to compare favorably with the results of the Fourier analysis of Section 4.4.1.

The shapes of the eigenmodes are illustrated in Figure 4.12, which shows the two most unstable eigenfunctions $\varphi_1(s)$ and $\varphi_2(s)$ for values of the elasto-gravitation number β in the range $1 \times 10^{-4} - 5 \times 10^{-3}$. Note that in the limit of $\beta \to \infty$ (stiff filaments), the eigenfunctions are simply eigenfunctions of the biharmonic operator, but these lose symmetry with decreasing β as the filament becomes more flexible and hence susceptible to buckling in a nonuniform fashion as we have described. The modal stability in Figure 4.11(a) shows real parts of eigenvalues merging as β decreases: this is seen here as the shapes of eigenfunctions $\varphi_{1,2}$ become identical below $\beta \approx 2.5 \times 10^{-4}$ when the two eigenvalues $\sigma_{1,2}$ become complex conjugates. Additionally, $\varphi_{1,2}$ remains the most unstable buckling mode as β decreases further and more complicated shapes involving higher wavenumbers arise. We see that the eigenvalues for the problem on the whole interval roughly agree with the predicted growth rates from the previous section as a consequence of the most unstable eigenfunction only taking significant values on the leading half of the filament, $s \in (1/2, 1)$. We note a striking similarity between the linearly unstable eigenmodes calculated here for $n = 1, 2$ and the finite-amplitude buckled shapes observed in the nonlinear numerical simulations of Figures 4.8 and 4.9.

The increasing wavenumber content of the unstable eigenfunctions with increasing flexibility is consistent with the widening range of unstable wavenumbers predicted by the Fourier analysis of Section 4.4.1. To compare both results more

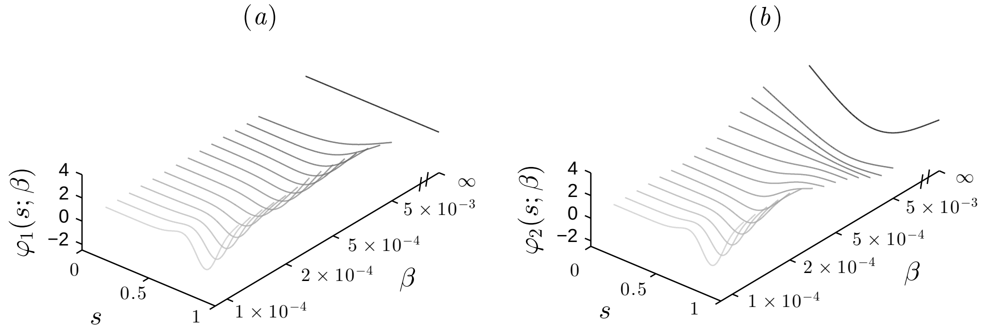

Figure 4.12: Eigenfunctions φ_1 and φ_2 for β in the range $1\times10^{-4} - 5\times10^{-3}$. In the limit of $\beta\to\infty$, the eigenfunctions are biharmonic functions, and the shapes progressively become less symmetric for more flexible filaments. Note that φ_1 and φ_2 become identical below $\beta\approx2.5\times10^{-4}$.

quantitatively, we project the leading half $s\in(1/2,1)$ of $\varphi_1(s)$ onto a discrete Fourier cosine basis $\cos(4\pi ks)$ and compare the wavenumber k_m with the dominant projection to the most unstable wavenumber predicted by the dispersion relation of Section 4.4.1. As shown in Figure 4.11(*b*), both values match closely, which further corroborates the use of a countable Fourier basis for the stability analysis.

4.5 Conclusion

In this chapter, we investigated some of the fundamental dynamics of a single flexible filament as it sediments in a viscous fluid. The competition between elastic forces and viscous forces induced by gravity was characterized by a dimensionless quantity that we termed the elasto-gravitation number, β. We first considered the weakly flexible regime, where the filament is nearly rigid, and using a multiple-scale analysis found a self-similar scaling of the filament shape with an amplitude dependent upon the body orientation. Equilibrium shapes and trajectories were then analyzed in this regime, and we gave predictions for the dynamics of clouds of multiple (non-interacting) filaments. By comparing against full numerical simulations, the analytical predictions were found to be accurate for elasto-gravitation numbers down to $\beta\approx0.01$ in the case of spheroidal filaments with thickness profile $r(s)=2\sqrt{s(1-s)}$. A similar analysis was provided in Appendix C for the shapes, velocities, and rotation rates of filaments with uniform thickness.

We then turned our attention to the buckling of a very flexible filament sedimenting along its long axis, which can occur for sufficiently small elasto-gravitation numbers. While arbitrarily small wavenumbers can be supported by a free-filament, the critical value of β for which one wavelength of buckling can be observed was found to be $\beta^* = 15/(8(8\pi)^2) \approx 0.0030$ in the case of the spheroidal filament with $B(s) = 16s^2(1-s^2)$. Two approaches were taken to study the most unstable wavelength perturbations and their growth rates. In the first approach, we assumed highly oscillatory perturbations so that the non-local integral operator could be handled analytically and the filament endpoints did not play a role. In the second, we solved numerically an eigenvalue problem for the most unstable eigenmodes on the full interval. Both approaches yielded predictions that were in agreement, and matched very closely with the results of full numerical simulations.

Future work might consider the sedimentation of many flexible bodies from experimental, numerical, and analytical perspectives. A step in this direction follows immediately, in Chapter 5. As a final observation, we note that the filament shapes, trajectories, and instabilities studied in this chapter can be interpreted equivalently as those of a positively buoyant flexible filament rising against gravity.

Chapter 4 is based largely on material that has appeared in *Journal of Fluid Mechanics* (2013), authored by Lei Li, Harishankar Manikantan, David Saintillan, and Saverio E. Spagnolie [4].

Chapter 5

Sedimenting suspensions of weakly flexible fibers: Theory

5.1 Introduction

We briefly discussed the effects of shape anisotropy and long ranged hydrodynamics interactions on sedimenting particles in Section 1.2.1. At a suspension level, the dependence of particle velocities on their orientations seriously complicates the dynamics as the disturbance velocity field in the suspension can now reorient particles and hence dramatically affect their trajectories over large length scales. This problem was first studied by Koch and Shaqfeh [125], who modeled a dilute suspension of rigid spheroids using a Smoluchowski equation for the continuous probability field of particle positions and orientations. Perturbing around a spatially homogeneous and orientationally isotropic base-state distribution, they predicted a linear concentration instability in which perturbations with the longest wavelengths are the most unstable. In short, the mechanism is as follows: hydrodynamic interactions cause denser particle clusters to sediment faster than their surroundings, inducing a disturbance field that orients neighboring particles in such a way that they preferentially migrate towards the already dense clusters, thereby amplifying the concentration fluctuations.

The instability predicted by Koch and Shaqfeh has been amply confirmed by experiments on rigid fibers [126, 137, 138] and by numerical simulations with various levels of sophistication [127, 128, 139–142]. More complex theoretical models have also been developed to address issues such as the effects of stratification in finite-sized containers [143], particle alignment under electric fields [144], Brownian fluctuations [145], and fluid inertia [146, 147]. In all cases, the key ingredient remains the lateral migration due to the orientability of the anisotropic particles at the micromechanical level, and a suspension of rigid spheres is indeed stable to concentration fluctuations as elucidated by Koch and Shaqfeh [125] using the same linear stability analysis. Suspensions of isotropic particles, however, can exhibit an instability if the particles are allowed to deform and become anisotropic under flow [127], as in the sedimentation of emulsions [148, 149]. More generally, suspensions of isotropic particles have also been found to be unstable due to other types of nonlinear couplings between the direction of sedimentation of the particles and the local disturbance flow field they induce, for instance due to Marangoni stresses in suspensions of spherical bubbles covered with surfactants [150], or to viscoelastic stresses in suspensions of rigid spheres in non-Newtonian fluids [151].

We have seen in the preceding chapters that when a flexible filament is placed in a flow, the competition between viscous and elastic forces can result in complex deformations and dynamics at the particle level. These, in turn, can drive drastic bulk behavioural changes at the macroscopic level [152]. Of particular relevance within the scope of this chapter is the limit of weak flexibility where the filament departs only slightly from its straightened state. This regime is realized in many physical systems involving stiff polymers, carbon nanotubes, rod-like bacteria or microtubules. While it is a useful and often illustrative simplification to neglect fiber compliance completely in such suspensions [62, 153], even weak flexibility has been shown to change the rheology [154] and phase behaviour [155] of flexible fiber suspensions.

Pertinent to the present context is the fact that a compliant filament breaks the symmetry enjoyed by a rigid rod and is therefore susceptible to an additional coupling between translational and rotational motions. Under sedimentation, this leads to a new mechanism for fiber reorientation and, due to drag anisotropy, to a change in the direction and magnitude of the settling velocity. There is no reason to expect steady and trivial trajectories any more, as was previously illustrated by Xu and Nadim [132] and Cosentino Lagomarsino *et al.* [133] who predicted that flexible fibers should spontaneously align perpendicular to gravity. Such reorientation dynamics and structural deformations were also reported in suspensions of filaments made of superparamagnetic colloids [156] and electrophoretically-driven microtubules [157], the role of gravity in these cases being played by a magnetic and electric field, respectively.

In Chapter 4, we applied slender-body theory and a multiple-scale asymptotic analysis [4] to theoretically describe, and verify using numerical simulations, the reorientation dynamics and shape evolution of a single flexible fiber undergoing sedimentation. In the regime of weak flexibility, we saw that to leading order, a filament translates at the same velocity as a rigid rod:

$$\boldsymbol{u}_s(\boldsymbol{p}) = (\lambda_1 \boldsymbol{I} + \lambda_2 \boldsymbol{pp}) \cdot \frac{\boldsymbol{F}_G}{8\pi\mu L} + O(\beta^{-2}), \tag{5.1}$$

where $\boldsymbol{p}$ is a unit vector tangent to the filament at its center, and μ is the viscosity of the suspending fluid. The filament also reorients as a result of flexibility at an angular velocity given by

$$\dot{\boldsymbol{p}}_s(\boldsymbol{p}) = \frac{F_G}{8\pi\mu L^2} \frac{A}{2\beta} \sin(2\theta)\, \hat{\boldsymbol{\theta}} + O(\beta^{-2}), \tag{5.2}$$

where $\theta = \cos^{-1}(\boldsymbol{p} \cdot \hat{\boldsymbol{z}})$ is the instantaneous angle made by the fiber with gravity and $\hat{\boldsymbol{\theta}}$ is the corresponding polar unit vector in spherical coordinates. The constants λ_1, λ_2 and A are geometric factors given by $c+1$, $c-3$, and $3(c-7/2)/80$, respectively, where $c = \ln(1/\epsilon^2)$ with $\epsilon = a/L$ the particle aspect ratio. Clearly, the changing orientation of the filament affects its speed and direction of sedimentation, leading to non-trivial trajectories. As can be seen from Equation (5.2), the filament tends to align perpendicular to gravity, after which a quasi-steady state is achieved with steady vertical downward translation. The deflection of the filament was also seen in Chapter 4 to reach a maximum value of $L/256\beta$ attained at steady state. For a slender filament of aspect ratio $\epsilon = 0.01$, we find that the maximum deflection is approximately $0.004L$ when $\beta = 1$. This suggests that, to an excellent approximation, a stiff sedimenting filament behaves like a rigid rod with the added dynamics of reorientation and, through it, a non-constant sedimentation velocity. When many such filaments are allowed to interact hydrodynamically in a suspension, we expect the tendency to align horizontally to compete with the rotation of the particles in the disturbance flow they generate, with nontrivial consequences for the stability of the suspension as we analyze in this work.

The chapter is organized as follows. In Section 5.2, we describe a simple model for the sedimentation of a collection of hydrodynamically interacting weakly flexible fibers, and use it to derive a mean-field theory for the evolution of the distribution of particle positions and orientations in a large-scale suspension. As we shall see, this mean-field continuum model admits a steady uniform base state that is anisotropic in orientation space and depends on fiber flexibility. The stability of the system to spatial perturbations around this base state is then analyzed in Section 5.3, where we find that flexibility affects the stability in two distinct ways. On the one hand, the anisotropic base state is shown to render the suspension more unstable as compared to a suspension of rigid rods; on the other hand, reorientation of the weakly-flexible fibers under gravity can act to prevent clustering and stabilize the suspension by competing against rotation in the disturbance flow driven by density fluctuations.

5.2 Theoretical formulation

In this section, we formulate a theoretical model for the dynamics in a suspension of weakly-flexible filaments sedimenting under gravity. We first present a simple micromechanical model for a discrete collection of filaments in Section 5.2.1. This simple model is then used in Section 5.2.2 as the basis for a mean-field continuum theory that extends the model of Koch and Shaqfeh [125] to account for the leading effects of weak flexibility.

5.2.1 Micromechanical model

As rationalized in the discussion of the previous section, we model a dilute suspension of weakly flexible fibers using rigid rod dynamics, with flexibility entering only through an additional component to the rotational velocity. The instantaneous center-of-mass position and orientation of particle α in the suspension are given by $\boldsymbol{x}_\alpha = (x_\alpha, y_\alpha, z_\alpha)$ and $\boldsymbol{p}_\alpha = (\sin\theta_\alpha \cos\varphi_\alpha, \sin\theta_\alpha \sin\varphi_\alpha, \cos\theta_\alpha)$, where $\theta_\alpha \in [0, \pi]$ and $\varphi_\alpha \in [0, 2\pi)$ denote the polar and azimuthal angles on the unit sphere of orientations Ω, respectively. We take gravity to be in the $-\hat{\boldsymbol{z}}$ direction. In a dilute system and in the weakly flexible limit, the center-of-mass velocity of fiber α is modeled as the sum of its settling velocity obtained in Equation (5.1) and of the disturbance velocity $\boldsymbol{u}_d$ induced in the fluid by the motion of the other fibers:

$$\dot{\boldsymbol{x}}_\alpha = \boldsymbol{u}_s(\boldsymbol{p}_\alpha) + \boldsymbol{u}_d(\boldsymbol{x}_\alpha). \tag{5.3}$$

Similarly, its angular velocity also includes contributions from sedimentation and from the disturbance flow:

$$\dot{\boldsymbol{p}}_\alpha = \dot{\boldsymbol{p}}_s(\boldsymbol{p}_\alpha) + \dot{\boldsymbol{p}}_d(\boldsymbol{x}_\alpha, \boldsymbol{p}_\alpha), \tag{5.4}$$

where $\dot{\boldsymbol{p}}_s(\boldsymbol{p}_\alpha)$ is given by Equation (5.2) and accounts for the leading-order effect of flexibility. Recall that each filament is a spheroid. Then, particle reorientation due to the disturbance flow is modeled following Jeffery [102] as

$$\dot{\boldsymbol{p}}_d(\boldsymbol{x}_\alpha, \boldsymbol{p}_\alpha) = (\boldsymbol{I} - \boldsymbol{p}_\alpha \boldsymbol{p}_\alpha) \cdot [\gamma \boldsymbol{E}_d(\boldsymbol{x}_\alpha) + \boldsymbol{W}_d(\boldsymbol{x}_\alpha)] \cdot \boldsymbol{p}_\alpha \tag{5.5}$$

in terms of the disturbance rate-of-strain and rate-of-rotation tensors $\boldsymbol{E}_d = (\boldsymbol{\nabla}_x \boldsymbol{u}_d + \boldsymbol{\nabla}_x \boldsymbol{u}_d^T)/2$ and $\boldsymbol{W}_d = (\boldsymbol{\nabla}_x \boldsymbol{u}_d - \boldsymbol{\nabla}_x \boldsymbol{u}_d^T)/2$, respectively, having chosen the convention that $(\boldsymbol{\nabla}_x \boldsymbol{u})_{ij} = \partial u_i / \partial x_j$. In Equation (5.5), $\gamma = (1 - 4\epsilon^2)/(1 + 4\epsilon^2)$ is a measure of particle anisotropy, and we take $\gamma \approx 1$ in this work, corresponding to the limit of very slender fibers. It should be noted that Equations (5.3)–(5.5) technically describe the motion of a fiber in a linear flow field. They are expected to hold in dilute suspensions where spatial variations of the disturbance field occur on length scales much greater than the particle dimensions, and could be corrected to account for small-scale velocity fluctuations using more general Faxén relations for spheroidal particles in arbitrary flows [60].

Integration of Equations (5.3)–(5.4) requires knowledge of the disturbance velocity induced in the fluid by the other particles. This disturbance velocity arises from the net gravitational force on each fiber, which is transmitted to the fluid. In the dilute limit and to leading order, the velocity experienced by particle α therefore solves the forced Stokes equations

$$-\mu \nabla_x^2 \boldsymbol{u}_d + \boldsymbol{\nabla}_x q_d = \boldsymbol{F}_G \sum_{\beta \neq \alpha} \delta(\boldsymbol{x} - \boldsymbol{x}_\beta), \quad \boldsymbol{\nabla}_x \cdot \boldsymbol{u}_d = 0. \tag{5.6}$$

Here, $\delta(\boldsymbol{x})$ is the three-dimensional Dirac delta function, $q_d(\boldsymbol{x})$ is the disturbance pressure field set up by the flow, and we have assumed that the viscosity of the fluid is unaffected by the particles. Equation (5.6) also implicitly assumes that particles are widely separated so that the effects of higher force moments on the particles are negligible compared to the flow induced by the net gravitational force. In the limit of rigid rods ($\beta \rightarrow \infty$ and $\dot{\boldsymbol{p}}_s \rightarrow \mathbf{0}$), the model posed here is identical to that used by Mackaplow and Shaqfeh [158] in their discrete particle simulations.

5.2.2 Mean-field theory

Following Koch and Shaqfeh [125], we now introduce a continuum mean-field theory based on the micromechanical model described above. Rather than tracking the motions of individual fibers, we describe the configuration of the suspension in terms of the probability distribution function $\Psi(\boldsymbol{x}, \boldsymbol{p}, t)$ of finding a particle at position $\boldsymbol{x}$ with orientation $\boldsymbol{p}$ at time t. The distribution function is normalized as

$$\frac{1}{V} \int_V \int_\Omega \Psi(\boldsymbol{x}, \boldsymbol{p}, t) \, \mathrm{d}\boldsymbol{p} \, \mathrm{d}\boldsymbol{x} = n, \tag{5.7}$$

where V is the volume of the suspension and n the mean number density. Conservation of particles is expressed by the Smoluchowski equation [122]

$$\frac{\partial \Psi}{\partial t} + \boldsymbol{\nabla}_x \cdot (\dot{\boldsymbol{x}} \Psi) + \boldsymbol{\nabla}_p \cdot (\dot{\boldsymbol{p}} \Psi) - \boldsymbol{\nabla}_x \cdot (\boldsymbol{D} \cdot \boldsymbol{\nabla}_x \Psi) - \boldsymbol{\nabla}_p \cdot (d \, \boldsymbol{\nabla}_p \Psi) = 0, \tag{5.8}$$

where differential operators with a subscript x act on spatial coordinates while those with a subscript p act on the sphere of orientations:

$$\boldsymbol{\nabla}_p \equiv (\boldsymbol{I} - \boldsymbol{p}\boldsymbol{p}) \cdot \frac{\partial}{\partial \boldsymbol{p}} = \hat{\boldsymbol{\theta}} \frac{\partial}{\partial \theta} + \frac{\hat{\boldsymbol{\varphi}}}{\sin \theta} \frac{\partial}{\partial \varphi}. \tag{5.9}$$

In Equation (5.8), $\dot{\boldsymbol{x}}$ and $\dot{\boldsymbol{p}}$ denote the translational and rotational flux velocities. Based on the discussion of Section 5.2.1, these include contributions from sedimentation and from the disturbance flow field $\boldsymbol{u}_d$ in the suspension:

$$\dot{\boldsymbol{x}} = \boldsymbol{u}_s(\boldsymbol{p}) + \boldsymbol{u}_d(\boldsymbol{x}), \tag{5.10}$$

$$\dot{\boldsymbol{p}} = \dot{\boldsymbol{p}}_s(\boldsymbol{p}) + \dot{\boldsymbol{p}}_d(\boldsymbol{x}, \boldsymbol{p}), \tag{5.11}$$

where $\boldsymbol{u}_s(\boldsymbol{p})$ and $\dot{\boldsymbol{p}}_s(\boldsymbol{p})$ were defined in Equations (5.1) and (5.2), respectively, and where $\dot{\boldsymbol{p}}_d(\boldsymbol{x}, \boldsymbol{p})$ is related to $\boldsymbol{u}_d(\boldsymbol{x})$ through Jeffery's equation (5.5). Equation (5.8) also accounts for translational and rotational diffusion with constant diffusivities $\boldsymbol{D}$

and d. In this work, we assume that these diffusivities arise primarily from Brownian motion and can be related via the Stokes-Einstein relation [122] to the translational and rotational mobilities of the particles obtained from slender-body theory:

$$\boldsymbol{D} = \frac{k_B T}{8\pi\mu L}(\lambda_1 \boldsymbol{I} + \lambda_2 \boldsymbol{pp}), \quad d = \frac{k_B T \lambda_3}{8\pi\mu L^3}, \tag{5.12}$$

where $\lambda_3 = 12(c-1)$, and $k_B T$ is the thermal energy unit. More sophisticated models may be used for these diffusivities in the case of non-Brownian suspensions, where their origin is hydrodynamic rather than thermal [159, 160].

The above system is closed with a description of the mean-field disturbance velocity $\boldsymbol{u}_d(\boldsymbol{x})$. In the continuum limit, the forced Stokes equations (5.6) become

$$-\mu\nabla_x^2 \boldsymbol{u}_d + \boldsymbol{\nabla}_x q_d = \boldsymbol{F}_G\, c(\boldsymbol{x}, t), \quad \boldsymbol{\nabla}_x \cdot \boldsymbol{u}_d = 0, \tag{5.13}$$

where $c(\boldsymbol{x}, t)$ denotes the local concentration of particles and is obtained from the distribution function as

$$c(\boldsymbol{x}, t) = \int_\Omega \Psi(\boldsymbol{x}, \boldsymbol{p}, t)\, \mathrm{d}\boldsymbol{p}. \tag{5.14}$$

The flow is driven by the forcing term on the right-hand side of the momentum equation, which can be interpreted as a body force acting on the fluid that is everywhere proportional to the local weight of the suspension. In the limit of rigid rods ($\beta \to \infty$ and $\dot{\boldsymbol{p}}_s \to \boldsymbol{0}$) and in the absence of diffusion ($\boldsymbol{D} = \boldsymbol{0}$ and $d = 0$), this continuum model reduces to the original model of Koch and Shaqfeh [125] for a non-Brownian suspension of sedimenting rigid rods.

5.2.3 Homogeneous base-state distribution

We first seek a steady and spatially homogeneous solution $\Psi(\boldsymbol{x}, \boldsymbol{p}, t) = n\,\Psi_0(\boldsymbol{p})$ of the mean-field model in an infinite domain, which will serve as the base-state distribution for the linear stability analysis of Section 5.3. In this case, the body force in the Stokes equations (5.13) reduces to $n\boldsymbol{F}_G$, with an obvious solution given by

$$\boldsymbol{u}_d(\boldsymbol{x}) = \boldsymbol{0}, \quad q_d(\boldsymbol{x}) = -nF_G z + q_d^0. \tag{5.15}$$

Therefore, in the absence of concentration fluctuations, the disturbance flow is zero and a hydrostatic pressure gradient balances the buoyant weight of the suspension.

In this case, the Smoluchowski equation (5.8) simplifies to

$$\boldsymbol{\nabla}_p \cdot (\dot{\boldsymbol{p}}_s \varPsi_0) = d\,\nabla_p^2 \varPsi_0, \tag{5.16}$$

expressing the balance of reorientation due to flexibility and rotational diffusion. We expect the base state to only depend on the inclination θ of the particles from $\hat{\boldsymbol{z}}$. This allows us to solve for $\varPsi_0$ exactly as

$$\varPsi_0(\theta) = m_0 \exp\left[-\frac{AF_G^2 L^3}{4k_B T \lambda_3 \kappa}\cos 2\theta\right], \tag{5.17}$$

where m_0 is a normalization constant, with $m_0 = (4\pi)^{-1}$ for an isotropic orientation distribution. Let us introduce the gravitational Péclet number Pe, or ratio of the gravitational potential to the thermal energy:

$$Pe = \frac{F_G L}{k_B T}. \tag{5.18}$$

The base-state distribution (5.17) can then be rewritten as

$$\varPsi_0(\theta) = \frac{1}{2\pi}\frac{\mathrm{e}^{-2\eta\cos^2\theta}}{\displaystyle\int_{-1}^{1}\mathrm{e}^{-2\eta u^2}\,\mathrm{d}u}, \tag{5.19}$$

where we have defined $\eta = APe/4\lambda_3\beta$.

As illustrated in Figure 5.1, any amount of flexibility causes the fibers to preferentially align in the plane normal to the direction of gravity, and this tendency strengthens in the limits of weak rotational diffusion (large Pe) and of increasing flexibility (small β, although we recall that the micromechanical model is technically valid for $\beta \gtrsim 1$). Two limits of interest can be noted: if $\eta \ll 1$ the distribution is isotropic ($\varPsi_0(\theta) \to (4\pi)^{-1}$), while if $\eta \gg 1$ all the filaments assume nearly horizontal orientations ($\varPsi_0(\theta) \to \delta(\theta - \pi/2)/2\pi$). In the following, we shall explore the regime where $\eta \gtrsim O(1)$, and frequently return to the case of small η for comparison with the already established results for an isotropic suspension [125].

5.3 Linear stability

5.3.1 Eigenvalue problem

We now perturb the system about the base-state distribution as $\varPsi(\boldsymbol{x}, \boldsymbol{p}, t) = n[\varPsi_0(\theta) + \varepsilon\psi'(\boldsymbol{x}, \boldsymbol{p}, t)]$, with $|\varepsilon| \ll 1$ and $|\psi'| \sim O(1)$. This weak perturbation in

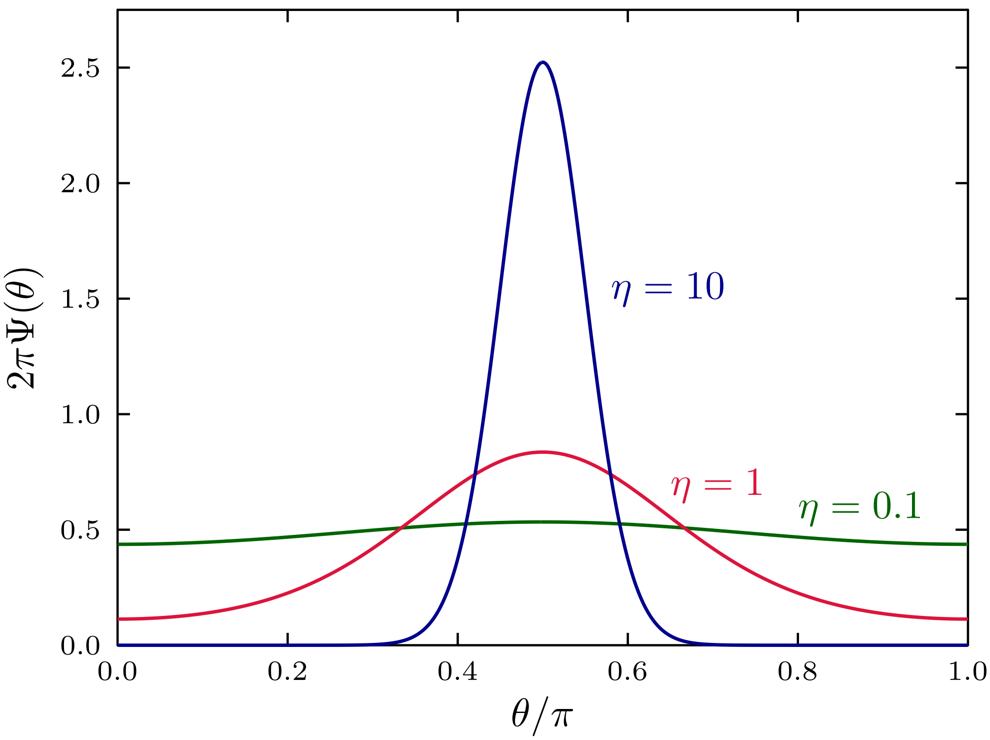

Figure 5.1: The anisotropic base-state orientation distribution $\Psi_0(\theta)$ for different values of $\eta = APe/4\lambda_3\beta$. Flexibility causes particles to preferentially align in directions perpendicular to gravity.

concentration leads to a weak disturbance velocity and an associated angular velocity: $\boldsymbol{u}_d = \varepsilon \boldsymbol{u}'_d$ and $\dot{\boldsymbol{p}}_d = \varepsilon \dot{\boldsymbol{p}}'_d$. Substituting these along with the base state (5.19) into the conservation equation (5.8) and collecting terms of $O(\varepsilon)$, we obtain:

$$\begin{aligned}\frac{\partial \psi'}{\partial t} + \boldsymbol{\nabla}_x \psi' \cdot \boldsymbol{u}_s + \boldsymbol{\nabla}_p \Psi_0 \cdot \dot{\boldsymbol{p}}'_d + \Psi_0\, \boldsymbol{\nabla}_p \cdot \dot{\boldsymbol{p}}'_d \\ + \boldsymbol{\nabla}_p \psi' \cdot \dot{\boldsymbol{p}}_s + \psi' \boldsymbol{\nabla}_p \cdot \dot{\boldsymbol{p}}_s - \boldsymbol{\nabla}_x \cdot (\boldsymbol{D} \cdot \boldsymbol{\nabla}_x \psi') - d\, \nabla_p^2 \psi' = 0.\end{aligned} \tag{5.20}$$

To proceed, we impose Fourier modes with wavevector $\boldsymbol{k}$ and complex frequency $\omega = \omega_R + \mathrm{i}\omega_I$ on the perturbed quantities, e.g., $\psi'(\boldsymbol{x}, \boldsymbol{p}, t) = \tilde{\psi}(\boldsymbol{k}, \boldsymbol{p}, \omega) \exp[\mathrm{i}(\boldsymbol{k} \cdot \boldsymbol{x} - \omega t)]$. In doing so, we have assumed that the fluid occupies all space. In real systems, this could be the case if the container is large enough that walls have negligible effects on the dynamics of the suspension. The disturbance velocity and angular velocity then accomodate similar normal modes due to the linearity of the Stokes equations.

Following Hasimoto [161], we know the velocity from (5.13) in Fourier space as:

$$\tilde{\boldsymbol{u}}(\boldsymbol{k},\boldsymbol{p},\omega) = \frac{n}{\mu k^2}(\boldsymbol{\mathsf{I}} - \hat{\boldsymbol{k}}\hat{\boldsymbol{k}})\boldsymbol{\cdot}\boldsymbol{F}_G\,\tilde{c}(\boldsymbol{k},\omega), \tag{5.21}$$

with $\hat{\boldsymbol{k}} = \boldsymbol{k}/k$ and $k = |\boldsymbol{k}|$. Here, correspondingly, $c(\boldsymbol{x},t) = n[1+\varepsilon c'(\boldsymbol{x},t)]$ and $c'(\boldsymbol{x},t) = \tilde{c}(\boldsymbol{k},\omega)\exp[\mathrm{i}(\boldsymbol{k}\boldsymbol{\cdot}\boldsymbol{x} - \omega t)]$, so that $\tilde{c} = \int_{\Omega}\tilde{\psi}\,\mathrm{d}\boldsymbol{p}$. Then, using Jeffery's equation (5.5), we find the Fourier coefficients of the angular velocity and its orientational divergence:

$$\tilde{\dot{\boldsymbol{p}}}(\boldsymbol{k},\boldsymbol{p},\omega) = \mathrm{i}\frac{n}{\mu k^2}(\boldsymbol{p}\boldsymbol{\cdot}\boldsymbol{k})(\boldsymbol{\mathsf{I}} - \boldsymbol{p}\boldsymbol{p})\boldsymbol{\cdot}(\boldsymbol{\mathsf{I}} - \hat{\boldsymbol{k}}\hat{\boldsymbol{k}})\boldsymbol{\cdot}\boldsymbol{F}_G\,\tilde{c}(\boldsymbol{k},\omega), \tag{5.22}$$

$$\boldsymbol{\nabla}_p\boldsymbol{\cdot}\tilde{\dot{\boldsymbol{p}}}(\boldsymbol{k},\boldsymbol{p},\omega) = -3\,\mathrm{i}\frac{n}{\mu k^2}(\boldsymbol{p}\boldsymbol{\cdot}\boldsymbol{k})\boldsymbol{p}\boldsymbol{\cdot}(\boldsymbol{\mathsf{I}} - \hat{\boldsymbol{k}}\hat{\boldsymbol{k}})\boldsymbol{\cdot}\boldsymbol{F}_G\,\tilde{c}(\boldsymbol{k},\omega). \tag{5.23}$$

Using $\boldsymbol{F}_G = -F_G\hat{\boldsymbol{z}}$ and the Fourier coefficients obtained in (5.21)–(5.23), the linearized conservation equation (5.20) simplifies to

$$\begin{aligned}(-\mathrm{i}\omega + \mathrm{i}\boldsymbol{k}\boldsymbol{\cdot}\boldsymbol{u}_s + \boldsymbol{\nabla}_p\boldsymbol{\cdot}\dot{\boldsymbol{p}}_s + \boldsymbol{k}\boldsymbol{\cdot}\boldsymbol{\mathsf{D}}\boldsymbol{\cdot}\boldsymbol{k})\tilde{\psi} - d\nabla_p^2\tilde{\psi} + \dot{\boldsymbol{p}}_s\boldsymbol{\cdot}\boldsymbol{\nabla}_p\tilde{\psi}\\ +\mathrm{i}\frac{nF_G}{\mu k^2}[3\,\Psi_0(\boldsymbol{p}\boldsymbol{\cdot}\boldsymbol{k})\boldsymbol{p}\boldsymbol{\cdot}(\boldsymbol{\mathsf{I}} - \hat{\boldsymbol{k}}\hat{\boldsymbol{k}})\boldsymbol{\cdot}\hat{\boldsymbol{z}} - (\boldsymbol{p}\boldsymbol{\cdot}\boldsymbol{k})\boldsymbol{\nabla}_p\Psi_0\boldsymbol{\cdot}(\boldsymbol{\mathsf{I}} - \boldsymbol{p}\boldsymbol{p})\boldsymbol{\cdot}(\boldsymbol{\mathsf{I}} - \hat{\boldsymbol{k}}\hat{\boldsymbol{k}})\boldsymbol{\cdot}\hat{\boldsymbol{z}}]\,\tilde{c} = 0.\end{aligned} \tag{5.24}$$

For simplicity, we assume that $\hat{\boldsymbol{k}}\boldsymbol{\cdot}\hat{\boldsymbol{z}} = 0$ as horizontal waves are known to be the most unstable in the case of rigid rods [125]. Equations (5.1) and (5.2) can be inserted for $\boldsymbol{u}_s$ and $\dot{\boldsymbol{p}}_s$. After scaling lengths by the filament length L and time by the sedimentation timescale $8\pi\mu L^2/F_G$, we recast the above equation as

$$\begin{aligned}\left\{-\mathrm{i}\omega - \mathrm{i}\boldsymbol{k}\boldsymbol{\cdot}(\lambda_1\boldsymbol{\mathsf{I}} + \lambda_2\boldsymbol{p}\boldsymbol{p})\boldsymbol{\cdot}\hat{\boldsymbol{z}} + A\beta^{-1}(3\cos^2\theta - 1) + Pe^{-1}\left[\lambda_1 k^2 + \lambda_2(\boldsymbol{p}\boldsymbol{\cdot}\boldsymbol{k})^2\right]\right\}\tilde{\psi}\\ -\lambda_3 Pe^{-1}\nabla_p^2\tilde{\psi} + \frac{A}{2}\beta^{-1}\sin 2\theta\frac{\partial\tilde{\psi}}{\partial\theta} + \mathrm{i}\mathcal{F}\,\tilde{c} = 0.\end{aligned} \tag{5.25}$$

Here, $\mathcal{F}$ is a scalar function defined as:

$$\begin{aligned}\mathcal{F} &= \frac{\mathcal{N}}{k^2}\left[3\,\Psi_0(\boldsymbol{p}\boldsymbol{\cdot}\boldsymbol{k})(\boldsymbol{p}\boldsymbol{\cdot}\hat{\boldsymbol{z}}) - (\boldsymbol{p}\boldsymbol{\cdot}\boldsymbol{k})\boldsymbol{\nabla}_p\Psi_0\boldsymbol{\cdot}(\boldsymbol{\mathsf{I}} - \boldsymbol{p}\boldsymbol{p})\boldsymbol{\cdot}\hat{\boldsymbol{z}}\right] &(5.26)\\ &= -\frac{\mathcal{N}}{k^2}\boldsymbol{\nabla}_p\boldsymbol{\cdot}\left[\Psi_0(\boldsymbol{p}\boldsymbol{\cdot}\boldsymbol{k})(\boldsymbol{\mathsf{I}} - \boldsymbol{p}\boldsymbol{p})\boldsymbol{\cdot}\hat{\boldsymbol{z}}\right], &(5.27)\end{aligned}$$

where $\mathcal{N} = 8\pi nL^3$ can be interpreted as an effective volume fraction. As previously noted by Koch and Shaqfeh [125], the only intrinsic length scale of the problem at

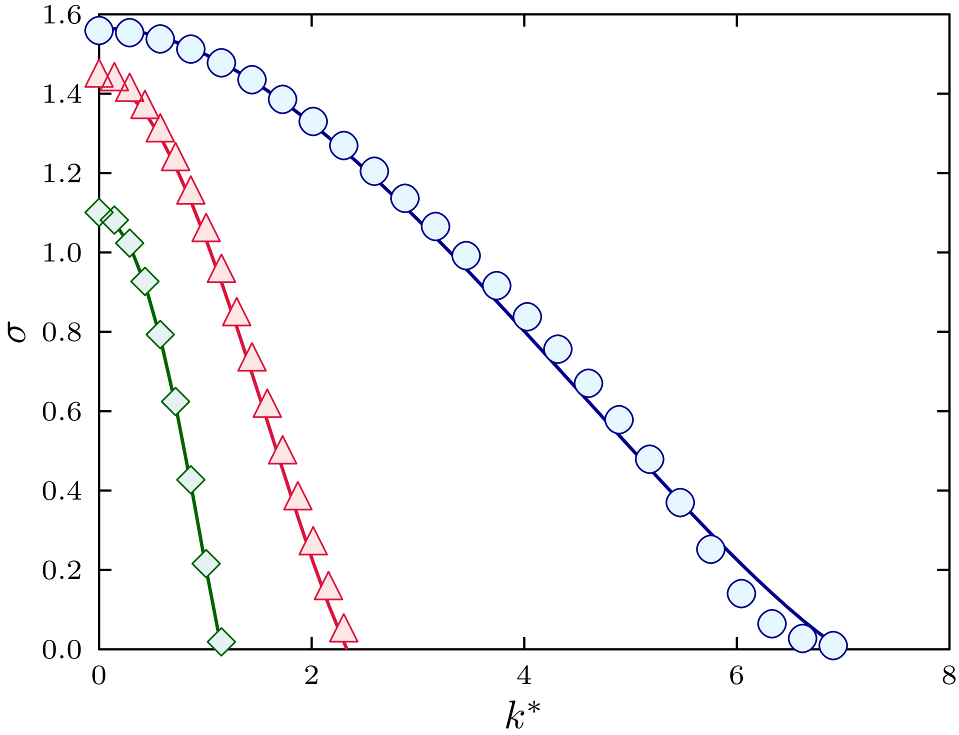

Figure 5.2: Spectral solution of the growth rate, σ, as a function of the horizontal perturbation wavenumber k^*. Here, $Pe = 10^6$ and $\beta = 1000(\diamond)$, $100(\triangle)$, and $10(\circ)$. The solid lines show the theoretical predictions of Equation (5.44) for the base-state-driven instability for corresponding values of η, demonstrating that the leading effect of flexibility on the stability occurs primarily through the anisotropy of the base-state orientation distribution.

the suspension level is $(nL)^{-1/2}$. For the mean-field description used here to be valid, this length scale should be much greater than the particle size L, which implies that $nL^3 \ll 1$, consistent with the assumption of a dilute suspension. Another restriction arises from the use of Equations (5.3) and (5.4) for the particle motions, which assume that the disturbance velocity field varies smoothly on the scale of the fibers. This condition limits the validity of the above model to Fourier perturbations such that $k^{-1} \gg L$.

Equation (5.25) is an eigenvalue problem for the complex frequency ω, with corresponding eigenfunctions given by $\tilde{\psi}$. In the limit of rigid rods and negligible Brownian motion ($\beta, Pe \to \infty$ with $\eta \to 0$), it reduces to the eigenvalue problem previously obtained and solved by Koch and Shaqfeh [125]. It is interesting to note that flexibility and Brownian motion alter the problem in several distinct ways. First, they both have a direct influence through the terms involving β^{-1} and Pe^{-1} in Equation (5.25), which capture rotation away from the direction of gravity as a result of flexibility and diffusive processes, respectively. In addition, they also both affect the base-state orientation distribution $\Psi_0(\theta)$ appearing in the function $\mathcal{F}$ through the parameter $\eta = APe/4\lambda_3\beta$ setting the degree of anisotropy as previously explained in Section 5.2.3. As we shall show below, the direct and indirect effects of β and Pe are subtle and have nontrivial consequences for the stability. Before analyzing successively the roles played by base-state anisotropy, flexibility and diffusion, we first discuss the full numerical solution of the eigenvalue problem (5.25) using a spectral method.

5.3.2 Spectral solution

Noting that Equation (5.25) is an eigenvalue problem of the form $\mathcal{L}[\tilde{\Psi}] = \mathrm{i}\omega\tilde{\Psi}$, where $\mathcal{L}$ is a linear integro-differential operator, we first seek a spectral solution for the eigenvalues ω by projecting the eigenmodes $\tilde{\psi}$ on the basis of spherical harmonics as detailed in Appendix E. The eigenvalue ω with the largest imaginary part ω_I decides the stability of the system. In Figure 5.2, we plot the normalized growth rate $\sigma = \omega_I/\omega_m$ against the normalized wavenumber $k^* = k/k_m$ for different values of Pe and β. Here, the variables ω_m and k_m are, respectively, the zero-wavenumber growth rate and zero-growth-rate wavenumber for an isotropic suspension as in Saintillan *et al.* [143], and we shall asymptotically rederive them in Section 5.3.3. As shown previously by Hoffman and Shaqfeh [145] and confirmed by our numerical experiments, the leading effect of Brownian motion is to stabilize the system. Therefore, we first focus on the regime where Pe is large and hence the effects of diffusion are weak.

The impact of flexibility in this case is clearly shown in Figure 5.2. Here and in all spectral calculations shown below, we use the value of $\mathcal{N} = 1$ for the effective volume fraction. In the limit of stiff rods, obtained by letting $\beta \to \infty$ for finite Pe (and therefore $\eta \to 0$), the solution tends to the benchmark case previously analyzed by Koch and Shaqfeh [125] and Saintillan *et al.* [143], with a maximum growth rate of $\sigma = 1$ reached for $k^* = 0$. As the filaments become more flexible (i.e., as β decreases),

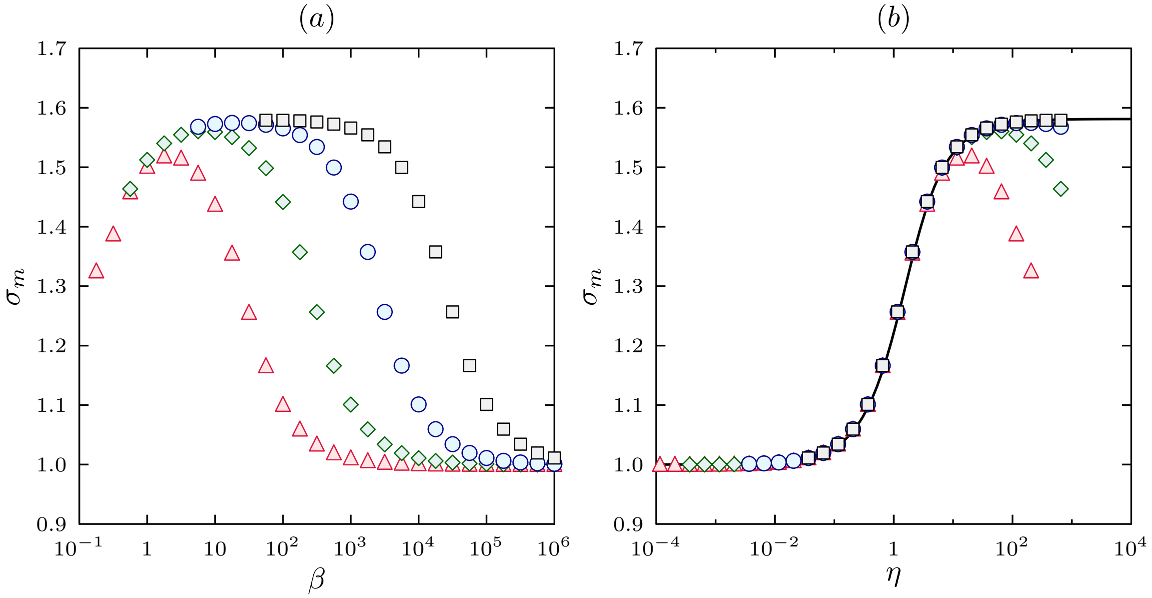

Figure 5.3: Zero-wavenumber (maximum) growth rate of the instability obtained from the spectral solution. (a) Normalized growth rate at zero wavenumber for $Pe = 10^8(\square)$, $10^7(\circ)$, $10^6(\diamond)$, and $10^5(\triangle)$. All cases asymptote to the isotropic rigid rod limit as $\beta \to \infty$. (b) Same data scaled according to the parameter $\eta = APe/4\lambda_3\beta$, with the predicted maximum growth rate (5.41) for the base-state-driven instability shown in a solid line.

both the range of unstable wavenumbers and the highest growth rate are observed to increase. In other words, we find that filament flexibility further destabilizes the perturbed suspension. Recall however that β cannot be arbitrarily small as Equation (5.2) for the angular velocity is valid only in the weakly flexible regime of $\beta \gtrsim 1$. Interestingly, the destabilization with decreasing β is found to be primarily the consequence of the indirect effect of flexibility on the anisotropy of the base state through Equation (5.17), as the spectral solution to the full dispersion relation compares very well with an approximation (shown by the full lines in Figure 5.2) that ignores the independent effects of Brownian motion and flexibility and only accounts for their contribution to the base state. This peculiar point and the physical mechanism for this base-state-driven destabilization will be addressed more precisely in Section 5.3.3.

We look more closely at the dependence of the maximum growth rate σ_m on β and Pe in Figure 5.3(a), still focusing on the regime where the independent effect of Brownian motion is weak ($Pe \gtrsim 10^4$). The case of an isotropic suspension of rigid rods is recovered by letting $\beta \to \infty$ for all considered values of the Péclet number, as illustrated by a unique asymptote in the limit of large β. While all four curves for different values of Pe show similar shapes in this limit, we observe quite interestingly that the asymptote is approached faster with respect to β when the Péclet number is large. More precisely, an increase by a decade in Pe causes the range of β where the asymptote is approached to decrease by a decade, suggesting a self-similar dependence of the largest growth rate on Pe/β. This is confirmed in Figure 5.3(b) showing the zero-wavenumber growth rates plotted vs η, where the values for all Pe and β collapse onto a single curve in the low-η range. This dependence on η, rather than on β and Pe independently, confirms that the dominant effect is that of the base state, and indeed we find that the self-similar curve matches an analytical prediction derived in Section 5.3.3 by neglecting the independent effects of flexibility and diffusion. As η exceeds unity, self-similarity is no longer observed, and Figure 5.3(b) shows an eventual stabilization with decreasing β (or increasing η for a fixed Pe), presumably as a result of the independent effect of flexibility that competes against particle alignment by the flow and therefore hinders the growth of fluctuations.

5.3.3 Effect of the base state

As demonstrated by the full spectral solution in Section 5.3.2, both flexibility and Brownian motion primarily impact the stability by controlling the degree of anisotropy of the base state, and it is this effect that we further analyze here. The original instability mechanism proposed by Koch and Shaqfeh [125] for an isotropic suspension of rigid rods is illustrated in Figure 5.4(a). The key point is that a plane wave perturbation in the number density sets up a vertical shear flow that causes neighboring particles to reorient so that they sediment preferentially towards the regions of higher concentration, thereby bolstering the initial density fluctuation. This is a direct consequence of the shape anisotropy of the particles and of their ability to orient in the disturbance flow. This effect was further illustrated by Saintillan *et al.* [143], who considered an anisotropic base state given by an Onsager distribution. In contrast with the current work, they considered a distribution with a preferred orientation parallel to the direction of gravity, and found that the weak horizontal

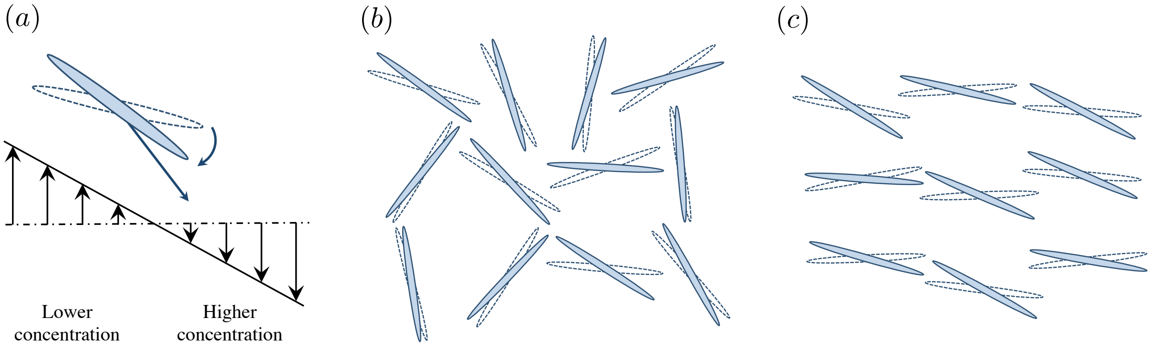

Figure 5.4: The mechanism for growth of concentration fluctuations and the effect of base-state anisotropy. (*a*) Instability mechanism proposed by Koch and Shaqfeh [125]: the vertical shear flow set up by a horizontal density wave reorients particles such that they migrate preferentially towards high-concentration regions. (*b*) Effect of the vertical shear flow on an isotropic distribution: after a weak rotation, the distribution remains nearly isotropic, with only a weak net lateral migration towards the right. Empty shapes depict initial orientations in the base state, while filled ones represent orientations after rotation in the disturbance flow for a short duration. (*c*) Effect of the vertical shear flow on a strongly anisotropic orientation distribution: the weak rotation by the flow causes a large fraction of fibers to migrate towards the right, suggesting that base-state anisotropy can have a destabilizing effect on the suspension.

drift of the nearly vertical fibers led to a decrease in the growth rate of the instability. However, as illustrated in figures 5.4(*b*)–(*c*), the base state in the present study favors the direction perpendicular to gravity when $\eta > 0$, and this configuration increases the probability for a fiber to migrate toward the denser regions after a weak rotation by the disturbance flow. Thus, we expect the anisotropy of the base state to enhance the concentration instability in this case.

We restrict our attention here to the regime where both Brownian motion and filament flexibility are weak, i.e., $Pe^{-1} \ll 1$ and $\beta^{-1} \ll 1$. Notice that in the limiting case, we require for a well-defined base state that both Pe and β tend to infinity at the same speed so that η remains finite but arbitrary. Then, the leading-order terms in Equation (5.25) for the eigenfunctions $\tilde{\psi} = \tilde{\psi}_0 + O(\beta^{-1}, Pe^{-1})$ and eigenvalues $\omega = \omega_0 + O(\beta^{-1}, Pe^{-1})$ become

$$\tilde{\psi}_0 = \frac{\mathcal{F}\,\tilde{c}_0}{\omega_0 + \lambda_2(\boldsymbol{p}\cdot\boldsymbol{k})(\boldsymbol{p}\cdot\hat{\boldsymbol{z}})}, \tag{5.28}$$

where $\mathcal{F}$ is defined in Equations (5.26)–(5.27) and involves the base state Ψ_0. Integrating over all orientations and simplifying by $\tilde{c}_0$ yields

$$\int_\Omega \frac{\mathcal{F}}{\omega_0 + \lambda_2(\boldsymbol{p}\cdot\boldsymbol{k})(\boldsymbol{p}\cdot\hat{\boldsymbol{z}})}\,\mathrm{d}\boldsymbol{p} = 1, \tag{5.29}$$

which is a dispersion relation for $\omega_0(k)$. Note that both flexibility and Brownian motion only enter this dispersion relation through the ratio of β and Pe appearing in the base state. In neglecting Pe^{-1} and β^{-1} in the governing equation, we have assumed that the correct order has been maintained with respect to the magnitude of perturbation in the linearized equation (5.20).

The isotropic base state

Before delving into the general case of the anisotropic base state from Equation (5.17), we first revisit the limit of perfectly rigid rods ($\beta^{-1} = 0$) in the absence of thermal diffusion ($Pe^{-1} = 0$). This isotropic limit, formally reached by letting $\eta \to 0$ in Equation (5.29), was previously explored by Koch and Shaqfeh [125], Saintillan *et al.* [143] and Hoffman and Shaqfeh [145] and will provide us with a reference point to compare the effects of flexibility and Brownian motion with. In this case, the base state is simply $\Psi_0 = (4\pi)^{-1}$, and the dispersion relation (5.29) simplifies to

$$\frac{3\mathcal{N}}{4\pi k^2}\int_\Omega \frac{(\boldsymbol{p}\cdot\boldsymbol{k})(\boldsymbol{p}\cdot\hat{\boldsymbol{z}})}{\omega_0 + \lambda_2(\boldsymbol{p}\cdot\boldsymbol{k})(\boldsymbol{p}\cdot\hat{\boldsymbol{z}})}\,\mathrm{d}\boldsymbol{p} = 1. \tag{5.30}$$

A numerical solution for $\omega_0(k)$ was first obtained by Koch and Shaqfeh [125] and showed that the growth rate is maximum at $k = 0$ and decays monotonically with increasing wavenumber to reach zero at a critical wavenumber k_m, defining the marginal stability limit and indicating the range of unstable wavenumbers. Clearly, setting $\omega_0 = 0$ in Equation (5.30) gives $k_m = \sqrt{3\mathcal{N}/\lambda_2}$. An approximation to $\omega_0(k)$ in the limit of small wavenumber can also be obtained by expanding Equation (5.30) with error $O(k^4)$,

$$\begin{split}\frac{3\mathcal{N}}{4\pi\omega_0 k^2}\int_\Omega (\boldsymbol{p}\cdot\boldsymbol{k})(\boldsymbol{p}\cdot\hat{\boldsymbol{z}})\Bigg[1 - \frac{\lambda_2}{\omega_0}(\boldsymbol{p}\cdot\boldsymbol{k})(\boldsymbol{p}\cdot\hat{\boldsymbol{z}}) + \frac{\lambda_2^2}{\omega_0^2}(\boldsymbol{p}\cdot\boldsymbol{k})^2(\boldsymbol{p}\cdot\hat{\boldsymbol{z}})^2 \\ -\frac{\lambda_2^3}{\omega_0^3}(\boldsymbol{p}\cdot\boldsymbol{k})^3(\boldsymbol{p}\cdot\hat{\boldsymbol{z}})^3 + O(k^4)\Bigg]\,\mathrm{d}\boldsymbol{p} = 1.\end{split} \tag{5.31}$$

Now, recall that $\boldsymbol{p} = (\sin\theta\cos\varphi, \sin\theta\sin\varphi, \cos\theta)$ and that we have assumed a plane wave perturbation in a direction perpendicular to gravity. In this case, the only dependence on the azimuthal angle φ comes from $\boldsymbol{p}\cdot\hat{\boldsymbol{k}} = \sin\theta\cos\varphi$. Noting that

$$\int_0^{2\pi} (\boldsymbol{p}\cdot\hat{\boldsymbol{k}})^2 \mathrm{d}\varphi = \pi\sin^2\theta, \tag{5.32a}$$

$$\int_0^{2\pi} (\boldsymbol{p}\cdot\hat{\boldsymbol{k}})^4 \mathrm{d}\varphi = \frac{3\pi}{4}\sin^4\theta, \tag{5.32b}$$

$$\int_0^{2\pi} (\boldsymbol{p}\cdot\hat{\boldsymbol{k}})^{2m+1} \mathrm{d}\varphi = 0, \tag{5.32c}$$

for all $m \in \mathbb{Z}$, it follows that all terms in odd powers of k are zero in Equation (5.31), which becomes

$$\omega_0^2 = -\frac{3\mathcal{N}\lambda_2}{4}\int_{-1}^{1} u^2(1-u^2)\,\mathrm{d}u - \frac{9\mathcal{N}\lambda_2^3 k^2}{16\,\omega_0^2}\int_{-1}^{1} u^4(1-u^2)^2\,\mathrm{d}u + O(k^4), \tag{5.33}$$

and can be simplified to

$$\omega_0^2 = -\frac{\mathcal{N}\lambda_2}{5} + \frac{\mathcal{N}\lambda_2^2 k^2}{7} + O(k^4). \tag{5.34}$$

This readily provides the zero-wavenumber growth rate as $\omega_0 = \pm\mathrm{i}\omega_m = \pm\mathrm{i}\sqrt{\mathcal{N}\lambda_2/5}$. Henceforth, we use $k^* = k/k_m$ and $\sigma = \omega_I/\omega_m$ as the scaled wavenumber and scaled imaginary part of the complex frequency (or growth rate), respectively. We also restrict our attention to positive solutions for the growth rate as only these drive the instability. The solution (5.34) for ω_0 can be recast with this new scaling as:

$$\sigma = 1 - \frac{15}{14}k^{*2} + O(k^{*4}). \tag{5.35}$$

The perfectly-aligned base state

Another interesting limiting case is realized when $\eta \gg 1$, corresponding to a base state where the filaments are perfectly aligned in directions perpendicular to gravity. We have seen than any amount of flexibility introduces a rotational velocity that favors such an alignment, so this situation is relevant to the case of negligible diffusion ($Pe \to \infty$). The limiting base state is then readily shown to be $\varPsi_0(\theta) = \delta(\theta - \pi/2)/2\pi$, where δ is the one-dimensional Dirac delta function. Inserting $\varPsi_0$ into Equation (5.26) for $\mathcal{F}$ and using the property of the Dirac delta function that

$$(\boldsymbol{I} - \boldsymbol{pp})\cdot\hat{\boldsymbol{z}}\cdot\boldsymbol{\nabla}_p\delta = (\boldsymbol{I} - \boldsymbol{pp})\cdot\hat{\boldsymbol{z}}\cdot\hat{\boldsymbol{\theta}}\;\delta' = -\sin\theta\;\delta' \tag{5.36}$$

where $\delta' = \mathrm{d}\delta/\mathrm{d}\theta$, we rewrite the dispersion relation (5.29) as

$$\frac{2\pi k^2}{\mathcal{N}} = \int_{\varphi=0}^{2\pi} \int_{\theta=0}^{\pi} \frac{k \sin^3\theta \cos\varphi \; \delta'(\theta - \pi/2)}{\omega_0 + \lambda_2 k \sin\theta \cos\theta \cos\varphi} \, \mathrm{d}\theta \mathrm{d}\varphi. \tag{5.37}$$

The integrals are easily performed after an integration by parts with respect to θ, allowing us to evaluate the complex frequency as

$$\omega_0(k) = \pm \mathrm{i} \sqrt{\frac{\mathcal{N}\lambda_2}{2}} = \pm \mathrm{i}\sqrt{5/2}\, \omega_m, \tag{5.38}$$

which, surprisingly, is independent of k. In other words, the growth rate in the perfectly aligned case exceeds the maximum growth rate in the isotropic case by a factor of $\sqrt{5/2}$ regardless of the value of the wavenumber k. This supports our initial speculation schematically illustrated in Figure 5.4(*b*)–(*c*) that the preferred base orientation of the fibers towards the horizontal plane due to flexibility reinforces their tendency to drift horizontally in response to a density wave perturbation, thereby feeding in to the growth of the instability.

The general anisotropic base state

We now analyze the dispersion relation (5.29) for the general anisotropic base state found in Equation (5.17), written under the current non-dimensionalization as $\Psi_0(\theta) = m_0 \exp\left[-\eta \cos(2\theta)\right]$, where we recall that $\eta = APe/4\lambda_3\beta$. The degree of anisotropy is set by the value of η, and the two limits $\eta \to 0$ (isotropic base state) and $\eta \to \infty$ (perfectly aligned base state) have already been examined. First, we insert Equation (5.27) into Equation (5.29) and note the following divergence theorem for a vector field $\boldsymbol{w}$ in orientational space Ω, as derived in Appendix F:

$$\int_{\Omega} \boldsymbol{\nabla}_p \cdot \boldsymbol{w} \, \mathrm{d}\boldsymbol{p} = 2 \int_{\Omega} \boldsymbol{p} \cdot \boldsymbol{w} \, \mathrm{d}\boldsymbol{p}. \tag{5.39}$$

The integrand can then be expanded for $k \to 0$, and once again terms involving odd powers of k contain odd functions of the azimuthal angle φ and do not contribute. We find

$$\frac{\omega_0^2}{\mathcal{N}\lambda_2} = -\int_{\Omega} \Psi_0 (\boldsymbol{p}\cdot\hat{\boldsymbol{k}})^2 \left[1 - (\boldsymbol{p}\cdot\hat{\boldsymbol{z}})^2\right] \left[1 + \frac{3\lambda_2^2 k^2}{\omega_0^2} (\boldsymbol{p}\cdot\hat{\boldsymbol{k}})^2 (\boldsymbol{p}\cdot\hat{\boldsymbol{z}})^2\right] \mathrm{d}\boldsymbol{p} + O(k^4). \tag{5.40}$$

Using the change of variables $u = \boldsymbol{p}\cdot\hat{\boldsymbol{z}} = \cos\theta$, the above integrals can be evaluated analytically. After normalizing the imaginary part of the eigenvalue by ω_m and the wavenumber by k_m, we obtain the following expansion for the growth rate in the long-wave limit:

$$\sigma(\eta) = \sqrt{\frac{5}{2}} J_1^{1/2} - \frac{27\sqrt{10}}{8} \frac{J_2}{J_1^{3/2}} k^{*2} + O(k^{*4}), \tag{5.41}$$

where $J_1(\eta)$ and $J_2(\eta)$ denote the following functions:

$$J_1(\eta) = \frac{\displaystyle\int_{-1}^{1} \mathrm{e}^{-2\eta u^2}(1-u^2)(1-2u^2)\,\mathrm{d}u}{\displaystyle\int_{-1}^{1} \mathrm{e}^{-2\eta u^2}\,\mathrm{d}u} = \frac{2\eta - 3}{2\sqrt{2\pi\eta^3}} \frac{\mathrm{e}^{-2\eta}}{\mathrm{erf}(\sqrt{2\eta})} + \frac{8\eta^2 - 6\eta + 3}{8\eta^2}, \tag{5.42}$$

and

$$\begin{aligned} J_2(\eta) &= \frac{\displaystyle\int_{-1}^{1} \mathrm{e}^{-2\eta u^2} u^2 (1-u^2)^2(1-2u^2)\,\mathrm{d}u}{\displaystyle\int_{-1}^{1} \mathrm{e}^{-2\eta u^2}\,\mathrm{d}u} \\ &= \frac{8\eta^2 - 10\eta + 105}{32\sqrt{2\pi\eta^7}} \frac{\mathrm{e}^{-2\eta}}{\mathrm{erf}(\sqrt{2\eta})} + \frac{32\eta^3 - 96\eta^2 + 150\eta - 105}{128\eta^2}. \end{aligned} \tag{5.43}$$

In the limit of $\eta \to 0$, we expect to retrieve the results from our discussion of the isotropic base state. Indeed, we find that $J_1(0) = 2/5$ and $J_2(0) = 8/315$, which reduces Equation (5.41) to (5.35). On the other hand, the limit of $\eta \to \infty$ corresponds to the perfectly aligned base state, and here we have $J_1(\infty) = 1$ and $J_2(\infty) = 0$ recovering Equation (5.38). The monotonic behavior of $J_1(\eta)$ further suggests that the maximum growth rate $\sigma_m(\eta) = \sigma(\eta; k = 0)$ is bounded between 1 as $\eta \to 0$ as we expect from the isotropic case and $\sqrt{5/2}$ as $\eta \to \infty$ as predicted earlier for the perfectly aligned case. The $O(k^{*2})$ correction to σ in Equation (5.41) captures the change in the growth rate as we depart from the long-wave limit. As $\eta \to 0$, this correction asymptotes to $-15/14$ as predicted by Equation (5.35). Further, it approaches zero for large η, consistent with the prediction of Equation (5.38) that the growth rate in the perfectly aligned case takes the constant value of $\sqrt{5/2}$ independent of wavenumber.

The zero-wavenumber growth rate $\sigma_m = \sigma(\eta; k = 0)$ following (5.41) is plotted in figure 5.5(*b*) and is overlaid upon the full spectral solution data in figure

5.3(b), where we see that for $\beta \gg 1$ the effects of Brownian motion and flexibility occur almost exclusively through their influence on the base state, rather than through the terms of order Pe^{-1} and β^{-1} in (5.25) which were neglected when deriving Equation (5.41) above. Therefore, the instability is predominantly affected by the anisotropy of the base state in this regime. The departure from the above prediction as seen in figure 5.3(b) for large values of η is the result of these terms coming into play, and this suppressive effect of diffusion and flexibility will be considered in Section 5.3.4.

The dependence of the zero-growth-rate wavenumber on η may be calculated by seeking the value of k for which $\omega_0 = 0$. For this, we use Equation (5.26) and note that $\boldsymbol{\nabla}_p \varPsi_0 = -4u\eta\varPsi_0(\boldsymbol{I} - \boldsymbol{pp})\cdot\hat{\boldsymbol{z}}$ to rewrite the dispersion relation (5.29) as

$$\frac{\mathcal{N}}{k^2}\int_{\varOmega} \frac{\varPsi(\boldsymbol{p}\cdot\boldsymbol{k})(\boldsymbol{p}\cdot\hat{\boldsymbol{z}})[3+4\eta(1-(\boldsymbol{p}\cdot\hat{\boldsymbol{z}})^2)]}{\omega_0 + \lambda_2(\boldsymbol{p}\cdot\boldsymbol{k})(\boldsymbol{p}\cdot\hat{\boldsymbol{z}})}\,\mathrm{d}\boldsymbol{p} = 1. \tag{5.44}$$

Letting $\omega_0 = 0$, this simplifies to

$$\frac{k^2\lambda_2}{\mathcal{N}} = 3 + 4\eta\,\frac{\displaystyle\int_{-1}^{1} \mathrm{e}^{-2\eta u^2}(1-u^2)\,\mathrm{d}u}{\displaystyle\int_{-1}^{1} \mathrm{e}^{-2\eta u^2}\,\mathrm{d}u}, \tag{5.45}$$

where the case of $\eta = 0$ yields the value of k_m obtained previously in the isotropic case. The integrals can be evaluated, and after scaling by k_m we express the zero-growth-rate wavenumber as

$$k_m^*(\eta) = \left[1 + \frac{4}{3}\sqrt{\frac{\eta}{2\pi}}\frac{\mathrm{e}^{-2\eta}}{\operatorname{erf}(\sqrt{2\eta})} + \frac{4\eta-1}{3}\right]^{1/2}. \tag{5.46}$$

The range of unstable wavenumbers is shown in figure 5.5(c), and is found to grow without bound as $\sqrt{\eta}$ for large η (which, at a fixed value of the Péclet number, corresponds to increasing elastic flexibility of the filament backbones). Of course, we recall that values of η are limited by the underlying assumptions of the micromechanical model in Section 5.2.1, which is only valid for relatively stiff filaments ($\beta \gtrsim 1$). Another limitation also exists on the value of k^{-1}, which must be much greater that the particle length: under the present non-dimensionalization, this restricts the validity of the solution to $k^* \lesssim \sqrt{\lambda_2/3\mathcal{N}}$.

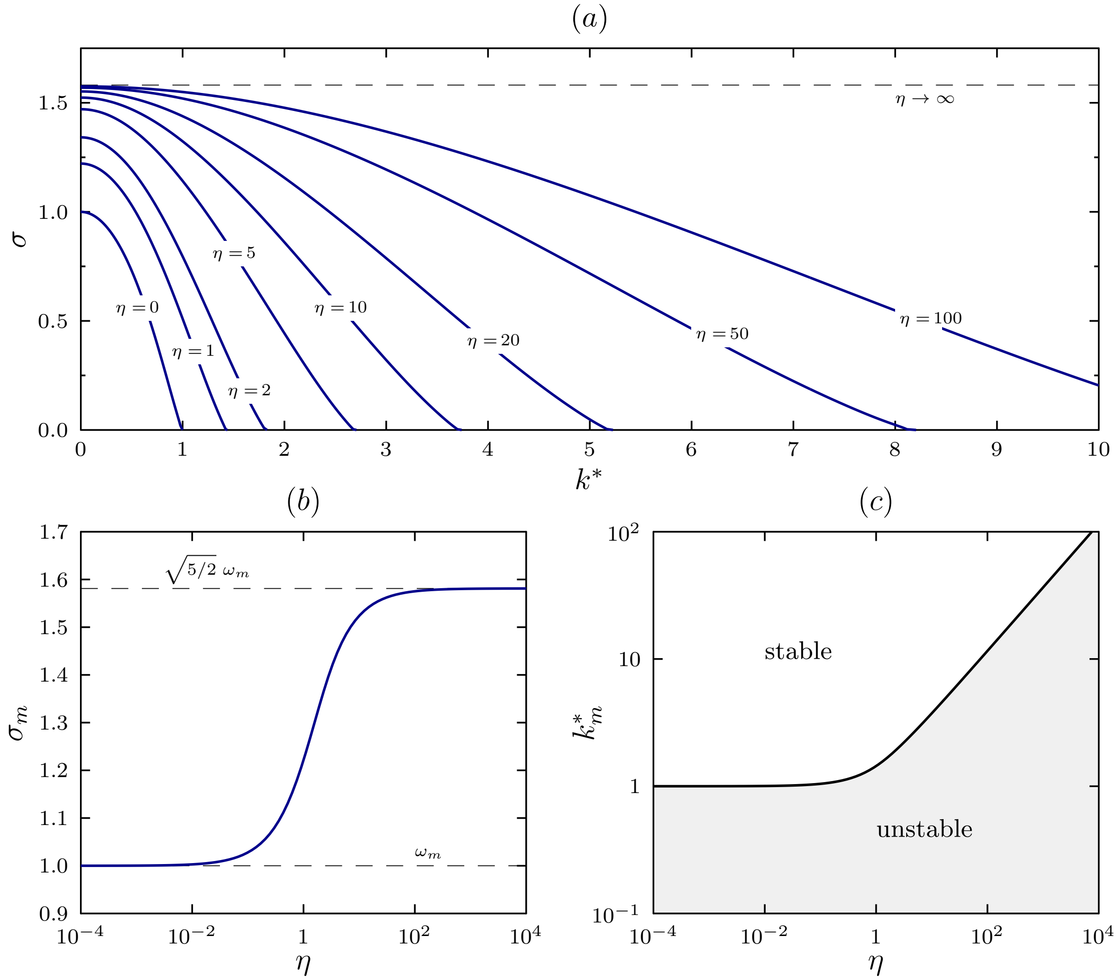

Figure 5.5: Numerical solution of the dispersion relation for various values of η, showing the effects of base-state anisotropy. The limiting case $\eta = 0$ corresponds to the isotropic base state discussed, whereas $\eta \to \infty$ corresponds to the perfectly-aligned base state. Also shown are the zero-wavenumber (maximum) growth rate as a function of η following Equation (5.41), and the range of unstable wavenumbers as a function of η following Equation (5.46).

A full solution to the dispersion relation (5.29) for arbitrary k cannot be obtained analytically. However, we solve it numerically using an end-corrected trapezoidal quadrature and a secant method to find the roots, and the solution $\omega_0(k)$ is shown for different values of η in Figure 5.5(a). In agreement with the previous analyses, we recover the case of isotropically oriented rigid rods as $\eta \to 0$, whereas increasing η causes both the range of unstable wavenumbers and the value of the growth rate to increase. In the limit of $\eta \to \infty$, the solution asymptotes to the constant value of $\sigma = \sqrt{5/2}$ for a perfectly aligned suspension.

5.3.4 Direct effect of flexibility and Brownian motion

We now turn our attention to the direct effect of flexibility and Brownian motion through the terms of order β^{-1} and Pe^{-1} in the eigenvalue problem (5.25), which were previously neglected in the discussion of Section 5.3.3. Hoffman and Shaqfeh [145] previously analyzed the effect of Brownian motion in the case of rigid rods, and found that it stabilizes the suspension by randomizing orientations. On the other hand, flexibility causes reorientation perpendicular to gravity. This reorientation competes against alignment by the disturbance flow and is now expected to suppress the instability. This is indeed observed in the spectral solution presented in figure 5.6: for a given value of η (i.e., for a given base-state distribution), we found that increasing flexibility causes a decrease in the maximum growth rate below the prediction of Equation (5.44) for the base-state effect, as a result of the independent contribution of the $O(\beta^{-1})$ terms in the linearized equation (5.25).

It is useful to remember that for a fixed value of η, specifying either Pe or β implicitly defines the other. This suggests that the terms capturing the direct effects of Brownian motion and flexibility in Equation (5.25) can be expressed in terms of only one parameter when η is given. In the subsequent analysis, we choose to use Pe^{-1} as the expansion parameter, though the exact same results could be obtained with the alternate choice of β^{-1}. Substituting $\beta^{-1} = (4\lambda_3\eta/A)Pe^{-1}$ into (5.25) lets us recast the eigenvalue problem as

$$\begin{aligned}-\mathrm{i}\left[\omega + \lambda_2(\boldsymbol{p}\cdot\boldsymbol{k})(\boldsymbol{p}\cdot\hat{\boldsymbol{z}})\right]\tilde{\psi} + \mathrm{i}\mathcal{F}\,\tilde{c} + Pe^{-1}\left[\lambda_1 k^2 + \lambda_2(\boldsymbol{p}\cdot\boldsymbol{k})^2\right]\tilde{\psi}& \\ -\lambda_3 Pe^{-1}\boldsymbol{\nabla}_p\cdot\left[\boldsymbol{\nabla}_p\tilde{\psi} - 2\eta\tilde{\psi}\sin 2\theta\,\hat{\boldsymbol{\theta}}\right] = 0,&\end{aligned} \tag{5.47}$$

where η is fixed and finite and Pe^{-1} is assumed to be small. It is worth reiterating here that we are considering the regime where the effects of Brownian motion and flexibility are weak and of comparable magnitude, i.e., both Pe and β are large. The

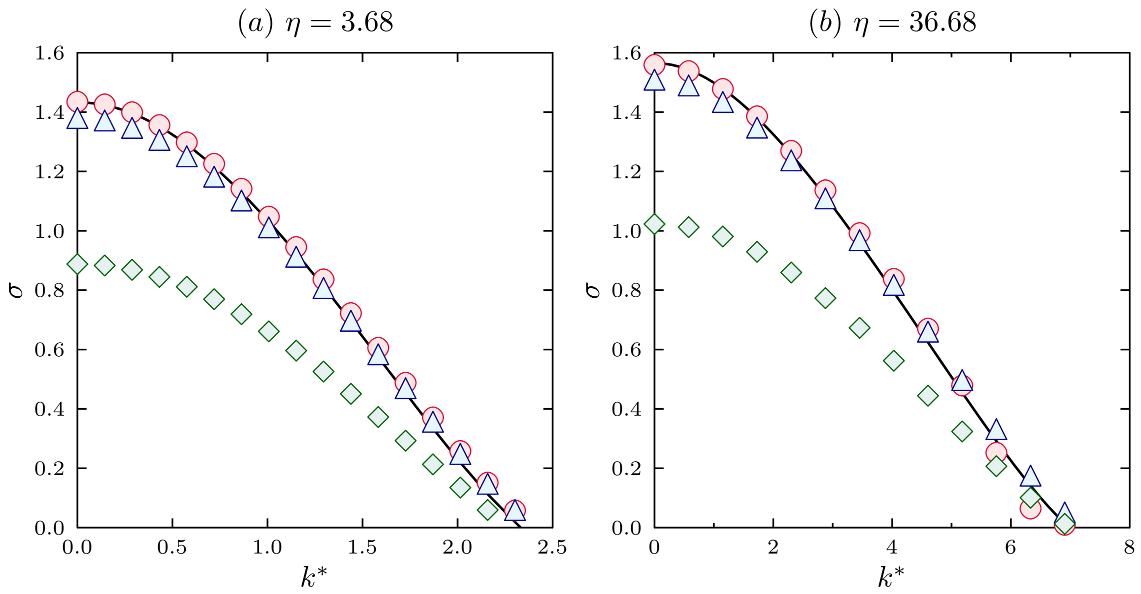

Figure 5.6: Suppression of the instability due to fiber flexibility for fixed η. The symbols denote the spectral solutions for: (a) $\beta = 0.1, Pe = 10^3(\diamond)$; $\beta = 1, Pe = 10^4(\triangle)$, and $\beta = 10, Pe = 10^5(\circ)$. (b) $\beta = 0.1, Pe = 10^4(\diamond)$; $\beta = 1, Pe = 10^5(\triangle)$, and $\beta = 10, Pe = 10^6(\circ)$. The solid line in each case is the prediction for the effect of the base state alone, following Equation (5.44). The suppression of the growth rate as β decreases (i.e., the filaments are made more flexible) is clear.

eigenfunction and eigenvalue can be then expanded as:

$$\tilde{\psi} = \tilde{\psi}_0 + Pe^{-1}\tilde{\psi}_1 + O(Pe^{-2}), \tag{5.48}$$

$$\omega = \omega_0 + Pe^{-1}\omega_1 + O(Pe^{-2}), \tag{5.49}$$

and substituted into (5.47). The leading-order terms follow Equation (5.28), where Pe and β only affect the base state through their ratio appearing in Ψ_0. The next order in Pe^{-1} then gives us

$$\omega_0\tilde{\psi}_1 + \omega_1\tilde{\psi}_0 + \lambda_2(\boldsymbol{p}\cdot\boldsymbol{k})(\boldsymbol{p}\cdot\hat{\boldsymbol{z}})\tilde{\psi}_1 - \mathcal{F}\,\tilde{c}_1 + \mathrm{i}\,(\mathcal{G} - \mathcal{H}) = 0, \tag{5.50}$$

where we have defined

$$\mathcal{G} = \left[\lambda_1 k^2 + \lambda_2(\boldsymbol{p}\cdot\boldsymbol{k})^2\right]\tilde{\psi}_0, \tag{5.51}$$

$$\mathcal{H} = \lambda_3 \boldsymbol{\nabla}_p \cdot \left[\boldsymbol{\nabla}_p\tilde{\psi}_0 - 2\eta\tilde{\psi}_0 \sin 2\theta\,\hat{\boldsymbol{\theta}}\right]. \tag{5.52}$$

This can be rearranged to read

$$\frac{\omega_0 + \lambda_2(\boldsymbol{p}\cdot\boldsymbol{k})(\boldsymbol{p}\cdot\hat{\boldsymbol{z}})}{\mathcal{F}}\tilde{\psi}_1 + \frac{\tilde{\psi}_0}{\mathcal{F}}\omega_1 - \tilde{c}_1 + \mathrm{i}\,\frac{\mathcal{G}-\mathcal{H}}{\mathcal{F}} = 0. \tag{5.53}$$

A simple expression for the first-order correction ω_1 of the complex frequency due to Brownian motion is then easily obtained after multiplication of (5.53) by $\tilde{\psi}_0$ and integration over the sphere of orientations Ω:

$$\omega_1 = -\mathrm{i}\,\frac{\displaystyle\int_\Omega \frac{(\mathcal{G}-\mathcal{H})\tilde{\psi}_0}{\mathcal{F}}\,\mathrm{d}\boldsymbol{p}}{\displaystyle\int_\Omega \frac{\tilde{\psi}_0^2}{\mathcal{F}}\,\mathrm{d}\boldsymbol{p}}, \tag{5.54}$$

where we have used Equation (5.28) to cancel the first and third terms in (5.53).

We now proceed to evaluate each term in (5.54) in the long-wave limit. Using the leading-order Equation (5.47) to substitute for $\tilde{\psi}_0$ and taking $\tilde{c}_0 = 1$ without loss of generality, we find that the denominator is

$$\int_\Omega \frac{\tilde{\psi}_0^2}{\mathcal{F}}\,\mathrm{d}\boldsymbol{p} = \int_\Omega \frac{\mathcal{F}}{[\omega_0 + \lambda_2(\boldsymbol{p}\cdot\boldsymbol{k})(\boldsymbol{p}\cdot\hat{\boldsymbol{z}})]^2}\,\mathrm{d}\boldsymbol{p}. \tag{5.55}$$

Following the same procedure as in Section 5.3.3, we expand the right-hand side to $O(k^4)$ and integrate by parts using the divergence theorem (5.39) to obtain:

$$\int_\Omega \frac{\tilde{\psi}_0^2}{\mathcal{F}}\,\mathrm{d}\boldsymbol{p} = -\frac{\mathcal{N}\lambda_2}{\omega_0^3}\left[J_1(\eta) + \frac{3}{8}\left(\frac{\lambda_2}{\omega_0}\right)^2 J_2(\eta)\;k^2\right] + O(k^4), \tag{5.56}$$

where $J_1(\eta)$ and $J_2(\eta)$ were previously defined in (5.42)–(5.43). In a similar fashion, we can evaluate the first part of the numerator as

$$\int_\Omega \frac{\mathcal{G}\tilde{\psi}_0}{\mathcal{F}}\,\mathrm{d}\boldsymbol{p} = \int_\Omega \frac{[\lambda_1 k^2 + \lambda_2(\boldsymbol{p}\cdot\boldsymbol{k})^2]\,\mathcal{F}}{[\omega_0 + \lambda_2(\boldsymbol{p}\cdot\boldsymbol{k})(\boldsymbol{p}\cdot\hat{\boldsymbol{z}})]^2}\,\mathrm{d}\boldsymbol{p} \tag{5.57}$$

$$= -\frac{\mathcal{N}\lambda_2}{\omega_0^3}\left[\lambda_1 K_1(\eta) + \frac{3\lambda_2}{4}K_2(\eta)\right]k^2 + O(k^4), \tag{5.58}$$

where the two functions $K_1(\eta)$ and $K_2(\eta)$ are given by

$$K_1(\eta) = \frac{\displaystyle\int_{-1}^{1} \mathrm{e}^{-2\eta u^2} u^2(1-u^2)(4\eta(1-u^2)+3)\,\mathrm{d}u}{\displaystyle\int_{-1}^{1} \mathrm{e}^{-2\eta u^2}\,\mathrm{d}u}, \tag{5.59}$$

and

$$K_2(\eta) = \frac{\displaystyle\int_{-1}^{1} \mathrm{e}^{-2\eta u^2} u^2(1-u^2)^2(4\eta(1-u^2)+3)\,\mathrm{d}u}{\displaystyle\int_{-1}^{1} \mathrm{e}^{-2\eta u^2}\,\mathrm{d}u}. \tag{5.60}$$

Finally, the second part of the numerator becomes after integration by parts

$$\int_\Omega \frac{\mathcal{H}\tilde{\psi}_0}{\mathcal{F}}\,\mathrm{d}\boldsymbol{p} = -\lambda_3 \int_\Omega \left[\boldsymbol{\nabla}_p\tilde{\psi}_0 - 2\eta\tilde{\psi}_0 \sin 2\theta\,\hat{\boldsymbol{\theta}}\right] \boldsymbol{\cdot} \boldsymbol{\nabla}_p \left[\frac{1}{\omega_0 + \lambda_2(\boldsymbol{p}\boldsymbol{\cdot}\boldsymbol{k})(\boldsymbol{p}\boldsymbol{\cdot}\hat{\boldsymbol{z}})}\right] \mathrm{d}\boldsymbol{p}. \tag{5.61}$$

We substitute again for $\tilde{\psi}_0$ from the leading-order equation, and integrate an expansion in small k. All calculations done, this yields

$$\int_\Omega \frac{\mathcal{H}\tilde{\psi}_0}{\mathcal{F}}\,\mathrm{d}\boldsymbol{p} = \frac{\mathcal{N}\lambda_2\lambda_3}{2\omega_0^3}\left[L_1(\eta) + \left(\frac{\lambda_2}{\omega_0}\right)^2 L_2(\eta)\;k^2\right] + O(k^4), \tag{5.62}$$

where $L_1(\eta)$ and $L_2(\eta)$ are defined as

$$\begin{aligned} L_1(\eta) = \int_{-1}^{1} &\mathrm{e}^{-2\eta u^2}\left[-(24\eta+12)u^2(1-u^2) + (4\eta+3)(1+u^2)\right.\\ &\left.-4\eta(u^2+u^4) + 32\eta(1-u^2)u^4\right]\mathrm{d}u \Bigg/ \int_{-1}^{1} \mathrm{e}^{-2\eta u^2}\,\mathrm{d}u, \end{aligned} \tag{5.63}$$

and

$$\begin{aligned} L_2(\eta) = \int_{-1}^{1} &\mathrm{e}^{-2\eta u^2}\left\{-(156\eta+90)u^4(1-u^2)^2\right.\\ &+10(4\eta+3)\left[u^4(1-u^2) + \frac{3}{4}u^2(1-u^2)^2\right]\\ &-40\eta\left[(1-u^2)u^6 + \frac{3}{4}(1-u^2)^2u^4\right]\\ &\left.+192\eta(1-u^2)^2u^6\right\}\mathrm{d}u \Bigg/ \int_{-1}^{1} \mathrm{e}^{-2\eta u^2}\,\mathrm{d}u. \end{aligned} \tag{5.64}$$

We now have all the ingredients to estimate the correction to the growth rate. Substituting (5.56), (5.58) and (5.62) into Equation (5.54), we obtain an approximation for the correction to the eigenvalue in the limit of low wavenumbers:

$$\omega_1 = -\mathrm{i}\,\frac{\lambda_3}{2}\frac{L_1}{J_1} - \mathrm{i}k^2\left[-\frac{\lambda_2\lambda_3}{\mathcal{N}}\frac{L_2}{J_1^2} + \frac{\lambda_1 K_1}{J_1} + \frac{3\lambda_2}{4}\frac{K_2}{J_1} + \frac{3\lambda_2\lambda_3}{8\mathcal{N}}\frac{L_1 J_2}{J_1^3}\right] + O(k^4). \tag{5.65}$$

The stabilizing effect of Brownian motion is best illustrated in the long-wavelength limit. At $k = 0$, the growth rate is given by

$$\sigma_m^{Pe}(Pe;\eta) = \sigma_m - \frac{\lambda_3}{2\omega_m}\frac{L_1}{J_1}\,Pe^{-1} + O(Pe^{-2}), \tag{5.66}$$

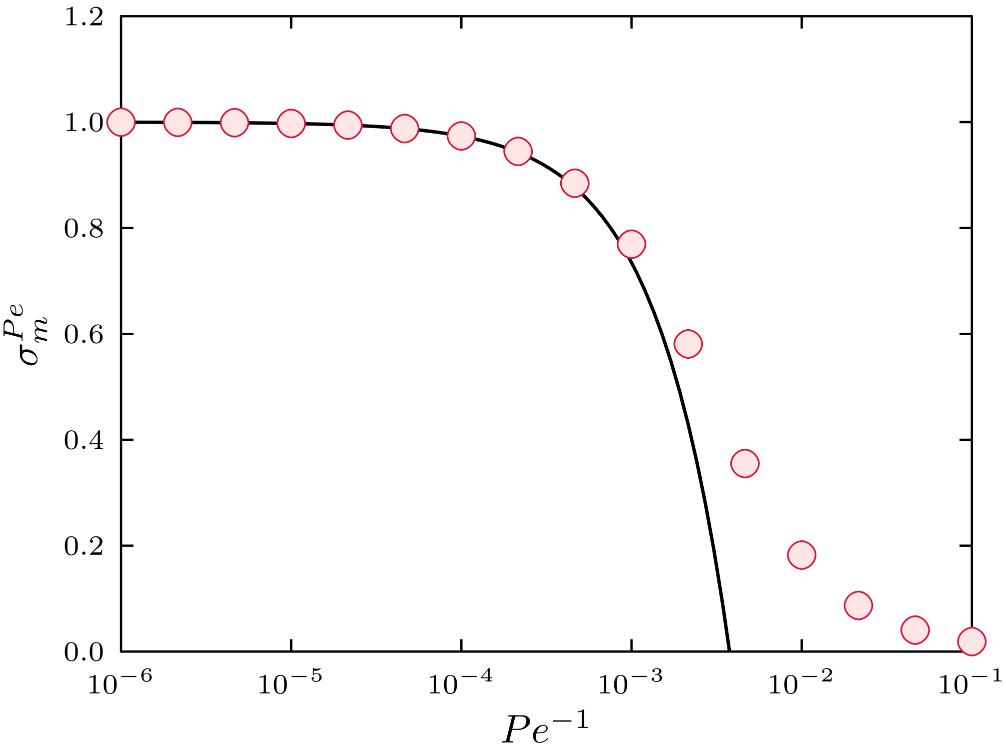

Figure 5.7: Suppression of the growth rate due to Brownian motion. The solid line shows the leading-order correction to the maximum growth rate as obtained in (5.66). The symbols are spectral solutions of the full eigenvalue problem obtained using spherical harmonics, all for $\beta = 10^6$.

where we have again normalized with respect to the isotropic rigid rod limit of ω_m. The subscript m indicates that this is the maximum growth rate reached in the long-wave limit, and σ_m is the base-state effect following (5.41) evaluated at $k = 0$. Equation (5.66) captures the leading correction to the growth rate due to thermal diffusion, and is compared to the spherical harmonics solution to the full eigenvalue problem in Figure 5.7. As expected, Brownian motion leads to the randomization of individual particle orientations and hence stabilizes the suspension. A similar conclusion was reached by Hoffman and Shaqfeh [145] who considered the effect of Brownian motion on a suspension of polarizable rods placed in an electric field and also derived an expression similar to (5.41) in the simpler case of an isotropic base state.

As we explained earlier, Pe and β are interchangeable for a given value of η

up to a constant factor depending on particle shape. Within the framework of the asymptotic expansion above, it is therefore possible to rewrite (5.66) in terms of β as

$$\sigma_m^\beta(\beta;\eta) = \sigma_m - \frac{A}{8\omega_m\eta}\frac{L_1}{J_1}\,\beta^{-1} + O(\beta^{-2}), \tag{5.67}$$

providing the leading effect of flexibility on the growth rate. This expression is shown to compare excellently with the numerical solution to the full eigenvalue problem in Figure 5.8. Once again, it should be kept in mind that the asymptotic expansion is valid for $\beta \gtrsim 1$, and Equation (5.67) does an excellent job of predicting the behavior as the direct effect of flexibility becomes significant. The dual effect of flexibility is now obvious. On the one hand, we saw in Section 5.3.3 that it creates a base state that is more prone to instability, and this effect is the dominant one for stiff filaments. On the other hand, at the next order flexibility causes alignment of the filaments perpendicular to gravity in a way that hinders their rotation in the disturbance flow and therefore suppresses the growth rate. In the limit of large η, L_1/J_1 asymptotes to 4η. This means that the correction due to flexibility in (5.67) above goes like β^{-1} as flexibility becomes more important. The suppression of the growth rate as seen in Figure 5.8 then becomes independent of η for sufficiently small values of β, which explains the collapse of all the curves corresponding to different values of Pe onto a single one. Finally, recall that the expansion is still first order in Pe^{-1}, and this means that the prediction becomes less accurate as rotational diffusion becomes stronger as was observed in Figure 5.7. The same is the case again in Figure 5.8 where the spectral solution departs slightly from the prediction for the smallest value of Péclet number shown.

5.3.5 Effect of flexibility in the perfectly-aligned state

Finally, we also analyze the effect of flexibility in the perfectly-aligned state (absent Brownian motion), with the base orientation distribution given by $\Psi_0 = \delta(\theta - \pi/2)/2\pi$ corresponding to fibers aligned perpendicular to gravity. As seen in Equation (5.67) by letting $\eta \to \infty$, the direct effect of flexibility at first order is to reduce the zero-wavenumber growth rate by the value $A/(2\omega_m\beta)$. However, thanks to the special form of the base-state distribution in this case, we show here that we are in fact able to find the exact dispersion relation analytically for all permissible

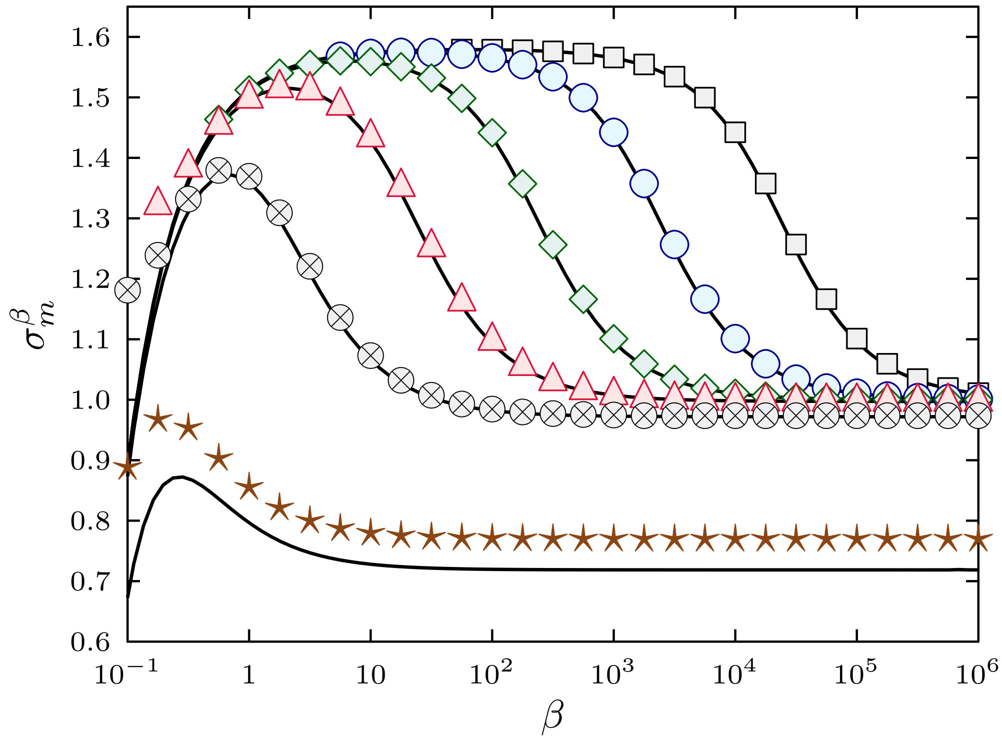

Figure 5.8: Suppression of the growth rate due to fiber flexibility. The solid line shows the leading-order correction to the maximum growth rate as obtained in Equation (5.67). The symbols are spectral solutions of the full eigenvalue problem obtained using spherical harmonics for different Péclet numbers: $Pe = 10^8(\Box)$, $10^7(\circ)$, $10^6(\diamond)$, $10^5(\triangle)$, $10^4(\otimes)$, and $10^3(\star)$. The self-similar behavior continues as low as $Pe \sim 10^4$ beyond which diffusion independently suppresses the growth rate.

values of k and β. Two identities for the Dirac delta function $\delta(\theta - \pi/2)$ are useful in the derivation below:

$$h(\theta)\delta' = -h'(\pi/2)\delta + h(\pi/2)\delta', \tag{5.68}$$

$$h(\theta)\delta'' = h''(\pi/2)\delta - 2h'(\pi/2)\delta' + h(\pi/2)\delta''. \tag{5.69}$$

Inserting the expression for Ψ_0 into Equation (5.27) for $\mathcal{F}$ yields

$$\mathcal{F} = -\frac{\mathcal{N}}{k^2}\boldsymbol{\nabla}_p \cdot [\Psi_0(\boldsymbol{p}\cdot\boldsymbol{k})(\boldsymbol{I} - \boldsymbol{pp})\cdot\hat{\boldsymbol{z}}] = \frac{\mathcal{N}}{2\pi k}\cos\varphi\,\delta'. \tag{5.70}$$

Upon inspection of the dispersion relation (5.25) in the limit of $Pe \to \infty$,

$$\left\{-\mathrm{i}\omega - \mathrm{i}\boldsymbol{k}\cdot(\lambda_1\boldsymbol{I} + \lambda_2\boldsymbol{pp})\cdot\hat{\boldsymbol{z}} + A\beta^{-1}(3\cos^2\theta - 1)\right\}\tilde{\psi} + \frac{A}{2\beta}\sin 2\theta\frac{\partial\tilde{\psi}}{\partial\theta} + \mathrm{i}\mathcal{F}\,\tilde{c} = 0, \tag{5.71}$$

we are led to consider the ansatz $\tilde{\psi} = f_1(\varphi)\delta(\theta - \pi/2) + f_2(\varphi)\delta'(\theta - \pi/2)$, so that (5.71) then reduces to

$$-(\mathrm{i}\omega + A\beta^{-1})(f_1\delta + f_2\delta') - \mathrm{i}\lambda_2 k \cos\varphi f_2\delta + \frac{A}{2\beta}(2f_1\delta + 4f_2\delta') + \mathrm{i}\frac{\mathcal{N}}{2\pi k}\cos\varphi\,\tilde{c}\,\delta' = 0. \tag{5.72}$$

Expressions for f_1 and f_2 are determined without difficulty, and the eigenvalue problem is thus solved exactly. With the normalization requirement $\int_\Omega \tilde{\psi}\,\mathrm{d}\boldsymbol{p} = \tilde{c}$, the exact formulae for the dispersion relation and the growth rate $\sigma = \omega_I/\omega_m$ are given by

$$\omega = -\frac{\mathrm{i}A}{2\beta} \pm \mathrm{i}\sqrt{\frac{A^2}{4\beta^2} + \frac{\lambda_2\mathcal{N}}{2}}, \tag{5.73}$$

$$\sigma = -\frac{A}{2\omega_m\beta} \pm \sqrt{\frac{A^2}{4\omega_m^2\beta^2} + \frac{5}{2}}. \tag{5.74}$$

The $O(\beta^{-1})$ correction to the zero-wavenumber growth rate is $-A/(2\omega_m\beta)$, which agrees with the limit of $\eta \to \infty$ in (5.67). From this more complete expression, we see that the dispersion relation is independent of the wavelength of the horizontal perturbation in the perfectly aligned state as previously found in Section 5.3.3 in the analysis of the effect of the base state.

Using the same approach, we can also obtain the dispersion relation for a more general initial perturbation with arbitrary wave direction $\hat{\boldsymbol{k}} = (\sin\alpha, 0, \cos\alpha)$ and find that

$$\omega = -\lambda_1 k\cos\alpha - \frac{\mathrm{i}A}{2\beta} \pm \mathrm{i}\sqrt{\frac{A^2}{4\beta^2} + \frac{\lambda_2\mathcal{N}\sin^4\alpha}{2}}. \tag{5.75}$$

For a perturbation wave vector parallel to gravity ($\alpha = 0$), Equation (5.75) shows that ω is real, so the initial response of the suspension is a propagating density wave. Physically, the perturbation takes the form of regions of higher and lower fiber density layered in the direction of gravity, which travel vertically due to sedimentation. Instability only occurs when $\alpha \neq 0$, and in agreement with Koch and Shaqfeh [125] we find that the maximum growth rate is achieved for a horizontal wave ($\alpha = \pi/2$). Equation (5.75) also shows that the growth rate is wavelength-independent even for non-horizontal perturbations, and perturbations of all wavelengths are therefore equally unstable in this case. To understand this curious result, we first note that the shear flow velocity set up by the initial perturbation scales as $\nabla_x \boldsymbol{u}_d \sim 1/k$. For small departures of fiber orientations from $\pi/2$, Jeffery's equation (5.5) then gives $\dot{\boldsymbol{p}} \sim 1/k$. Then, since the horizontal translational velocity of the fibers due to their rotation in the flow scales approximately as $u_1 \sim 1/(k\omega)$, the conservation of particles $\partial_t c_1 \sim \partial_x (c_0 u_1)$ results in $\omega \sim 1/\omega$, indicating a growth rate independent of k. In other words, the larger sedimentation speed of particles in the more concentrated regions for higher-wavenumber perturbations balances the decreasing number of nearby fibers that are migrating into these regions.

5.4 Conclusion

We have investigated the effects of flexibility on the stability of a suspension of sedimenting fibers. Specifically, we considered the dynamics of weakly-flexible fibers, characterised by large elasto-gravitation numbers, which are resistant to large deformations during the sedimentation process. In particular, we exploited two facts that are known about the sedimentation of isolated flexible filaments [4]: to leading order in the inverse elasto-gravitation number, a fiber translates with the same velocity as if it were a rigid rod and maintains a nearly straight shape as it sediments. We were therefore able to treat the suspension as one composed of rigid rods with the added ingredient of individual fiber reorientation during sedimentation.

We developed a mean-field model much akin to the one first described by Koch and Shaqfeh [125], in which the probability density function describing the filament positions and orientations evolves according to a Smoluchowski equation. We first derived the statistical base state in the undisturbed and spatially homogeneous situation and found that it is in general anisotropic in the fiber orientation. In terms of a new variable η which is a scaled ratio of the Péclet number to the elasto-gravitation number, the base state describes in one limit the isotropic distribution of rigid rods ($\eta = 0$), and in the other the perfectly-aligned distribution that results when the suspension is athermal ($\eta \to \infty$). Speculating based on the mechanism that leads to an instability in the case of a suspension of rigid rods, we surmised that an anisotropic suspension composed of fibers oriented perpendicular to gravity would be more unstable to concentration fluctuations, owing to the fact that individual particles are more likely to be reoriented by the disturbance flow in a way that enhances the instability. This speculation was confirmed when we perturbed the governing equation about the base state and performed a linear stability analysis. The resulting eigenvalue problem is defined on the sphere of orientations, and admits a spectral solution on the basis of spherical harmonics. A numerical solution did indeed show that the system not only has a larger growth rate with increasing fiber flexibility, but also renders more wavenumbers unstable.

We then proceeded to examine separately the contributions of the anisotropic base state and of the direct effect of flexibility (or Brownian motion, which may be interpreted alternatively through the variable η). Expanding the eigenvalue problem in an asymptotic series in β^{-1} and Pe^{-1}, we first saw that the base state is almost entirely responsible for the enhancement of the instability, unless flexibility-induced reorientation is very strong. We showed that the growth rate increases monotonically with the variable η, continuously interpolating between the previously known value in the case of a suspension of isotropically distributed rigid rods to the limit of a perfectly aligned suspension where the growth rate is a factor of $\sqrt{5/2}$ faster. The range of unstable wavenumbers, too, was shown to grow with increasing values of η, and the window of instability in fact expands indefinitely as the suspension becomes more anisotropic.

Next, we derived the correction to the growth rate due to the terms of order β^{-1} and Pe^{-1}, thereby capturing the direct effect of flexibility and rotational diffusion, which would be present even if not for the anisotropic base-state distribution. Since β and Pe are related through the variable η, flexible reorientation and rotational diffusion could both be studied simultaneously, and both effects were found to stabilize the suspension. These results confirmed intuition, as reorientation towards the direction perpendicular to gravity competes against rotation in the disturbance flow: this has the effect of preventing particles from migrating into already dense clusters and thereby suppresses the growth of the instability. Similarly, increased thermal motion randomizes fiber orientations and disrupts the mechanism that would entrain more particles into regions of higher concentration.

The results of this work are summarized in a phase diagram in Figure 5.9. The phase boundaries are only to guide the eye, and the transitions are by no means

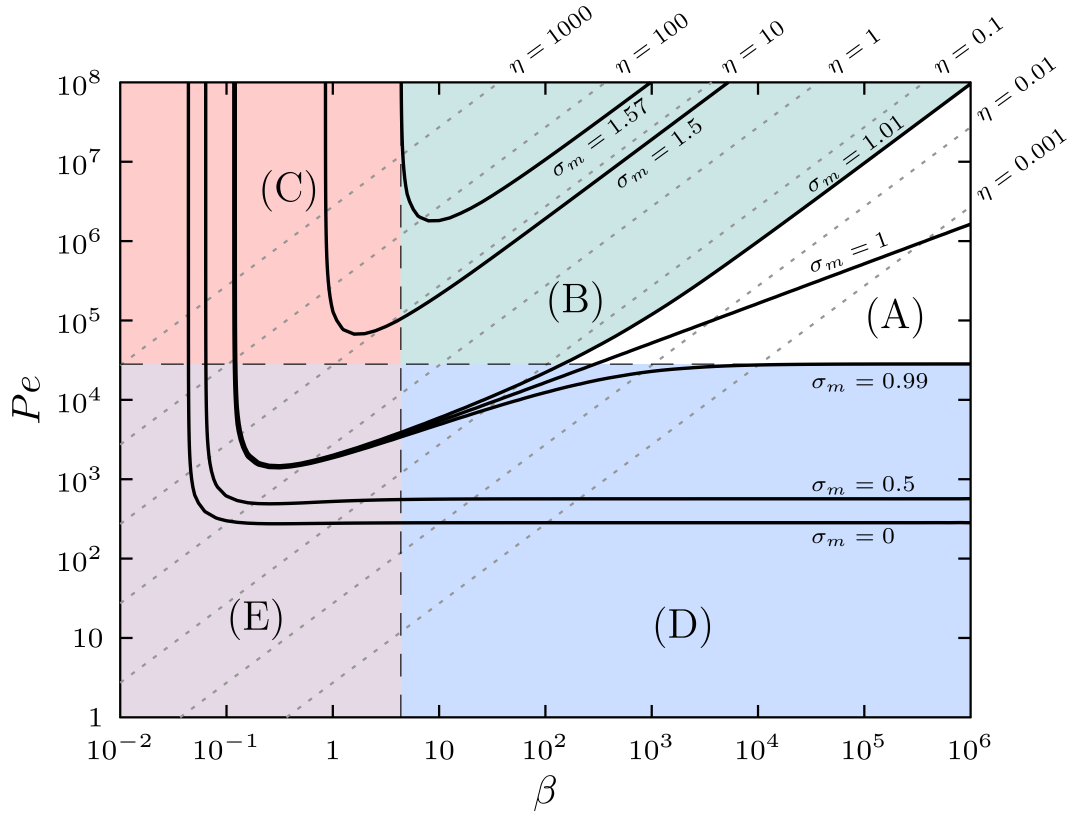

Figure 5.9: A phase diagram summarizing the effects of flexibility and Brownian motion on the stability of a suspension. The dotted lines denote the η co-ordinate, and solid lines are contours of the maximum growth rate σ_m at the indicated values. The dashed lines are meant to divide the phase space qualitatively into regions labeled (A)–(E): (A) Negligible diffusion and fiber flexibility, and a near-isotropic orientation distribution in the base state; the dynamics are indistinguishable from the case of a rigid rod suspension. (B) Negligible direct effect of diffusion and fiber flexibility, although the base state is rendered anisotropic and a self-similar enhancement of the instability is seen. (C) Stabilization due to the direct effect of fiber-flexibility-induced reorientation. (D) Stabilization due to the direct effect of rotational diffusion. (E) Combined non-trivial effects of flexibility and Brownian motion.

sharp. The axes cover the range of β and Pe discussed here, as well as the pertinent range of the variable η. Contour lines of the maximum (zero-wavenumber) growth rate trace out regions where the growth rate is predicted to be negative, positive or greater than unity (which, under our normalization, is the case of a suspension of rigid rods). The entire phase-space can be qualitatively divided into regions where one effect or the other becomes predominant. Here, (A) corresponds to the case of a base state that is nearly isotropic, and the independent effects of fiber flexibility and thermal fluctuations are negligible. We dealt with this in Section 5.3.3 and saw that $\sigma_m = 1$ in this regime, and in Figure 5.9 we concede a departure of ± 0.01 from unity to define this regime. Regime (B) is encountered as one departs from (A) along the η-coordinate, and we saw in Section 5.3.3 that this corresponds to the self-similar enhancement of the rigid rod instability, solely due to the anisotropy of the base-state distribution. Particles preferentially align perpendicular to gravity, which increases their chance of migrating into dense regions as a result of hydrodynamic interactions, thereby enhancing the instability. Here again, the independent effects of flexibility and Brownian motion are negligible. Increasing the fiber flexibility takes us to (C) where the independent effect of flexibility was shown in Section 5.3.4 to be stabilizing. The propensity of individual particles to reorient perpendicular to gravity during sedimentation hinders their horizontal migration and thus stabilizes the suspension. (D) depicts the regime where randomization due to thermal fluctuations suppresses the growth rate, which we named the direct effect of Brownian motion and analyzed quantitatively in Section 5.3.4. Finally, regime (E) is where the independent effects of both fiber flexibility and diffusion are significant and the observed stabilization cannot be individually attributed to either mechanism alone. Further, there are more regimes that can be identified and that are not shown in Figure 5.9 for the sake of simplicity. For instance, near the border between (B) and (D) lies a region where the anisotropic base state enhances the instability but Brownian motion suppresses it.

We have assumed throughout that the base state has already been established, and restricted our attention to the linear stability of perturbations with respect to such an orientation distribution. In a well-stirred suspension, particles can be assumed to be isotropically oriented and it remains to be seen how the time over which such a base state is achieved compares with the growth rate of disturbances in an isotropically oriented suspension. Quantitatively, this is decided by the solution to an advection-diffusion equation in orientation space. Qualitatively, assuming weak diffusion, the base state is established on a timescale $|\dot{\boldsymbol{p}}_s|^{-1} \sim 2\beta/A$. Balancing this with the timescale ω_m^{-1} associated with the instability in an isotropic suspension, we find the condition $\mathcal{N} \lesssim A^2/\lambda_2\beta^2$ on the effective volume fraction of particles. This essentially states that the concentration has to be sufficiently low for hydrodynamic interactions not to hinder the establishment of the base state. The condition points to a very dilute suspension, which may require a very large container for the instability to be observed. Nevertheless, in a hypothetical infinite suspension, the instability does exist regardless of dilution since the maximum growth rate is achieved in the limit of $k \to 0$. Furthermore, the suppression of the instability due to individual particle reorientation (direct effect of flexibility) is independent of the base-state distribution, and this effect can be relevant even in nearly isotropic suspensions.

In this work we have neglected the effect of the disturbance field on the shape of each fiber: strong interactions could potentially deform individual fibers from the assumed straight orientation, and change the settling dynamics. However, such detailed internal dynamics are not straightforward to describe in a mean-field kinetic model such as the one we have developed. Furthermore, it would seem to be a fair assumption that the diluteness of the suspension prevents particles from imposing strong disturbance fields upon one another. The same rationale applies to neglecting excluded volume effects and steric interactions between fibers. Particle inertia, which we have neglected here as well, has been shown to eliminate growth at zero wavenumber [146] and could be relevant in rationalizing the formation of finite-sized vertical structures seen in experiments [138]. Particle simulations could hold the key to revealing microstructural changes and detailed internal dynamics in dilute as well as concentrated suspensions, and test the validity of our predictions as other physical effects become relevant. Chapter 6 which follows is the first step in that direction. Further, while we have considered an infinite domain for analytical convenience, simulations could also lead the way in describing the effects of walls, which are known to become vital in real systems [78, 80, 143]. As a closing statement, we note that the stronger instability associated with the anisotropic base state described here is not necessarily exclusive to flexible fibers, and the approach used here can in principle apply to any suspension wherein a physical mechanism exists that causes orientable particles to align perpendicular to the direction of forcing.

Chapter 5 is based largely on material that has appeared in *Journal of Fluid Mechanics* (2014), authored by Harishankar Manikantan, Lei Li, Saverio E. Spagnolie, and David Saintillan [5].

Chapter 6

Sedimenting suspensions of weakly flexible fibers: Simulations

6.1 Introduction

In the last chapter, we applied our knowledge of single filament dynamics to study the stability of a suspension of weakly flexible fibers using a continuum method [5]. We followed the linear stability analysis first proposed by Koch and Shaqfeh [125] with the added ingredient of flexibility-induced reorientation. In the case of a suspension of perfectly rigid rods, the base-state distribution is uniform in space and isotropic in orientation. The effect of a spatial fluctuation in number density is to set up a vertical disturbance flow that is downward in areas of higher particle density and upward outside. This vertical shear field causes particles to rotate in such a way as to enable their orientation-dependent settling velocity to draw them into regions of already higher density, thus enhancing concentration fluctuations. Adapting this study to the case of weakly flexible fibers revealed two opposing effects of fiber flexibility. First, in the absence of fluctuations, the balance between rotational diffusion and reorientation due to flexibility gives rise to an anisotropic orientation distribution in the base state. Introducing a gravitational Péclet number $Pe = F_G L/k_B T$, and defining $\eta = APe/48(c-1)\beta$, this base-state distribution was found to be

$$\Psi_0(\theta) = m_0 \exp[-2\eta \cos^2 \theta], \tag{6.1}$$

where m_0 is a normalization constant. We saw that η plays the role of an anisotropy parameter. The limit of $\eta \to 0$ renders the base state isotropic, while large values of η correspond to increasingly anisotropic distributions with a preferential alignment perpendicular to gravity – a direct consequence of flexibility-induced reorientation. Perturbing about this configuration and following through the linear stability analysis in the continuum approach, this base-state anisotropy was shown to be the prime factor responsible for an enhanced instability as long $\beta \gtrsim 1$. The mechanism suggested was straightforward: a nearly horizontal alignment of fibers made it more likely for each to be reoriented by the disturbance fields of the others in a way as to be drawn towards regions of already higher number density. The second and opposite effect of flexibility becomes stronger as the fibers become less rigid, specifically as $\beta \lesssim 1$, when the effect of the reorientation of individual particles due to flexibility becomes comparable to that due to the disturbance field. Recall that, in dimensional form, the rate of reorientation is:

$$\frac{\partial \theta}{\partial t} = \frac{F_G}{8\pi\mu L^2}\frac{A}{2\beta}\sin(2\theta), \tag{6.2}$$

where θ is the instantaneous angle the fiber makes with the direction of gravity. Note that all orientations but those parallel or perpendicular to gravity feel this rotational velocity, causing an isolated fiber to rotate towards a terminal horizontal configuration. The fluid has viscosity μ, and $A = 3(c - 7/2)/80$. Strong horizontal alignment then tends to hinder horizontal drift and therefore the very mechanism of growth of fluctuations. On approaching the problem asymptotically, we indeed showed that the growth rate has a $O(\beta^{-1})$ negative correction due to this 'independent' effect of flexibility, contrasting it with the effect of the base state that hinges on the relative magnitude of flexibility and rotational diffusion through the parameter η.

These theoretical results were derived from a continuum approach where the fibers were abstracted as point forces with a director that determined their translational and rotational velocities. While this simplified model was analytically tractable and extremely insightful into the short-time growth of fluctuations, we draw in the present chapter a more detailed picture using discrete particle simulations. Not only do we show the validity of the continuum theory, but we also go on to elucidate the microstructural changes that the particle simulation affords us, which will in turn reveal the mechanisms involved in the enhancement or suppression of the instability. Here, again, we exploit the approximations that weak flexibility grants us – namely that each fiber can be approximated to leading-order as a rigid rod, with the effect of flexibility entering solely through the rotational velocity in Equation (6.2). This allows us to use efficient and fast methods that have been previously developed for simulating suspensions of rigid rods [139, 141].

The chapter is organized as follows. In Section 6.2, we describe the slender-body model used to describe the dynamics of each fiber and its hydrodynamic interaction with every other fiber in the suspension. The numerical method used to integrate the configuration of the fibers in time in the presence of Brownian motion is also described there. Results from simulations are presented in Section 6.3 where we systematically analyze the changes in number density fluctuations and migration of particles, which reveals the mechanism of the instability. We also make use of our simulation method to consider the evolution of a well-stirred isotropic suspension of weakly flexible particles, which was outside the purview of the linear continuum theory.

6.2 Slender-body model and numerical method

As previously discussed, the deflection of a fiber from a nearly straightened state is small when it is weakly flexible ($\beta \gg 1$), and we exploit this fact to model each fiber as a rigid rod with the effect of flexibility entering only through flexibility-induced reorientation. We consider a periodic collection of N fibers, where each fiber indexed by α is described entirely by the position of its center $\boldsymbol{x}_\alpha$ and a director $\boldsymbol{p}_\alpha$, which is the tangent to the filament at its center. We shall assume zero Reynolds number flow, without any particle inertia. In a dilute suspension of such particles, the leading-order effect of each particle on every other is that due to a net force on the fluid (Stokeslet) equal to its weight corrected for buoyancy and acting at the particle center. Within these approximations, it is implicit that we do not take into account the effect of the disturbance field of one fiber on the shape of another – the suspension will be assumed to be sufficiently dilute to render such effects negligible.

We use slender-body theory for Stokes flow to model the dynamics of each fiber.

To non-dimensionalize the equations, we choose as characteristic scales the length of each filament L, the sedimentation timescale $8\pi\mu L^2/F_G$, and the gravitational force on a fiber F_G. We shall be primarily concerned with cases where Brownian motion is weak, hence the choice of fiber weight as the characteristic scale for force. Parametrized along its length by $s_\alpha \in [-1/2, 1/2]$, each fiber then follows the local slender-body equation [56]:

$$\dot{\boldsymbol{x}}_\alpha + s\dot{\boldsymbol{p}}_\alpha - \boldsymbol{u}_\alpha^\infty(\boldsymbol{x}_\alpha + s_\alpha \boldsymbol{p}_\alpha) - s\dot{\boldsymbol{p}}_\alpha^s(\boldsymbol{p}_\alpha) = (\lambda_1 \boldsymbol{I} + \lambda_2 \boldsymbol{p}_\alpha \boldsymbol{p}_\alpha) \cdot \boldsymbol{f}_\alpha(\boldsymbol{x}_\alpha + s_\alpha \boldsymbol{p}_\alpha). \tag{6.3}$$

Here, $\boldsymbol{u}_\alpha^\infty$ is the external velocity felt by fiber α, which in the present case is the disturbance field generated by the forces exerted on the fluid by all other fibers in the suspension as well as their periodic images, and $\dot{\boldsymbol{p}}_\alpha^s$ is the flexibility-induced reorientation velocity that depends on the instantaneous orientation of fiber α as described by Equation (6.2). This can be interpreted as an external rotational velocity imposed on each rod that captures the leading order effect of elastohydrodynamic interactions. Written this way, Equation (6.3) is accurate to $O(\beta^{-2})$. $\boldsymbol{f}_\alpha$ is the force distribution along the length of the fiber, and $\lambda_1 = c + 1$ and $\lambda_2 = c - 3$ are the anisotropic mobility coefficients for a slender rod.

The force distribution $\boldsymbol{f}_\alpha(s_\alpha)$ on each fiber has contributions coming from both gravity and Brownian fluctuations in the solvent. Following previous works [139, 141, 162], this distribution is approximated by a truncated Legendre polynomial expansion:

$$\boldsymbol{f}_\alpha(\boldsymbol{x}_\alpha + s_\alpha \boldsymbol{p}_\alpha) = \boldsymbol{F}_\alpha^{(0)} + 12 s_\alpha \boldsymbol{F}_\alpha^{(1)} + O(s_\alpha^2), \tag{6.4}$$

where $\boldsymbol{F}_\alpha^{(n)}$ is the n-th moment of the force distribution over the length of the fiber and where only the first two moments are retained. The zeroth moment has contributions from both gravity and Brownian forces: $\boldsymbol{F}_\alpha^{(0)} = -\hat{\boldsymbol{z}} + \boldsymbol{F}_{\alpha,B}^{(0)}$. For the purpose of the simulation algorithm that we describe below, it is convenient to write the first moment as a sum of parts along and orthogonal to the director:

$$\boldsymbol{F}_\alpha^{(1)} = \mathsf{S}_\alpha \boldsymbol{p}_\alpha + (\boldsymbol{I} - \boldsymbol{p}_\alpha \boldsymbol{p}_\alpha) \cdot \boldsymbol{F}_\alpha^{(1)}. \tag{6.5}$$

This, respectively, captures the effects of a scalar stresslet $\mathsf{S}_\alpha = \boldsymbol{p}_\alpha \cdot \boldsymbol{F}_\alpha^{(1)}$ acting to ‘stretch’ the fiber along its director, and of a torque that reorients the fiber. It is worth noting here that a net torque can only result from Brownian fluctuations;

neither gravity nor its interaction with flexibility contributes to a torque over the entire body. Inverting the single-fiber equation (6.3) above enables us to express the scalar stresslet as

$$\mathsf{S}_\alpha = -\frac{1}{\lambda_1 + \lambda_2} \int_{-1/2}^{1/2} s_\alpha \boldsymbol{p}_\alpha \cdot \boldsymbol{u}_\alpha^\infty \, \mathrm{d}s_\alpha. \tag{6.6}$$

The motion of each fiber and its periodic images affects every other fiber due to long-ranged hydrodynamic interactions. This enters the dynamics of fiber α via the disturbance field $\boldsymbol{u}_\alpha^\infty$, which is given by

$$\boldsymbol{u}_\alpha^\infty(\boldsymbol{x}_\alpha + s_\alpha \boldsymbol{p}_\alpha) = \sum_{\gamma=1}^{N} \int_{-1/2}^{1/2} \tilde{\boldsymbol{G}}(\boldsymbol{x}_\alpha + s_\alpha \boldsymbol{p}_\alpha, \boldsymbol{x}_\gamma + s_\gamma \boldsymbol{p}_\gamma) \cdot \boldsymbol{f}_\gamma(\boldsymbol{x}_\gamma + s_\gamma \boldsymbol{p}_\gamma) \, \mathrm{d}s_\gamma. \tag{6.7}$$

Here, $\tilde{\boldsymbol{G}}_{\alpha\gamma} \equiv \tilde{\boldsymbol{G}}(\boldsymbol{x}_\alpha + s_\alpha \boldsymbol{p}_\alpha, \boldsymbol{x}_\gamma + s_\gamma \boldsymbol{p}_\gamma)$ is the periodic Green's function for Stokes flow, with the direct Stokeslet contribution removed when $\alpha = \gamma$.

We now have all the ingredients needed to derive evolution equations for the position and orientation of each fiber. Calculating the zeroth and first moments of Equation (6.3) yields after manipulations

$$\dot{\boldsymbol{x}}_\alpha = \dot{\boldsymbol{x}}_\alpha^s + \sum_{\gamma=1}^{N} \left[\boldsymbol{Q}_{\alpha\gamma}^{(0)} \cdot \boldsymbol{F}_\gamma^{(0)} + 12 \boldsymbol{Q}_{\alpha\gamma}^{(1)} \cdot (\boldsymbol{I} - \boldsymbol{p}_\gamma \boldsymbol{p}_\gamma) \cdot \boldsymbol{F}_\gamma^{(1)} + 12 \boldsymbol{q}_{\alpha\gamma} \mathsf{S}_\gamma \right], \tag{6.8}$$

and

$$\dot{\boldsymbol{p}}_\alpha = \dot{\boldsymbol{p}}_\alpha^s + 12 (\boldsymbol{I} - \boldsymbol{p}_\alpha \boldsymbol{p}_\alpha) \cdot \sum_{\gamma=1}^{N} \left[\boldsymbol{R}_{\alpha\gamma}^{(0)} \cdot \boldsymbol{F}_\gamma^{(0)} + 12 \boldsymbol{R}_{\alpha\gamma}^{(1)} \cdot (\boldsymbol{I} - \boldsymbol{p}_\gamma \boldsymbol{p}_\gamma) \cdot \boldsymbol{F}_\gamma^{(1)} + 12 \boldsymbol{r}_{\alpha\gamma} \mathsf{S}_\gamma \right]. \tag{6.9}$$

Here, $\dot{\boldsymbol{x}}_\alpha^s$ and $\dot{\boldsymbol{p}}_\alpha^s$ denote the linear and angular velocities of an isolated fiber under the effect of gravity and of Brownian fluctuations:

$$\dot{\boldsymbol{u}}_\alpha^s = (\lambda_1 \boldsymbol{I} + \lambda_2 \boldsymbol{p}_\alpha \boldsymbol{p}_\alpha) \cdot \boldsymbol{F}_\alpha^{(0)}, \tag{6.10}$$

$$\dot{\boldsymbol{p}}_\alpha^s = 12 \lambda_1 (\boldsymbol{I} - \boldsymbol{p}_\alpha \boldsymbol{p}_\alpha) \cdot \boldsymbol{F}_\alpha^{(1)} + \frac{A}{2\beta} \sin(2\theta_\alpha) \hat{\boldsymbol{\theta}}_\alpha. \tag{6.11}$$

Hydrodynamic interactions between fibers are captured by the sums on the right-hand sides of Eqs. (6.8)–(6.9), where $\boldsymbol{Q}_{\alpha\gamma}^{(n)}$, $\boldsymbol{R}_{\alpha\gamma}^{(n)}$, $\boldsymbol{q}_{\alpha\gamma}$ and $\boldsymbol{r}_{\alpha\gamma}$ are double integrals over pairs of fibers as described below, the former two being second-order tensors and the latter two vectors:

$$\boldsymbol{Q}_{\alpha\gamma}^{(n)} = \iint s_\gamma^n \, \tilde{\boldsymbol{G}}_{\alpha\gamma} \, \mathrm{d}s_\alpha \, \mathrm{d}s_\gamma, \tag{6.12a}$$

$$\boldsymbol{R}_{\alpha\gamma}^{(n)} = \iint s_\alpha \; s_\gamma^n \, \tilde{\boldsymbol{G}}_{\alpha\gamma} \, \mathrm{d}s_\alpha \, \mathrm{d}s_\gamma, \tag{6.12b}$$

$$\boldsymbol{q}_{\alpha\gamma} = \iint s_\gamma \, \tilde{\boldsymbol{G}}_{\alpha\gamma} \cdot \boldsymbol{p}_\gamma \, \mathrm{d}s_\alpha \, \mathrm{d}s_\gamma, \tag{6.12c}$$

$$\boldsymbol{r}_{\alpha\gamma} = \iint s_\alpha s_\gamma \, \tilde{\boldsymbol{G}}_{\alpha\gamma} \cdot \boldsymbol{p}_\gamma \, \mathrm{d}s_\alpha \, \mathrm{d}s_\gamma. \tag{6.12d}$$

Lastly, we note that the stresslets on each fiber remain unknown. They are coupled through Equation (6.6), which, when written out, yields the linear system:

$$(\lambda_1 + \lambda_2)\mathsf{S}_\alpha + 12 \; \boldsymbol{p}_\alpha \cdot \sum_{\gamma=1}^{N} \left[\boldsymbol{r}_{\alpha\gamma} \; \mathsf{S}_\gamma \right] = -\boldsymbol{p}_\alpha \cdot \sum_{\gamma=1}^{N} \left[\boldsymbol{R}_{\alpha\gamma}^{(0)} \cdot \boldsymbol{F}_\gamma^{(0)} + \boldsymbol{R}_{\alpha\gamma}^{(1)} \cdot (\boldsymbol{I} - \boldsymbol{p}_\gamma \boldsymbol{p}_\gamma) \cdot \boldsymbol{F}_\gamma^{(1)} \right]. \tag{6.13}$$

Advancing the configuration of the particles in the suspension involves integrating Equations (6.8)–(6.9) in time. To this end, we need to evaluate the integral operators in Equation (6.12) as well as determine the yet unknown stresslets acting on each fiber. Solving Equation (6.13) for the stresslets, in turn, also requires knowledge of the integral operators. Each of the integrals in Equation (6.12) involves a three-dimensional summation of periodic Stokeslets that decay as $\sim 1/r$, which in general diverges if performed directly. Furthermore, these integrals are pairwise operators over a system of N fibers and, if calculated naively, require $O(N^2)$ operations, which can be computationally prohibitive in large systems. Here, we choose to use the Smooth Particle-Mesh Ewald (SPME) algorithm [141] to perform these operations. The algorithm relies on an Ewald summation technique to resolve the divergence of the periodic sum by decomposing it into convergent real and Fourier parts, and then applies fast Fourier transforms to accelerate the evaluation of the Fourier part. The reader is directed to Saintillan *et al.* [141] for more details, and we shall only mention here that SPME reduces the cost of each such operation to approximately $O(N \log N)$.

The stresslet equation Equation (6.13), which is an $N \times N$ linear system as mentioned above, forbids the use of conventional inversion techniques such as LU decomposition when SPME is used to evaluate the integrals. Indeed, the SPME algorithm forgoes the direct calculation of the entries of the matrix, but rather provides an efficient and accurate ‘black box’ to perform matrix-vector products. This hints at using an iterative method for the system inversion, and a convenient choice is the Generalized Minimal Residual (GMRES) method [163]. At each iteration, GMRES delegates the matrix-vector product to an external routine, which in our case can be set to the SPME algorithm, and in this way the stresslets can be determined efficiently with the same order of computational cost as SPME.

The last ingredient that is needed to complete the formulation is a description of Brownian forces. The persistence length ($\ell_p = \kappa/k_B T$) of the fibers, which measures its elastic rigidity to thermal fluctuations, can be alternatively expressed as

$$\frac{\ell_p}{L} = \frac{\kappa}{k_B T L} = \frac{\kappa}{F_G L^2} \times \frac{F_g L}{k_B T} = \beta \times Pe. \tag{6.14}$$

In other words, as long as the product of the elasto-gravitation number and Péclet number is sufficiently large, which is the regime we shall work with here, we can safely ignore filament distortions due to thermal fluctuations. Therefore, consistent with the formulation above, we need only the first two moments of the Brownian force distribution on each fiber, which in turn affect its translational and rotational motion. These depend on the instantaneous configuration of the suspension through the fluctuation-dissipation theorem, and thus require knowledge of the grand mobility tensor. To describe the Brownian forces, we make use of a shorthand notation and formally rewrite the evolution equations Equations (6.8)–(6.9) as:

$$\begin{pmatrix} \dot{\mathcal{U}} \\ \dot{\mathcal{P}} \end{pmatrix} = \mathcal{M} \cdot \begin{pmatrix} \mathcal{F}^{(0)} \\ \mathcal{F}^{(1)} \end{pmatrix}, \tag{6.15}$$

where the left-hand side consists of a concatenation of the generalized $3N$ translational and rotational velocities $\dot{\mathcal{U}}$ and $\dot{\mathcal{P}}$. $\mathcal{M}$ is the $6N \times 6N$ grand mobility tensor corresponding to this problem, which incorporates all the dynamics, local and non-local, occurring as a result of the forces acting on the fibers; and $\mathcal{F}^{(n)}$ is a $3N$ vector that is the concatenation of the n-th moment of forces on each of the fibers. Note that the contribution from the stresslets S_α is implicit in $\mathcal{M}$. This notation is especially convenient in specifying the moments of the Brownian forces $\mathcal{F}_B$ following the fluctuation-dissipation theorem:

$$\left\langle \begin{pmatrix} \mathcal{F}_B^{(0)} \\ \mathcal{F}_B^{(1)} \end{pmatrix} (t) \right\rangle = \mathbf{0}, \tag{6.16}$$

$$\left\langle \begin{pmatrix} \mathcal{F}_B^{(0)} \\ \mathcal{F}_B^{(1)} \end{pmatrix} (t) \otimes \left(\mathcal{F}_B^{(0)} \mathcal{F}_B^{(1)} \right) (t') \right\rangle = 2\delta(t - t')\mathcal{M}^{-1}. \tag{6.17}$$

For the purpose of numerical evaluation, we model the generalized Brownian force vector acting during one time step $\varDelta t$ as

$$\begin{pmatrix} \mathcal{F}_B^{(0)} \\ \mathcal{F}_B^{(1)} \end{pmatrix} \approx \sqrt{\frac{2}{\varDelta t}}\, \boldsymbol{\mathcal{B}} \cdot \boldsymbol{w}, \tag{6.18}$$

where $\boldsymbol{w}$ is a $6N$ vector containing a Gaussian variate distribution with zero mean and unit variance, and $\boldsymbol{\mathcal{B}}$ is an approximation to the square root of the inverse of the grand mobility tensor, $\boldsymbol{\mathcal{B}} \cdot \boldsymbol{\mathcal{B}}^T = \mathcal{M}^{-1}$.

Finding $\boldsymbol{\mathcal{B}}$ is not a straightforward exercise, again because the coefficients of the grand mobility matrix are not known explicitly. In previous works [61, 145, 164, 165], this problem was overcome by using a spectral approximation to the matrix square root, and by expressing $\boldsymbol{\mathcal{B}}$ in terms of a polynomial expansion involving the grand mobility matrix, the action of which on any vector can then be performed using SPME. In the same spirit, we resort here to a simpler approximation that exploits the diluteness of the suspension: specifically, we decompose the grand mobility matrix into a dominant contribution from the independent and local viscous drag on each fiber and a weaker contribution due to far-field hydrodynamic interactions. To illustrate this approximation, it is convenient to abstract the $6N \times 6N$ matrix $\mathcal{M}$ as a $N \times N$ matrix $\boldsymbol{M}$, each element M_{ij} of which is a 6×6 sub-matrix describing the hydrodynamic coupling between fibers i and j. Formally, we can then decompose the matrix into a sum of local and non-local parts:

$$\boldsymbol{M} = \boldsymbol{L} + \epsilon \boldsymbol{H}, \tag{6.19}$$

where $\epsilon \ll 1$ because, in a dilute suspension, the contribution from hydrodynamic interactions is small compared to the local effect due to viscous drag. Here, $\boldsymbol{L}$ has only diagonal entries, each of which represents the known 6×6 local mobility tensor of individual fibers, while $\boldsymbol{H}$ contains the off-diagonal components accounting for interactions. To proceed, we seek an approximation to the inverse of $\boldsymbol{M}$ of the form $\boldsymbol{M}^{-1} = \boldsymbol{A} + \epsilon\boldsymbol{K}$. Using the fact that $\boldsymbol{M} \cdot \boldsymbol{M}^{-1} = \boldsymbol{I}$ and retaining only terms up to order ϵ, it is straightforward to see that $\boldsymbol{A} = \boldsymbol{L}^{-1}$ and $\boldsymbol{K} = -\boldsymbol{L}^{-1} \cdot \boldsymbol{H} \cdot \boldsymbol{L}^{-1}$. Finding the square root is then a similar exercise, where we seek a matrix $\boldsymbol{B} = \boldsymbol{N} + \epsilon\boldsymbol{J}$ which satisfies $\boldsymbol{B} \cdot \boldsymbol{B}^T = \boldsymbol{M}^{-1}$. We easily find that $\boldsymbol{N} = \boldsymbol{L}^{-1/2}$ and $\boldsymbol{J} = -1/2\ \boldsymbol{L}^{-1/2} \cdot \boldsymbol{H} \cdot \boldsymbol{L}^{-1}$.

Now, recall that each diagonal entry of $\boldsymbol{L}$ is not a scalar but a local 6 × 6 mobility matrix corresponding to a given fiber. This matrix is known explicitly using Equations (6.10)–(6.11) and can be inverted analytically. The final form of the inverse square root as used in the matrix-vector operation in Equation (6.18) above is then

$$\boldsymbol{B} \cdot \boldsymbol{w} \approx \boldsymbol{L}^{-1/2} \cdot \boldsymbol{w} - \frac{1}{2}\ \boldsymbol{L}^{-1/2} \cdot \boldsymbol{H} \cdot (\boldsymbol{L}^{-1} \cdot \boldsymbol{w}), \tag{6.20}$$

where we have omitted the ϵ in the second term. Using Equation (6.20), the evaluation of the generalized force vector $\mathcal{F}_B$ now only requires local operations (of powers of the matrix $\boldsymbol{L}$) as well as a small number of calls to the SPME routine (to evaluate the action of the matrix $\boldsymbol{H}$). Finally, we use the second-order midpoint algorithm of Fixman [166] and Grassia *et al.* [167] for time integration of Equations (6.8)–(6.9), which accurately treats the drift term [145, 165] known to arise in Brownian dynamics simulations of systems with configuration-dependent mobilities.

6.3 Results and discussion

Our main motivation for this study is the verification of the predictions of the continuum model [5] we described in Chapter 5, and so we reiterate here the main results of the linear stability analysis following that model. Flexibility-induced reorientation has two conflicting effects on suspension stability. First, the base-state distribution in a suspension of flexible fibers is anisotropic with a preferential alignment perpendicular to gravity following Equation (6.1). This base state renders the suspension more unstable to number density fluctuations as compared to an isotropic suspension. The central mechanism behind the growth of fluctuations requires particles to be reoriented by the disturbance flow in a way that causes them to be drawn into regions of higher concentration. This mechanism, however, can also be hindered by the second effect wherein flexibility-induced reorientation, if sufficiently strong, acts to keep particles aligned perpendicular to gravity. As previously mentioned, this effect enters at $O(\beta^{-1})$. The relative magnitude of this reorientation with respect to rotational diffusion as well as hydrodynamic disturbances decides which effect dominates.

In order to verify the predictions of the theory using particle simulations, we set as the initial condition a homogeneous distribution in space, with an orientation distribution $\Psi(\theta)$ that depends on the values of the Péclet and elasto-gravitation numbers according to Equation (6.1). In this way, we have a discrete analogue of the continuum problem and can perform direct comparisons. However, we shall also look for completeness at the evolution of a well-stirred suspension, which is expected to have an isotropic orientation distribution regardless of Pe and β – this initial condition, which is perhaps the most relevant to experiments and is addressed in Sec. 6.3.3, is not a steady base state in the continuum model and is therefore not easily addressed by a stability analysis. For the sake of illustration, we select four representative cases to parametrically study the effects of flexibility and thermal fluctuations. These cases are summarized in Figure 6.1, and we shall refer to them as cases A through D from here on. They were chosen to compare and contrast the destabilizing effect of the base state, the suppression due to flexibility-induced reorientation, and the randomizing effect of Brownian motion. Of course, the linear stability results only describe the evolution of the suspension at short times and for small perturbations away from the base state; we shall accordingly only compare the short-time statistics to the mean-field predictions.

	β	Pe	Description
case A	10^6	10^6	Benchmark case: negligible effects of flexibility or Brownian motion
case B	10	10^6	Anisotropic base state with weak flexibility-induced reorientation
case C	0.01	10^6	Anisotropic base state with strong flexibility-induced reorientation
case D	10^6	100	Strong thermal fluctuations

Figure 6.1: The four representative cases used in the simulations to compare and contrast the different regimes of instability.

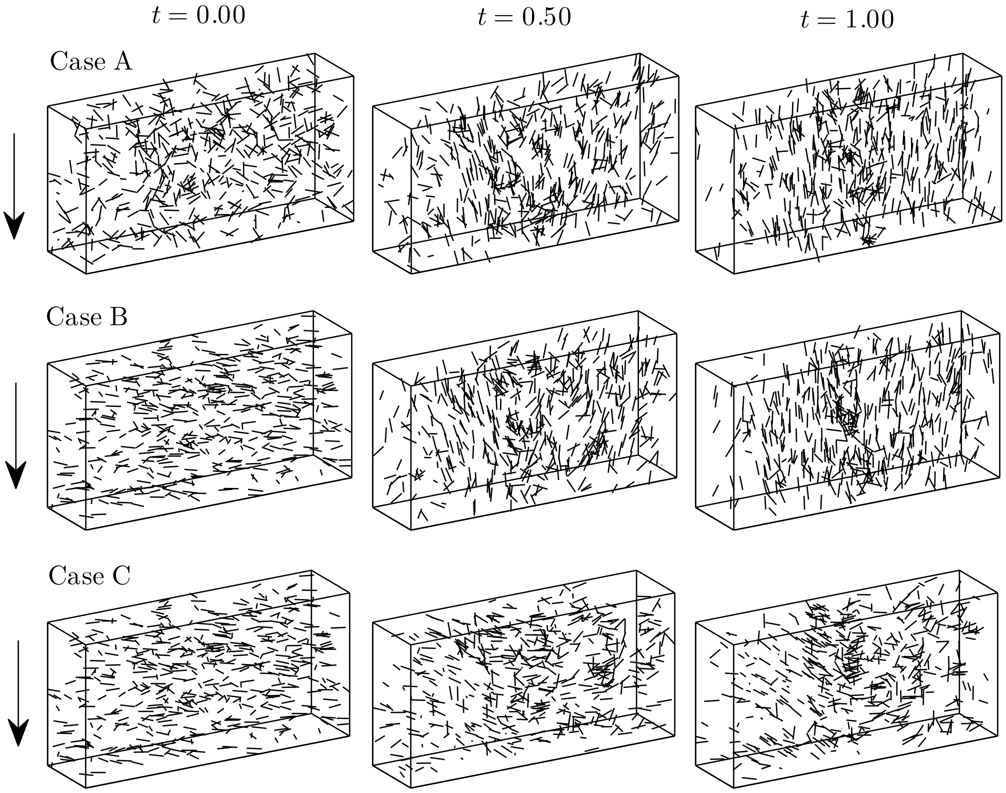

Figure 6.2: Snapshots from simulations of 500 fibers in a 3-D periodic box of size $20 \times 5 \times 10$ particles lengths. Gravity acts in the direction indicated by the arrows. A larger number density of $nL^3 = 0.5$ is used here to better visualize the formation of particle clusters. Case A is the benchmark case of an isotropic suspension of rigid rods. Cases B and C depict the effect of flexibility, the former being when the anisotropic base state dominates and enhances the instability, while the latter is when the rate of reorientation dominates and impedes particle clustering. The initial spatial distribution is homogeneous and identical at $t = 0$; the orientations, however, follow the appropriate distribution of Equation (6.1).

All the simulations discussed here were performed in a periodic box of dimensions $L_x \times L_y \times L_z = 20 \times 5 \times 10$, with gravity pointing downwards in the third dimension. Unless otherwise specified, the data below are ensemble averaged over 16 simulations each of 200 fibers in a periodic box, corresponding to an effective volume fraction of $nL^3 = 0.2$. Snapshots from a set of simulations are shown in Figure 6.2, where the growth of density fluctuations in the different cases described above can be assessed.

6.3.1 Number density fluctuations

The growth of number density fluctuations is a very clear feature of unstable particle suspensions. It has been observed in previous experiments as well as simulations that rigid rods tend to cluster into vertical 'streamers' that sediment much faster than the average settling speed and are surrounded by clarified regions with a preferential alignment in the direction of gravity. Recall that case A corresponds exactly to this well-studied situation, and many of these features are indeed visible in Figure 6.2.

In order to systematically quantify the spatial non-uniformity of the particles in the system, we define a measure $d(t)$ as the standard deviation of the number density distribution across cubic inspection boxes of a given size and placed at arbitrary locations throughout the simulation domain. This quantity is normalized by the standard deviation of the corresponding Poisson distribution, so that $d = 1$ for a randomly distributed suspension of particles. The size of the inspection box was checked to have no qualitative impact on the results shown here, all of which used cubical test sections of volume $(2.5L)^3$ where L is the length of a fiber. Physically, d is a qualitative index of the perturbations to the number density, playing the analogue of the magnitude of concentration fluctuations in the mean-field model.

Figure 6.3(a) shows this quantity for the four representative cases over the length of the entire simulation. Clearly, all cases are destabilized although at different rates. Over a short timescale, these differences are significant. Over long times, however, and especially after persistent clusters are formed, d is no longer found to characterize the minor differences between the four cases. We are primarily interested in the effects of flexibility on the initial growth of fluctuations, and so we look at the short-time behavior of cases A–C in Figure 6.3(b). Recall that $d(t)$ is a proxy for the magnitude of concentration fluctuations, and we use it to extract a linear 'growth rate' by approximating it as $d(t)/d(0) = \exp \varsigma t \approx 1 + \varsigma t$ for short times. We see that the predictions of the continuum theory are qualitatively reproduced in these simulations. As compared to the case of a suspension of initially isotropically oriented rods (case A), an anisotropic suspension with weak flexibility-induced reorientation (case B) is found to be more unstable to concentration fluctuations due to the effect of the base

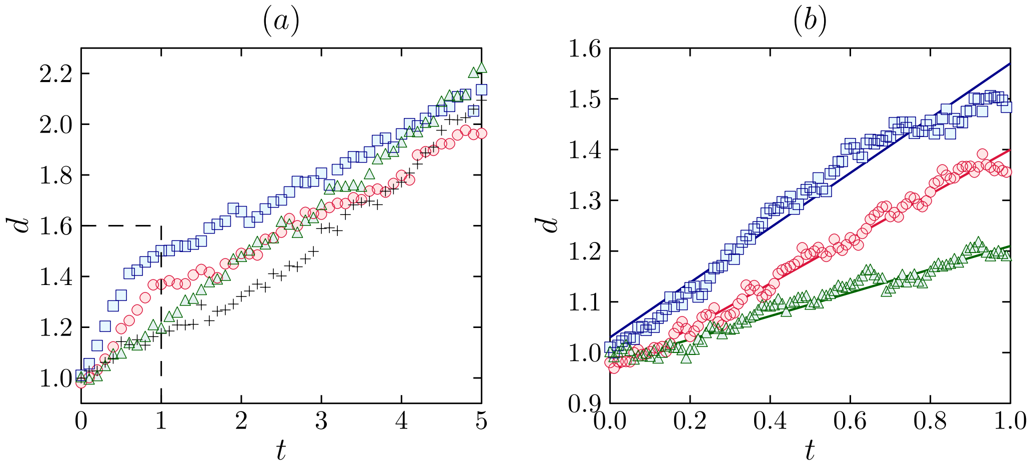

Figure 6.3: (*a*) Growth of number density fluctuations as visualized by the measure $d(t)$. Here, case A is in red (◯), B in blue (□), C in green (△) and D in black (+). $d = 1$ corresponds to a homogeneous spatial distribution of fibers at $t = 0$, and this is seen to be immediately disturbed in all cases. (*b*) A close-up of the region indicated by the dashed box in (*a*) shows the short-time effect of flexibility on suspension stability (cases A–C). The linear fits used to determine the growth rate ς are also shown in solid lines.

state. For yet smaller values of β (more flexible filaments), this base-state effect is overtaken by the independent effect of flexibility in case C, where reorientation under gravity is strong enough to hinder the instability.

A more quantitative comparison to the theory can be obtained by investigating the variations of the measured growth rate in the $Pe - \beta$ parameter space. The theoretical phase diagram from Chapter 5 is overlaid in Figure 6.4 with data from simulations, where the radii of the circles are proportional to ensemble averages of ς across 16 distinct simulations at the corresponding values of β and Pe. In other words, since ς is a qualitative analogue to the linear growth rate in the continuum model, a larger circle in Figure 6.4 corresponds to a suspension that on average is destabilized faster. The trends are obvious and excellently corroborate the theoretical predictions. Moving down along the vertical Pe axis demonstrates that the suspension is always stabilized by thermal randomization. On the other hand, the dependence upon β is non-monotonic. As β is decreased from large values (limit of rigid rods), an increase in the growth rate is first seen due to an increased value of the parameter η which determines the anisotropy of the base state, until $\beta \lesssim 1$ below which the independent

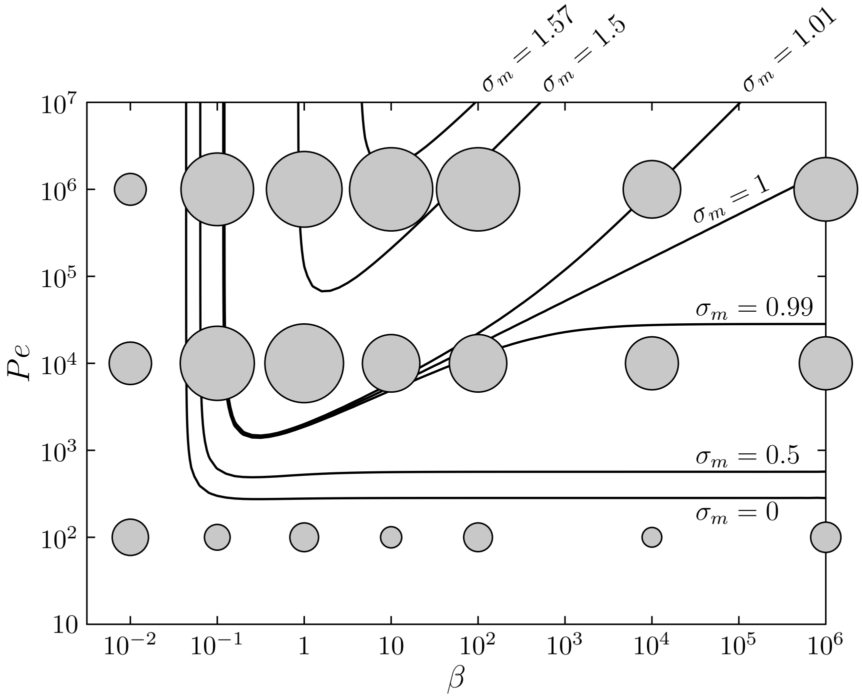

Figure 6.4: A phase diagram of suspension stability in the $\beta - Pe$ parameter space. The circles are proportional to the ς parameter which is a qualitative index of the growth rate of number density fluctuations in particle simulations. The contours in solid lines correspond to the our linear theory [5] from Chapter 5, with predicted maximum growth rates σ_m indicated. According to the normalization used, $\sigma_m = 1$ is the theoretical growth rate when $\beta \to \infty$ and $Pe \to \infty$ (rigid non-Brownian rods).

effect of flexibility-induced reorientation kicks in and tends to suppress the instability by resisting rotation of the fibers by the disturbance flow.

6.3.2 Horizontal particle migration

The mechanism of destabilization first described by Koch and Shaqfeh [125] is based on the migration of particles in the direction of the most unstable wavevector, which in the present case is the longest periodic direction perpendicular to gravity. Orientability of the particles in the disturbance flow is key to this mechanism, and a suspension of spherical particles is indeed known to be stable due to their isotropic mobility that prevents this lateral drift. At the particle level, suppression of the growth rate of fluctuations should therefore have a direct footprint on the horizontal

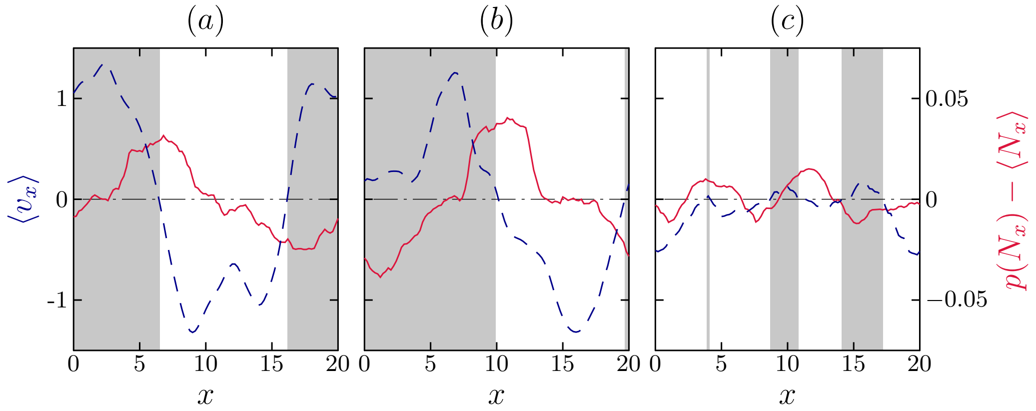

Figure 6.5: Horizontal drift velocity and number density distribution as a function of the most unstable direction. $\langle v_x \rangle$ is shown in blue dashed lines with its axis on the left, and $p(N_x)$ is in red solid lines with its axis on right. The mean number density is subtracted from the distribution for clarity, and the shaded areas are meant to guide the eye towards regions where the measured drift is to the right (and to the left otherwise). (a), (b), and (c) represent one simulation corresponding to cases A, B, and C respectively, each at time $t = 1.00$.

migration of fibers, which in turn is intricately linked to the instantaneous orientation distribution of the filaments.

We first check that the migration of fibers is indeed towards regions of higher concentration. Figure 6.5 shows the ensemble-averaged mean velocity $\langle v_x \rangle$ and the number density distribution $p(N_x)$ in the horizontal (most unstable) direction at a specific time instant for the three representative cases. Both number density and velocity fields are averaged over the height and width of the simulation box so as to be a function of x only, and the velocity is normalized by the settling speed of an isolated vertical fiber. For cases A and B, when the flexibility-induced rotation is not overwhelmingly large, the drift of particles towards clusters is evident, as is the suppression of this mechanism due to strong horizontal reorientation because of flexibility in case C. The instantaneous orientation distribution determines, via Equation (6.10), this drift velocity, and we look next to quantify this microstructural link.

Figure 6.6 illustrates the key differences in lateral drift and orientation distributions between cases A–C, leading to the differences in the growth of number density fluctuations discussed above. We define $\langle |v_x| \rangle$ as the ensemble-averaged mean of the absolute value of the velocity component in the x-direction perpendicular to gravity, which is the most unstable direction. We choose the absolute value as a quantifiable measure of the drift rather than the mean drift velocity $\langle v_x \rangle$ used above because the latter would be zero based on symmetry and periodicity. This is plotted versus time in Figure 6.6(a). We also show in Figure 6.6(b)–(e) the evolution of the orientation distribution $\psi(\theta)$ in each case, where θ denotes the polar angle between the fiber axis and the direction of gravity.

The effect of the base state is very clear at very short times $t \approx 0$, where the orientation distribution is nearly isotropic for case A but increasingly anisotropic and peaked around $\theta = \pi/2$ in cases B and C. The lateral drift velocity depends directly on the instantaneous orientation of a fiber. Due to the form of the settling velocity of an individual fiber following Equation (6.3), particles migrate more slowly in the x-direction when oriented nearly perpendicular to gravity. This is evident from the values of $\langle |v_x| \rangle$ at $t \approx 0$, where cases B and C display much weaker drift than case A. In case B, where the flexibility-induced reorientation is weak and the disturbance field immediately dominates the dynamics, the effect of the base-state anisotropy on suspension stability is seen in the rapid increase of $\langle |v_x| \rangle$ due to the rapid reorientation of the particles in a direction that facilitates migration. This is indeed the origin of the enhanced growth rate due to base-state anisotropy first proposed in the last chapter. Particles in case B have a higher chance of being rotated by the disturbance field into configurations that allow them to migrate towards regions of larger concentration, thereby bolstering the instability.

In case C, however, we observe that flexibility-induced reorientation is sufficiently strong to maintain an anisotropic orientation distribution well past the initial growth of the instability. Correspondingly, the horizontal drift velocity remains much weaker than in cases A and B. This directly reflects the independent effect of flexibility. Particles now feel the competition between the disturbance velocity field, that tends to orient them away from a nearly horizontal configuration, and flexibility that tries to keep them horizontally aligned. For the value of β chosen in case C, the latter dominates at short times, which tends to slow the instability by hindering horizontal particle migration.

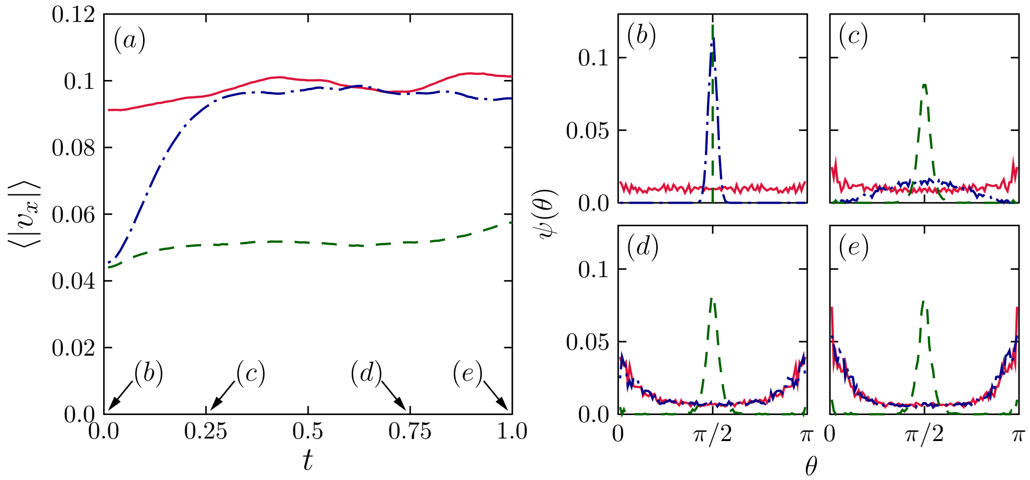

Figure 6.6: (*a*) The effect of flexibility on mean horizontal drift velocities. Case A is the red solid line, case B is the blue dash-dot line, and case C is the dotted green line. (*b*)–(*e*) show the corresponding orientation distributions averaged across all fibers in all simulations at times indicated by the arrows in (*a*).

6.3.3 Stability of a well-stirred suspension

We have thus far used our simulations as a means to verify the predictions of the linear stability analysis from Chapter 5. Recall that the linear theory considers a Smoluchowski equation for the concentration field, and perturbs it around a particular base state that solves the conservation equation exactly when the suspension is homogeneous in space. An arbitrary initial condition, however, is not amenable to a stability analysis the way it was performed because it may not solve a steady base state exactly. In the previous discussion, we initialized the particle configurations in our simulations according to the exact theoretical base state, assuming that such a state was somehow established prior to the onset of the instability. In a physical experiment, the initial stirring of the suspension is expected to lead to a random isotropic suspension, and the question remains whether the orientation distribution in that case would evolve towards the theoretical base state sufficiently fast for the predictions of the linear theory to hold, or whether the growth of the concentration instability would occur more rapidly. Here, we shed light on some of these questions using our simulations.

We have seen enough of the physics of the problem to postulate what might

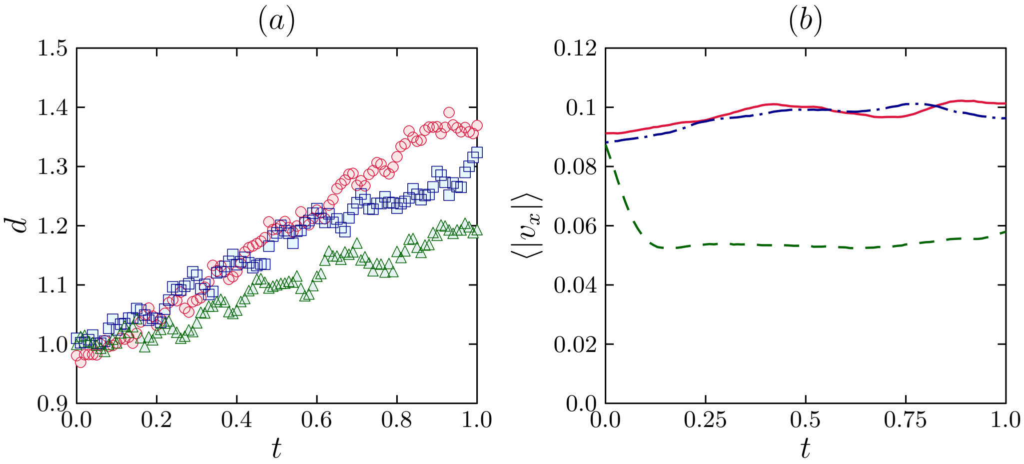

Figure 6.7: The stability of a well stirred (initially isotropic) suspension. We now only see the independent effect of flexibility, as expected. Case A is in red (◯ or a solid line), B is in blue (□ or a dash-dot line), and C is in green (△ or dashed line).

happen. If the suspension were to be isotropic in orientation at $t = 0$, we expect the effect of the base-state anisotropy to vanish. Flexibility-induced reorientation then only has one effect, namely, to oppose the rotation of the fibers towards orientations that cause them to be drawn into regions of higher concentration. This effect must become more significant as β decreases, and always acts to suppress the instability. In other words, we expect a well-stirred suspension of weakly flexible fibers to experience, on average, a weaker concentration instability than in the benchmark case of a suspension of rigid rods.

Figure 6.7 summarizes the results of simulations corresponding to an initially isotropic particle distribution and confirms our hypothesis. Flexibility is seen always to suppress the instability, as demonstrated in Figure 6.7(a) by the effective growth rate of the parameter d, which monotonically decreases with increasing flexibility (decreasing β). Figure 6.7(b) also shows the horizontal drift velocity, which should be contrasted with Figure 6.6(a). In all cases, $\langle |v_x| \rangle$ now starts at the same value at $t = 0$, but is immediately suppressed in case C as a result of the rapid establishment of anisotropy in the orientation distribution leading to a weaker instability. In this case, the time scale over which the suspension evolves from the well-stirred isotropic distribution to the horizontally-aligned configuration is fast compared to the growth of the instability. This time scale has a relevant effect only when β is sufficiently small, as we see no discernible difference for case B in the statistics of $\langle |v_x| \rangle$ – the leading-order effect of the base state predicted by the linear theory is absent here.

The stability analysis stemmed from a steady base-state solution, which is not necessarily the case in a randomized suspension. One way to gain insight into such a system would be a stability analysis based on a quasi-steady base state, if one exists. However, our simulations reveal that the anisotropic orientation distribution is quickly established for the case with $\beta = 0.01$. This is particularly evident in Figure 6.7(b) where the absolute horizontal drift $\langle |v_x| \rangle$ rapidly evolves to the values corresponding to the steady-state orientation distribution used in the stability analysis (compare with Figure 6.6(a)), suggesting that the analysis holds thereafter.

6.4 Conclusion

In this chapter, we have investigated the sedimentation of a suspension of weakly flexible fibers using particle simulations, in an attempt to shed light on the effect of fiber flexibility on the microstructural changes at the single particle level as well as on the stability of the suspension as a whole. We used the result from our previous work on individual elastic filaments to isolate the single additional effect of weak flexibility on the settling dynamics of a fiber, i.e., flexibility-induced reorientation. The effect of this reorientation on a suspension of such particles has already been studied using a linear stability on a mean-field model. The primary objective of the current study was to validate the predictions of the continuum model using simulations that captured the detailed dynamics of each fiber in the suspension.

We presented a numerical method for simulating large periodic systems of weakly flexible filaments, which we adapted from previous work on rigid particles. The entire set of evolution equations for the positions and orientations of N fibers was reduced to a set of matrix-vector multiplications only requiring knowledge of the current configuration of the particles in suspension. The calculation of these matrix-vector multiplications was further accelerated using the efficient smooth particle-mesh Ewald (SPME) summation algorithm of Saintillan *et al.* [141] together with an approximate form for the determination of Brownian displacements based on diluteness, leading to a total computational cost of $O(N \log N)$.

We then went on to study systematically the effect of flexibility on suspension stability. Representative sets of parameters were chosen to illustrate most dramatically the different regimes of instability and the phenomena that demarcate them. Three cases were brought up repeatedly: one where the effect of flexibility was negligible, a second where flexibility-induced reorientation was known to establish an anisotropic base state leading to an enhancement of the growth of fluctuations, and a third where that same reorientation mechanism was strong enough to compete with rotation by the disturbance flow so as to impede the instability.

We first examined the evolution of number density fluctuations by means of a parameter $d(t)$ capturing the magnitude of fluctuations with respect the random Poisson distribution imposed at $t = 0$. The time evolution of d was shown to follow the trends predicted by the linear continuum theory. The effect of the anisotropic base state was seen to enhance the instability, while increasing flexibility further eventually impedes the growth of fluctuations. Extracting a short-time growth rate from the evolution of $d(t)$ allowed us to populate a phase diagram in $\beta - Pe$ space, which showed excellent qualitative agreement with the theory.

A more detailed picture of the microstructural changes and their influence on stability was obtained by calculating the horizontal drift of the particles in the simulation. Recall that the mechanism of destabilization hinges on the ability of particles to migrate perpendicular to gravity towards regions of higher concentration. We saw that, on an average, the effect of the anisotropic base state alone is to enhance this horizontal migration as soon as the suspension is allowed to sediment. This verifies the hypothesized mechanism for an enhanced instability, i.e., a larger fraction of particles now reorient in a way as to destabilize the suspension. The independent effect of flexibility, as expected, was to suppress this horizontal migration and prevent particle clustering by forcing particle orientations to remain close to horizontal.

Finally, we also used our simulations to analyze the case of a well-stirred suspension in which the initial orientation distribution is isotropic regardless of the values of β and Pe. This situation is outside the purview of the linear stability analysis performed on the mean-field model, but is perhaps the most relevant to describe experiments where the initial mixing of the suspension would lead to a random distribution. We speculated in this case that the destabilizing effect of the base state would vanish, and that flexibility would therefore only have a stabilizing effect. This was seen to be the case indeed: the number density fluctuations were shown to systematically decrease with increasing flexibility.

The effects of physically relevant considerations like walls and fluid inertia on flexible fiber suspensions are still open problems, theoretically as well as via simulations. While we expect the twofold consequences of flexibility to arise regardless, the relative strength of these effects may vary depending on the particular problem at hand. Future work might consider this problem from an experimental perspective, to which end we note that our predictions are also valid for a suspension of weakly flexible fibers raising against gravity due to buoyancy, or more generally to any situation where a body force exists that causes particles to reorient perpendicular to it. Finally, we emphasize that we have primarily focused on short-time statistics in dilute systems with weak deformations; more detailed numerical methods would be needed to capture near-field lubrication interactions, entanglements, and particle shape deflections due to the disturbance field, all of which might become relevant over long times when local concentrations are sufficiently large.

The material in Chapter 6 is being considered for publication in *Physics of Fluids* (2015), authored by Harishankar Manikantan and David Saintillan.

Chapter 7

Conclusion and future directions

7.1 Conclusion

In this work, we have considered a myriad of problems where the interplay between viscous, elastic, Brownian, and gravitational forces result in interesting configurational and dynamical behavior of flexible filaments. The strategy in most problems that we explored was to probe analytically when possible, and to use detailed numerical simulations to confirm predictions or explore more complex situations, with the central effort being directed towards elucidating the physical mechanisms underlying these dynamics.

In Chapter 2, we developed a model for semiflexible polymers immersed in a viscous fluid, and applied it to cases relevant to microfluidic flow setups. We saw that polymers tumble in shear flow, and stretch or buckle depending on orientation in extensional flow. Where possible, comparisons were drawn from experiments involving typical examples of semiflexible biopolymers such as actin. A recurring theme in this chapter was the competition between the line tension induced in the backbone of the filament, which serves to keep it inextensible, and its elastic rigidity. We also developed in this chapter a theory that describes the stretch-coil transition of polymers as a stochastic supercritical bifurcation, with the resulting expression specifying the exact nature of the finite-temperature rounding of the transition. While this analysis solves a vital facet of fluid-filament interaction problems at the microscale, it also provides a powerful tool for experimentalists to extract mechanical properties of single macromolecules by fitting shape deformations around critical points.

We then used the idea of buckling and subsequent reorientation of polymers around a stagnation point to propose a problem that mimics certain bio-assays. Specifically, in Chapter 3, we studied the dynamics and transport properties of semi-flexible polymers in a periodic two-dimensional cellular flow. We found that thermal fluctuations tend to cause the filaments to drift towards and become trapped inside vortical cells for long periods of time. These frequent trapping events significantly hinder the spatial transport of the polymers, which shifts from diffusive to subdiffusive as fluctuations become significant. We also highlighted the subtle effect of flexibility on the transport properties, suggesting that while some level of flexibility is critical for the effective transport across cells as it enables buckling, very floppy filaments with short persistence lengths are strongly affected by thermal fluctuations, which cause their frequent trapping and hinder their transport across the lattice.

In Chapter 4, we investigated the fundamental dynamics of a single flexible filament as it sediments in a viscous fluid. The competition between elastic and gravitational forces was characterized by a dimensionless quantity that we termed the elasto-gravitation number. We first considered the weakly flexible regime, where the filament is nearly rigid, and using a multiple-scale analysis found a self-similar scaling of the filament shape with an amplitude dependent upon the body orientation. A mechanistic illustration of the shape and reorientation of filaments was provided, and we saw how translational velocity coupled with flexibility-induced reorientation results in non-trivial trajectories of settling filaments. We also explored the regime of highly flexible filaments sedimenting along its long axis, where a buckling instability was hypothesized to occur in the leading half alone. This was then then described using a linear stability analysis, and illustrated further with full numerical simulations.

In Chapter 5, we exploited the previously obtained results on the sedimentation of isolated weakly flexible filaments to develop a mean-field model for a suspension of such particles. The purpose was to explore the effect of anisotropic particles that reorient due to weak flexibility in the presence of long-ranged hydrodynamic interactions. Speculating based on the mechanism that leads to an instability in the case of a suspension of rigid rods, we surmised that an anisotropic suspension composed of fibers oriented perpendicular to gravity would be more unstable to concentration fluctuations, owing to the fact that individual particles are more likely to be reoriented by the disturbance flow in a way that enhances the instability. A second and more direct effect of particle reorientation was to suppress the instability by preventing clustering. Possible mechanisms for these opposing effects were suggested based on solutions of the eigenvalue problem that governs the stability of the suspension.

In Chapter 6, we took to detailed numerical simulations to verify these mechanisms, and to gain insight into cases more representative of experimental studies. Particle simulations provided us with a more detailed picture of the microstructural changes and their influence on stability. The mechanism behind our mean-field theoretical predictions were clarified with statistics of particle migration and clustering. Finally, we also used our simulations to analyze the case of a well-stirred suspension in which the initial orientation distribution is random. This situation is outside the purview of the linear stability analysis performed on the mean-field model, but is perhaps the most relevant to describe experiments where the initial mixing of the suspension would lead to a random orientation distribution. We had speculated that the destabilizing effect of the base state would vanish, and that flexibility would therefore only have a stabilizing effect. This was seen indeed to be the case: the number density fluctuations were shown to systematically decrease with increasing flexibility.

7.2 Directions for future work

There are many avenues along which this work might be extended to study more complex physical processes. Three broad categories are listed below:

- *Confinement and wall effects:* In all of our studies, we have assumed an infinite fluid with no wall effects whatsoever. While this is a fair assumption in many scenarios, many biological polymers naturally exist close to walls whose effects might not always be negligible. This is also true of micro-channel experiments involving semiflexible polymers, polymer translocation through pores, as well as in tanks used to study sedimentation where confinement could play prominent roles. In particular, hydrodynamic interactions with walls are crucial in pressure-driven flows, as they can lead to cross-streamline migration [55, 168].

Rods sedimenting near vertical walls, for instance, are known to show curious trajectories involving 'glancing' and 'sliding' dynamics [169]. One approach to study such problems numerically would be to use the appropriate Green's functions [170] that account for image singularities and the consequent corrections to the flow field to ensure wall boundary conditions. Such techniques have been applied successfully [55] to study migration of short-chain flexible polymers. Another computational approach, proposed by Hernández-Ortiz *et al.* [95], is based on the particle-mesh framework and has been proven to be efficient and accurate in treating hydrodynamic interactions with walls. Analytically, reduced-order models based on the method of images have been recently shown [171] to predict very well the dynamics of a rigid spheroid sedimenting near a vertical wall. The case of a sedimenting flexible particle will be more involved, but promises to reveal a wide range of non-trivial dynamics.

- *Electrokinetics and electrophoresis:* Our model holds the capability to be extended to study electrokinetic transport of charged polymers in nanochannels [46, 172]. This will require coupling the equations described in this work to a Laplace solver for the electric potential inside the channels, and inclusion of an additional electric force acting on the polymer chains. This extension of the algorithm can be applied to study, for instance, the electrophoretic separation of short-chain flexible polymers such as DNA fragments, which has been reported in experiments but has yet to be fully explained theoretically. Also, while the effect of electric fields on the stability of a suspension of rods has been well studied in the past decade [145, 165], the corresponding physics in a suspension of flexible fibers warrants attention.

- *Entanglements and concentration effects:* In all the cases considered here, we steered clear of situations where a polymer could fold over itself. Such excluded volume considerations could become important in the long-time dynamics of highly flexible filaments, and a careful inclusion of steric forces within this framework is an open problem. Such transient entanglements are crucial to the viscoelastic properties of the cytoskeleton [173]. In the sedimentation of multiple close-packed filaments, for example, issues such as entanglements may dominate the dynamics. Even in the case of a suspension of weakly flexible fibers, we have neglected the effect of disturbance field of one particle on the shape of the other under the assumption of sufficient dilution. This approximation is obviously void when particles come very close to each other, which is often the case in a concentrated dispersion of flexible filaments. A more detailed continuum theory that incorporates filament shapes is a challenging open problem, and so is the development of efficient numerical algorithms to study such systems.

Appendix A

Linear eigenmodes of the stretching problem

A.1 The eigenvalue problem

We first derive the eigenvalue problem widely used in the context of suppression of fluctuations in Chapter 2, abbreviated here as $D_{\tilde{\Sigma}} W^{(n)} = \Lambda_n W^{(n)}$. Consider a filament aligned very close to the x-axis due the extensional flow $\boldsymbol{u}_0 = (\dot{\gamma}x, -\dot{\gamma}y)$ between $-L/2$ and $L/2$ with its center at the stagnation point at $\boldsymbol{x} = (0,0)$. Following Equation (2.36), we have the (potential) energy of the filament due to elasticity and induced tension for small amplitude fluctuations $h(x)$ away from the x-axis as

$$\mathcal{E} = \frac{1}{2}\int_{-L/2}^{L/2} \left[\kappa h_{xx}^2 + T(x) h_x^2\right] \mathrm{d}x, \tag{A.1}$$

where the tension is (Equation (2.39))

$$T(x) = \frac{2\pi\mu\dot{\gamma}}{\ln(1/\epsilon^2 e)}\left[\frac{L^2}{4} - x^2\right]. \tag{A.2}$$

Now, the Euler-Lagrange equations that minimises $\mathcal{E}$ for $h(x)$ is

$$\frac{\partial \mathcal{E}}{\partial x} - \frac{\partial}{\partial x}\left(\frac{\partial \mathcal{E}}{\partial h_x}\right) + \frac{\partial^2}{\partial x^2}\left(\frac{\partial \mathcal{E}}{\partial h_{xx}}\right) = f(x), \tag{A.3}$$

where subscripts denote differentiation with respect to x, and $f(x)$ is a force distribution per unit length that causes the filament to assume this shape. The Euler-Lagrange equation gives us the governing equation for the energetically most favorable positions $h(x)$:

$$\kappa h_{xxxx} - \left(T(x)h_x\right)_x = f(x), \tag{A.4}$$

which, using Equation (A.2) for $T(x)$, gives

$$\kappa h_{xxxx} - \frac{2\pi\mu\dot{\gamma}}{\ln(1/\epsilon^2 e)}\left[\left(\frac{L^2}{4} - x^2\right)h_x\right]_x = f(x). \tag{A.5}$$

This is a linear fourth-order differential equation for $h(x)$, and gives the eigenvalue problem with eigenfunctions $W^{(n)}(x)$ and corresponding eigenvalues λ_n:

$$\kappa W^{(n)}_{xxxx} - \frac{2\pi\mu\dot{\gamma}}{\ln(1/\epsilon^2 e)}\left[\left(\frac{L^2}{4} - x^2\right)W^{(n)}_x\right]_x = \lambda_n W^{(n)}, \tag{A.6}$$

with the boundary condition $W^{(n)}_{xx}(\pm L/2) = W^{(n)}_{xxx}(\pm L/2) = 0$, representing force-free and moment-free ends.

A convenient rescaling is $\xi = \pi x/L$, so that $\xi \in [-\pi/2, \pi/2]$. The system then becomes

$$W^{(n)}_{\xi\xi\xi\xi} - \tilde{\Sigma}\left[\left(\frac{\pi^2}{4} - \xi^2\right)W^{(n)}_\xi\right]_\xi = \varLambda_n W^{(n)}, \tag{A.7}$$

or

$$D_{\tilde{\Sigma}}W^{(n)} = \varLambda_n W^{(n)},$$

where $\tilde{\Sigma}$ is a dimensionless strain rate defined in Equation (2.41), and $\varLambda_n$ are the rescaled eigenvalues $\varLambda_n = L^4\lambda_n/\pi^4\kappa$. Equation (A.7), along with the boundary conditions, defines the basis for positions of the filament.

A.2 Energy and variance

From Equation (A.1), we have by repeated integration by parts

$$\mathcal{E} = \frac{1}{2}\int_{-L/2}^{L/2}\left[\kappa h_{xx}^2 + T(x)h_x^2\right]\mathrm{d}x \tag{A.8}$$

$$= \frac{1}{2}\left[\left(\kappa h_{xx}h_x\right)\Big|_{-L/2}^{L/2} - \kappa\int_{-L/2}^{L/2} h_{xxx}h_x\mathrm{d}x + \left(Th_xh\right)\Big|_{-L/2}^{L/2} - \int_{-L/2}^{L/2}\left(Th_x\right)_x h\mathrm{d}x\right] \tag{A.9}$$

$$= \frac{1}{2}\left[-\kappa\left\{\left(h_{xxx}h\right)\Big|_{-L/2}^{L/2} - \int_{-L/2}^{L/2} h_{xxxx}h\mathrm{d}x\right\} - \int_{-L/2}^{L/2}\left(Th_x\right)_x h\mathrm{d}x\right] \tag{A.10}$$

$$= \frac{1}{2}\int_{-L/2}^{L/2}\left[\left\{\kappa h_{xxxx} - \left(Th_x\right)_x\right\}h\right]\mathrm{d}x, \tag{A.11}$$

where all boundary terms (in Equations (A.9) and (A.10)) are zero due to the boundary conditions and the fact that tension is zero at the ends by definition. Now, since $h(x)$ is projected onto the $\{W^{(n)}(x)\}$ basis, we may write

$$h(x) = \sum_{n=1}^{\infty} a_n W^{(n)}(x). \tag{A.12}$$

This then leads to

$$\begin{aligned}
\mathcal{E} &= \frac{1}{2}\int_{-L/2}^{L/2} \left\{ \kappa \sum_{n=1}^{\infty} a_n W^{(n)}_{xxxx} - \left(T \sum_{n=1}^{\infty} a_n W^{(n)}_{x} \right)_x \right\} \left(\sum_{n=1}^{\infty} a_n W^{(n)} \right) \mathrm{d}x && \text{(A.13)}\\
&= \frac{1}{2}\int_{-L/2}^{L/2} \left(\sum_{n=1}^{\infty} \left\{ \kappa W^{(n)}_{xxxx} - \left(T W^{(n)}_{x} \right)_x \right\} a_n \right) \left(\sum_{n=1}^{\infty} a_n W^{(n)} \right) \mathrm{d}x && \text{(A.14)}\\
&= \frac{1}{2}\int_{-L/2}^{L/2} \left(\sum_{n=1}^{\infty} a_n \lambda_n W^{(n)} \right) \left(\sum_{n=1}^{\infty} a_n W^{(n)} \right) \mathrm{d}x, && \text{(A.15)}
\end{aligned}$$

where we have used the expression for tension and Equation (A.6). Now, the basis $\{W^{(n)}(x)\}$ is orthogonal with

$$\frac{1}{L}\int_{-L/2}^{L/2} W^{(m)}(x) W^{(n)}(x) \mathrm{d}x = \delta_{mn}. \tag{A.16}$$

Using this property, Equation (A.15) simplifies to

$$\mathcal{E} = \frac{L}{2}\sum_{n=1}^{\infty} a_n^2 \lambda_n. \tag{A.17}$$

This tells us that the energy decomposes into a sum of contributions from independent modes. It then follows from the the equipartition principle that each of these independent contributions $\langle a_n^2 \lambda_n L/2 \rangle$ must equal $k_B T/2$. In other words, emphasising the independence of contributions from different modes, we may write

$$\langle a_m a_n \rangle = \delta_{mn} \frac{k_B T}{\lambda_n L}. \tag{A.18}$$

Using the rescaled eigenvalue $\varLambda_n = \lambda_n L^4/\pi^4 \kappa$ and the definition of the persistence length $\ell_p = \kappa/k_B T$, this simplifies to

$$\langle a_m a_n \rangle = \delta_{mn} \frac{L^3}{\varLambda_n \pi^4 \ell_p}. \tag{A.19}$$

We now define the variance of amplitude fluctuations as

$$V(x) = \left\langle [h(x) - \bar{h}]^2 \right\rangle , \tag{A.20}$$

where $\bar{h}$ is the mean filament amplitude. When aligned approximately with the x-axis, we can set $\langle a_n \rangle = 0$ and so $\bar{h} = 0$. This also follows from the variance of the mean filament angle from the x-axis being very small. Then, using Equation (A.19),

$$\begin{aligned} V(x) &= \left\langle h(x)^2 \right\rangle && \text{(A.21)} \\ &= \left\langle \left[\sum_{n=1}^{\infty} a_n W^{(n)}(x) \right]^2 \right\rangle && \text{(A.22)} \\ &= \sum_{n=1}^{\infty} \frac{L^3}{\varLambda_n \pi^4 \ell_p} W^{(n)}(x)^2 && \text{(A.23)} \\ \Rightarrow \quad V(x;\tilde{\Sigma}) &= \frac{L^3}{\ell_p \pi^4} \sum_{n=1}^{\infty} \frac{W^{(n)}(x;\tilde{\Sigma})^2}{\varLambda_n(\tilde{\Sigma})}. && \text{(A.24)} \end{aligned}$$

Equation (A.24) appears in Chapter 2 as Equation (2.43).

A.3 Solving for the eigenfunctions

In the special case of $\tilde{\Sigma} = 0$, the operator $D_{\tilde{\Sigma}}$ reduces to a one-dimensional biharmonic equation: Equation (A.7) reduces to

$$W^{(n)}_{\xi\xi\xi\xi} = k_n^4 W^{(n)}. \tag{A.25}$$

We solve the system for $x \in [0, L]$ as the solution is relatively simpler when shifted to this range. $W^{(n)}(x)$ admits solutions of the form:

$$W^{(n)}(x) = A \sin k_n x + B \cos k_n x + C \sinh k_n x + D \cosh k_n x. \tag{A.26}$$

Clearly, the boundary conditions $W^{(n)}_{xx}(0) = W^{(n)}_{xxx}(0) = 0$ yields $A = C$ and $B = D$. The conditions $W^{(n)}_{xx}(L) = W^{(n)}_{xxx}(L) = 0$ then has

$$\frac{A}{B} = \frac{\sin k_n L + \sinh k_n L}{\cos k_n L - \cosh k_n L}. \tag{A.27}$$

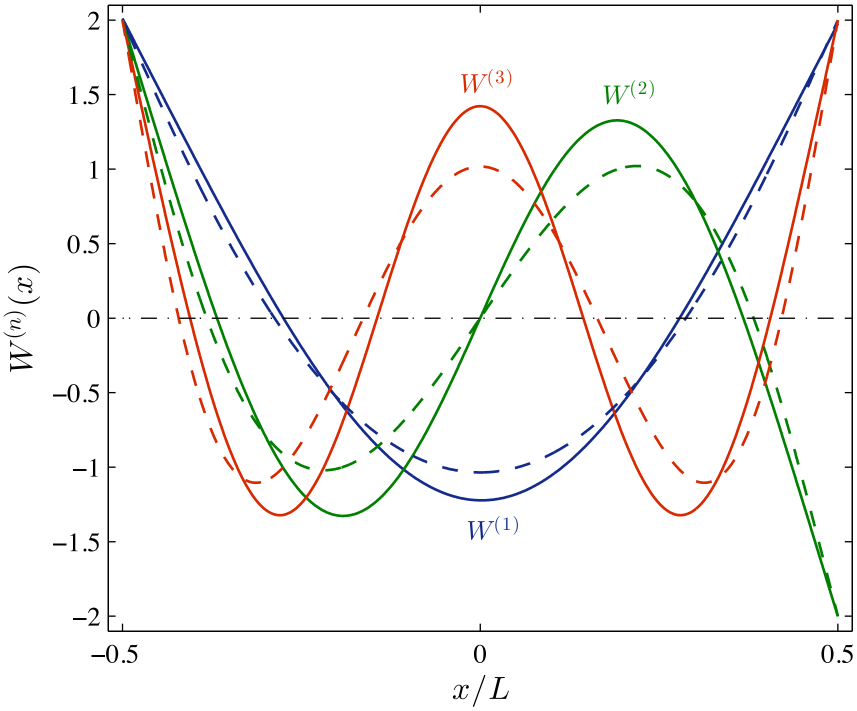

Figure A.1: Normalized eigenfunctions $W^{(n)}(x)$ of the $D_{\tilde{\Sigma}}$ operator. Eigenfunctions of the biharmonic operator corresponding to D_0 are in solid lines, and the corresponding eigenfunctions of D_{100} are in dashed lines.

This is subject to a solvability condition on the wavevectors k_n[†] which, for free-end boundary conditions, is

$$\cos k_n L \cosh k_n L = 1, \tag{A.28}$$

with $k_0 = 0$ (corresponding to the constant solution $W^{(0)} = 1$) and $k_n L \simeq (n + 1/2)\pi$ for $n \geq 1$. Since $k_n^4 = \lambda_n / A = \Lambda_n \pi^4 / L^4$, we can immediately see that $\Lambda_n \simeq (n+1/2)^4$. This fact was used in Section 2.6.1 to justify the resemblance of the variance profile to the contribution from fundamental mode: $V(x, \tilde{\Sigma})$ in Equation (A.24) is dominated by the first term.

The corresponding eigenfunctions are plotted in Figure A.1. Eigenfunctions of $D_{\tilde{\Sigma}}$ when $\tilde{\Sigma} \neq 0$ cannot be determined analytically but a numerical solution is relatively straightforward, and the shapes are seen to be similar to the $\tilde{\Sigma} = 0$ case.

[†] The interested reader is directed to Problems 4 through 6 in section 25 of Landau and Lifshitz [108] or Appendix B of Wiggins *et al.* [59] for a comprehensive treatment of the solvability conditions and eigenfunctions for not just free-end boundaries, but also a wide range of possible scenarios including clamped ends, hinged ends, and combinations thereof.

Appendix B

Flux velocities for the Fokker-Planck equation

In the continuum approach used in Chapter 3, the conservation equation (3.2) has as unknowns the flux velocities of the rod. For this, we turn to the leading terms in the slender-body equation (1.10), now written in terms of the center-of-mass position and orientation of the particle. For a rod of aspect ratio $\epsilon = a/L$ as before and parametrized by $s \in [-L/2, L/2]$, the position of a point along the rod is now written $\boldsymbol{x}_0 + s\boldsymbol{p}$, where $\boldsymbol{x}_0$ is its center ($s = 0$) and $\boldsymbol{p}$ the unit tangent vector at the center. To leading order in $\ln \epsilon$, the slender-body equation (1.10) is then

$$\dot{\boldsymbol{x}}_0 + s\dot{\boldsymbol{p}} - \boldsymbol{u}_0(\boldsymbol{x}_0 + s\boldsymbol{p}) = \frac{\ln \epsilon}{4\pi\mu}(\boldsymbol{I} + \boldsymbol{p}\boldsymbol{p}) \cdot \boldsymbol{f}(\boldsymbol{x}_0 + s\boldsymbol{p}). \tag{B.1}$$

Integrating Equation (B.1) across the length of the rod and requiring that the total hydrodynamic force acting on the particle be zero gives the translational flux velocity:

$$\dot{\boldsymbol{x}}_0 = \frac{1}{L}\int_{-L/2}^{L/2} \boldsymbol{u}(\boldsymbol{x}_0 + s\boldsymbol{p})\,\mathrm{d}s. \tag{B.2}$$

In order to determine $\dot{\theta}$, we multiply Equation (B.1) by s and then integrate with respect to s giving

$$\dot{\boldsymbol{p}}\frac{L^3}{12} - \int_{-L/2}^{L/2} s\boldsymbol{u}(\boldsymbol{x}_0 + s\boldsymbol{p})\,\mathrm{d}s = \frac{\ln \epsilon}{4\pi\mu}(\boldsymbol{I} + \boldsymbol{p}\boldsymbol{p}) \cdot \int_{-L/2}^{L/2} s\boldsymbol{f}(\boldsymbol{x}_0 + s\boldsymbol{p})\,\mathrm{d}s. \tag{B.3}$$

Since the angular flux is purely in the orthoradial directions (as $\dot{\boldsymbol{p}} \cdot \boldsymbol{p} = 0$), we may pre-multiply Equation (B.3) with $(\boldsymbol{I} - \boldsymbol{pp})$, and it follows that

$$\dot{\boldsymbol{p}}\frac{L^3}{12} = (\boldsymbol{I} - \boldsymbol{pp}) \cdot \int_{-L/2}^{L/2} s\boldsymbol{u}(\boldsymbol{x}_0 + s\boldsymbol{p})\,\mathrm{d}s - \frac{\ln\epsilon}{4\pi\mu}\boldsymbol{p} \times \int_{-L/2}^{L/2} \boldsymbol{p} \times s\boldsymbol{f}(\boldsymbol{x}_0 + s\boldsymbol{p})\,\mathrm{d}s. \tag{B.4}$$

Noting that the last term in Equation (B.4) represents the net torque acting on the particle, which is zero for a freely-suspended particle, we obtain the final form of $\dot{\boldsymbol{p}}$:

$$\dot{\boldsymbol{p}} = \frac{12}{L^3}(\boldsymbol{I} - \boldsymbol{pp}) \cdot \int_{-L/2}^{L/2} s\boldsymbol{u}(\boldsymbol{x}_0 + s\boldsymbol{p})\,\mathrm{d}s. \tag{B.5}$$

The angular velocity required in Equation (3.2) is then $\dot{\theta} = \dot{\boldsymbol{p}} \cdot \hat{\boldsymbol{e}}_\theta$, where $\hat{\boldsymbol{e}}_\theta = (-\sin\theta, \cos\theta)$.

The Fokker-Planck equation is now closed, with all terms known. We nondimensionalize Equation (3.2) using characteristic scales of L for length, $8\pi\mu L^3/k_BT$ for time and $L\dot{\gamma}$ for background velocities, yielding

$$\begin{aligned}\frac{k_BT}{8\pi\mu L^3}\frac{\partial\Psi}{\partial t} + \dot{\gamma}\boldsymbol{\nabla}_x \cdot (\dot{\boldsymbol{x}}\Psi) + \dot{\gamma}\frac{\partial(\dot{\theta}\Psi)}{\partial\theta} - \frac{k_BT\ln(1/\epsilon)}{4\pi\mu L^3}(\boldsymbol{I} + \boldsymbol{pp}) : \boldsymbol{\nabla}_x\boldsymbol{\nabla}_x\Psi& \\ - \frac{3k_BT\ln(1/\epsilon)}{\pi\mu^3}\frac{\partial^2\Psi}{\partial\theta^2} = 0.&\end{aligned} \tag{B.6}$$

The coefficients are collected in the form of the Péclet number defined in Equation (3.5), and using Equations (B.2) and (B.5) for the flux velocities, we arrive at the final form given in Equation (3.4).

Appendix C

Sedimentation of a filament of uniform thickness

In both Sections 4.3 and 4.4, we considered the spheroidal filament profile $r(s) = 2\sqrt{s(1-s)}$ for mathematical convenience. The equilibrium shapes found in Figure 4.3, for instance, were a consequence of variations in gravitational potential and viscous drag along the filament length. However, filaments of uniform thickness, $r(s) = 1$, are expected to result in qualitatively similar shapes but instead as a consequence of a secondary effect, namely by non-local hydrodynamic interactions. As illustrated in Figure 4.1, the central segments of the filament experience a stronger disturbance flow and will sediment faster than segments nearer to the filament ends. An accompanying reorientation is also to be expected. This case was considered by Xu and Nadim [132]. Similarly, as illustrated in Figure 4.7, a sufficiently flexible filament of uniform thickness is also expected to buckle when sedimenting along its long axis. While the effects due to variations in the filament thickness are $O(1)$, the effects due to non-local hydrodynamic interactions will be shown to be considerably smaller, $O(\ln(1/\epsilon)^{-1})$.

In both regimes (weakly and highly flexible filaments), the leading-order hydrodynamic interaction appears in the equations of motion through the spatially varying function $c(s)$ in the local operator (Equation (1.11)), while a higher-order correction is given by the integration of the non-local operator (Equation (1.12)), which is now made considerably more challenging analytically. We will now proceed to derive the shapes and velocities of filaments with uniform thickness in the weakly flexible regime, as well as the base-state tension for sedimentation along the filament's long axis.

C.1 Reorientation of a weakly flexible filament

Choosing $r(s) = 1$, we have a uniform distribution of gravitational potential and bending stiffness, $F_g(s) = -1$ and $B(s) = 1$. Equations (4.20) and (4.21) then become:

$$U^{(0)} = 2(c(s)-1)\left[T_s^{(0)} + \cos\theta^{(0)}\right] + 2S\left[T_s^{(0)}\right], \tag{C.1}$$

$$V^{(0)} + (s-1/2)\theta_t^{(0)} = -(c(s)+1)\left[u_{ssss} + \sin\theta^{(0)}\right] - S\left[u_{ssss}\right], \tag{C.2}$$

where now $c(s) = c_0 + \ln(4s(1-s))$, with $c_0 = \ln(1/\epsilon^2) \gg 1$. We pursue approximate expressions at leading order in the small number $1/c_0$. It is straightforward to show that $U^{(0)} = O(c_0)$, $V^{(0)} = O(c_0)$, $T^{(0)} = O(c_0^{-1})$, and $u = O(c_0^{-1})$. Therefore we assume the following series expansions,

$$V^{(0)} = \sum_{n=0}^{+\infty} V_n c_0^{1-n}, \quad \theta^{(0)} = \sum_{n=0}^{+\infty} \theta_n c_0^{-n}, \quad \sin\theta^{(0)} = \sum_{n=0}^{+\infty} a_n c_0^{-n}, \quad u(s) = \sum_{n=0}^{+\infty} u_n(s) c_0^{-n-1}. \tag{C.3}$$

Upon insertion into Equation (C.2), we obtain:

$$V_1 + (s-1/2)\partial_t\theta_0 = -[1+\ln(4s(1-s))]a_0 - u_0'''', \tag{C.4}$$

$$V_{n+1} + (s-1/2)\partial_t\theta_n = -[1+\ln(4s(1-s))](a_n + u_{n-1}'''') - u_n'''' - S[u_{n-1}'''']. \tag{C.5}$$

Multiplying by $(s-1/2)$ and integrating, and using the boundary conditions $u_n'''(0) = u_n'''(1) = 0$, $u_n''(0) = u_n''(1) = 0$, we find that $u_n(s)$ is symmetric about $1/2$ for all n and $\partial_t\theta_n = 0$ by induction. Therefore, there is no rotation at leading order in $1/\beta$, $\theta_t^{(0)} = 0$.

For the sake of convenience we again let $\zeta = s - 1/2$. Then, defining the series expansions

$$U^{(0)} = c_0 U_0 + U_1 + O(c_0^{-1}), \qquad V^{(0)} = c_0 V_0 + V_1 + O(c_0^{-1}),$$
$$T^{(0)} = c_0^{-1} T_0 + O(c_0^{-2}), \quad u = c_0^{-1} u_0 + O(c_0^{-2}),$$
$$\theta^{(0)} = \theta_0 + c_0^{-1}\theta_1 + O(c_0^{-2}),$$

we find

$$U_0 = 2\cos\theta_0, \quad V_0 = -\sin\theta_0, \tag{C.6}$$

$$U_1 + 2\theta_1 \sin\theta_0 = 2[\ln(1-4\zeta^2) - 1]\cos\theta_0 + 2T_0', \tag{C.7}$$

$$V_1 + \theta_1\cos\theta_0 = -u_0'''' - [\ln(1-4\zeta^2)+1]\sin\theta_0. \tag{C.8}$$

Using the boundary conditions on $T_0(s)$ and $u_0(s)$, we find:

$$T_0' + [\ln(1-4\zeta^2) + 2(1-\ln 2)]\cos\theta_0 = 0, \tag{C.9}$$

$$u_0'''' + [\ln(1-4\zeta^2) + 2(1-\ln 2)]\sin\theta_0 = 0, \tag{C.10}$$

leading to the leading-order tension profile,

$$T_0(\zeta) = \left[2\ln(2)\zeta - \left(\zeta - \frac{1}{2}\right)\ln(1-2\zeta) - \left(\zeta + \frac{1}{2}\right)\ln(1+2\zeta)\right]\cos\theta_0, \tag{C.11}$$

and the leading-order filament deflection profile,

$$\begin{aligned} u_0(\zeta) = \frac{1}{24}\Big[&-(\zeta - 1/2)^4 \ln(1-2\zeta) - (\zeta+1/2)^4\ln(1+2\zeta) \\ &+ \left(\frac{13}{6} + 2\ln 2\right)\zeta^4 + \frac{1}{4}\left(12\ln 2 + 1\right)\zeta^2\Big]\sin\theta_0. \end{aligned} \tag{C.12}$$

This shape is the same as that derived by Xu and Nadim [132] when $\theta_0 = \pi/2$, though with the correction of a small typo. Reinserting $\zeta = s - 1/2$, we have that

$$T^{(0)}(s) = c_0^{-1}\nu(s)\cos\theta^{(0)} + O(c_0^{-2}), \tag{C.13}$$

$$u(s) = c_0^{-1}h(s)\sin\theta^{(0)} + O(c_0^{-2}), \tag{C.14}$$

with

$$\nu(s) = (1-s)\ln(1-s) - s\ln s, \tag{C.15}$$

and

$$\begin{aligned} h(s) = -\frac{1}{24}\Big[&(s-1)^4\ln(2-2s) - s^4\ln(2s) \\ &+ \left(\frac{13}{6} + 2\ln 2\right)(s-1/2)^4 + \left(3\ln 2 + \frac{1}{4}\right)(s-1/2)^2\Big]. \end{aligned} \tag{C.16}$$

The tension is therefore zero at leading order when the filament is sedimenting perpendicular to its long axis, but otherwise varies along the filament. A plot of $\nu(s)$ is shown in figure C.1. Consequently, (4.30) may now be written as:

$$\begin{aligned} V^{(1)} + (s-1/2)\left(\theta_\tau^{(0)} + \theta_t^{(1)}\right) &= (c(s)+1)\left[(T^{(0)}u_s)_s - u_1'''' - \theta^{(1)}\cos\theta^{(0)}\right] \\ &+ (c(s)-3)(T_s^{(0)} + \cos\theta^{(0)})u_s + S\left[(T^{(0)}u_s)_s - u_1'''' - \theta^{(1)}\cos\theta^{(0)}\right] \\ &+ \int_0^1 \frac{\mathit{\Delta} u(T_s^{(0)}(s') + \cos\theta^{(0)}) - u_s(s)(T_s^{(0)}(s) + \cos\theta^{(0)})}{|s-s'|}\,\mathrm{d}s'. \end{aligned} \tag{C.17}$$

Multiplying by $(s-1/2)$ and integrating, and imposing $\theta_t^{(1)} = 0$ to remove the secular term, we have:

$$\theta_\tau^{(0)} = 6[J_0 + c_0^{-1}(J_1 + J_2 + J_3)]\sin(2\theta^{(0)}) + O(c_0^{-2}), \tag{C.18}$$

where

$$J_0 = \int_0^1 (s-1/2)h_s\,\mathrm{d}s, \tag{C.19}$$

$$J_1 = \int_0^1 (s-1/2)(\nu h_s)_s\,\mathrm{d}s, \tag{C.20}$$

$$J_2 = \int_0^1 (s-1/2)\nu_s h_s\,\mathrm{d}s, \tag{C.21}$$

$$J_3 = \int_0^1 (s-1/2)[\ln(4s(1-s)) - 3]h_s\,\mathrm{d}s. \tag{C.22}$$

Inserting $\nu(s)$ and $h(s)$ from above, the resulting rotation rate in terms of the single time t is given by

$$\begin{aligned} \theta_t &= \frac{1}{\beta}\left(\frac{7}{400} + \ln(1/\epsilon^2)^{-1}\frac{749 - 150\pi^2 + 315\ln(2)}{9000}\right)\sin(2\theta) + O(\ln(1/\epsilon^2)^{-2}, \beta^{-2}) \\ &= \frac{1}{\beta}\left(0.003 - 0.057\ln(1/\epsilon^2)^{-1}\right)\sin(2\theta) + O(\ln(1/\epsilon^2)^{-2}, \beta^{-2}). \end{aligned} \tag{C.23}$$

The result is physical for $\epsilon < 2\exp(107/45 - 10\pi^2/21) \approx 0.196$. This expression may be compared to that for the spheroidal filament shown in Equation (4.38). The timescale for reorientation is now significantly longer than that found for the spheroidal filament.

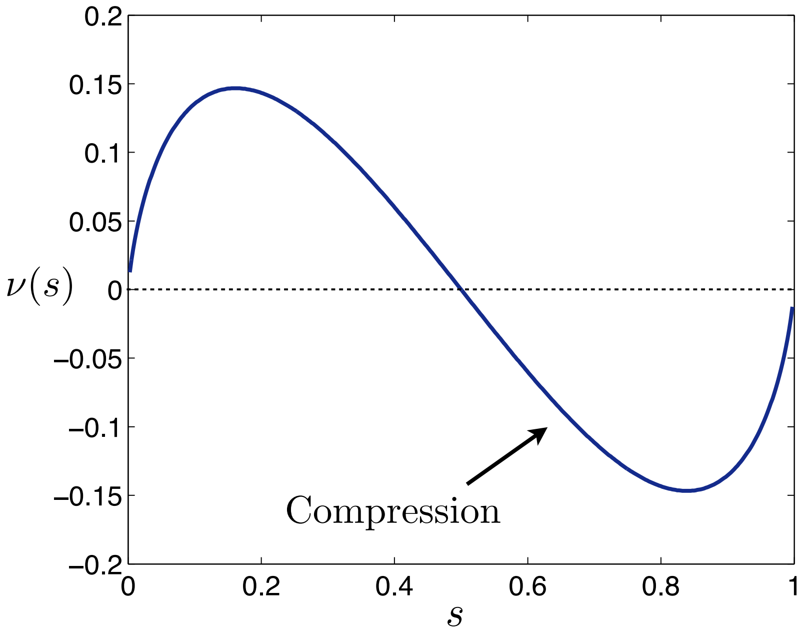

Figure C.1: The tension profile along a straight filament of uniform thickness due to non-local hydrodynamic interactions. Once again, buckling is possible in the leading half of the filament, where $s \in (1/2, 1)$ (see Figure 4.7).

C.2 Compression of a uniform flexible filament

As illustrated in Figure 4.7(b), the tension in the leading half of a filament with uniform thickness, sedimenting along its long axis, is still expected to be negative in the straightened state due to non-local hydrodynamic interactions. The base-state tension and sedimentation speed was already derived for this case in the previous section as the special case $\theta^{(0)} = 0$, from which we find

$$U = 2c_0 + 2(2\ln(2) - 3) + O(c_0^{-1}), \tag{C.24}$$

$$T(s) = c_0^{-1}\nu(s) + O(c_0^{-2}), \tag{C.25}$$

with $c_0 = \ln(1/\epsilon^2)$, and $\nu(s)$ defined in Equation (C.15) and plotted in Figure C.1. We observe that $T(s) > 0$ in the trailing half of the filament, $s < 1/2$, and that $T(s) < 0$ in the leading half of the filament, $s > 1/2$. Buckling is therefore still possible in the leading half of the filament as a consequence of non-local hydrodynamic interactions even if the filament has uniform thickness.

Appendix D

Reduction of integral operators for large wavenumbers

When analyzing the instability of the two halves of the filament in Section 4.4, we use that the Fourier basis functions approximately diagonalize the integral operators in Equation (4.10) for large wavenumbers, $k \gg 1$, and we also decouple the integral operators into operations on the two halves of the filament separately. We now justify both approximations.

Consider a point $s \in [\varDelta, 1-\varDelta]$, with $\varDelta > 0$. Then for $\lambda \geq 1$, with $k \gg 1$ such that $k\varDelta$ is sufficiently large, the action of the integral operators in Equation (1.12) on the Fourier basis functions yield

$$S[\mathrm{e}^{\mathrm{i}\lambda k s}] \approx (-2\gamma - 2\ln(\lambda k) - \ln(s(1-s)))\mathrm{e}^{\mathrm{i}\lambda k s}, \tag{D.1}$$

$$P[\mathrm{e}^{\mathrm{i}\lambda k s}] \approx 2\mathrm{i}(\lambda k)\mathrm{e}^{\mathrm{i}\lambda k s}, \tag{D.2}$$

where $\gamma \approx 0.577$ is Euler's constant. To show this, we simply consider a change of variables, $\xi = \lambda k s'$ so that

$$S[\mathrm{e}^{\mathrm{i}\lambda k s}](s) = \varLambda(k,s)\mathrm{e}^{\mathrm{i}\lambda k s}, \tag{D.3}$$

with

$$\begin{aligned} \varLambda(k,s) &= \int_{-\lambda k s}^{\lambda k(1-s)} \frac{\mathrm{e}^{\mathrm{i}\xi} - 1}{|\xi|}\,\mathrm{d}\xi \\ &\approx 2\int_0^1 \frac{\cos\xi - 1}{\xi}\,\mathrm{d}\xi + 2\int_1^{+\infty} \frac{\cos(\xi)}{\xi}\,\mathrm{d}\xi - 2\ln(\lambda k) - \ln(s(1-s)), \end{aligned} \tag{D.4}$$

which gives the desired result. The same change of variables gives

$$\begin{aligned} P[\mathrm{e}^{\mathrm{i}\lambda ks}] &= \lambda k\mathrm{e}^{\mathrm{i}\lambda ks}\int_{-\lambda ks}^{\lambda k(1-s)} \frac{\mathrm{e}^{\mathrm{i}\xi}-1-\mathrm{i}\xi\mathrm{e}^{\mathrm{i}\xi}}{\xi|\xi|}\,\mathrm{d}\xi \\ &\approx 2\mathrm{i}\lambda k\mathrm{e}^{\mathrm{i}\lambda ks}\int_0^{+\infty}\frac{\sin\xi-\xi\cos\xi}{\xi^2}\,\mathrm{d}\xi = 2\mathrm{i}\lambda k\mathrm{e}^{\mathrm{i}\lambda ks}. \end{aligned} \tag{D.5}$$

Moreover, the main contribution of $S[\mathrm{e}^{\mathrm{i}\lambda ks}](s)$ and $P[\mathrm{e}^{\mathrm{i}\lambda ks}](s)$ comes from the neighborhood of s. Specifically, for an interval $I \subset [0,1]$ we define

$$S_I[\mathrm{e}^{\mathrm{i}\lambda ks}] = \int_I \frac{\mathrm{e}^{\mathrm{i}\lambda ks'}-\mathrm{e}^{\mathrm{i}\lambda ks}}{|s'-s|}\,\mathrm{d}s', \tag{D.6}$$

$$P_I[\mathrm{e}^{\mathrm{i}\lambda ks}] = \int_I \frac{(\mathrm{e}^{\mathrm{i}\lambda ks'}-\mathrm{e}^{\mathrm{i}\lambda ks})/(s'-s)-\mathrm{i}\lambda k\mathrm{e}^{\mathrm{i}\lambda ks'}}{|s'-s|}\,\mathrm{d}s', \tag{D.7}$$

and we will show that

$$S_{[0,1/2]}[\mathrm{e}^{\mathrm{i}\lambda ks}] \approx (-2\gamma - 2\ln(\lambda k) - \ln(s(1/2-s)))\mathrm{e}^{\mathrm{i}\lambda ks}, \tag{D.8}$$

$$P_{[0,1/2]}[\mathrm{e}^{\mathrm{i}\lambda ks}] \approx 2\mathrm{i}\lambda k\mathrm{e}^{\mathrm{i}\lambda ks}, \tag{D.9}$$

when $s \in (\mathit{\Delta}, 1/2-\mathit{\Delta})$, and

$$S_{[1/2,1]}[\mathrm{e}^{\mathrm{i}\lambda ks}] \approx (-2\gamma - 2\ln(\lambda k) - \ln((s-1/2)(1-s)))\mathrm{e}^{\mathrm{i}\lambda ks}, \tag{D.10}$$

$$P_{[1/2,1]}[\mathrm{e}^{\mathrm{i}\lambda ks}] \approx 2\mathrm{i}\lambda k\mathrm{e}^{\mathrm{i}\lambda ks}, \tag{D.11}$$

when $s \in (1/2+\mathit{\Delta}, 1-\mathit{\Delta})$. To see this, let

$$S_{[0,1/2]}[\mathrm{e}^{\mathrm{i}\lambda ks}] = I_1\mathrm{e}^{\mathrm{i}ks}, \tag{D.12}$$

$$S_{[1/2,1]}[\mathrm{e}^{\mathrm{i}\lambda ks}] = I_2\mathrm{e}^{\mathrm{i}ks}. \tag{D.13}$$

and

$$P[\mathrm{e}^{i\lambda ks}] = P_{[0,1/2]}[\mathrm{e}^{\mathrm{i}\lambda ks}] + P_{[1/2,1]}[\mathrm{e}^{\mathrm{i}\lambda ks}] \tag{D.14}$$

We have when $s \in [\mathit{\Delta}, 1/2-\mathit{\Delta}]$, with $k \gg 1$,

$$I_1 \approx -2\gamma - 2\ln(\lambda k) - \ln(s(1/2-s)), \tag{D.15}$$

$$I_2 \approx \ln((1-s)/(1/2-s)). \tag{D.16}$$

and

$$P_{[0,1/2]}/(\lambda k) \approx 2\mathrm{i}\mathrm{e}^{\mathrm{i}\lambda k s}, \tag{D.17}$$

$$P_{[1/2,1]}/(\lambda k) \approx 0. \tag{D.18}$$

We observe on this interval that I_1 dominates I_2 and the first integral for P dominates the second. Similar computation yields for $s \in [\mathit{\Delta}, 1/2-\mathit{\Delta}]$. A further approximation, leading to (4.62), is obtained using

$$2\int_0^{1/2} \ln(s(1/2-s))\,\mathrm{d}s = 2\int_{1/2}^{1} \ln((s-1/2)(1-s))\,\mathrm{d}s = -2-2\ln 2. \tag{D.19}$$

We now simply replace the term $\ln(s(1/2-s))$ in Equation (D.8) and the term $\ln((s-1/2)(1-s))$ in Equation (D.10) by $-2-2\ln 2$. In addition, we see that $P[u] \approx 2u_s \approx P_I[u]$ for high wavenumber perturbations.

Appendix E

Spherical harmonics expansion

In Chapter 5, the full eigenvalue problem in Equation (5.25) is too complicated to be solved analytically in the general case due to the additional terms arising from flexibility and thermal diffusion and to the nontrivial form of the base-state distribution (Equation (5.19)). Instead, noticing that Equation (5.25) is in the form $\mathcal{L}[\tilde{\psi}] = \mathrm{i}\omega\tilde{\psi}$ where $\mathcal{L}$ is a linear integro-differential operator, we seek numerical solutions to the eigenvalues ω by projecting $\tilde{\psi}$ onto an appropriate basis. As $\tilde{\psi}$ is defined continuously on the sphere of orientations, a natural choice is Laplace's spherical harmonics:

$$Y_\ell^m(\theta,\varphi) = \sqrt{\frac{2\ell+1}{4\pi}\frac{(\ell-m)!}{(\ell+m)!}}\, P_\ell^m(\cos\theta)\mathrm{e}^{\mathrm{i}m\varphi}, \tag{E.1}$$

where P_ℓ^m are the associated Legendre polynomials. Projecting the unknown eigenfunctions onto this basis,

$$\tilde{\psi}(\theta,\varphi) = \sum_{\ell=0}^{\infty}\sum_{m=-\ell}^{\ell} a_{\ell m} Y_\ell^m(\theta,\varphi), \tag{E.2}$$

the linearity of the operator $\mathcal{L}$ then implies:

$$\sum_{\ell=0}^{\infty}\sum_{m=-\ell}^{\ell} a_{\ell m}\mathcal{L}[Y_\ell^m] = \mathrm{i}\omega\sum_{\ell=0}^{\infty}\sum_{m=-\ell}^{\ell} a_{\ell m} Y_\ell^m. \tag{E.3}$$

The spherical harmonics are orthonormal over the orientational space:

$$\langle Y_\ell^m, Y_{\ell'}^{m'}\rangle = \int_\Omega Y_\ell^m \bar{Y}_{\ell'}^{m'}\,\mathrm{d}\boldsymbol{p} = \delta_{\ell\ell'}\delta_{mm'}, \tag{E.4}$$

where the overbar denotes the complex conjugate. Using this property, we multiply Equation (E.3) by $\bar{Y}_{\ell'}^{m'}$ and integrate over all orientations to obtain

$$\sum_{\ell=0}^{\infty} \sum_{m=-\ell}^{\ell} a_{\ell m} \langle \mathcal{L}[Y_\ell^m], Y_{\ell'}^{m'} \rangle = \mathrm{i}\omega a_{\ell' m'}. \tag{E.5}$$

Truncating the expansion at $\ell = M$ (where we choose $M = 30$ in the results presented here), Equation (E.5) then yields an algebraic eigenvalue problem of the form $\boldsymbol{L} \cdot \boldsymbol{a} = \mathrm{i}\omega \boldsymbol{a}$, where $\boldsymbol{L}$ is a $(M+1)^2 \times (M+1)^2$ matrix with entries $\langle \mathcal{L}[Y_\ell^m], Y_{\ell'}^{m'} \rangle$ and the vector $\boldsymbol{a}$ contains the coefficients $a_{\ell m}$ of the spectral expansion of the eigenfunction. Solving this system provides a discrete set of $(M+1)^2$ eigenvalues ω. We verify *a posteriori* that only one of these eigenvalues is unstable ($\omega_I > 0$), consistent with the results of Koch and Shaqfeh [125].

The following properties of spherical harmonics are useful in evaluating the matrix $\boldsymbol{L}$:

$$\int_\Omega Y_\ell^m \, \mathrm{d}\boldsymbol{p} = 2\sqrt{\pi}\, \delta_{l0} \delta_{m0}, \tag{E.6}$$

$$\nabla_p^2 Y_\ell^m = -\ell(\ell+1) Y_\ell^m, \tag{E.7}$$

$$\frac{\partial Y_\ell^m}{\partial \theta} = \frac{1}{\sin\theta} \left(\ell \cos\theta \, Y_\ell^m - \sqrt{\frac{(2\ell+1)(\ell^2 - m^2)}{2\ell - 1}} \, Y_{\ell-1}^m \right). \tag{E.8}$$

Appendix F

The divergence theorem in orientational space

Let $\boldsymbol{w}(\boldsymbol{p})$ be any smooth function defined on the surface Ω of a unit sphere such that $\boldsymbol{p} = (\sin\theta\cos\varphi, \sin\theta\sin\varphi, \cos\theta)$. Also, let $\boldsymbol{w}(\boldsymbol{p})$ be any smooth function defined on the surface Ω of a unit sphere. We also define $\boldsymbol{v}(r, \boldsymbol{p}) = r^n \boldsymbol{w}$ where $n \geq 1$ to ensure regularity. Now, Gauss's divergence theorem reads

$$\int_V \boldsymbol{\nabla} \cdot \boldsymbol{v} \, \mathrm{d}V = \int_\Omega \boldsymbol{p} \cdot \boldsymbol{v} \, \mathrm{d}\boldsymbol{p}. \tag{F.1}$$

Noticing that $\boldsymbol{\nabla} = \boldsymbol{p}\frac{\partial}{\partial r} + \frac{1}{r}\boldsymbol{\nabla}_p$, the left-hand side becomes

$$\int_V \boldsymbol{\nabla} \cdot \boldsymbol{v} \, \mathrm{d}V = \int_V \left(n r^{n-1} \boldsymbol{p} \cdot \boldsymbol{w} + r^{n-1} \boldsymbol{\nabla}_p \cdot \boldsymbol{w}\right) \mathrm{d}V \tag{F.2}$$

$$= \int_\Omega \left(\frac{n}{n+2} \boldsymbol{p} \cdot \boldsymbol{w} + \frac{1}{n+2} \boldsymbol{\nabla}_p \cdot \boldsymbol{w}\right) \mathrm{d}\boldsymbol{p}, \tag{F.3}$$

where we have used $\mathrm{d}V = r^2 \, \mathrm{d}r \, \mathrm{d}\boldsymbol{p}$. The right-hand side of Equation (F.1) simplifies readily as $\boldsymbol{v} = \boldsymbol{w}$ on Ω. Rearranging the terms, we obtain the divergence theorem in orientational space:

$$\int_\Omega \boldsymbol{\nabla}_p \cdot \boldsymbol{w} \, \mathrm{d}\boldsymbol{p} = 2 \int_\Omega \boldsymbol{p} \cdot \boldsymbol{w} \, \mathrm{d}\boldsymbol{p}. \tag{F.4}$$

Bibliography

[1] H. Manikantan, *The dynamics of single semiflexible polymers in a viscous fluid*, Master's thesis, University of Illinois at Urbana-Champaign (2012).

[2] H. Manikantan and D. Saintillan, "Buckling transition of a semiflexible filament in extensional flow," *Phys. Rev. E* **92**, 041002 (2015).

[3] H. Manikantan and D. Saintillan, "Subdiffusive transport of fluctuating elastic filaments in cellular flows," *Phys. Fluids* **25**, 073603 (2013).

[4] L. Li, H. Manikantan, D. Saintillan, and S. E. Spagnolie, "The sedimentation of flexible filaments," *J. Fluid Mech.* **735**, 705–736 (2013).

[5] H. Manikantan, L. Li, S. E. Spagnolie, and D. Saintillan, "The instability of a sedimenting suspension of weakly flexible fibres," *J. Fluid Mech.* **756**, 935–964 (2014).

[6] M. L. Gardel, F. Nakamura, J. H. Hartwig, J. C. Crocker, T. P. Stossel, and D. A. Weitz, "Prestressed f-actin networks cross-linked by hinged filamins replicate mechanical properties of cells," *Proc. Natl. Acad. Sci. USA* **103**, 1762–1767 (1995).

[7] S. Reinsch and P. Gönczy, "Mechanisms of nuclear positioning," *J. Cell Sci.* **111**, 2283–2295 (1998).

[8] T. Shinar, M. Mano, F. Piano, and M. J. Shelley, "A model of cytoplasmically-driven microtubule-based motion in the single-celled *C. elegans* embryo," *Proc. Natl. Acad. Sci. USA* **108**, 10508–10513 (2011).

[9] C. Brennen and H. Winet, "Fluid mechanics of propulsion by cilia and flagella," *Annu. Rev. Fluid Mech.* **9**, 339–398 (1977).

[10] E. Lauga and T. R. Powers, "The hydrodynamics of swimming microorganisms," *Rep. Prog. Phys.* **72**, 096601 (2009).

[11] L. J. Fauci and R. Dillon, "Biofluidmechanics of reproduction," *Annu. Rev. Fluid Mech.* **38**, 371–394 (2006).

[12] E. A. Gaffney, H. Gadêlha, D. J. Smith, J. R. Blake, and J. C. Kirkman-Brown, "Mammalian sperm motility: observation and theory," *Annu. Rev. Fluid Mech.* **43**, 501–528 (2011).

[13] G. R. Fulford and J. R. Blake, "Mucociliary transport in the lung," *J. Theoret. Biol.* **121**, 381–402 (1986).

[14] H. P. Ehrlich, G. Grislis, and T. K. Hunt, "Evidence for the movement of the microtubules in wound contraction," *Am. J. Surg.* **133**, 706–709 (1977).

[15] L. G. Tilney, M. S. Tilney, and D. J. DeRosier, "Actin filaments, stereocilia, and hair cells: How cells count and measure," *Annu. Rev. Cell Biol.* **8**, 257–274 (1992).

[16] F. Gittes, B. Mickey, J. Nettleton, and J. Howard, "Flexural rigidity of microtubules and actin filaments measured from thermal fluctuations in shape." *J. Cell Biol.* **120**, 923–934 (1993).

[17] E. S. G. Shaqfeh, "The dynamics of single-molecule DNA in flow," *J. Non-Newtonian Fluid Mech.* **130**, 1–28 (2005).

[18] M. D. Graham, "Fluid dynamics of dissolved polymer molecules in confined geometries," *Annu. Rev. Fluid Mech.* **43**, 273–298 (2011).

[19] P. G. de Gennes, "Coil-stretch transition of dilute flexible polymers under ultrahigh velocity gradients," *J. Chem. Phys.* **6012**, 5030–5042 (1974).

[20] C. M. Schroeder, H. P. Babcock, E. S. G. Shaqfeh, and S. Chu, "Observation of polymer conformation hysteresis in extensional flow," *Science* **301**, 1515–1519 (2003).

[21] C. Hsieh, L. Li, and R. Larson, "Modeling hydrodynamic interaction in Brownian dynamics: Simulations of extensional flows of dilute solutions of DNA and polystyrene," *J. Non-Newtonian Fluid Mech.* **113**, 147–191 (2003).

[22] R. G. Larson, *The Structure and Rheology of Complex Fluids*, Oxford University Press, New York (1999).

[23] E. S. G. Shaqfeh, "Purely elastic instabilities in viscometric flows," *Annu. Rev. Fluid Mech.* **28**, 129–185 (1996).

[24] P. E. Arratia, C. C. Thomas, J. Diorio, and J. P. Gollub, "Elastic instabilities of polymer solutions in cross-channel flow," *Phys. Rev. Lett.* **96**, 144502 (2006).

[25] A. Groisman and V. Steinberg, "Elastic turbulence in a polymer solution flow," *Nature* **405**, 53–55 (2000).

[26] E. J. Hinch, "The distortion of a flexible inextensible thread in a shearing flow," *J. Fluid Mech.* **74**, 317–333 (1976).

[27] L. E. Becker and M. J. Shelley, "Instability of elastic filaments in shear flow yields first-normal-stress differences," *Phys. Rev. Lett.* **87**, 198301 (2001).

[28] A.-K. Tornberg and M. J. Shelley, "Simulating the dynamics and interactions of flexible fibers in Stokes flows," *J. Comput. Phys.* **196**, 8–40 (2004).

[29] T. Munk, O. Hallatschek, C. H. Wiggins, and E. Frey, "Dynamics of semiflexible polymers in a flow field," *Phys. Rev. E* **74**, 041911 (2006).

[30] Y.-N. Young, "Hydrodynamic interactions between two semiflexible inextensible filaments in Stokes flow," *Phys. Rev. E* **79**, 046317 (2009).

[31] M. Harasim, B. Wunderlich, O. Peleg, M. Kröger, and A. R. Bausch, "Direct observation of the dynamics of semiflexible polymers in shear flow," *Phys. Rev. Lett.* **110**, 108302 (2013).

[32] V. Kantsler and R. E. Goldstein, "Fluctuations, dynamics, and the stretch-coil transition of single actin filaments in extensional flows," *Phys. Rev. Lett.* **108**, 038103 (2012).

[33] L. Guglielmini, A. Kushwaha, E. S. G. Shaqfeh, and H. A. Stone, "Buckling transitions of an elastic filament in a viscous stagnation point flow," *Phys. Fluids* **24**, 123601 (2012).

[34] D. Steinhauser, S. Köster, and T. Pfohl, "Mobility gradient induces cross-streamline migration of semiflexible polymers," *ACS Macro Lett.* **1**, 541–545 (2012).

[35] Y.-N. Young and M. J. Shelley, "Stretch-coil transition and transport of fibers in cellular flows," *Phys. Rev. Lett.* **99**, 058303 (2007).

[36] E. Wandersman, N. Quennouz, M. Fermigier, A. Lindner, and O. du Roure, "Buckled in translation," *Soft Matter* **6**, 5715–5719 (2010).

[37] N. Autrusson, L. Guglielmini, S. Lecuyer, R. Rusconi, and H. A. Stone, "The shape of an elastic filament in a two-dimensional corner flow," *Phys. Fluids* **23**, 063602 (2011).

[38] J. S. Wexler, P. H. Trinh, H. Berthet, N. Quennouz, O. du Roure, H. E. Huppert, A. Lindner, and H. A. Stone, "Bending of elastic fibres in viscous flows: the influence of confinement," *J. Fluid Mech.* **720**, 517–544 (2013).

[39] U. Seifert, W. Wintz, and P. Nelson, "Straightening of thermal fluctuations in semiflexible polymers by applied tension," *Phys. Rev. Lett.* **77**, 5389–5392 (1996).

[40] C. H. Wiggins and R. E. Goldstein, “Flexive and propulsive dynamics of elastica at low Reynolds number,” *Phys. Rev. Lett.* **80**, 3879–3882 (1998).

[41] E. Lauga, “Floppy swimming: Viscous locomotion of actuated elastica,” *Phys. Rev. E* **75**, 041916 (2007).

[42] S. E. Spagnolie and E. Lauga, “The optimal elastic flagellum,” *Phys. Fluids* **22**, 031901 (2010).

[43] G. Jayaraman, S. Ramachandran, S. Ghose, A. Laskar, M. Bhamla, P. Kumar, and R. Adhikari, “Autonomous motility of active filaments due to spontaneous flow-symmetry breaking,” *Phys. Rev. Lett.* **109**, 158302 (2012).

[44] I. Llopis, I. Pagonabarraga, M. Cosentino Lagomarsino, and C. P. Lowe, “Sedimentation of pairs of hydrodynamically interacting semiflexible filaments,” *Phys. Rev. E* **76**, 061901 (2007).

[45] A. A. Evans, S. E. Spagnolie, D. Bartolo, and E. Lauga, “Elastocapillary self-folding: buckling, wrinkling, and collapse of floating filaments,” *Soft Matter* **9**, 1711–1720 (2013).

[46] S. Pennathur and J. G. Santiago, “Electrokinetic transport in nanochannels. 2. Experiments,” *Anal. Chem.* **77**, 6782–6789 (2005).

[47] M. Tanyeri, E. M. Johnson-Chavarria, and C. M. Schroeder, “Hydrodynamic trap for single particles and cells,” *App. Phys. Lett.* **96**, 224101 (2010).

[48] M. Tanyeri, M. Ranka, N. Sittipolkul, and C. M. Schroeder, “A microfluidic-based hydrodynamic trap: design and implementation,” *Lab Chip* **11**, 1786–1794 (2011).

[49] R. B. Bird, R. C. Armstrong, and O. Hassager, *Dynamics of polymeric liquids. I. Fluid Mechanics*, Wiley Interscience (1987).

[50] L. Pan, C. Morozov, C. Wagner, and P. Arratia, “Nonlinear elastic instability in channel flows at low Reynolds numbers,” *Phys. Rev. Lett.* **110**, 174502 (2013).

[51] B. Thomases, M. J. Shelley, and J.-L. Thiffeault, “A Stokesian viscoelastic flow: transition to oscillations and mixing,” *Physica D* **240**, 1602–1614 (2011).

[52] P. S. Doyle and P. T. Underhill, “Brownian dynamics simulations of polymers and soft matter,” in S. Yip, editor, “Handbook of Materials Modeling,” pages 2619–2630, Springer (2005).

[53] C. M. Schroeder, E. S. G. Shaqfeh, and S. Chu, “Effect of hydrodynamic interactions on DNA dynamics in extensional flow: Simulation and single molecule experiment,” *Macromolecules* **37**, 9242–9256 (2004).

[54] A. Montesi, D. C. Morse, and M. Pasquali, “Brownian dynamics algorithm for bead-rod semiflexible chain with anisotropic friction,” *J. Chem. Phys.* **122**, 084903 (2005).

[55] D. Saintillan, E. S. G. Shaqfeh, and E. Darve, “Effect of flexibility on the shear-induced migration of short-chain polymers in parabolic channel flow,” *J. Fluid Mech.* **557**, 297–306 (2006).

[56] G. K. Batchelor, “Slender-body theory for particles of arbitrary cross-section in Stokes flow,” *J. Fluid Mech.* **44**, 419–440 (1970).

[57] R. E. Johnson, “An improved slender-body theory for Stokes flow,” *J. Fluid Mech.* **99**, 411–431 (1980).

[58] J. B. Keller and S. I. Rubinow, “Slender-body theory for slow viscous flow,” *J. Fluid Mech.* **75**, 705–714 (1976).

[59] C. H. Wiggins, D. X. Riveline, A. Ott, and R. E. Goldstein, “Trapping and wiggling: Elastohydrodynamics of driven microfilaments,” *Biophys. J.* **74**, 1043–1060 (1998).

[60] S. Kim and S. J. Karrila, *Microhydrodynamics: Principles and Selected Applications*, Dover (2005).

[61] A. J. Banchio and J. F. Brady, “Accelerated Stokesian dynamics: Brownian motion,” *J. Chem. Phys.* **118**, 10323–10332 (2003).

[62] D. Saintillan and M. J. Shelley, “Active suspensions and their nonlinear models,” *C. R. Physique* **14**, 497–517 (2013).

[63] H. Zhao, A. H. Isfahani, L. N. Olson, and J. B. Freund, “A spectral boundary integral method for flowing blood cells,” *J. Comput. Phys.* **229**, 3726–3744 (2010).

[64] G. K. Batchelor, “Sedimentation in a dilute dispersion of spheres,” *J. Fluid Mech.* **52**, 245–268 (1972).

[65] É. Guazzelli and J. F. Morris, *A Physical Introduction to Suspension Dynamics*, Cambridge University Press (2011).

[66] E. M. Purcell, “Life at low Reynolds number,” *Am. J. Phys.* **45**, 3–11 (1977).

[67] J. Happel and H. Brenner, *Low Reynolds Number Hydrodynamics*, Prentice Hall (1965).

[68] R. G. Cox, “The motion of long slender bodies in a viscous fluid. Part 1. General theory,” *J. Fluid Mech.* **44**, 791–810 (1970).

[69] R. G. Cox, "The motion of long slender bodies in a viscous fluid. Part 2. Shear flow," *J. Fluid Mech.* **45**, 625–657 (1971).

[70] T. Götz, *Interactions of Fibers and Flow: Asymptotics, Theory and Numerics*, Ph.D. thesis, University of Kaiserslautern (2000).

[71] É. Guazzelli and J. Hinch, "Fluctuations and instability in sedimentation," *Annu. Rev. Fluid Mech.* **43**, 97–116 (2011).

[72] R. E. Caflisch and J. H. C. Luke, "Variance in the sedimentation speed of a suspension," *Phys. Fluids* **28**, 759–760 (1985).

[73] S. Ramaswamy, "Issues in the statistical mechanics of steady sedimentation," *Adv. Phys.* **50**, 297–341 (2001).

[74] P. N. Segrè, E. Herbolzheimer, and P. M. Chaikin, "Long-range correlations in sedimentation," *Phys. Rev. Lett.* **79**, 2574–2577 (1997).

[75] É. Guazzelli, "Evolution of particle-velocity correlations in sedimentation," *Phys. Fluids* **13**, 1537–1540 (2001).

[76] L. Bergougnoux, S. Ghicini, É. Guazzelli, and E. J. Hinch, "Spreading fronts and fluctuations in sedimentation," *Phys. Fluids* **15**, 1875–1887 (2001).

[77] D. L. Koch and E. S. G. Shaqfeh, "Screening in sedimenting suspensions," *J. Fluid Mech.* **224**, 275–303 (1991).

[78] M. P. Brenner, "Screening mechanisms in sedimentation," *Phys. Fluids* **11**, 754–772 (1999).

[79] E. J. Hinch, "Sedimentation of small particles," in E. Guyon, J.-P. Nadal, and Y. Pomeau, editors, "Disorder and Mixing," chapter 9, pages 153–161, Kluwer (1987).

[80] A. J. C. Ladd, "Effects of container walls on the velocity fluctuations of sedimenting spheres," *Phys. Rev. Lett.* **88**, 048301 (2002).

[81] J. H. C. Luke, "Decay of velocity fluctuations in a stably stratified suspension," *Phys. Fluids* **12**, 1619–1621 (2000).

[82] P. J. Mucha, S.-Y. Tee, D. A. Weitz, B. I. Shraiman, and M. P. Brenner, "A model for velocity fluctuations in sedimentation," *J. Fluid Mech.* **501**, 71–104 (2004).

[83] F. Gittes, E. Meyhöfer, S. Baek, and J. Howard, "Directional loading of the kinesin motor molecule as it buckles a microtubule," *Biophys. J.* **70**, 418–429 (1996).

[84] M. Elbaum, D. Kuchnir Fygenson, and A. Libchaber, “Buckling microtubules in vesicles,” *Phys. Rev. Lett.* **76**, 4078–4081 (1996).

[85] R. E. Goldstein and A. Goriely, “Dynamic buckling of morphoelastic filaments,” *Phys. Rev. E* **74**, 010901 (2006).

[86] T. R. Powers, “Dynamics of filaments and membranes in a viscous fluid,” *Rev. Mod. Phys.* **82**, 1607–1631 (2010).

[87] H. Yamakawa, *Helical Wormlike Chains in Polymer Solutions*, Springer-Verlag (1997).

[88] R. Granek, “From semi-flexible polymers to membranes: Anomalous diffusion and reptation,” *J. Phys. II* **7**, 1761–1788 (1997).

[89] R. Chelakkot, R. G. Winkler, and G. Gompper, “Flow-induced helical coiling of semiflexible polymers in structured microchannels,” *Phys. Rev. Lett.* **109**, 178101 (2012).

[90] L. Bourdieu, T. Duke, M. B. Elowitz, D. A. Winkelmann, S. Leibler, and A. Libchaber, “Spiral defects in motility assays: A measure of motor protein force,” *Phys. Rev. Lett.* **75**, 176–179 (1995).

[91] L. Bourdieu, M. O. Magnasco, D. A. Winkelmann, and A. Libchaber, “Actin filaments on myosin beds: The velocity distribution,” *Phys. Rev. E* **52**, 6573–6579 (1995).

[92] I. Kirchenbuechler, D. Guu, N. A. Kurniawan, G. H. Koenderink, and M. P. Lettinga, “Direct visualization of flow-induced conformational transitions of single actin filaments in entangled solutions,” *Nat. Commun.* **5**, 5060 (2014).

[93] F. G. Woodhouse and R. E. Goldstein, “Cytoplasmic streaming in plant cells emerges naturally by microfilament self-organization,” *Proc. Natl. Acad. Sci. U.S.A.* **110**, 14132–14137 (2013).

[94] R. M. Jendrejack, D. C. Schwartz, M. D. Graham, and J. J. de Pablo, “Effect of confinement on DNA dynamics in microfluidic devices,” *J. Chem. Phys.* **119**, 1165 (2003).

[95] J. P. Hernández-Ortiz, J. J. de Pablo, and M. D. Graham, “Fast computation of many-particle hydrodynamic and electrostatic interactions in a confined geometry,” *Phys. Rev. Lett.* **98**, 140602 (2007).

[96] R. E. Goldstein, T. R. Powers, and C. H. Wiggins, “Viscous nonlinear dynamics of twist and writhe,” *Phys. Rev. Lett.* **80**, 5232–5235 (1998).

[97] R. Cao and S. B. Pope, "Numerical integration of stochastic differential equations: weak second-order mid-point scheme for application in the composition pdf method," *J. Comput. Phys.* **185**, 194 – 212 (2003).

[98] H. C. Öttinger, *Stochastic processes in polymeric fluids*, Springer-Verlag (1996).

[99] E. A. J. F. Peters, *Polymers in Flow*, Ph.D. thesis, Delft University of Technology (2000).

[100] J. Wilhelm and E. Frey, "Radial distribution function of semiflexible polymers," *Phys. Rev. Lett.* **77**, 2581–2584 (1996).

[101] L. Le Goff, O. Hallatschek, E. Frey, and F. Amblard, "Tracer studies on f-actin fluctuations," *Phys. Rev. Lett.* **89**, 258101 (2002).

[102] G. B. Jeffery, "The motion of ellipsoidal particles immersed in a viscous fluid," *Proc. R. Soc. London A* **102**, 161–179 (1922).

[103] S. Strogatz, *Nonlinear Dynamics and Chaos*, Addison-Wesley (1994).

[104] A. Puliafito and K. Turitsyn, "Numerical study of polymer tumbling in linear shear flows," *Physica D* **211**, 9 – 22 (2005).

[105] C. M. Schroeder, R. E. Teixeira, E. S. G. Shaqfeh, and S. Chu, "Characteristic periodic motion of polymers in shear flow," *Phys. Rev. Lett.* **95**, 018301 (2005).

[106] R. E. Teixeira, H. P. Babcock, E. S. G. Shaqfeh, and S. Chu, "Shear thinning and tumbling dynamics of single polymers in the flow-gradient plane," *Macromolecules* **38**, 581–592 (2005).

[107] H. Kobayashi and R. Yamamoto, "Tumbling motion of a single chain in shear flow: A crossover from Brownian to non-Brownian behavior," *Phys. Rev. E* **81**, 041807 (2010).

[108] L. D. Landau and E. M. Lifshitz, *Theory of Elasticity*, Pergamon Press (1970).

[109] J. Deschamps, V. Kantsler, E. Segre, and V. Steinberg, "Dynamics of a vesicle in general flow," *Proc. Natl. Acad. Sci. U.S.A.* **106**, 11444–11447 (2009).

[110] K. Baczynski, R. Lipowsky, and J. Kierfeld, "Stretching of buckled filaments by thermal fluctuations," *Phys. Rev. E* **76**, 061914 (2007).

[111] M. Emanuel, H. Mohrbach, M. Sayar, H. Schiessel, and I. M. Kulić, "Buckling of stiff polymers: Influence of thermal fluctuations," *Phys. Rev. E* **76**, 061907 (2007).

[112] M. Deng, L. Grinberg, B. Caswell, and G. E. Karniadakis, "Effects of thermal noise on the transitional dynamics of an inextensible elastic filament in stagnation flow," *Soft Matter* **11**, 4962 (2015).

[113] G. Agez, M. G. Clerc, and E. Louvergneaux, “Universal shape law of stochastic supercritical bifurcations: Theory and experiments,” *Phy. Rev. E* **77**, 026218 (2008).

[114] V. Schaller, C. Weber, C. Semmrich, E. Frey, and A. R. Bausch, “Polar patterns of driven filaments,” *Nature* **467**, 73–77 (2010).

[115] T. Sanchez, D. Chen, S. DeCamp, M. Heymann, and Z. Dogic, “Spontaneous motion in hierarchically assembled active matter,” *Nature* **491**, 431–434 (2012).

[116] N. Quennouz, *Déformation et transport d’un filament élastique dans un écoulement cellulaire visqueux*, Ph.D. thesis, Université Paris IV (2013).

[117] M. F. Shlesinger, J. Klafter, and G. Zumofen, “Above, below and beyond Brownian motion,” *Amer. J. Phys.* **67**, 1253–1259 (1999).

[118] A. M. Lacasta, J. M. Sancho, A. H. Romero, I. M. Sokolov, and K. Lindenberg, “From subdiffusion to superdiffusion of particles on solid surfaces,” *Phys. Rev. E* **70**, 051104 (2004).

[119] J.-P. Bouchaud and A. Georges, “Anomalous diffusion in disordered media: Statistical mechanisms, models and physical applications,” *Phys. Rep.* **195**, 127 – 293 (1990).

[120] Q. Xu, L. Feng, R. Sha, N. C. Seeman, and P. M. Chaikin, “Subdiffusion of a sticky particle on a surface,” *Phys. Rev. Lett.* **106**, 228102 (2011).

[121] J. S. Park and D. Saintillan, “From diffusive motion to local aggregation: Effect of surface contamination in dipolophoresis,” *Soft Matter* **7**, 10720 (2011).

[122] M. Doi and S. F. Edwards, *The Theory of Polymer Dynamics*, Oxford University Press (1986).

[123] V. E. Terrapon, Y. Dubief, P. Moin, E. S. G. Shaqfeh, and S. K. Lele, “Simulated polymer stretch in a turbulent flow using Brownian dynamics,” *J. Fluid Mech.* **504**, 61–71 (2004).

[124] J. S. Paschkewitz, Y. Dubief, and E. S. G. Shaqfeh, “The dynamic mechanism for turbulent drag reduction using rigid fibers based on Lagrangian conditional statistics,” *Phys. Fluids* **17**, 063102 (2005).

[125] D. L. Koch and E. S. G. Shaqfeh, “The instability of a dispersion of sedimenting spheroids,” *J. Fluid Mech.* **209**, 521–542 (1989).

[126] B. Metzger, É. Guazzelli, and J. E. Butler, “Large-scale streamers in the sedimentation of a dilute fiber suspension,” *Phys. Rev. Lett.* **95**, 164506 (2005).

[127] D. Saintillan, E. S. G. Shaqfeh, and E. Darve, "The growth of concentration fluctuations in dilute dispersions of orientable and deformable particles under sedimentation," *J. Fluid Mech.* **553**, 347–388 (2006).

[128] K. Gustavsson and A.-K. Tornberg, "Gravity induced sedimentation of slender fibers," *Phys. Fluids* **21**, 123301 (2009).

[129] S. Jung, S. E. Spagnolie, K. Parikh, M. Shelley, and A.-K. Tornberg, "Periodic sedimentation in a stokesian fluid," *Phys. Rev. E* **74**, 035302 (2006).

[130] E. J. Tozzi, C. T. Scott, D. Vahey, and D. J. Klingenberg, "Settling dynamics of asymmetric rigid fibers," *Phys. Fluids* **23**, 033301 (2011).

[131] J. Wang, E. J. Tozzi, M. D. Graham, and D. J. Klingenberg, "Flipping, scooping, and spinning: drift of rigid curved nonchiral fibers in simple shear flow," *Phys. Fluids* **24**, 123304 (2012).

[132] X. Xu and A. Nadim, "Deformation and orientation of an elastic slender body sedimenting in a viscous liquid," *Phys. Fluids* **6**, 2889 (1994).

[133] M. Cosentino Lagomarsino, I. Pagonabarraga, and C. P. Lowe, "Hydrodynamic induced deformation and orientation of a microscopic elastic filament," *Phys. Rev. Lett.* **94**, 148104 (2005).

[134] X. Schlagberger and R. R. Netz, "Orientation of elastic rods in homogeneous Stokes flow," *Europhys. Lett.* **70**, 129–135 (2005).

[135] A. E. H. Love, *A Treatise on the Mathematical Theory of Elasticity*, Cambridge University Press (1892).

[136] C. M. Bender and S. A. Orszag, *Advanced mathematical methods for scientists and engineers I: Asymptotic methods and perturbation theory*, volume 1, Springer Verlag (1999).

[137] B. Herzhaft, É. Guazzelli, M. B. Mackaplow, and E. S. G. Shaqfeh, "Experimental investigation of the sedimentation of a dilute fiber suspension," *Phys. Rev. Lett.* **77**, 290 (1996).

[138] B. Metzger, J. E. Butler, and É. Guazzelli, "Experimental investigation of the instability of a sedimenting suspension of fibres," *J. Fluid Mech.* **575**, 307–332 (2007).

[139] J. E. Butler and E. S. G. Shaqfeh, "Dynamic simulations of the inhomogeneous sedimentation of rigid fibres," *J. Fluid Mech.* **468**, 205–237 (2002).

[140] E. Kuusela, J. M. Lahtinen, and T. Ala-Nissila, "Collective effects in settling of spheroids under steady-state sedimentation," *Phys. Rev. Lett.* **90**, 094502 (2003).

[141] D. Saintillan, E. Darve, and E. S. G. Shaqfeh, "A smooth particle-mesh Ewald algorithm for Stokes suspension simulations: The sedimentation of fibers," *Phys. Fluids* **17**, 033301 (2005).

[142] A.-K. Tornberg and K. Gustavsson, "A numerical method for simulations of rigid fiber suspensions," *J. Comp. Phys.* **215**, 172–196 (2006).

[143] D. Saintillan, E. S. G. Shaqfeh, and E. Darve, "The effect of stratification on the wave number selection in the instability of sedimenting spheroids," *Phys. Fluids* **18**, 121503 (2006).

[144] D. Saintillan, E. S. G. Shaqfeh, and E. Darve, "Stabilization of a suspension of sedimenting rods by induced-charge electrophoresis," *Phys. Fluids* **18**, 121701 (2006).

[145] B. D. Hoffman and E. S. G. Shaqfeh, "The effect of Brownian motion on the stability of sedimenting suspensions of polarizable rods in an electric field," *J. Fluid Mech.* **624**, 361–388 (2009).

[146] A. Dahlkild, "Finite wavelength selection for the linear instability of a suspension of settling spheroids," *J. Fluid Mech.* **689**, 183–202 (2011).

[147] F. Zhang, A. Dahlkild, and F. Lundell, "Nonlinear disturbance growth during sedimentation of dilute fibre suspensions," *J. Fluid Mech.* **719**, 268–294 (2013).

[148] M. Manga and H. A. Stone, "Collective hydrodynamics of deformable drops and bubbles in dilute low Reynolds number suspensions," *J. Fluid Mech.* **300**, 231–263 (1995).

[149] A. Z. Zinchenko and R. H. Davis, "Large-scale simulations of concentrated emulsion flows," *Phil. Trans. R. Soc. Lond. A* **361**, 813–845 (2003).

[150] V. Narsimhan and E. S. G. Shaqfeh, "Lateral drift and concentration instability in a suspension of bubbles induced by marangoni stresses at zero reynolds number," *Phys. Fluids* **22**, 101702 (2010).

[151] R. Vishnampet and D. Saintillan, "Concentration instability of sedimenting spheres in a second-order fluid," *Phys. Fluids* **24**, 073302 (2012).

[152] L. H. Switzer III and D. J. Klingenberg, "Rheology of sheared flexible fiber suspensions via fiber-level simulations," *J. Rheol.* **47**, 759–778 (2003).

[153] T. Gao, R. Blackwell, M. A. Glaser, M. D. Betterton, and M. J. Shelley, "Multiscale polar theory of microtubule and motor-protein assemblies," *Phys. Rev. Lett.* **114**, 048101 (2015).

[154] M. Keshtkar, M. C. Heuzey, and P. J. Carreau, "Rheological behavior of fiber-filled model suspensions: effect of fiber flexibility," *J. Rheol.* **53**, 631–650 (2009).

[155] P. van der Schoot, "The nematic-smectic transition in suspensions of slightly flexible hard rods," *J. Phys. II* **6**, 1557–1569 (1996).

[156] C. Goubault, P. Jop, M. Fermigier, J. Baudry, E. Bertrand, and J. Bibette, "Flexible magnetic filaments as micromechanical sensors," *Phys. Rev. Lett.* **91**, 260802 (2003).

[157] M. G. L. van den Heuvel, R. Bondesan, M. Cosentino Lagomarsino, and C. Dekker, "Single-molecule observation of anomalous electrohydrodynamic orientation of microtubules," *Phys. Rev. Lett.* **101**, 118301 (2008).

[158] M. B. Mackaplow and E. S. G. Shaqfeh, "A numerical study of the sedimentation of fibre suspensions," *J. Fluid Mech.* **376**, 149–182 (1998).

[159] J. M. Ham and G. M. Homsy, "Hindered settling and hydrodynamic dispersion in quiescent sedimenting suspensions," *Intl. J. Multiphase Flow* **14**, 533–546 (1988).

[160] P. J. Mucha and M. P. Brenner, "Diffusivities and front propagation in sedimentation," *Phys. Fluids* **15**, 1305–1313 (2003).

[161] H. Hasimoto, "On the periodic fundamental solutions to the Stokes equations and their application to viscous flow past a cubic array of spheres," *J. Fluid Mech.* **5**, 317–328 (1959).

[162] O. G. Harlen, R. R. Sundararajakumar, and D. L. Koch, "Numerical simulations of a sphere settling through a suspension of neutrally buoyant fibres," *J. Fluid Mech.* **388**, 355–388 (1999).

[163] Y. Saad and M. H. Schultz, "GMRES: A generalized minimal residual algorithm for solving nonsymmetric linear systems," *SIAM J. Sci. Stat. Comp.* **7**, 856–869 (1986).

[164] M. Fixman, "Construction of Langevin forces in the simulation of hydrodynamic interaction," *Macromolecules* **19**, 1204–1207 (1986).

[165] D. Saintillan, E. Darve, and E. S. G. Shaqfeh, "Hydrodynamic interactions in the induced-charge electrophoresis of colloidal rod dispersions," *J. Fluid Mech.* **563**, 223–259 (2006).

[166] M. Fixman, "Simulation of polymer dynamics. I. General theory," *J. Chem. Phys.* **69**, 1527–1537 (1978).

[167] P. S. Grassia, E. J. Hinch, and L. C. Nitsche, "Computer simulations of Brownian motion of complex systems," *J. Fluid Mech.* **282**, 373–403 (1995).

[168] H. Ma and M. D. Graham, "Theory of shear-induced migration in dilute polymer solutions near solid boundaries," *Phys. Fluids* **17**, 083103 (2005).

[169] W. B. Russel, E. J. Hinch, L. G. Leal, and G. Tieffenbruck, "Rods falling near a vertical wall," *J. Fluid Mech.* **83**, 273–287 (1977).

[170] M. E. Staben, A. Z. Zinchenko, and R. H. Davis, "Motion of a particle between two parallel plane walls in low-Reynolds-number Poiseuille flow," *Phys. Fluids* **15**, 1711–1733 (2003).

[171] W. H. Mitchell and S. E. Spagnolie, "Sedimentation of spheroidal bodies near walls in viscous fluids: glancing, reversing, tumbling and sliding," *J. Fluid Mech.* **772**, 600–629 (2015).

[172] S. Pennathur and J. G. Santiago, "Electrokinetic transport in nanochannels. 1. Theory," *Anal. Chem.* **77**, 6772–6781 (2005).

[173] F. C. MacKintosh, J. Käs, and P. A. Janmey, "Elasticity of semiflexible biopolymer networks," *Phys. Rev. Lett.* **75**, 4425–4428 (1995).